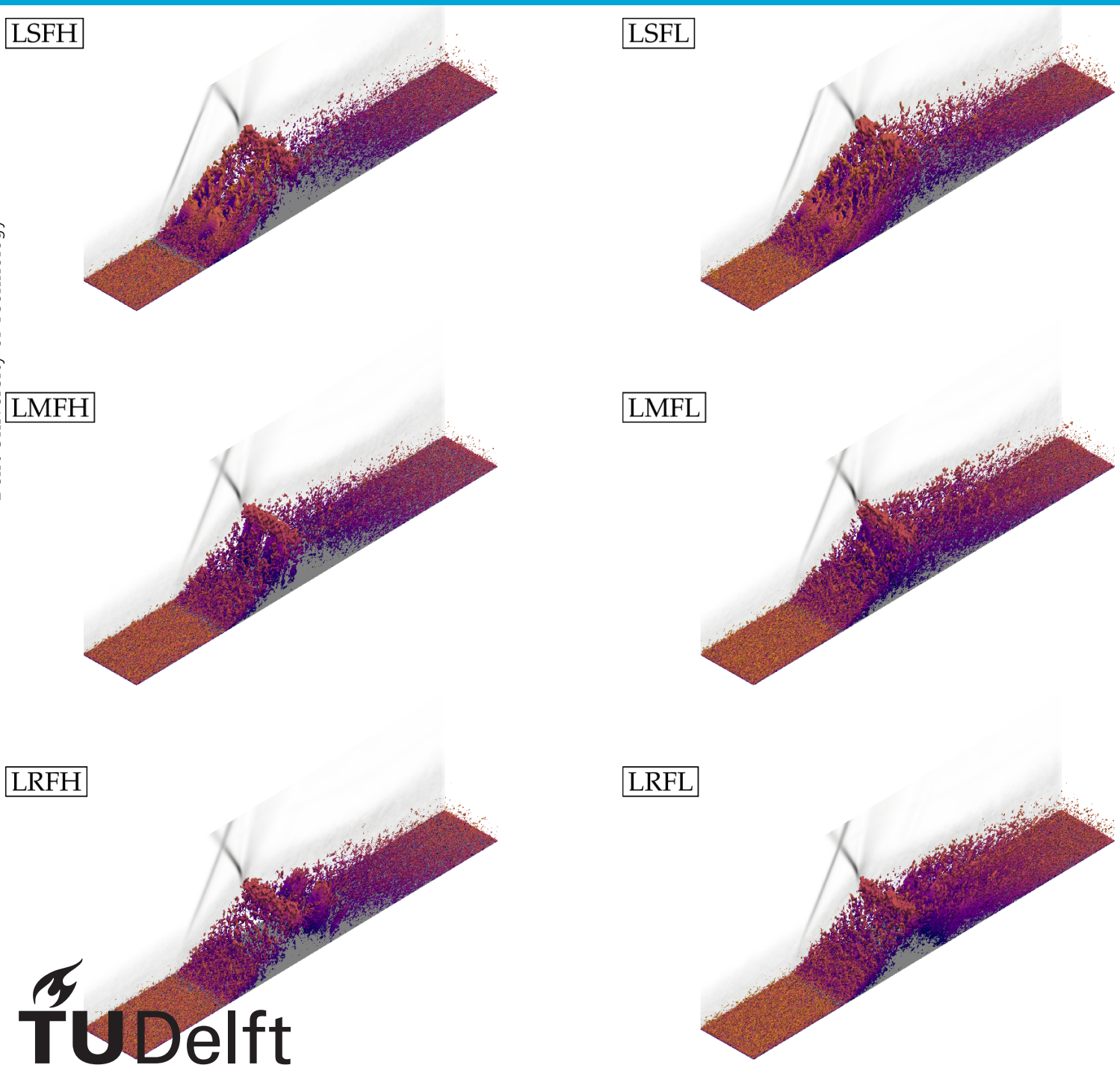
Jet Actuated Control of SWBLI

The Modulation of Separation Using Injection

K.P.M. Teunissen



Delft University of Technology

TU Delft

Jet Actuated Control of SWBLI

The Modulation of Separation Using Injection

by

K.P.M. Teunissen

Supervisor: Prof.Dr.Ir. Hickel
Assisted by: Luis Laguarda Sanchez
Project Duration: March, 2023 - July, 2025
Faculty: Faculty of Aerospace Engineering, Delft



Abstract

This study investigated the control of Shock-Wave/Boundary-Layer Interactions (SWBLI) using jet actuators at several locations, both upstream and within the separation bubble. Such interactions are critical in high-speed aerodynamic applications, where flow separation can lead to performance losses. Using Large Eddy Simulation (LES), the effects of injection on the separation region are studied. Where both the time-averaged as unsteady effects are examined. The results show that size reduction of the separation bubble is not effective when the actuators are placed within the separation region. However the actuators were able to modulate the large scale motion of the separation independent of the injection frequency or location. Indicating that the instabilities of SWBLI are potentially inherent and can be modulated from within the bubble. The proposed driving mechanism behind this are the pressure disturbances created by the injection, which is supported by the results.

Summary

This research investigated the ability to control a SWBLI system using jet actuators. While much of the existing literature focuses on upstream injection, this research focused on the actuation form within the separation bubble. Recent literature suggested that is a viable method of control and this could potentially provide insight into the mechanisms that cause the low-frequency instability that SWBLI experience.

A lower-fidelity parametric study was first conducted to identify promising actuator locations and frequencies. The ability to control was split into two aspects: reducing the separation bubble and modulation of unsteadiness. From this six cases were selected for high-fidelity LES which provided the wall-resolved data. Three locations were tested: at separation, at reattachment and in the middle of the bubble. For all these locations a low- and high-frequency case was tested.

The ability of the actuators to reduce the separation size when placed upstream of separation has been shown in several experimental studies. These studies also indicated that control from within the separation bubble was ineffective. The results of this study found that the separation size could indeed be reduced when actuators were placed upstream and that the influence of the actuators placed inside the bubble was minimal. With the actuators placed at reattachment being least effective. This is because the actuators function like vortex generators which need a high velocity airflow to create vortices.

However control ability was not merely defined by reduction of the separation size, the modulation of the unsteadiness was also considered. These results show that the ability of the modulation was independent of location and frequency. Although the large scale motion, especially of the separation shock, was diminished as the actuators moved further towards reattachment, the locking of the frequency was observed.

The proposed driving mechanism for this modulation is pressure disturbances created by the actuators, which fits all the data examined in this research. This is observed in the wall pressure signals and in the pressure variance.

The driving mechanism behind the actuator potentially provided more insight into the unsteadiness of the SWBLI system. By modulating the pressure inside the system, the unsteadiness could be modulated effectively, indicating that pressure fluctuations within the separation bubble could be the cause of the unsteadiness.

So while control from within the separation bubble is possible, it should not be used to reduce the size of the bubble. Not only is the possibility to do this very limited, it is also ineffective. It is more effective to modulate the low-frequency unsteadiness as this can likely be set to a range of different frequencies, without the downside of creating unwanted unsteadiness downstream of the bubble.

Contents

Abstract ii

Summary iii

1 Introduction 1
- 1.1 Influences on SWBLI characteristics . . . 2
- 1.2 Flow control . . . 4
  - 1.2.1 Passive control methods . . . 4
  - 1.2.2 Active control methods . . . 6
- 1.3 Contribution of this work . . . 7

2 Methodology 9
- 2.1 Governing equations . . . 9
- 2.2 Numerical method . . . 10
- 2.3 Flow configuration . . . 10
- 2.4 Boundary conditions . . . 11
  - 2.4.1 Jet actuator routine . . . 11
- 2.5 Flow settings . . . 14
- 2.6 Computational grid . . . 14
- 2.7 Data generation and processing . . . 15
  - 2.7.1 Snapshots . . . 15
  - 2.7.2 Statistics . . . 15
  - 2.7.3 Probes . . . 15
  - 2.7.4 Data processing . . . 15
- 2.8 Control outcome metrics . . . 15

3 Parametric Study Results 16
- 3.1 Parametric study setup . . . 16
  - 3.1.1 Frequency variation . . . 17
  - 3.1.2 Location variation . . . 17
- 3.2 Injection velocity influence . . . 18
- 3.3 Influence of injection location and frequency on flow organization . . . 19
  - 3.3.1 Injection location effects . . . 21
  - 3.3.2 Injection frequency effects . . . 22
- 3.4 Influence of injection location and frequency on unsteadiness . . . 24
  - 3.4.1 Injection location effects . . . 24
  - 3.4.2 Injection frequency effects . . . 25
- 3.5 Case selection . . . 28
  - 3.5.1 Peak power and frequency for selected cases . . . 29
  - 3.5.2 Power per range for selected cases . . . 30
  - 3.5.3 Coherence with injection velocity for selected cases . . . 31

4 Results 35
- 4.1 Control case settings . . . 35
- 4.2 Results I: Jet actuation effects on SWBLI organization . . . 35
  - 4.2.1 Instantaneous flow organization . . . 37
  - 4.2.2 Skin friction comparison . . . 44
  - 4.2.3 Probe and statistical wall data compared . . . 45
  - 4.2.4 Time-averaged flow organization . . . 46
  - 4.2.5 Bubble shape . . . 48
  - 4.2.6 Phase-averaged flow organization . . . 50

4.2.6.1 Peak-phase-averaged . . . 50
4.2.6.2 Injection-phase-averaged . . . 53
4.2.7 Reynolds stresses . . . 56
4.2.8 Pressure variance . . . 59
4.3 Results II: Jet actuation effects on SWBLI unsteadiness . . . 61
4.3.1 PSD maps . . . 61
4.3.2 Bubble motions compared . . . 63
4.3.3 PDFs of bubble motion . . . 64
4.3.4 PSDs of the bubble motion . . . 65
4.3.5 Injection velocity response . . . 67
4.3.6 Coherence comparison . . . 68
4.3.7 Probe pressure signals . . . 70
4.3.8 Cross-correlation comparison . . . 72
4.3.9 Power per frequency range . . . 73
4.3.10 Peak power and frequency . . . 75
4.4 Results summary . . . 77

5 Discussion **78**

6 Conclusion **83**
6.0.1 Future Recommendations . . . 84

References **86**

A Data Analysis **91**
A.1 Non-Dimensionalization . . . 91
A.2 Statistics . . . 92
A.3 Instantaneous . . . 96
A.3.1 Spatial Characteristics Analysis . . . 96
A.3.2 Vorticity . . . 97
A.3.3 Pressure and Temperature . . . 98
A.3.4 Skin Friction . . . 98
A.4 Spectral Characteristics Analysis . . . 102
A.4.1 Power Spectral Density . . . 102
A.4.2 Probability Density Function . . . 108
A.5 Probe Analysis . . . 108
A.5.1 Probe PSD . . . 110
A.5.2 Probe PDF . . . 112

B Analysis Software Tips **113**
B.1 Software version control . . . 113
B.2 Computational resource management . . . 113
B.3 HPC usage . . . 113
B.4 Figure updating . . . 113

C Production Result Figures **114**
C.1 Instantaneous . . . 114
C.2 Instantaneous flow organization in 3D . . . 126
C.3 Phase-averaged flow organization in 3D . . . 130
C.3.1 Peak-phase-averaged . . . 130
C.3.2 Injection-phase-averaged . . . 133
C.4 Statistics . . . 142
C.4.1 Reynolds Stresses . . . 147
C.5 Cross-Correlation . . . 152
C.5.1 Bubble metrics . . . 152
C.5.2 Injection velocity cross-correlation . . . 153
C.5.3 Pressure cross-correlation . . . 154
C.5.3.1 Pressure at separation . . . 154
C.5.3.2 Pressure at actuator . . . 154

C.5.4 Pressure cross-correlation separated per cases 159
C.6 Results separated per production case 166
C.6.1 Reference case 166
C.6.2 Case LSFH 170
C.6.3 Case LSFL 176
C.6.4 Case LMFH 182
C.6.5 Case LMFL 188
C.6.6 Case LRFH 194
C.6.7 Case LRFL 200

List of Figures

1.1 SWBLI Schematic . . . 1

2.1 Computational domain setup. . . . 10
2.2 Jet actuator design variables. . . . 13
2.3 Block distribution . . . 14

3.1 Combinations of AL and AF used in the parametric study. . . . 18
3.2 Results for PIV variation at AL = 4.096115 δ_0 and AF = 0.098765 St_L. . . . 19
3.3 Results for AL variation for all simulations in the parametric study. . . . 20
3.4 Results for AF variation for all simulations in the parametric study. . . . 21
3.5 Results for AL variation for Group 1and Group 4. . . . 22
3.6 Results for AF variation for Group 2and Group 3. . . . 23
3.7 Peak and total PSD power for varying control locations for Group 1. . . . 25
3.8 Total PSD power for AF variation for Group 2 and Group 3. . . . 26
3.9 Peak PSD for AF variation for Group 2 and Group 3. . . . 27
3.10 Schematic for the placement of the actuators for the different control cases. . . . 29
3.11 Peak PSD power and corresponding frequency of p'_w for all coarse cases. . . . 30
3.12 Power per frequency range for p'_w for all coarse cases. . . . 31
3.13 Coherence and phase between bubble motion and injection velocity for case LSFHp. . . . 32
3.14 Coherence and phase between bubble motion and injection velocity for case LSFLp. . . . 32
3.15 Coherence and phase between bubble motion and injection velocity for case LMFHp. . . . 33
3.16 Coherence and phase between bubble motion and injection velocity for case LMFLp.. . . . 33
3.17 Coherence and phase between bubble motion and injection velocity for case LRFLp. . . . 34

4.1 Instantaneous numerical Schlieren comparison. . . . 38
4.2 Instantaneous wall temperature comparison. . . . 39
4.3 Instantaneous C_f comparison. . . . 40
4.4 Instantaneous vortical structures visualized with the λ_{ci} criterion. . . . 42
4.5 Span-wise slices of v velocity at peak injection for case LSFL. . . . 43
4.6 Instantaneous bubble shape viewed from above. . . . 44
4.7 Time- and spanwise-averaged skin friction compared. . . . 45
4.8 Comparison of temporally averaged probe data for the production cases. . . . 46
4.9 Time- and spanwise-averaged streamwise velocity comparison. . . . 47
4.10 Numerical Schlieren based on time- and spanwise-averaged ρ comparison. . . . 48
4.11 Isocontours of $\langle u \rangle = 0$ . . . 49
4.12 Peak-phase-averaged vortical structures visualized with the λ_{ci} criterion. . . . 51
4.13 Peak-phase-averaged ω_x. . . . 52
4.14 Peak-phase-averaged bubble shape. . . . 53
4.15 Injection-phase-averaged vortical structures visualized with the λ_{ci} for case LSFH.. . . . 54
4.16 Injection-phase-averaged iso-surfaces of ω_x for case LSFH. . . . 55
4.17 Injection-phase-averaged iso-contours of ω_x for case LSFL. . . . 55
4.18 Time- and spanwise-averaged streamwise Reynolds stress $u'u'$ comparison.. . . . 57
4.19 Time- and spanwise-averaged wall-normal Reynolds stress $v'v'$ comparison. . . . 58
4.20 Time- and spanwise-averaged Reynolds shear stress $u'v'$ comparison. . . . 59
4.21 Time- and spanwise-averaged $p'p'$ comparison. . . . 60
4.22 Log scaled PSD map of p'_w at the center line for the production cases. . . . 62
4.23 Bubble motion cases compared . . . 63
4.24 Bubble motion PDFs cases compared. . . . 65
4.25 PSD of bubble motion for the production case compared.. . . . 66

4.26 x_{sep}, x_{rea} and IV over the simulation time for case LSFL. . . . 68
4.27 Coherence and phase between bubble motion and injection velocity for all control cases. . . . 68
4.28 Coherence and phase of bubble motion for production cases. . . . 70
4.29 Wall-pressure for case LSFL. . . . 71
4.30 Cross-correlation with injection velocity for the high-frequency production cases. . . . 73
4.31 Power per frequency range for p'_w for all production cases. . . . 74
4.32 Peak PSD power and corresponding frequency of p'_w for all production cases. . . . 76

A.1 Statistical boundary layer profile for reference production case. . . . 91
A.2 Time- and spanwise-averaged velocity fields. . . . 93
A.3 Time- and spanwise-averaged T, ρ and p fields. . . . 94
A.4 Time- and spanwise-averaged Reynolds stresses: $u'u'$, $v'v'$ and $w'w'$. . . . 94
A.5 RMS of the time- and spanwise-averaged velocity fluctuations. . . . 95
A.6 Instantaneous span-wise velocity fields. . . . 96
A.7 Instantaneous wall velocity fields. . . . 97
A.8 Instantaneous span-wise vorticity fields. . . . 98
A.9 Instantaneous wall pressure fields. . . . 98
A.10 Instantaneous wall temperature fields. . . . 98
A.11 Instantaneous skin friction computation. . . . 99
A.12 Instantaneous pressure field. . . . 100
A.13 Instantaneous span-wise averaged pressure field. . . . 100
A.14 Instantaneous span-wise averaged pressure gradient. . . . 101
A.15 Instantaneous T field. . . . 101
A.16 Bubble motion for the Reference case. . . . 102
A.17 PSD of bubble motion for the reference production case. . . . 104
A.18 Power per frequency range of bubble motion for the reference production simulation. . . . 105
A.19 Coherence and phase of bubble motion for the Reference case. . . . 106
A.20 Coherence and phase between bubble motion and injection velocity for case LMFH. . . . 107
A.21 PDFs of the bubble motion for the Reference case. . . . 108
A.22 Temporally averaged probe data for the reference production simulation. . . . 109
A.23 Statistical wall data along the centerline for the reference production simulation. . . . 110
A.24 PSDs of p'_w for the reference production simulation. . . . 110
A.25 PSDs of p'_w for the reference production simulation at common locations. . . . 111
A.26 Log scaled PSD map of wall-pressure at the center line for the Reference case. . . . 111
A.27 Power per frequency range for p'_w. . . . 111
A.28 Power of dominant p'_w PSD with corresponding frequency for the Referencecase. . . . 112
A.29 PDFs of p'_w for the reference production simulation. . . . 112

C.1 Instantaneous$u$ field comparison. . . . 115
C.2 Instantaneous v field comparison. . . . 116
C.3 Instantaneous w field comparison. . . . 117
C.4 Instantaneous span-wise temperature comparison. . . . 118
C.5 Instantaneous p field comparison middle of span. . . . 119
C.6 Instantaneous p field through actuator comparison. . . . 120
C.7 Instantaneous u velocity at the wall comparison. . . . 121
C.8 Instantaneous v velocity at the wall comparison. . . . 122
C.9 Instantaneous w velocity at the wall comparison. . . . 123
C.10 Instantaneous p field at the wall comparison. . . . 124
C.11 Instantaneous span-wise mean skin friction from snapshots. . . . 125
C.12 Instantaneous λ_{ci} criterion, viewed from above. . . . 126
C.13 Instantaneous isocontour of ω_x. . . . 127
C.14 Instantaneous isocontour of ω_x, viewed from above. . . . 128
C.15 Instantaneous bubble shape visualized with the iso-contour of $u = 0$. . . . 129
C.16 Peak-phase-averaged λ_{ci} criterion, viewed from above. . . . 130
C.17 Peak-phase-averaged bubble shape, viewed from above. . . . 131
C.18 Peak-phase-averaged ω_x, viewed from above. . . . 132

C.19 Injection-phase-averaged vortical structures visualized with the λ_{ci} criterion for case LSFL. . . 133
C.20 Injection-phase-averaged vortical structures visualized with the λ_{ci} criterion for case LMFH. . 134
C.21 Injection-phase-averaged vortical structures visualized with the λ_{ci} criterion for case LMFL. . 135
C.22 Injection-phase-averaged vortical structures visualized with the λ_{ci} criterion for case LRFH. . 136
C.23 Injection-phase-averaged vortical structures visualized with the λ_{ci} criterion for case LRFL. . . 136
C.24 Injection-phase-averaged ω_x for case LMFH. 137
C.25 Injection-phase-averaged ω_x for case LMFL. 137
C.26 Injection-phase-averaged ω_x for case LRFH. 138
C.27 Injection-phase-averaged ω_x for case LRFL. 138
C.28 Injection-phase-averaged bubble shape for case LSFH. 139
C.29 Injection-phase-averaged bubble shape for case LSFL. 139
C.30 Injection-phase-averaged bubble shape for case LMFH. 140
C.31 Injection-phase-averaged bubble shape for case LMFL. 140
C.32 Injection-phase-averaged bubble shape forcase LRFH. 141
C.33 Injection-phase-averaged bubble shape for case LRFL. 141
C.34 Time- and spanwise-averaged wall-normal velocity v field comparison. 142
C.35 Time- and spanwise-averaged spanwise velocity w field comparison. 143
C.36 Time- and spanwise-averaged density ρ comparison. 144
C.37 Time- and spanwise-averaged temperature T comparison. 145
C.38 Time- and spanwise-averaged pressure p comparison. 146
C.39 Time- and spanwise-averaged Reynolds wall-normal stress $w'w'$ comparison. 147
C.40 Time- and spanwise-averaged RMS of $u'u'$ comparison. 148
C.41 Time- and spanwise-averaged RMS of $v'v'$ for production cases. 149
C.42 Time- and spanwise-averaged RMS of $w'w'$ comparison. 150
C.43 Wall-pressure gradient for production cases. 151
C.44 Cross-correlation between different bubble metrics high-frequency 152
C.45 Cross-correlation between different bubble metrics low-frequency 153
C.46 Cross-correlation with injection velocity for the low-frequency production cases. 154
C.47 Cross-correlation with pressure at S_x and the other probes for the high-frequency cases. . . . 155
C.48 Cross-correlation with pressure at S_x and the other probes for the low-frequency cases. . . . 156
C.49 Cross-correlation with pressure at AL and the other probes for the high-frequency cases. . . . 157
C.50 Cross-correlation with pressure at AL and the other probes for the low-frequency cases. . . . 158
C.51 Cross-correlation with pressure at S_x and the other probes for case Reference. 159
C.52 Cross-correlation with pressure at S_x and the other probes for case LSFH. 160
C.53 Cross-correlation with pressure at S_x and the other probes for case LSFL. 161
C.54 Cross-correlation with pressure at S_x and the other probes for case LMFH. 162
C.55 Cross-correlation with pressure at S_x and the other probes for case LMFL. 163
C.56 Cross-correlation with pressure at S_x and the other probes for case LRFH. 164
C.57 Cross-correlation with pressure at S_x and the other probes for case LRFL. 165
C.58 Bubble motion for case Reference. 166
C.59 PSD of bubble motion for case Reference. 167
C.60 PSDs of p'_w for the case Reference at common locations. 167
C.61 Span-wise slices of v velocity at peak injection for case Reference. 168
C.62 Wall-pressure for case Reference obtained by probes. 169
C.63 Bubble motion for case LSFH. 170
C.64 PSD of bubble motion for case LSFH. 171
C.65 Coherence and phase between bubble motion and injection velocity for LSFH. 172
C.66 Coherence and phase of bubble motion for production case LSFH. 173
C.67 PSDs of p'_w for the case LSFHat selected locations. 173
C.68 PSDs of p'_w for the case LSFH at common locations. 173
C.69 PDFs of p'_w for case LSFH. 174
C.70 Span-wise slices of v velocity at peak injection for case LSFH. 174
C.71 Wall-pressure for case LSFH obtained by probes. 175
C.72 Bubble motion for case LSFL. 176
C.73 PSD of bubble motion for case LSFL. 177
C.74 Coherence and phase between bubble motion and injection velocity for LSFL. 178

C.75 Coherence and phase of bubble motion for production case LSFL. 179
C.76 PSDs of p'_w for the case LSFLat selected locations. 179
C.77 PSDs of p'_w for the case LSFL at common locations. 179
C.78 PDFs of p'_w for case LSFL. 180
C.79 Span-wise slices of v velocity at peak injection for case LSFL. 180
C.80 Wall-pressure for case LSFL obtained by probes. 181
C.81 Bubble motion for case LMFH. 182
C.82 PSD of bubble motion for case LMFH. 183
C.83 Coherence and phase between bubble motion and injection velocity for LMFH. 184
C.84 Coherence and phase of bubble motion for production case LMFH. 185
C.85 PSDs of p'_w for the case LMFH at common locations. 185
C.86 PDFs of p'_w for case LMFH. 185
C.87 Span-wise slices of v velocity at peak injection for case LMFH. 186
C.88 Wall-pressure for case LMFH obtained by probes. 187
C.89 Bubble motion for case LMFL. 188
C.90 PSD of bubble motion for case LMFL. 189
C.91 Coherence and phase between bubble motion and injection velocity for LMFL. 190
C.92 Coherence and phase of bubble motion for production case LMFL. 191
C.93 PDFs of p'_w for case LMFL. 191
C.94 Span-wise slices of v velocity at peak injection for case LMFL. 192
C.95 Wall-pressure for case LMFL obtained by probes. 193
C.96 Bubble motion for case LRFH. 194
C.97 PSD of bubble motion for case LRFH. 195
C.98 Coherence and phase between bubble motion and injection velocity for LRFH. 196
C.99 Coherence and phase of bubble motion for production case LRFH. 197
C.100 PSDs of p'_w for the case LRFHat selected locations. 197
C.101 PSDs of p'_w for case LRFHat common locations. 197
C.102 PDFs of p'_w for case LRFH. 198
C.103 Span-wise slices of v velocity at peak injection for case LRFH. 198
C.104 Wall-pressure for case LRFH obtained by probes. 199
C.105 Bubble motion for case LRFL. 200
C.106 PSD of bubble motion for case LRFL. 201
C.107 Coherence and phase between bubble motion and injection velocity for LRFL. 202
C.108 Coherence and phase of bubble motion for production case LRFL. 203
C.109 PSDs of p'_w for the case LRFL at common locations. 203
C.110 PSDs of p'_w for the LRFLcase. 203
C.111 PDFs of p'_w for case LRFL. 204
C.112 Span-wise slices of v velocity at peak injection for case LRFL. 204
C.113 Wall-pressure for case LRFL obtained by probes. 205

List of Tables

1.1 Overview of several SWBLI control methods. 4

2.1 Computational Domain Settings. 11
2.2 Jet Actuator Example Design Variables for Figure 2.2 12
2.3 Flow Settings. 14
2.4 Inflow plane parameters and grid size. 14

3.1 Jet Actuator Constant Variables 17
3.2 Parametric Study Groups. 18
3.3 Selected Cases. 28

4.1 Production Case Settings. 35
4.2 Relevant interaction topology parameters. 36
4.3 Results of the snapshot averages for production cases. 36
4.4 Topological properties of the separation bubble. 49

A.1 Production frequency ranges. 104

Acronyms

AD Actuator Diameter. 12, 16, 17, 18, 28, 35

AF Actuator Frequency. vii, 12, 13, 16, 17, 18, 19, 21, 23, 24, 26, 27, 28, 30, 32, 33, 34, 35, 62, 66, 76

AL Actuator Location. vii, ix, 13, 16, 17, 18, 19, 20, 21, 22, 24, 28, 30, 31, 35, 38, 39, 40, 47, 48, 49, 50, 57, 58, 59, 60, 62, 69, 74, 76, 115, 116, 117, 118, 119, 120, 121, 122, 123, 124, 142, 143, 144, 145, 146, 147, 148, 149, 150, 157, 158

ALDM Adaptive Local Deconvolution Method. 10

AS Actuator Shape. 13, 17

ASR Aspect Ratio. 19, 20, 21, 22, 23, 24, 25, 26, 27, 63, 65, 66, 100, 101, 102, 103, 104, 105, 108, 166, 167, 170, 171, 176, 177, 182, 183, 188, 189, 194, 195, 200, 201

BFS Backward-Facing Step. 2

BL Boundary Layer. 4

BLB Boundary Layer Bleeding. 4, 5, 6

BLC Boundary Layer Control. 4

CFD Computational Fluid Dynamics. 7

DAF Double Actuator Frequency. 12

DMD Dynamic Mode Decomposition. 81, 84, 102

DNS Direct Numerical Simulation. 3, 10

FFS Forward-Facing Step. 2

IA Injection Angle. 12, 16, 17

IP Injection Pressure. 12, 17, 35, 45, 46, 71, 79, 80

IPPR Integrated PSD power per frequency range. 103, 110, 112

IT Injection Temperature. 12, 17, 35, 45, 46, 71

IV Injection Velocity. viii, 11, 12, 13, 17, 18, 19, 20, 21, 28, 31, 32, 33, 34, 35, 67, 68, 69, 71, 72, 80, 172, 178, 184, 190, 196, 202

IZ Interaction Zone. 4

LES Large Eddy Simulation. ii, iii, 3, 7, 10, 79, 83

MeJ Membrane Jet. 4

MHD Magnetohydrodynamic. 4

MiJ Micro-Jets. 4, 6

MVG Micro-Vortex Generators. 4, 5, 6, 79, 83

NA Number of Actuators. 12, 16, 17, 18, 28, 35

PDF Probability Density Function. v, vii, viii, ix, x, 7, 64, 65, 66, 102, 108, 112, 174, 180, 185, 191, 198, 204

PEF Piezo Electric Flaps. 4, 6, 8

PFT Pressure Feedback Technique. 4, 5, 7, 8

PIV Peak Injection Velocity. vii, 12, 16, 17, 18, 19

PP Pulse Period. 12, 13

PPJ Pulsed Plasma Jet. 4, 7

PPR Pulse Period Ratio. 13, 16, 17

PPS Pulse Phase Start. 13, 16, 17

PSD Power Spectral Density. v, vii, viii, ix, x, 7, 24, 25, 26, 27, 29, 61, 62, 63, 65, 66, 67, 68, 69, 73, 74, 75, 76, 79, 80, 84, 92, 102, 103, 104, 108, 110, 111, 112, 167, 171, 173, 177, 179, 183, 185, 189, 195, 197, 201, 203

RANS Reynolds Averaged Navier-Stokes. 10

RMS Root Mean Square. viii, ix, 3, 45, 46, 58, 93, 95, 108, 109, 110, 149

SC Shock Control. 4

SCB Shock Control Bump. 4, 6

SGS Subgrid Scale. 10

SM Surface Morphing. 4, 6, 8

SPOD Spectral Proper Orthogonal Decomposition. 81, 84

SR Shock Reflection. 4, 5

ST Start Time. 12, 13, 17

SWBLI Shock-Wave/Boundary-Layer Interactions. ii, iii, v, xi, 1, 2, 3, 4, 5, 7, 15, 24, 29, 61, 63, 65, 67, 69, 70, 71, 73, 75, 76, 78, 79, 81, 82, 83, 84, 92

TB Tangential Blowing. 4, 6

TPP Total Pulse Period. 13, 16, 17

URANS Unsteady Reynolds Averaged Navier-Stokes. 10

VG Vortex Generators. 5

VR Volumetric Ratio. 100

List of Symbols

C_f Skin friction coefficient. vii, 39, 40, 42, 44, 45, 98, 99

C_{xy} Coherence between PSD signals. 103, 105

δ_0 Statistical boundary layer thickness. vii, 11, 14, 18, 19, 22, 24, 35, 36, 37, 64, 75, 91, 92, 93

δ^* Boundary layer displacement. 92

E Total energy. 9

η Separation shock angle. 19, 20, 21, 22, 23, 24, 25, 26, 27, 36, 37, 63, 64, 65, 66, 100, 101, 102, 103, 104, 105, 108, 166, 167, 170, 171, 176, 177, 182, 183, 188, 189, 194, 195, 200, 201

γ Specific heat ratio. 9

H Shape factor. 92

H_{sep} Separation bubble height. 19, 20, 21, 22, 23, 24, 25, 26, 27, 36, 48, 63, 65, 66, 99, 100, 101, 102, 103, 104, 105, 108, 166, 167, 170, 171, 176, 177, 182, 183, 188, 189, 194, 195, 200, 201

κ Thermal conductivity. 9

L_a Separation to apex length. 100

L_{imp} Inviscid impinging length. 11, 14

L_{sep} Separation length. 19, 20, 21, 22, 23, 24, 25, 26, 27, 36, 48, 63, 64, 65, 66, 67, 92, 99, 100, 101, 102, 103, 104, 105, 108, 166, 167, 170, 171, 176, 177, 182, 183, 188, 189, 194, 195, 200, 201

L_w Wedge length. 11

L_x Domain length. 11

L_y Domain height. 11

L_z Domain width. 11

Ma Mach number. 14

μ_F Dynamic viscosity. 9

μ_∞ Reference dynamic viscosity. 9

$|\omega|$ Vorticity magnitude. 97

$\vec{\omega}$ Vorticity vector. 97

ω_x Streamwise vorticity component. vii, viii, ix, 51, 52, 53, 54, 55, 97, 98, 127, 128, 132, 137, 138

ω_y Wall-normal vorticity component. 97, 98

ω_z Spanwise vorticity component. 97, 98

p Pressure. viii, ix, 9, 12, 15, 59, 93, 94, 100, 119, 120, 124, 146

p_0 Stagnation pressure. 14

ϕ Incident angle of oblique impinging shock wave. 14

∇p Pressure gradient. 100

$p'p'$ Pressure variance. vii, 45, 46, 60, 61, 81

Pr Prandtl number. 9

p_∞ Free-stream pressure. 17, 35, 45, 46, 108

p_w Wall pressure. 45, 46, 108, 109, 110

p'_w Wall pressure fluctuations. vii, viii, ix, x, 29, 30, 31, 45, 46, 61, 62, 67, 73, 74, 75, 76, 79, 80, 108, 109, 110, 111, 112, 167, 173, 174, 179, 180, 185, 191, 197, 198, 203, 204

q_i Heat flux. 9

$\mathcal{R}$ Specific gas constant. 9

R Radius of the curvature of the streamline. 92

Re Reynolds number. 14

ρ Density. vii, viii, ix, 9, 15, 46, 48, 93, 94, 144

ρ_∞ Free-stream density. 46

ρu Momentum. 9

SG_y Shock generator height. 11

σ^2 Variance. 108, 109, 110

St_L Strouhal number based on statistical separation length. vii, 12, 17, 18, 19, 23, 24, 28, 61, 69, 78, 80, 92, 103, 104

S_x Separation shock location. ix, 19, 20, 21, 22, 23, 24, 25, 26, 27, 36, 37, 63, 64, 65, 66, 67, 68, 69, 72, 75, 80, 100, 101, 102, 103, 104, 105, 108, 155, 156, 159, 160, 161, 162, 163, 164, 165, 166, 167, 170, 171, 176, 177, 182, 183, 188, 189, 194, 195, 200, 201

T Temperature. viii, ix, 9, 12, 15, 93, 94, 101, 145

τ_{ij} Viscous stress tensor. 9

θ Boundary layer momentum. 92

θ_p injection phase. 50, 51, 53, 54

ϑ Flow deflection angle. 11

θ_{xy} Phase between PSD signals. 104, 105

T_r Recovery temperature. 3, 4

T_∞ Free-stream temperature. 9, 35, 46, 108

T_s Static temperature. 9

T_w Wall temperature. 3, 4, 46, 108, 109, 110

u Streamwise velocity component. viii, 15, 44, 46, 47, 48, 49, 50, 53, 59, 92, 93, 94, 95, 96, 97, 98, 100, 115, 121, 129, 131, 139, 140, 141

u_i Velocity vector. 9

u' Streamwise velocity fluctuations. 92

$u'u'$ Streamwise Reynolds stress. vii, viii, 56, 57, 58, 60, 61, 93, 94

$u'v'$ Reynolds shear stress. vii, 56, 59, 61

u_∞ Free-stream velocity. 14, 91, 96, 97

v Wall-normal velocity component. vii, viii, ix, x, 15, 41, 43, 52, 56, 77, 92, 93, 96, 97, 116, 122, 142, 168, 174, 180, 186, 192, 198, 204

V_a Bubble volume before the apex point. 100

v' Wall-normal velocity fluctuations. 56

$v'v'$ Wall-normal Reynolds stress. vii, viii, ix, 56, 58, 61, 81, 93, 94, 149

V_{sep} Separation bubble volume. 19, 20, 21, 22, 23, 25, 26, 27, 36, 48, 63, 64, 65, 66, 99, 100, 101, 102, 103, 104, 105, 108, 166, 167, 170, 171, 176, 177, 182, 183, 188, 189, 194, 195, 200, 201

w Spanwise velocity component. viii, ix, 15, 92, 93, 96, 97, 117, 123, 143

$w'w'$ Spanwise Reynolds stress. viii, 56, 58, 61, 93, 94

x_a Apex point. 49, 100

x_{imp} Inviscid impinging location. 11, 36, 49, 91

x_{rea} Reattachment point. viii, 19, 20, 21, 22, 23, 24, 25, 26, 27, 32, 33, 34, 35, 36, 63, 64, 65, 66, 67, 68, 69, 72, 80, 98, 99, 101, 102, 103, 104, 105, 108, 166, 167, 170, 171, 172, 176, 177, 178, 182, 183, 184, 188, 189, 190, 194, 195, 196, 200, 201, 202

x_{sep} Separation point. viii, 19, 20, 21, 22, 23, 24, 25, 26, 27, 32, 33, 34, 35, 36, 44, 45, 63, 64, 65, 66, 67, 68, 69, 72, 80, 98, 99, 101, 102, 103, 104, 105, 108, 166, 167, 170, 171, 172, 176, 177, 178, 182, 183, 184, 188, 189, 190, 194, 195, 196, 200, 201, 202

1

Introduction

Shock-Wave/Boundary-Layer Interactions (SWBLI) are a phenomena of interest in high speed aerodynamics and has been for several decades [1, 2]. It plays a significant role in several systems such as supersonic inlets [3, 4], over-expanding nozzles [5] and high-speed airfoils [6, 7]. A particularly interesting case in SWBLI is where an impinging shock is sufficiently strong to cause flow separation [8, 9], as illustrated in Figure 1.1. The shock generates a sudden increase in pressure, which propagates upstream causing the boundary layer to thicken and eventually separate [8, 9, 10]. Typically the shock strength required to separate the flow with a turbulent boundary layer occur at Mach 1.3 and higher [10]. In between the separated boundary layer and the wall forms an area of recirculation called the separation bubble. At the point where the thickening of the boundary layer starts, which is well upstream of the impinging location of the incident shock [8], the incoming flow experiences an upward change of direction which results in a compression fan forming a shock known as the separation shock. This shock interacts with the incident shock and both continue traveling as two transmitted shocks [8]. The transmitted shock originating from the incident shock penetrates the shear layer and reflects at the sonic line as an expansion fan [8]. This, in turn, changes the direction of the free shear layer from upwards to downwards towards the wall. The reattachment process results in another compression fan forming the reattachment shock.

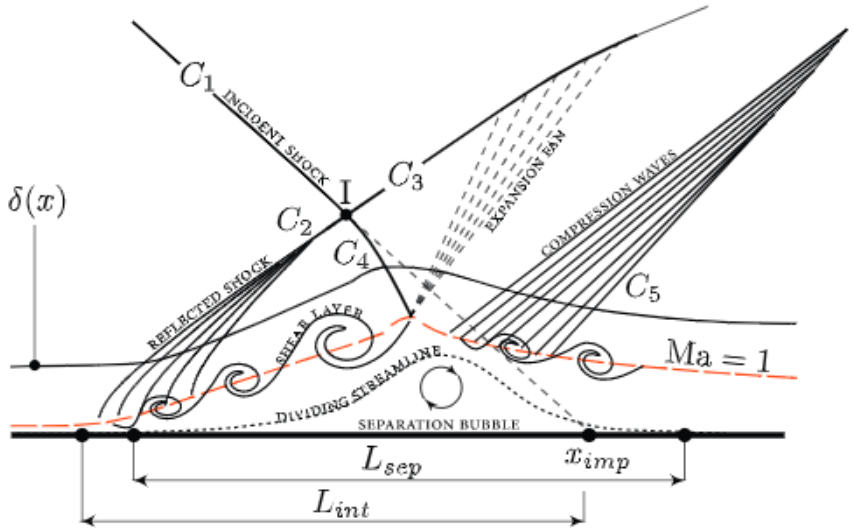


Figure 1.1: Schematic of the oblique shock-wave/boundary-layer interaction with mean separation [8].

There are several negative effects of SWBLI besides flow separation including increased drag, wave drag, pressure loss, shock oscillations and additional viscous dissipation [11]. However flow separation

will be the main focus of this research. The reverse-flow region in SWBLI is highly unsteady with a wide range of energetic frequencies [9, 12]. High-frequency unsteadiness is associated with turbulent velocity fluctuations, medium-frequency dynamics are related to vortex shedding and the low-frequency unsteadiness is associated with pressure fluctuations, related to motions of the shock and the separation bubble [12, 13]. While these frequency ranges have different characteristics the large scale motion associated with the low-frequency pressure fluctuations is generally the most concerning from an engineering standpoint, since unsteady pressure and friction forces could be in the resonant frequency of the structure, possibly leading to early failure due to fatigue [9, 14, 15].

Low-frequency unsteadiness is a characteristic of SWBLI which pose a serious problem for aircraft design [1, 11, 16]. Low-frequency unsteadiness is associated with pressure fluctuations with a typical frequency of two orders of magnitude less than the upstream boundary layer fluctuations [8, 9, 14]. Several unstable mechanisms resulting from these pressure fluctuations can be observed such as the progressive expansion and contraction of the separation bubble, also known as breathing [14], oscillations of the shock system, especially the separation shock and vortex shedding [13].

The mechanisms which are the origin of the low-frequency unsteadiness of SWBLI have been the focus of several experimental and numerical investigations [1, 11, 17, 18, 19, 20, 21]. However no consensus on the origin of these mechanisms has been reached yet [13, 15, 19]. There are two schools of thought: numerous papers suggest that intrinsic mechanisms, such as bubble breathing, global instability or acoustic feedback, are the cause of this unsteadiness, whereas other papers suggest that perturbations in the incoming flow are amplified by the system. For a more in-depth analysis of these theories the paper by Clemens and Narayanaswamy [19] is recommended.

For as long as the phenomena has been studied, solutions for control of the separation bubble and its the low-frequency behavior have been studied [22, 23]. Numerous methods have been proposed and tried while new and improved techniques are tested continuously [3, 11, 24, 25, 26, 27, 28, 29], yet there is no definitive answer for an optimal method of control. Several methods will be discussed in more detail in section 1.2. A part of this outstanding question on the optimal control method is the placement. Up to this point most research has been focused on control before or during separation [30, 31, 32, 33], however little is known about the possibility to control from within and especially near the reattachment point, while research has shown a correlation between the separation and reattachment locations [17, 18, 19]. For this reason control near the reattachment location will be one of the focuses of this research, additionally this location is chosen as it might provide further insight into the mechanisms of the bubble dynamics.

While in most practical applications SWBLI are caused by an impinging shock, as shown in Figure 1.1, for experiments and numerical simulations different methods can be used. This is done so that certain effects or techniques can be tested. Canonically there are four different methods to simulate SWBLI: impinging shock [9, 12, 34, 35, 36, 37], compression ramp [33, 38, 39], Backward-Facing Step (BFS)[40] and Forward-Facing Step (FFS) [13, 41]. As mentioned before, in case of an impinging shock, separation is caused by an adverse pressure gradient. Both the compression ramp and the FFS cases rely on a contraction of geometry to recreate the separation. For the BFS case a sudden expansion of the geometry is used create separation [13]. FFS cases are mainly used to study the mechanisms of separation while BFS cases are used to study the mechanisms of reattachment. As this research is interested in the influence of control on both separation and reattachment, the impinging setup is used.

1.1. Influences on SWBLI characteristics

There are several different factors which influence the characteristics of SWBLI. Some are more influential than others and the method of influence also varies. This section will shortly discuss the factors that should be taken into consideration.

SWBLI can either have a laminar or turbulent incoming boundary layer. Current research is done on both cases with a laminar boundary layer [15, 35, 37, 38] and cases with a turbulent boundary layer [9, 12, 16, 18, 22, 31, 33, 34, 36, 39, 42, 43, 44, 45, 46]. This research will examine the effects of control with a turbulent boundary layer, since it closer represents practical applications [22]. The main difference between laminar and turbulent boundary layers is the ease of separation. Laminar boundary layers are easier to separate than turbulent boundary layers under the same conditions [10], although easier

separation does help in the rehabilitation of the boundary layer. As only a small pressure rise is needed to separate the laminar boundary layer, the separation height remains smaller but is more elongated making it easier for the boundary layer to reattach [10]. However because the control method is applied within the separation bubble and the behavior of this bubble is of interest, a larger bubble is desired. In practical applications a smaller separation bubble is desirable as this has less induced drag, tends to be stabler and allows for easier reattachment of the flow [47, 48].

The Reynolds number is used for the translation between experimental and numerical investigations and is of paramount importance when the extrapolation is made to practical applications [49]. The influence of Reynolds number on SWBLI has been the topic of several experimental and numerical investigations[1, 19], in which both Direct Numerical Simulation (DNS) [50] and Large Eddy Simulation (LES) [51] have been used. These investigations have led to an adequate understanding of the influence on the interaction dynamics. In low Reynolds number cases with high shock strength, strong separation is to be expected whereas high Reynolds number boundary layer flows are expected to exhibit higher resistance to separation [19]. For low Reynolds number interactions the shockfoot of the separation shock does not penetrate the boundary layer as deeply as is the case for high Reynolds number cases [9, 51]. There is also a distinct peak in the Root Mean Square (RMS) of the wall-pressure fluctuations around the mean separation location [9]. Not only is the point of separation is dependent on Reynolds number, the frequency dynamics within the boundary layer are influenced by the Reynolds number [47, 52]. The separation length is influenced implicitly by the Reynolds number as this is commonly used to scale the boundary layer thickness [41].

Similar to the Reynolds number, the Mach number has a strong influence of the point of separation. An increase in Mach number will lead to a different shock strength. A higher Mach number will reduce the impinging shock angle, which moves the whole interaction region further downstream [52, 53]. Even with a constant deflection angle the flow separation is postponed leading to a reduction in separation length [52, 53]. The shape of the bubble becomes more asymmetric as the Mach number increases, with particular displacement upstream [54, 55]. The aspect ratio also increases while the bubble size is reduced [37, 54]. Furthermore the increase in Mach number causes coherent stream-wise structures to be elongated in stream-wise direction [54]. Finally the higher Mach number cases seem to be less perturbed by upstream noise [20, 54].

The shock strength is defined as the ratio of the pressures directly upstream and downstream of the shock. The shock strength is determined by the both the upstream Mach number and the deflection angle. Increasing the Mach number will result in a stronger impinging shock if the deflection angle is kept constant, for more information please refer to Chapter 9 of J.D. Anderson [56]. Equally, an increase in flow deflection angle induced by the shock generator will result in a stronger shock when the Mach number is kept constant [57]. Lee and Gross [58] found that an increase in shock angle significantly increased the height of the separation and the length by as much as 78%. An increased flow angle causes the flow inside and downstream of the separation bubble to be hotter, and there is a larger pressure increase across the shock system. An increase in the region and intensity of Reynolds normal stresses when the shock angle was increased [57, 58]. Increasing the shock angle for low Reynolds number interactions has the effect of elongating the separation length [47], the longer bubble also becomes more asymmetric with the leading side becoming longer than the trailing side [37], and increasing the aspect ratio. The length of the separation bubble also increases with shock intensity, which is defined as the ratio between the pressure jump across the incident shock and the incoming wall-shear stress [53]. The probability of flow separation increases with increasing shock strength [47]. For a more in depth information on the effect of shock intensity see the study by Dupont et al. [59] in which they performed experiments for a wide range of shock intensities by varying the wedge angle at a fixed Reynolds number and constant Mach number. For more information on the effect of the impinging shock strength and angle on the separation shock angle please refer to Baskaran et al. [57].

Wall temperature is another factor which can significantly influence the separation bubble behavior [60]. Research focused on the heating or cooling of the flow via the wall usually uses the ratio of wall temperature (T_w) and recovery temperature (T_r). Where T_r is the resulting temperature of the flow at the wall when the wall is adiabatic [61]. The ratio between these two temperatures is given by $s = \frac{T_w}{T_r}$. There are three types of ratios: cold $s < 1$, adiabatic $s = 1$ and hot $s > 1$. These three ratios have vastly different influence on the flow. Cooling reduces the characteristics scales of the upstream influence

and the length of the separation region. While heating increases the length of the separation region [22, 60]. Even though cooling might be a feasible method of control, it does have drawbacks, and it is not the focus of this research. Additionally in practical applications, supersonic speeds, the T_r can be considered equal to T_w as there is low heat exchange at the wall [61].

1.2. Flow control

As mentioned before, research into methods to control the negative effects of SWBLI have been proposed and tested [4, 22, 23], almost since they were first discovered. Mechanisms of control can be classified in terms of their deployment location which can either be in the incoming boundary layer or the interaction region. The SWBLI control techniques can be classified as either shock control, in which an attempt is made to diffuse one strong shock into multiple shocks and with that reduce the total pressure loss, or boundary layer control in which the incoming boundary layer is energized. Flow control methods for SWBLI can be further classified as either passive or active, characterized by their energy requirement. Active control methods require an additional source of energy where passive control methods use the energy of the flow itself [11]. Several passive control methods with their advantages, drawbacks and working principles are discussed in subsection 1.2.1, for active control this is discussed in subsection 1.2.2. An overview of several control methods are given in Table 1.1.

Table 1.1: Overview of several control methods of SWBLI with an indication of active or passive control, Boundary Layer Control (BLC) or Shock Control (SC) and Boundary Layer (BL) or Interaction Zone (IZ).

Control Methods	Active/Passive	Technique	Location	References
Boundary Layer Bleeding (BLB)	Active/Passive	BLC	IZ	[4, 62, 63]
Pressure Feedback Technique (PFT)	Passive	BLC	BL and IZ	[8, 25]
Shock Reflection (SR)	Passive	SC	Above BL	[23]
Micro-Vortex Generators (MVG)	Passive	BLC	BL	[30, 31, 32]
Shock Control Bump (SCB)	Passive	SC	IZ	[64]
Surface Morphing (SM)	Active/Passive	SC	IZ	[29, 46]
Tangential Blowing (TB)	Active	BLC	BL	[22]
Piezo Electric Flaps (PEF)	Active	BLC	IZ	[65, 66]
Micro-Jets (MiJ)	Active	BLC	BL and IZ	[26]
Pulsed Plasma Jet (PPJ)	Active	BLC	BL and IZ	[33, 38, 45, 67]
Membrane Jet (MeJ)	Active	BLC	BL and IZ	[68, 69]
Magnetohydrodynamic (MHD)	Active	BLC	BL and IZ	[70]

1.2.1. Passive control methods

Passive control methods can be a simple and effective method of control, easily implemented as it requires no additional energy, however as these are usually optimized of a single situation, their application is limited.

Boundary Layer Bleeding

Boundary Layer Bleeding (BLB) was one of the first techniques to be proposed [4] and is also the conventionally applied method [11, 32]. This relatively simple method is based on an effort to reduce the growth of the boundary layer by removing low momentum portions of the boundary layer through small holes in the wall. Although this method is simple to implement, it can not be applied without a penalty to non-separating boundary layers. Because the removed mass flow is usually not reintroduced into the flow, a small part of the mass flow is lost. This drawback is especially prevalent in supersonic engine inlets as this would mean a larger inlet would be required to achieve the same mass flow through the engine. Additionally the bled off air will be vented outside the vehicle incurring additional drag [3, 4].

Determining factors in the effectiveness of this control method are the inclination angle of the bleed hole, the distance between holes and the diameter of the hole. Additionally the ratio of the depth to the

diameter of the bleed hole is of importance, as a small ratio will cause the separation bubble to extend into the bleed chamber causing flow instability [63].

Pressure Feedback Technique

The Pressure Feedback Technique (PFT) is an attempt to address the problems of BLB as discussed above. Rather than excreting the bled off mass-flow this is reintroduced upstream of the separation region. By placing a channel between the separation region and a point upstream of the separation region, the pressure difference between the two points can be used to move the flow. This is similar to a feedback system hence the name [8, 25]. The placement of the inlet and outlet holes is of great importance for this method. Pasquariello et al. [8] found that when PFT is applied in the rear of the separation region it is most efficient in reducing the overall turbulence levels. It was also able to significantly reduce the separation-shock dynamics and the flapping motion of the incident-transmitted shock. This is a simple yet effective method although it does disturb the boundary layer unnecessarily when separation has not occurred.

Shock Reflection

Shock Reflection (SR) uses a plate placed in the path of the impinging shock, parallel to the wall, so that the shock reflects of it. This type of control is mainly focused on trying to reduce the adverse pressure gradient by reducing the shock strength [23]. Especially if holes are drilled into the plate to disperse the shock and thus the adverse pressure gradient. Even though this method should be relatively effective, it is dependent on a specific situation and thus is inflexible. This drawback is likely the reason it has not been widely applied. Another reason might be the fact that this is an impractical method to apply in physical situations as the plate needs to be suspended in the middle of the incoming flow and not at the wall.

Micro-Vortex Generators

Micro-Vortex Generators (MVG) are passive a control method which has been extensively tested both experimentally and computationally [30]. There are several forms of MVG such as microvanes, co-rotating ramps and counter rotating ramps. However for simplicity the grouping name of MVG is used when discussing the working principles of the devices unless specifically defined.

Conventional Vortex Generators (VG), with a height of order of the boundary layer thickness, create more drag compared to MVG with a height of about 40% of the boundary layer thickness, while both are able to reduce the boundary layer shape factor, making it less susceptible to separation [32]. Another benefit of MVG compared to conventional VG is that the counter rotating vortices remain within the boundary layer over a significant distance [32]. While the size of the devices differs, the working principle of MVG and VG is the same.

Whereas BLB and PFT attempt to improve the boundary layer by decreasing the adverse pressure gradient by physically removing mass flow, MVG intend to improve the boundary layer by energizing the flow using entrained high-momentum flow towards the wall while simultaneously depositing the low-momentum flow close to the wall to outside the boundary [32]. Another contribution to the prevention of separation is the oblique shock generated by the micro-ramps as this softens the pressure gradient through the SWBLI [30].

One of the drawbacks of MVG control is that it can only be optimized for one situation [25, 32] and the placement of the MVG is crucial to the effectiveness of the method. MVG should be placed before the separation point [31]. Placing them too close to the impingement location of the incident shock wave will significantly reduce the effectiveness. If the location and size of the MVG is chosen incorrectly, it could lead to an enlargement of the separation size [25]. Another drawback is the effect increasing and decreasing boundary layer momentum has on the wave and viscous drag which will both increase [46].

Vortex generation can also be done actively using jets such as is done in [71], this will be further discussed in the subsection 1.2.2. For an overview of several types and applications of MVG, please refer to John C. Lin [72].

Shock Control Bump

While most of the above mentioned techniques focus on improving the boundary layer, Shock Control Bump (SCB) is a method that focuses on reducing the shock strength [46, 64]. In certain situations such the reflected shock can even be completely eliminated if the wall, downstream of impinging location, is parallel to the nominal flow direction behind the imping shock [55]. This is a method which is highly dependent on the accuracy of hitting the bump and thus sensitive to Mach number variations[55]. A slightly more robust method is to use a bump which is used to split the strong impinging shock into a system of weaker shocks [55]. For example when using a concave shock bump, the separation and reattachment shocks both become a series of compression waves [55]. This is a simple method, but it does not perform well when the impinging location changes with respect to the optimal location, in some cases it can even have negative influence [46, 64]. The shape of the bump also has implications on the effectiveness of this control method and is a topic of current research [55].

1.2.2. Active control methods

Active control techniques are becoming more prevalent with the advancement of different and improved techniques. Even though they require an additional source of energy to function, they do provide the possibility for application in a wider range of situations.

Surface Morphing

Surface Morphing (SM) is a technique based on SCB and attempts to tackle the most prominent drawback which is the effectiveness when the shock location changes. Applying this method is very effective in reducing the flow separation and mitigating low-frequency unsteadiness. This method of control is constrained by the structural integrity of the surface and will thus be limited [46]. This method shows promising results in the controlling of the low-frequency dynamics of the separation bubble [73].

Tangential Blowing

Tangential Blowing (TB) is a technique where high speed fluid is injected into the boundary layer. This energizing of the boundary layer is similar to the effect MVG try to achieve. This is a very effective method in reducing the separation bubble size and is easy to control [11]. However this high speed fluid injection does come at a cost. In practical applications air would have to be pressurized by the engine which requires a significant amount of energy, effectively decreasing the efficiency of the system as a whole.

Piezo Electric Flaps

One of the drawbacks of BLB is the unnecessary removal of mass flow of a non-separated boundary layer. In order to reduce this loss Piezo Electric Flaps (PEF) actuators could be used [65]. These are closed during normal operation and opened at will during separation, giving greater control over when and where mass flow should be removed.

Micro-Jets

Whereas TB is done with an external source for the high speed fluid, Micro-Jets (MiJ) use in internal source for their flow injection. The working principle of the micro-jets are very similar to that of the MVG, they are even referred to as microjet vortex generators [26]. They generate a rotating vortex pair through the interaction between the injected fluid and the boundary layer, mixing the high and low energy flow layers of the boundary layer which improves the resistance to the adverse pressure gradient [26]. Just like MVG the microjet also generates shock wave which can weaken the separation shock.

A benefit of micro-jets over static MVG is that these can be essentially removed when turned off. A drawback is that they use additional energy.

Pulsed Plasma Jet

Pulsed Plasma Jet (PPJ)s can be used similar to micro-jets, however they can also be applied in different situations garnering them a significant amount of attention. Conventionally plasma actuators are deployed upstream in an effort to excite the the flow. However recent studies [33], have shown that plasma jets can also be used in the separated region and their effectiveness in stabilizing the low-frequency unsteadiness of SWBLI has been shown [11]. There are different methods to create this plasma, however as this research project pertains simulations, these are indistinguishable.

Benefits of plasma jets include their ability to work at different frequencies up to a maximum of around 5 kHz [74]. Additionally the heating of the flow does inject additional energy into the low energy flow.

When not in use, similar to micro-jets, the actuators do influence the flow although this is minimal. This can be seen in the results of Greene et al. [38] where the influence on the displacement of the separation line is shown comparing the situation where the jets are off versus when they are active. This shows that there is little influence on the flow behavior when the jets are not active.

1.3. Contribution of this work

While research into SWBLI an its control has been ongoing for decades, most of the current research is focused on the upstream turbulent boundary layer or the reduction in size of the bubble via suction or control bumps. This research aims to contribute to the current body of knowledge by exploring the effectiveness of forced injection. Building on previous studies by Narayanaswamy et al. [33] and Greene et al. [38], the aim is to analyze the effects at different locations, frequencies and using a numerical method, specifically Large Eddy Simulation (LES), rather than experiments. As the mechanisms driving low-frequency unsteadiness are still not well understood, exploring the effectiveness of forcing at different frequencies and locations might provide further insight. Using a numerical method allows for a more in depth lower-fidelity parametric study and more detailed analysis of high-fidelity results. Especially the high-fidelity simulations potentially provide great insight into the driving mechanisms of the instability. Although the high-fidelity simulations will be based on the lower-fidelity parametric study, based on recent results, forcing inside the separation bubble is of particular interest, as this might provide more insight into certain feedback mechanisms that are potentially at play.

Previous research found that the low-frequency motion of the separation bubble could be influenced from within. Pasquariello et al. [8] found that PFT is able to reduce the overall turbulence levels and the low-frequency motion when applied in the separation region. Laguarda et al. [73] used a flexible panel which altered the low-frequency dynamics. These studies indicate that there is a method of altering the low-frequency dynamics of the system and while these use passive methods of control an active method of control could potentially modulate the low-frequency motion. Even though Narayanaswamy et al. [33] concluded that control from within the separation region has limited impact on the low-frequency unsteadiness of SWBLI, the frequencies, locations and analysis tools used in this research will provide more evidence for or against this conclusion.

There are numerous variables and parameters that can obtained and studied from the Computational Fluid Dynamics (CFD) simulations. To gage the effectiveness of the control method's location and frequency, there are several metrics that can be examined and compared to a simulation where no control is applied, also called the Reference case. An obvious metric is the size of the separation zone, however this is not the only one. Metrics include separation and reattachment points, length, height, aspect ratio, location of the separation shock and separation shock angle. While these metrics are mainly conserned with the size and shape of the bubble, plotting these metrics over time will provide insight into the bubble unsteadiness. Additionally wall pressure signals can provide insight into the mechanisms at play. To analyze the low-frequency dynamics, the bubble metrics and pressure signals are analyzed using different techniques such as Probability Density Function (PDF), Power Spectral Density (PSD), coherence and cross-correlations. Finally the forcing effects can be isolated by phase-averaging to provide further insight into the internal mechanics of the system.

In order enact forcing, all the control methods discussed in section 1.2 were considered. The choice is mainly based on the abilities of the method and less on the drawbacks because this research is focused on the viability of control at different frequencies and locations and not on the practical application. As

the energy of the flow in the recirculation region is very low, a passive control method is not suitable. In practical applications an active control method can be more difficult to implement which is why passive control methods are usually preferred [11]. While the practical application is a secondary requirement, it is important enough to only consider real control methods. SM is an effective method for reducing the separation bubble and mitigating the low-frequency motion [46]. One drawback of using SM in viability simulations is the requirement for more complex simulations. PEF could work similarly to PFT but do not provide additional benefits when separation has occurred. Tangential blowing can only be applied in the upstream boundary layer and thus is not applicable in this research. This leaves just synthetic jets, which include micro-jets and pulsed plasma jets. While these are very similar in workings, the plasma jet would be most suitable as it has been proven to be able to control the low-frequency motion and work within the separation region [33]. Pulsed plasma jets give the option to vary the frequency of control, which might play a significant role in the control of the low-frequency motion and it has the additional benefit that it is able to heat the flow, injecting additional energy into the low-energy flow.

2

Methodology

2.1. Governing equations

The flow is governed by the three-dimensional compressible Navier-Stokes equations: continuity Equation 2.1, momentum Equation 2.2 and total energy Equation 2.3,

$$\frac{\partial \rho}{\partial t} + \frac{\partial}{\partial x_i}\left(\rho u_i\right) = 0, \tag{2.1}$$

$$\frac{\partial \rho u_j}{\partial t} + \frac{\partial}{\partial x_i}\left(\rho u_i u_j + \delta_{ij} p - \tau_{ij}\right) = 0, \tag{2.2}$$

$$\frac{\partial E}{\partial t} + \frac{\partial}{\partial x_i}\left(u_i E + u_i p - u_j \tau_{ij} + q_i\right) = 0, \tag{2.3}$$

where ρ is density, ρu is momentum, p is pressure and u_i is the velocity vector. E is total energy defined by

$$E = \frac{p}{\gamma - 1} + \frac{1}{2}\rho u_i u_i. \tag{2.4}$$

The viscous stress tensor τ_{ij} follows the Stokes hypothesis for a Newtonian fluid given in by

$$\tau_{ij} = \mu_F \left(\frac{\partial u_i}{\partial x_j} + \frac{\partial u_j}{\partial x_i} - \frac{2}{3}\delta_{ij}\frac{\partial u_k}{\partial x_k} \right), \tag{2.5}$$

where dynamic viscosity μ_F is the dynamic shear viscosity of the fluid. Finally the heat flux q_i is determined by Fourier's Law

$$q_i = -\kappa \frac{\partial T}{\partial x_i}, \tag{2.6}$$

where T is temperature and thermal conductivity κ is modeled as

$$\kappa = \frac{\gamma \mathcal{R}}{(\gamma - 1)Pr}\mu_F, \tag{2.7}$$

with a constant molecular Prandtl number, $Pr = 0.72$, specific gas constant $\mathcal{R} = 287.05$ Jkg^{-1}K^{-1} and specific heat ratio $\gamma = 1.4$. μ_F is a function of static temperature T_s and free-stream temperature T_∞ =160.15 given by

$$\mu_F = \mu_\infty \sqrt{\frac{T_s}{T_\infty}}, \tag{2.8}$$

where reference dynamic viscosity μ_∞.

In the simulations the fluid will be modeled as a perfect gas following the ideal gas equation

$$p = \rho \mathcal{R} T. \tag{2.9}$$

2.2. Numerical method

The compressible Navier-Stokes equations given in section 2.1 are solved using the Adaptive Local Deconvolution Method (ALDM) for the discretization of the convective fluxes [75]. ALDM is a nonlinear finite volume method that provides a physically consistent Subgrid Scale (SGS) turbulence model for implicit LES. ALDM is an efficient and reliable turbulence model which has been validated using numerous problems [76]. The simulations have been performed with INCA [77], an in-house solver. Even though LES might be less expensive than DNS, it still requires a significant amount of computational power. For this reason an efficient and robust model is required and why the implicit LES using a ALDM is used [76]. The simulations have been performed on DelftBlue [78].

2.3. Flow configuration

As alluded to section 1.3 this project will use LES to obtain the desired results and not use DNS, Reynolds Averaged Navier-Stokes (RANS) or Unsteady Reynolds Averaged Navier-Stokes (URANS). LES is the method of turbulence modeling chosen for this research because it is less computationally expensive than DNS, while still providing a time-accurate prediction of the unsteady flow. While DNS would resolve all the scales of the problem, in LES the large and energetic scales in the flow are well resolved by the computational grid while the effect of the unresolved scales is accounted for with a subgrid scale model. It is important to note that the simulations performed are wall-resolved LES, meaning that the mesh near the wall resolves all scales, functionally acting like a DNS. Even though RANS and URANS are computationally even less expensive than LES, these lower-fidelity approaches have shown to have limited predictive capabilities when it comes to mean flow and they can not predict the time evolution of the flow.

During this research simulations were performed on a coarse mesh and a finer mesh. The difference between the coarse and the fine mesh is the number and size of cells used to capture the flow behavior, where the fine mesh uses a significantly more cells. The computational power required per cell is similar between simulations, however the significant increase in cells means that running simulations on a course mesh takes significantly less computational power. Storing data is also done per cell, meaning that not only the required computational power is greater for a finer mesh, the required storage per saved data point is also much higher. For these reasons a coarser mesh is used initial parametric study. However the results of these coarse simulations are less accurate than simulations run on a finer mesh.

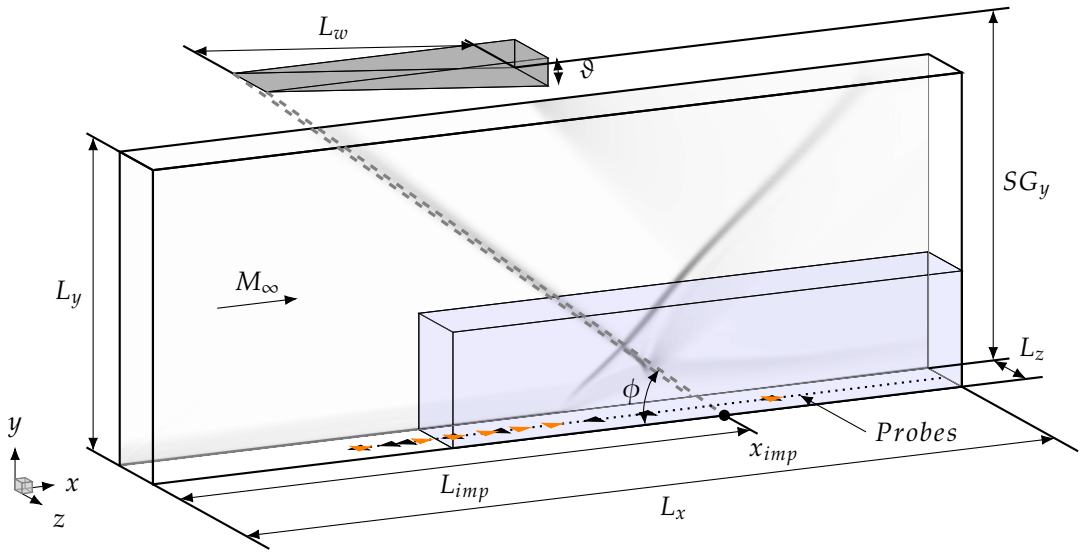


Figure 2.1: Computational domain setup. The blue box indicates the sub-domain used for snapshots. The dotted line indicates the centerline along which the probes are placed. Common probe locations are indicated by ▲ and selected probe locations are indicated by ▼.

The baseline setup of will consider a turbulent boundary layer where the shock is generated by a wedge placed above the wall. A schematic of the computational domain is given in Figure 2.1 and the values of the computational domain are given in Table 2.1

Table 2.1: Computational Domain Settings.

Symbol	Value	Dimension
L_x	236	mm
L_z	20.8	mm
L_y	86	mm
SG_y	96	mm
L_w	82.5369	mm
ϑ	10.6608	°

2.4. Boundary conditions

A non-reflecting boundary condition, based on the Riemann invariants, is used for both the top and outflow boundaries, while on the spanwise boundaries of the domain periodicity is imposed. By prescribing conditions based on the Rankine-Hugoniot relations and Prandtl-Meyer theory at the top boundary, the incident shock and trailing-edge expansion fan are created. The boundary condition of the inflow plane uses a digital filter technique to prescribe adequate turbulent boundary conditions with well-defined space and time correlations. For more details on the implementation of this digital filter technique see the publication of Laguarda & Hickel [79]. In order to ensure proper relaxation of the boundary layer, to an equilibrium state, the location of impingement, inviscid impinging location (x_{imp}) is located far downstream of the inflow plane, giving inviscid impinging length (L_{imp}) = 27.8837 δ_0. And finally the bottom boundary condition is based on an adiabatic wall, however as this is where the actuators are placed this is a special boundary, which will be discussed in more detail in subsection 2.4.1.

2.4.1. Jet actuator routine

The simulation software INCA did not have a jet actuator function at the time this research was conducted and therefore this had to be implemented. Due to time constraints the jet actuator function could not be experimentally validated. The implementation of the jet actuator is based on a adiabatic wall boundary condition, to eliminate the effect of wall-cooling, where the velocity of the injection is set based on the pulsing behavior of the jets. It first checks if there are any active jet actuator, if this is true the velocity of the active actuators is calculated. The Injection Velocity (IV) during one pulse is based on a parabola because this is a reasonable assumption based on experimental tests of plasma jets [38, 80] and analytical models [45, 81, 82, 83], but mainly because this gives a quick but smooth ramp up towards the maximum value. This is more suitable for simulations where an abrupt change in the wall velocity might cause problems with convergence. Additionally the implementation of analytical models would require significantly more effort while the effects could be very similar. After calculating the IV, the cells on the boundary are checked to see if they are inside an active actuator, and if they are the wall velocity is set based on the distance to the center of the active actuator. This method is efficient and does not require much overhead.

This method is a simplification of the experimental setups in which plasma is created which is injected into the domain[33, 38]. Therefore there are some significant differences between real experimental setups and the simulated cases. Firstly the holes of the plasma actuator jet exit are not present in the simulations, however the impact of these holes on the boundary layer is minimal as discussed in section 1.2.2. Therefore the decision was made to not model the holes in the simulations as this would be significantly more difficult and require more cells to accurately capture the geometry. Another difference is the suction created by the plasma jet actuator after injection. As it sucks in air to fill the cavity before the next pulse. This is also not modeled in the jet actuator routine for simplicity, however this can be done by simply computing the total volume that needs to be sucked in and setting a negative wall velocity to achieve this volume. As shown by studies such as Pasquariello et al. [8], suction can significantly impact the behavior of the bubble, so this could be point which makes the results of this study differ from studies done by Narayanaswamy et al. [33] and Greene et al. [38].

The jet actuator routine used to mimic the behavior of plasma jets has several design variables to its control system. These give the user options to test different use cases. All these variables are listed below and represented visually in Figure 2.2 using the settings given in Table 2.2.

Table 2.2: Jet Actuator Example Design Variables for Figure 2.2

Design Variable	Value	Dimension
NA	4	-
IV	250.0	m s^{-1}
AF	0.2137	kHz

Number of Actuators

This integer number describes the Number of Actuators (NA) which are used in the simulation. The NA is equally spaced in the span-wise direction, where the distance from the side of the domain is equal to the space between the actuators.

Actuator Diameter

The Actuator Diameter (AD) is the diameter of each actuator. All actuators will have the same diameter. The diameter of a single actuator is multiplied with the NA before the simulation starts to ensure that all actuators fit fully inside the domain.

Peak Injection Velocity

Peak Injection Velocity (PIV) is the absolute peak amplitude of the IV, indicated as PIV in Figure 2.2. As the IV, calculated at every time-step, is based on the a parabola, only a peak velocity is used as an input.

Injection Pressure and Temperature

Besides setting the PIV, the penetration and energy of the actuators can be adjusted with p and T using Injection Pressure (IP) and Injection Temperature (IT) respectively. While the PIV is a constant, the values of IP and IT are reference values, which is done for stability reasons. Rather than setting a constant value, Riemann invariants are solved inside the actuator to ensure a stable solution for the combination of the injection velocity, pressure and temperature. Therefore these values are not indicated in Figure 2.2.

Injection Angle

The Injection Angle (IA) angle at which the fluid is injected. This value is not indicated in Figure 2.2 as it is has not been used in the calculation of the IV. The value of the IA is calculated with respect to the wall, so an IA of 0° would be parallel to the wall and an IA of 90° would be orthogonal to the wall.

Actuator Frequency

The Actuator Frequency (AF), which is usually given as a function of Strouhal number based on separation length (St_L) rather than a frequency, controls the time between two pulses of the same actuator as shown in Figure 2.2. The actuators in the simulations are setup to pulse alternately. So if two actuators are used, one is pulsed first and then the other. When more than two actuators are used, every other actuator is pulsed at the same moment. This is done to get be able to have an effective pulsing frequency which is twice as high as the actual pulsing frequency, effectively getting Double Actuator Frequency (DAF) or Pulse Period (PP), which is also indicated in Figure 2.2. This allows for a broader spectra of frequencies to be used while the pulsing frequency of every individual actuator could still be achieved physically. This has been explained in section 1.2.2.

Start Time

The Start Time (ST) is the amount of time the pulsing of the actuators start after the simulation has started. Indicated in Figure 2.2 by ST, it can be used to delay the start of injection. This is useful if a flow still needs to be developed. However when a flow is already initialized this value should be set to 0 so that it starts immediately.

Pulse Period Ratio

The Pulse Period Ratio (PPR) is the ratio of the amount of the PP which is used for one pulse. Or how much of the pulse length is used for the injection time. Indicated in Figure 2.2 by PPR, it can be used to shorten the time of one pulse and thus increase the time between pulses while not shortening the amount of the pulse that is done.

Total Pulse Period

The Total Pulse Period (TPP) is an indication of much of π of a 2π phase is done during the period. Basically this is how much of a full rotation is done during one period. So a value of 2 would result in one full pulse. A value larger than 2 would result in a shorter pulse. For example a value of 4 would have resulted in two pulses, however the function only allows alternating pulses, not several in sequence. A value smaller than 2, would result in an incomplete pulse. So for example a value of 1 would result in half a pulse, till the peak velocity and after that the velocity would be 0.

Pulse Phase Start

The Pulse Phase Start (PPS) is the amount of one TPP elapses before injection starts. This allows the user to start later in the phase, which would result in a higher IV at the start of the injection. However this can result in instability. For all simulations this value has been set to 0 and therefore is not indicated in Figure 2.2.

Actuator Location

The Actuator Location (AL) is the placement of the actuators. The input value is the is used as the stream-wise value of the centerline of the actuators.

Actuator Shape

The shape of the actuator, Actuator Shape (AS), can also be changed. There are three different options: a constant distribution, gaussian and parabolic. This value indicates the shape the values set on the wall in the actuator. It does not change the shape of the injection profile as shown in Figure 2.2. While it is most realistic to use the Gaussian distribution [45], the tests in this study were performed using the parabolic distribution, the results of this can be seen in Figure C.8 . The constant distribution sets the wall velocity values the same for the entire actuator plane.

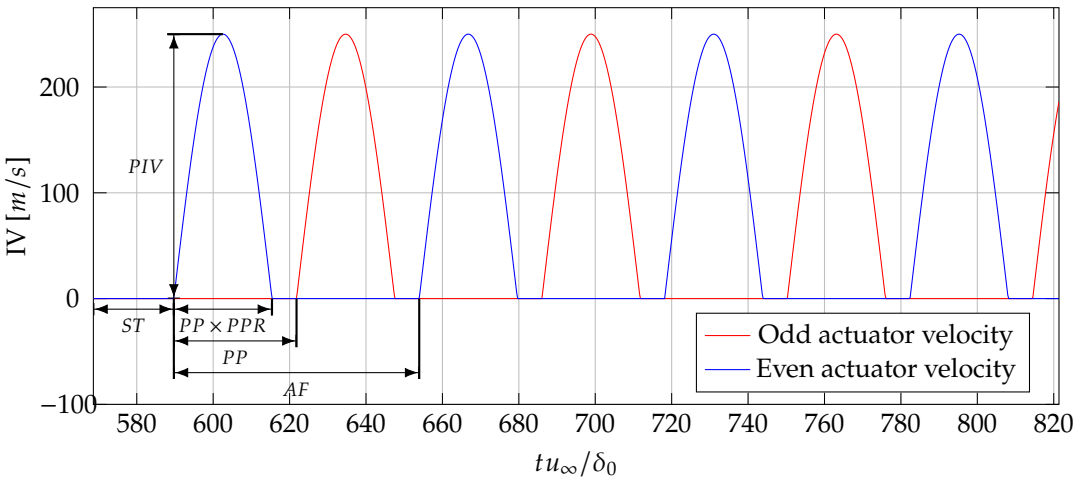


Figure 2.2: Jet actuator design variables.

2.5. Flow settings

The same flow settings are used for all cases in this research. As mentioned in section 1.1, cases with higher Mach number seem to be less perturbed by upstream noise, which is why the Mach number used in this research should be around 2.0 as the effects of upstream perturbations caused by injection should not be suppressed. Similarly to the reasoning for choosing a turbulent boundary layer, it is easier to see the difference in bubble size when the bubble is larger, which is another reason for keeping the Mach number low. Other values used in the simulations such as Reynolds number (Re), Mach number (Ma), free-stream velocity (u_∞), stagnation pressure (p_0), statistical boundary layer thickness (δ_0), L_{imp} and incident angle of oblique impinging shock wave (ϕ) are given in Table 2.3. The value of δ_0, which is obtained from the Reference case at x = 67.2426 mm downstream of the inflow plane, is used in the normalization of the domain and certain metrics across all cases. Thus it will be the same value for every control case.

Table 2.3: Flow Settings.

Symbol	Value	Dimension
Re	9,636	m m^{-1}
Ma	1.9985	-
u_∞	507	m s^{-1}
p_0	4.54×10^4	kPa
δ_0	6.0183	mm
L_{imp}	167.8117	mm
ϕ	40.1409	°

2.6. Computational grid

Both the coarse and fine grids used in this research were previously used in research [73, 84]. A block-structured, piecewise Cartesian grid is constructed in the domain, where each block has an equal number of cells but the grid spacing varies. The block size and number of blocks for both meshes are given in Table 2.4. The block distribution for the fine grid is shown in Figure 2.3.

Table 2.4: Inflow plane parameters and grid size.

Case	$Re_{\delta_{0,i}}$	$Re_{\tau,i}$	$\Delta x^+_{\min} \times \Delta y^+_{\min} \times \Delta z^+_{\min}$	$N_x^{\max} \times N_y \times N_z^{\max}$	Number of Blocks	Block Size
Coarse	50.1×10^3	935	$100 \times 24 \times 78$	$440 \times 78 \times 54$	36	$36 \times 36 \times 24$
Fine	50.1×10^3	935	$39 \times 0.94 \times 9.8$	$1088 \times 240 \times 384$	1408	$34 \times 24 \times 12$

The grid- and domain-sensitivity studies used to verify the adequacy of the grid resolution and domain size is shown in the appendix of Laguarda et al. [84]. The minimum cell dimensions and the inflow plane parameters are given in Table 2.4. The inflow parameters are the same for both the fine and coarse meshes. The cell sizes do change significantly between the two grids.

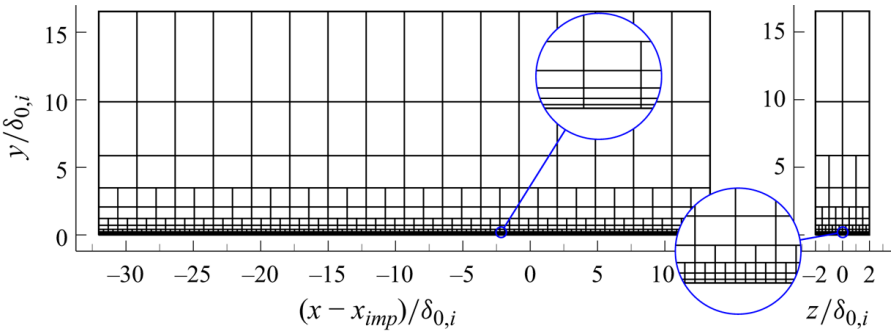


Figure 2.3: Block distribution of the numerical grid for the production cases [84].

2.7. Data generation and processing

INCA has the ability to output several data types and metrics. During this research the INCA outputs used were snapshots, statistics and probe data. Each of these will be discussed briefly here.

2.7.1. Snapshots

Snapshots provide the data, as the name suggests, as a snapshot in time. It captures all the values of cells without taking into account previous or upcoming data points. The capture moment can be set both at an time intervals and after a certain number of iterations has occurred. Additionally the start time or iteration and the final time or iteration can be set. A snapshot can contain data of all the cells in the entire domain, a sub-domain or a slice through the domain. The sub-domains, and slices are determined before the simulation is started. For the coarse simulations the entire domain was captured in snapshots, for the refined simulaitons only a subdomain was used. The used subdomain is indicated in blue in Figure 2.1. The output data of these domains can include amongst others p, T, ρ, streamwise velocity component (u), wall-normal velocity component (v) and spanwise velocity component (w). Additionally other data such as the precision and simulation time are also included with the snapshot data. The file size of these snapshots is directly related to the size of the domain which is captured. Refining the mesh will significantly increase the file size and therefore the total amount of data that needs to be transferred and stored per simulation.

2.7.2. Statistics

The statistics provide temporally averaged metrics. The statistics work very similar to the snapshots, as they can also be set to compute for a selected domain, the entire mesh or a slice. The difference between snapshots and statistics is that the statistics are averaged over the time in which they are taken and will only provide one value per cell, thus the duration of a simulation does not impact the size of the statistic files.

2.7.3. Probes

Probes are another tool which can be used in INCA to obtain metrics. Probes are placed on a boundary of the domain and take pressure and temperature samples at a set rate. These are useful as this is a non-intrusive method which is usually used in experimental setups and therefore having these in the software allows for a close matching of experimental setups and simulations. During the simulations the probes have been placed along the center line of the domain in the stream-wise direction as indicated in Figure 2.1. The amount of data the probes gather is very small as there are just 9 values obtained per probe per set number of steps. This allows for an very high number of probes to be placed with little overhead, therefore it advisable to place many and select the desired ones when data processing.

Two groups of probe locations were used: a common group of probes, of which the probe locations are based on the statistics of the Reference case and thus are the same for all simulations. The second is the selected group, of which the probe locaitons are based on the statistics of the case itself. The common group probes can be used to directly compare locations among cases while the selected group is placed at certain flow metrics such as separation and reattachment so that these features can be compared. Common probe locations are indicated by ▲ and selected probe locations are indicated by ▼.

2.7.4. Data processing

The processing of data is discussed in detail in Appendix A.

2.8. Control outcome metrics

The effectiveness of the control design settings are judged on two categories: the SWBLI mean flow organization and the ability of control/modulation of the SWBLI unsteadiness. How this data is obtained is disused above. The second category is harder to effectively compare, which is why a first judgment is made using the mean flow organization and if results either stand out or are not as expected they will be closer examined with spectral analysis tools.

3

Parametric Study Results

This section will discuss the setup and results of the parametric study performed coarse grid. In order to gain better insight the results are split up into the design variables of the control system, which have been discussed in subsection 2.4.1. Each variable is isolated while other variables are kept constant to evaluate the effects caused by a single variable. The results in this section are given as a difference compared to the reference simulation (Referencep).

First the setup of the parametric study is given in section 3.1. The influence of injection velocity is discussed in section 3.2, as this will be set constant for all further tests. Then the results for all the tested settings are shown in section 3.3, in order to see if there are any emerging trends. These trends are further explored by filtering groups and determining the influence of AL and AF separately. A distinction will also be made between the influence a setting has on the flow organization or on the unsteadiness of the bubble. The influence on the flow organization will be discussed in section 3.3 and the unsteadiness will be discussed in section 3.4. Finally the results of the parametric study will provide the guidance to select cases for the production simulations. The selection of these cases and the reasoning is given in section 3.5.

3.1. Parametric study setup

Since the methodology of injecting fluid, mimicking a jet actuator, had not been used in INCA, a parametric study was performed. Rather than running few high fidelity simulations, a large number of simulations on a coarser mesh were performed to gage whether simulating this method of control would resemble realistic results and whether settings could be found which showed effective control of the separation bubble. The reasoning for not running a large number of high fidelity simulations is due to a limited computational resources and time. As explained in section 2.7 running a course simulation requires less resources both in computational time and in data storage facilities.

The jet actuator function has several design variables which can be altered, as explained in subsection 2.4.1, however if multiple variables change it is not clear to what extend each one influences the outcome of the simulation. Some variables of the jet actuator routine were deemed less important or would introduce another variable that would exponentially increase the number of simulations that had to be performed to draw valid conclusions. For this reason several variables were set to one value and not changed during the simulations presented in this report. The design variables which were set to a constant value are: NA, AD, PIV, IA, PPR, TPP and PPS. The values of the constants are given in Table 3.1 and the reasoning is given below.

For these simulations the NA has been set to 4. Initially simulations have been performed using 2 actuators, however these did not influence the flow significantly enough to draw conclusions. Therefore the number of actuators was set to 4 to have an increased effect on the flow. Additionally research by Xu et al. [85] shows that the ratio between the AD and the actuator spacing should be large for close to the wall vortical structures. As the domain size is set, increasing the number of actuators decreases the spacing between them. However since the actuators are firing out of sequence this ratio is actually close

to 1.

The AD has been set to 4 mm, which is larger than the actuators used in literature [33, 38, 74, 85], the reason for this is the same as increasing the number of actuators, namely to increase the effectiveness of the actuators.

The PIV has been set to 250 m/s, which is typical for a plasma jet injector and in line with previous research [33, 38, 74]. A injection velocity sweep was performed, the results of which are discussed in detail in section 3.2. Additionally production simulations were tested at both 250 and 300 m/s but the additional computational resources required for the 300 m/s case provided more reasons not to use it. While the 300 m/s case was slightly more effective, is it computationally more expensive and less stable.

The IA has been set to 90 °. Even though previous research such as Greene et. al [38] has indicated that an IA of 22 ° is better when injecting upstream of separation, the decision was made to inject at 90 ° for the sake of simplicity.

The PPR has been set to 0.8, which mimics the injector running out of fluid in injection chamber and therefore loosing pressure instantaneously.

The PPS has been set to 0 for all simulations. This is because the assumption was made that there would not be an instantaneous velocity produced by the jets but more a ramp. This would also be better for simulation performance.

As mentioned in subsection 2.4.1, almost all of the values here are constants, except for IP and IT. These values are reference values for which the Riemann invariants are solved to ensure stability. However this was only implemented after the parametric study was performed. Pressure was also tested for by Xu et al. [85] and it shows that a large pressure ratio of IP over free-stream pressure (p_∞) is better at reducing the separation volume.

Table 3.1: Jet Actuator Constant Variables

Design Variable	Value	Dimension
NA	4	-
AD	4.0	mm
IV	250.0	$m\ s^{-1}$
IA	90	°
ST	7.0	ms
PPR	0.8	-
TPP	2.0	-
PPS	0.0	-
AS	Parabolic	-

3.1.1. Frequency variation

Even though previous research by Narayanaswamy et al. [33] and Greene et al. [38] indicated that the influence of AF on the separation region is limited, meaning that the variation of frequency does not yield significantly different results. They did not test very low-frequency injection frequencies. To confirm that the implemented jet actuator routine is also not over sensitive to variations in frequencies, several frequencies were tested. At first tests were performed at frequencies of 0.0494, 0.0988 and 0.4938 St_L. After the results of these tests did align relatively well with previously done studies [33, 38], when comparing the effectiveness of reducing separation length, additional tests were performed at lower frequencies to gage the effect this would have on the low-frequency motion of the separation bubble.

3.1.2. Location variation

The AL has been varied from way upstream, $x = 0$ to just after reattachment. Initially only 3 locations were tested, which were way upstream, just before separation and in the middle of the separation region. Then additional locations, upstream and throughout the separation region, were tested for selected frequencies. This was done to give a clear picture of an actual optimal location. All combinations of AF and AL, tested during the parametric study, are given in Figure 3.1.

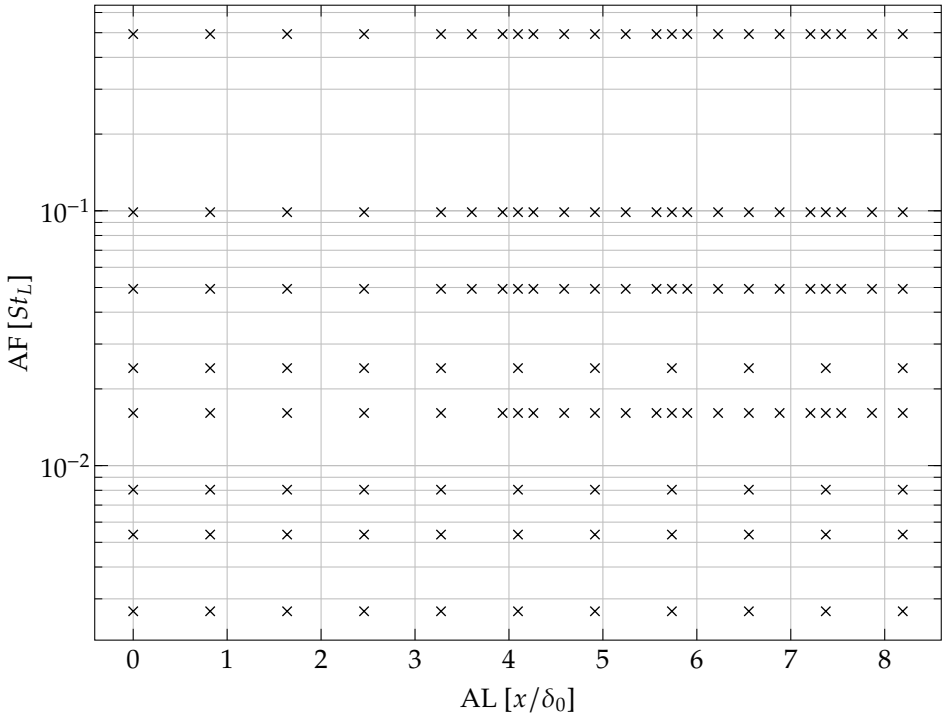


Figure 3.1: Combinations of ALs and AFs used in the parametric study.

The results for the combinations of AL and AF given in Figure 3.1 are shown in Figure 3.3 and Figure 3.4.

In this chapter, the results are sometimes grouped based on frequency or location, the groups and the settings that they have in common are given in Table 3.2.

Table 3.2: Parametric Study Groups.

Group Name	NA [-]	AD [mm]	AL $[\delta_0]$	AF $[St_L]$	IV [m/s]
Group 0	4	4	Varies	Varies	250
Group 1	4	4	Varies	0.0161	250
Group 2	4	4	4.0961	Varies	250
Group 3	4	4	6.5538	Varies	250
Group 4	4	4	Varies	0.0988	250

3.2. Injection velocity influence

The reasoning for doing the parametric study at 250 m/s was discussed shortly in section 3.1, it mentions that the 250 m/s case is less effective in the reduction of the spatial characteristics compared to 300 m/s. This claim is supported by the results shown in Figure 3.2, which show the difference of several spacial characteristics compared to case Referencep. This clearly shows that the effectiveness of reducing the spatial dimensions of the separation bubble is related to PIV. The test at 50 m/s shows no effect compared to the reference case. This is likely due to the inability to properly penetrate the boundary and create the vortical structures which will reduce the separation bubble at the tested location. 100 and 150 m/s show to be somewhat effective but the change compared to the reference case is very limited. And to accurately asses the influence of frequency and location it is desired that the actuator has a larger influence on the separation bubble behavior. The case tested at 250 m/s shows significantly more effect than the case at 200 m/s. And while it is less effective than 300 m/s, simulations at 250 m/s are more stable and much faster.

Therefore the trade-off between stability, speed and effectiveness is made and in this case the faster

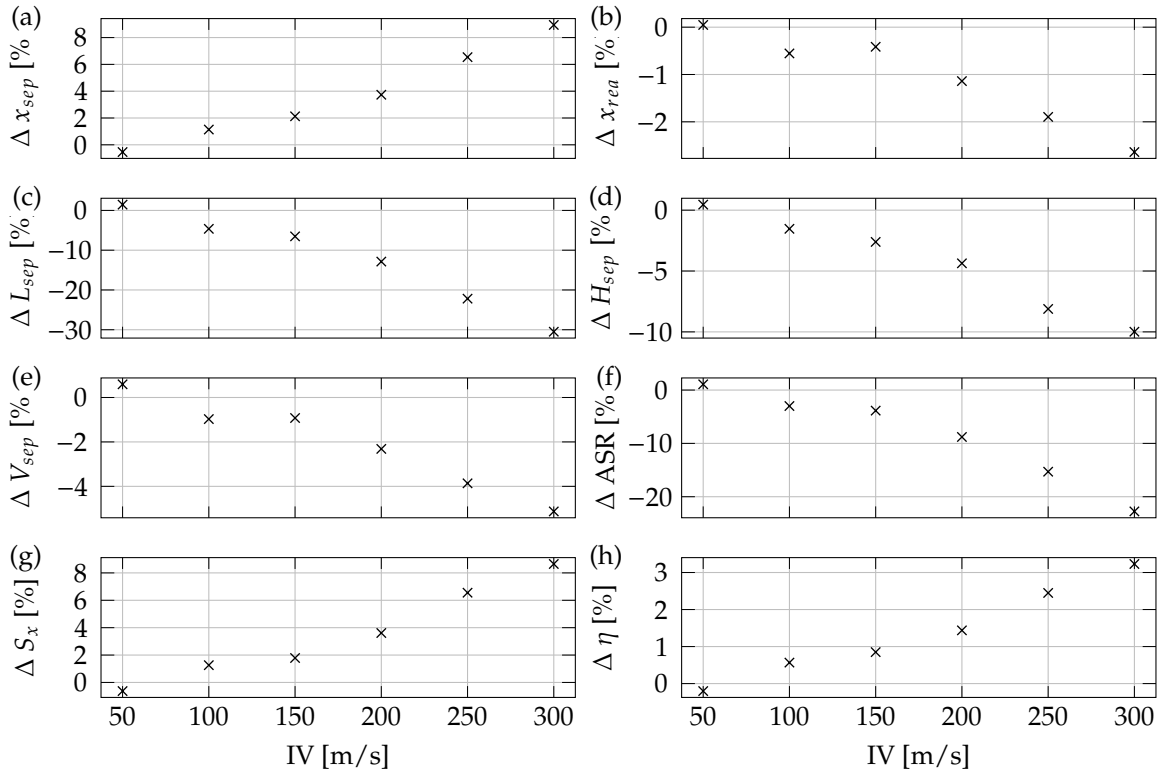


Figure 3.2: Results for PIV variation with AL = 4.096115 δ_0 and AF = 0.098765 St_L, for: (a) x_{sep}, (b) x_{rea}, (c) L_{sep}, (d) H_{sep}, (e) V_{sep}, (f) ASR, (g) S_x and (h) η.

computation and greater stability of the 250 m/s cases is selected for the rest of the parametric study and the production cases.. Therefore all the results given in the rest of this section will filter out the cases with different IVs.

3.3. Influence of injection location and frequency on flow organization

The results for the spatial metrics plotted against AL for Group 0 given in Figure 3.3. Even though these cases are not filtered by any particular frequency they already show the general influence the control location has on the spatial characteristics. This shows that the control location has a large influence in the spatial characteristics of the separation bubble. Way upstream of the reference separation location, the effectiveness of control is limited. Moving the control location towards the separation region the effectiveness increases significantly. Up to about about 1.5 δ_0 before the reference separation point, which is the optimal control location. Any closer to the separation bubble sharply reduces the effectiveness, a result also found by Greene et al. [38]. Then within the separation bubble the effectiveness of control decreases almost linearly as the control location is moved towards the statistical reattachment point. If the control actuator is placed behind the reattachment point, there is virtually no difference between the control cases and Referencep case.

The reason for this trends is how the flow is controlled, as both Greene et al. [38] and Narayanaswamy et al. [33] propose, the injectors act as vortex generators, which are most effective at a specific distance. The actuators would work in a similar manner as s the air jet vortex generators studied by Souverein and Debiève [48]. The variation in effectiveness is related to the length and strength of the vortices. After a certain length, they are less strong due to dissipation. Before the optimal length they are not fully developed meaning that they do not bring as much high energy flow close to the wall.

While Figure 3.3 clearly shows certain trends as a result of variation in AL, these trends are not clearly visible for a variation in AF as shown in Figure 3.4. One thing that doe become clear from Figure 3.4 is

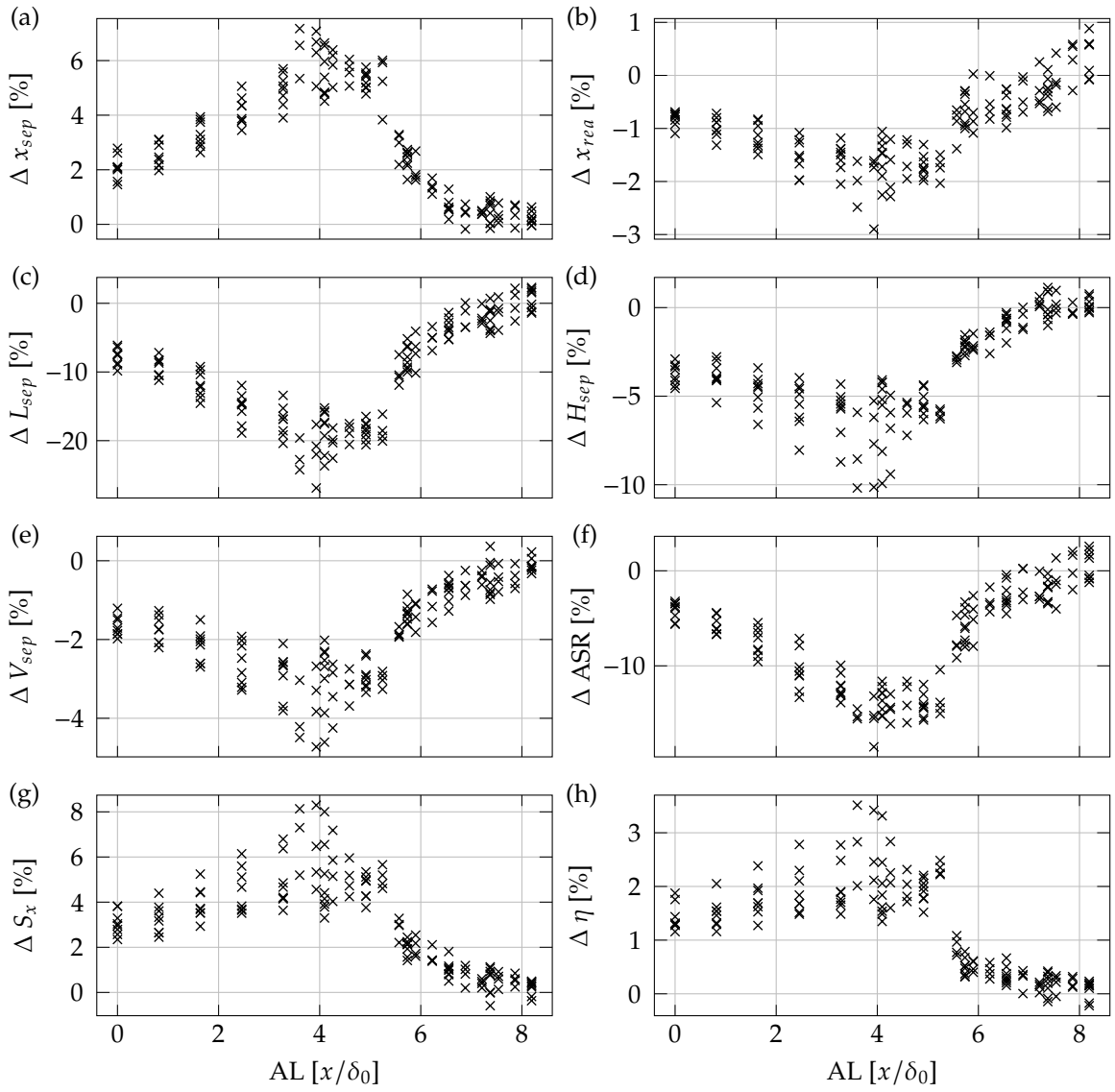


Figure 3.3: Results for AL variation for all simulations in the parametric study with a IV of 250 m/s, for (a) x_{sep}, (b) x_{rea}, (c) L_{sep}, (d) H_{sep}, (e) V_{sep}, (f) ASR, (g) S_x and (h) η.

that the variability of the effectiveness of the frequency increases as the frequency increases. This is especially clear for metrics such as statistical separation length (L_{sep}), separation shock location (S_x) and separation shock angle (η) given in Figure 3.4c,g-h respectively. This is can also be seen in Figure 3.3. Although it might be that it is a combination of frequency and location which causes this extra variability.

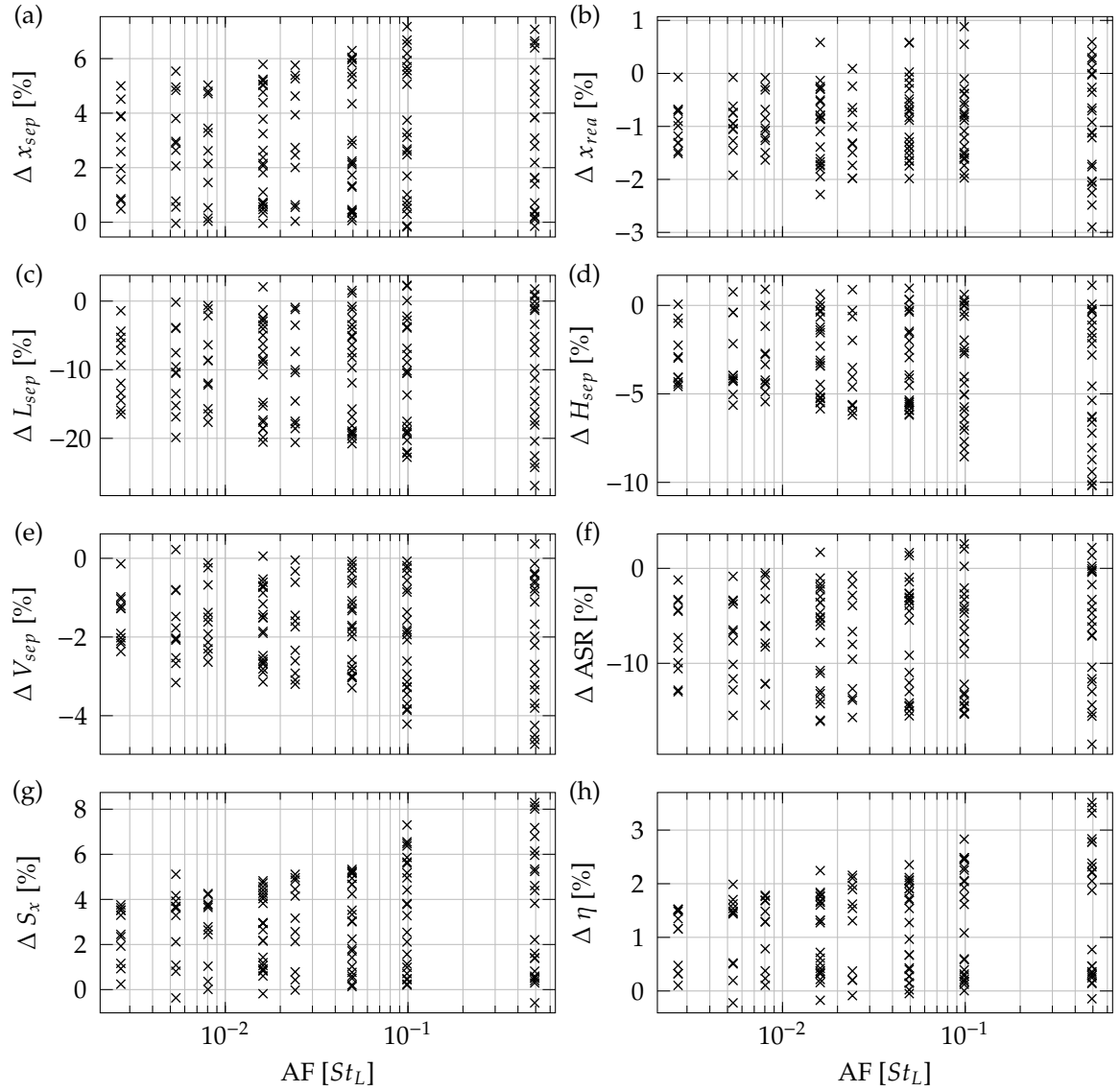


Figure 3.4: Results for AF variation for all simulations in the parametric study with a IV of 250 m/s, for (a) x_{sep}, (b) x_{rea}, (c) L_{sep}, (d) H_{sep}, (e) V_{sep}, (f) ASR, (g) S_x and (h) η.

3.3.1. Injection location effects

The results for the variation of the AL for Group 1 and Group 4 are given in Figure 3.5, confirming the trend observed in Figure 3.3.

Figure 3.5 also shows that not all metrics are influenced equally. The separation point (x_{sep}) and separation bubble height (H_{sep}) differ almost twice as much as reattachment point (x_{rea}) and separation bubble volume (V_{sep}) when comparing to the Referencep case. For almost all cases. L_{sep} and Aspect Ratio (ASR) show a significant difference, especially near the optimal location. Curiously there is only a small difference in η for cases far upstream and just upstream of separation. Inside the separation bubble the difference is only 0.5% and then drops towards 0. H_{sep} and S_x show somewhat similar behavior where they do not ramp up towards a maximum but rather have a similar difference until close to the optimal location.

Taking a closer look at Figure 3.5, there seem to be two optimal locations, which potentially can be dependent on frequency. It could also be that these cases are merely outliers. In any case, the ordering is different than expected, as Group 1 would presumably be the group with a peak further away from the separation region.

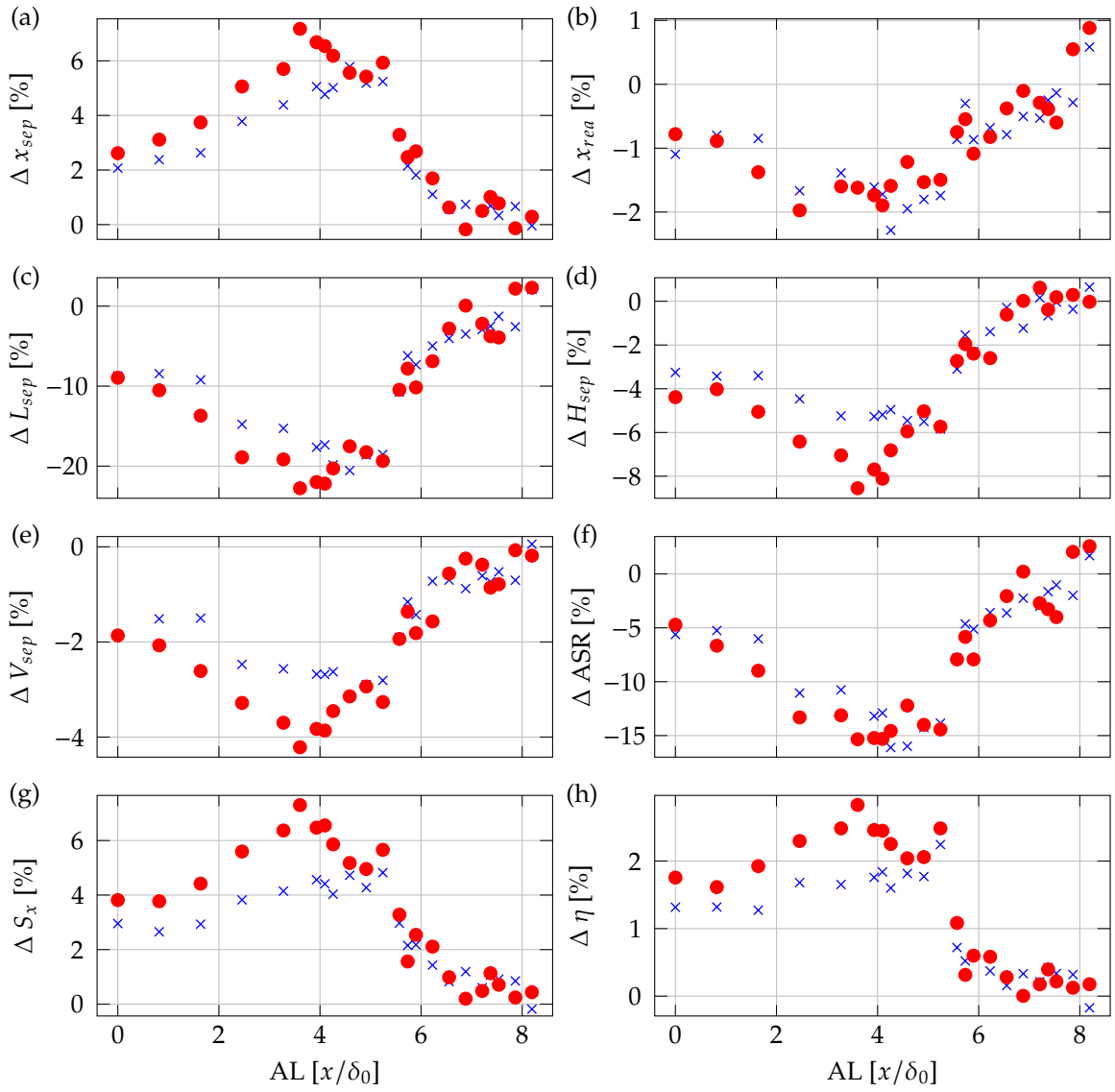


Figure 3.5: Results for AL variation for Group 1 × and Group 4 ●: (a) x_{sep}, (b) x_{rea}, (c) L_{sep}, (d) H_{sep}, (e) V_{sep}, (f) ASR, (g) S_x and (h) η.

One reason why the optimal location differs from previous research such as Greene et al. [38], which found it to be at around $3\delta_0$ before the compression corner and Narayanaswamy et al. [33], is that the setup is different. They used a compression corner whereas this study used an impinging shock thus making the comparison not directly comparable. Even with this discrepancy the parametric study did confirm that there is an optimal location upstream of the separation location, in this study this optimal location was about 1.5 δ_0 before the Referencep separation point.

The results show that there clearly is an optimal location, as was expected from experimental results. The results also show that the ability to change the spacial characteristics of the separation bubble diminishes sharply downstream of the optimal location and throughout the separation bubble. Thus it is likely that the spacial characteristics can only be altered only slightly in the middle of the separation bubble and minimally at reattachment.

3.3.2. Injection frequency effects

As subsection 3.3.1 showed there is a difference in the response of the bubble between controlling before separation and controlling from within. The two locations which are set for groups Group 2 and Group 3 are one close to the optimal location and one inside the bubble. This is done to get the optimally

effective actuator, and an actuator with reduced effectiveness to examine the role of frequency variation. The results for the AF variation for both groups are given in Figure 3.6.

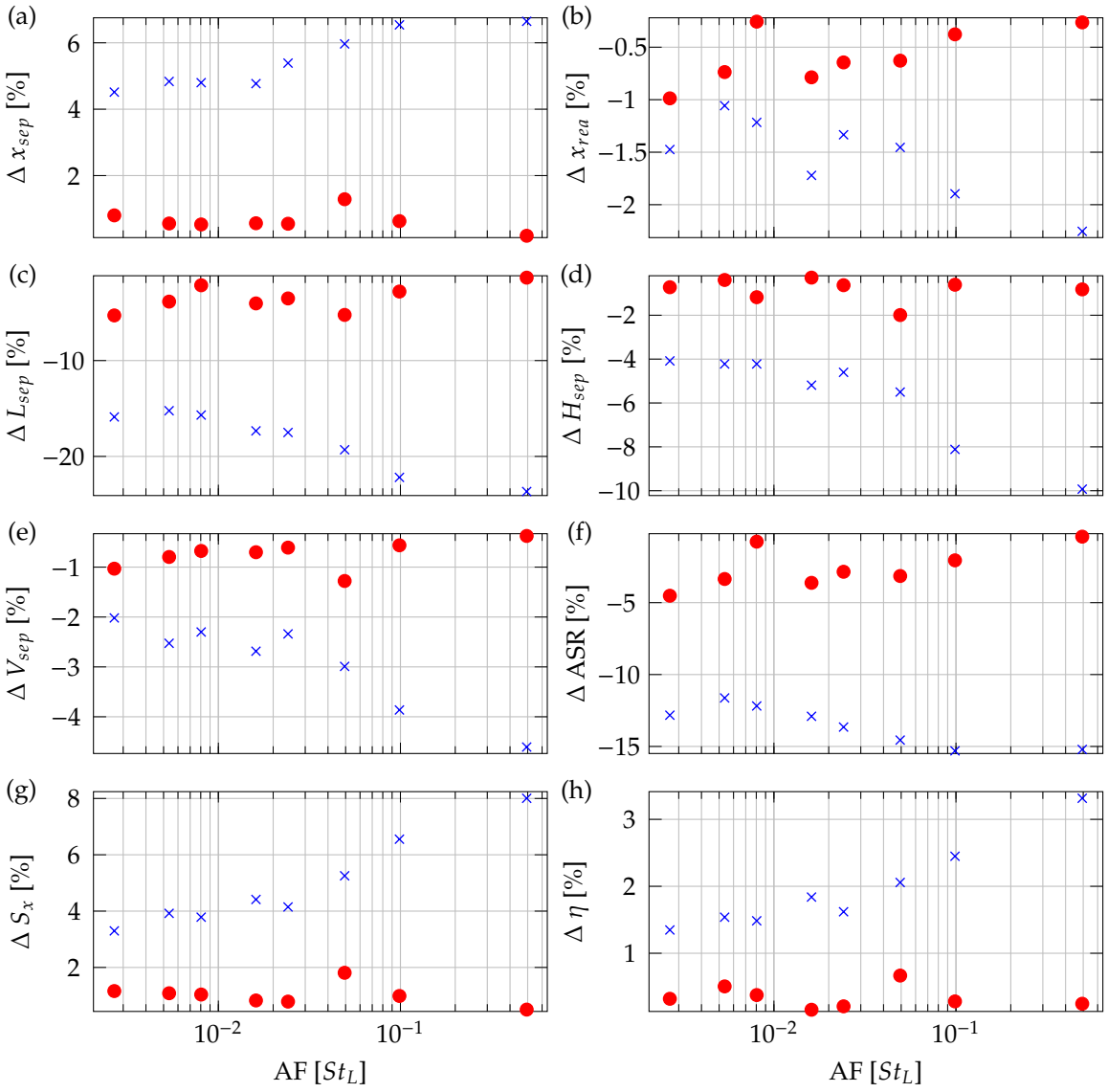


Figure 3.6: Results for AF variation for Group 2 × and Group 3 ●: (a) x_{sep}, (b) x_{rea}, (c) L_{sep}, (d) H_{sep}, (e) V_{sep}, (f) ASR, (g) S_x and (h) η.

The results for Group 2 in Figure 3.6, suggest that AF does influence the spacial characteristics when control is applied at the optimal location. Controlling at lower frequencies, from $2.681 \cdot 10^{-3}$ to 0.0161 St_L, is less effective than controlling at the higher frequencies. For several metrics such as H_{sep}, V_{sep}, η and S_x there is little difference in effectiveness when controlling at frequencies up to 0.0161 St_L. While control at higher frequencies control becomes 1.5 to 2 times as effective with respect to the low-frequency simulations. The only metric for which this is not as obvious is the x_{rea}, which overall is less effected by the application of control and does not significantly increase after 0.0161 St_L, except for the highest frequency.

This trend is not found for the cases where control was applied within the separation region, as shown Group 3 in Figure 3.6. There is no frequency which is optimal to use for all metrics, there is no clear point after which the metrics improve or deteriorate and the difference between the best and worst performing cases is smaller. One thing that is clear when comparing the datasets in Figure 3.6 is that controlling from inside the separation region is not as effective as controlling before separation which is consistent with observations in subsection 3.3.1 and results obtained by Greene et al. [38].

While setting the ramp location at 1.5 δ_0 downstream of the actuators, Greene et al. [38] found that a peak in effectiveness at a forcing frequency of 3.2 kHz or Strouhal number 0.018. In this case the peak effectiveness is considered to be the frequency which is most effective at increasing the momentum of the flow inside the interaction region of the SWBLI. The results of the parametric study showed that the higher frequency actuators, used at an AF of 0.0988 St_L, were significantly more effective than when used at an AF of 0.0161 St_L. So even though the Strouhal number was close to the low-frequency cases, the absolute frequency was much closer to the high-frequency cases of the parametric study which used a frequency of 3.6834 kHz.

3.4. Influence of injection location and frequency on unsteadiness

This section will discus the influences of the design variables on the spectral characteristics of the separation bubble as have been discussed in section A.4. It will first discuss the influence of AL and then of AF. During the analysis of the spectral characteristics, the main focus has been on the total and peak PSD powers. Examining the peak and total power might give us more insight into the potential drawbacks or unnoticed benefits of certain control locations or frequencies. It can also be shown in one value, without having to examine all the spectral dynamics of individual tests.

3.4.1. Injection location effects

Figure 3.7 shows both the peak and total PSD powers for the filtered group at 0.0161 St_L, the same as used in subsection 3.3.1. Interestingly both the peak and total PSD powers show similar behavior to variations in AL as the spatial characteristics did. The peak power, as shown in Figure 3.7 where it is indicated by ×, shows that far upstream there influence. As the control location is moved upstream and closer to the optimal location, an increase in maximum power is observed for every metric. Similarly to the spatial characteristics the spectral characteristics also do not all display the same behavior. H_{sep}, S_x and η all show little variability between the far upstream and closer to the optimal location, while x_{sep}, x_{rea}, L_{sep} and ASR all show a clear ramp up to the optimal location. There is also some variation in the behavior inside the separation bubble, where some metrics show a linear decline and some show greater variability.

For the total power most of these things also hold, except the variability in the separation region is more pronounced in almost all metrics. Curiously while the peak power is very similar when controlling from within the separation region, the total power shows the same almost linear decrease for the x_{rea} which is then also reflected in the L_{sep}.

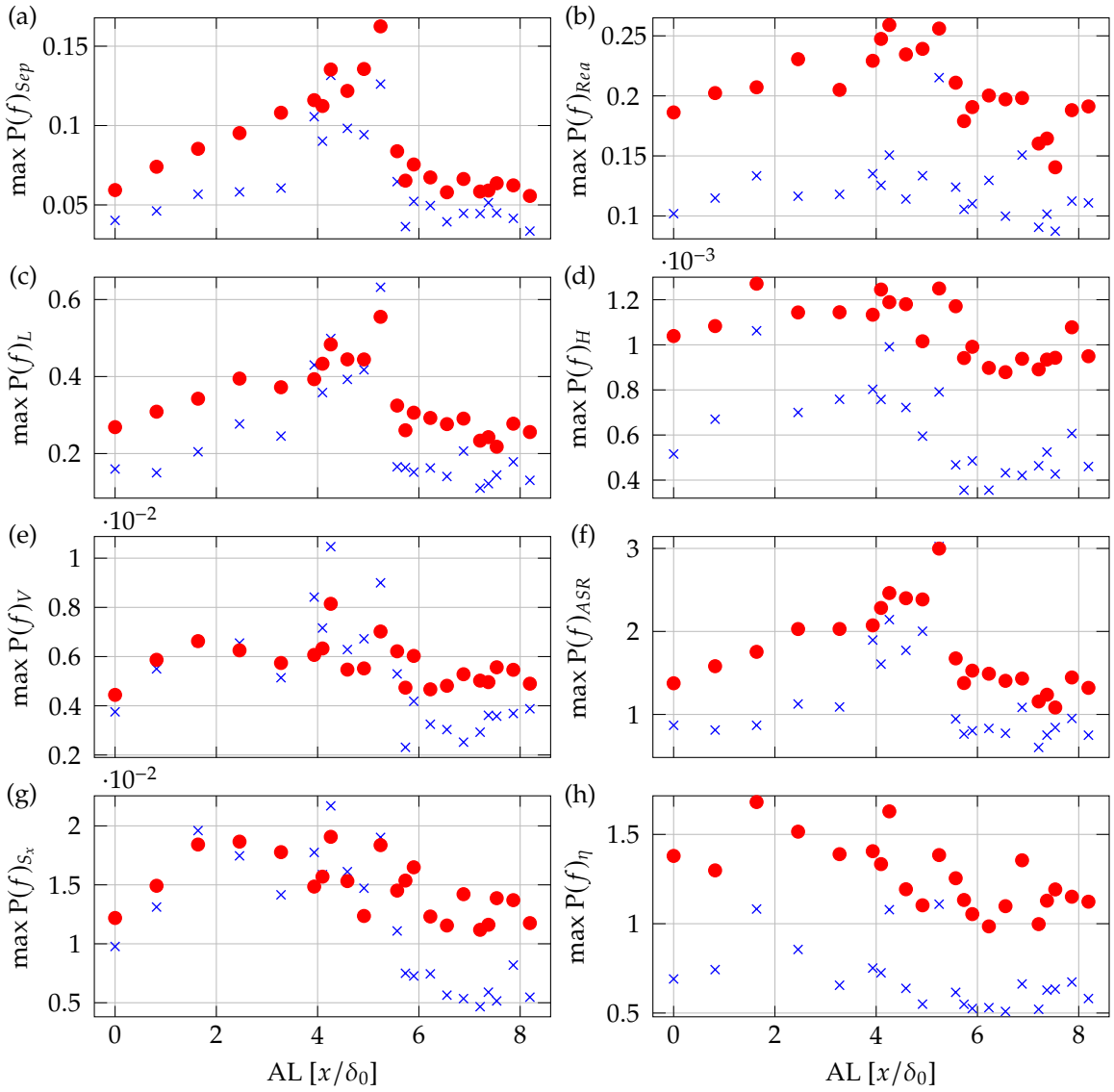


Figure 3.7: Peak PSD power × and total PSD power ● for varying control locations for Group 1: (a) x_{sep}, (b) x_{rea}, (c) L_{sep}, (d) H_{sep}, (e) V_{sep}, (f) ASR, (g) S_x and (h) η.

3.4.2. Injection frequency effects

Both Figure 3.8 and Figure 3.9 show that controlling before the separation bubble significantly increases the power when comparing to the cases where control is applied to within the separation region. However there is no clear pattern in the total PSD power given in Figure 3.8, while the peak PSD power given in Figure 3.9 looks similar to Figure 3.6 for the control cases before the separation region. Except for the S_x where the in peak power is much higher at low frequencies.

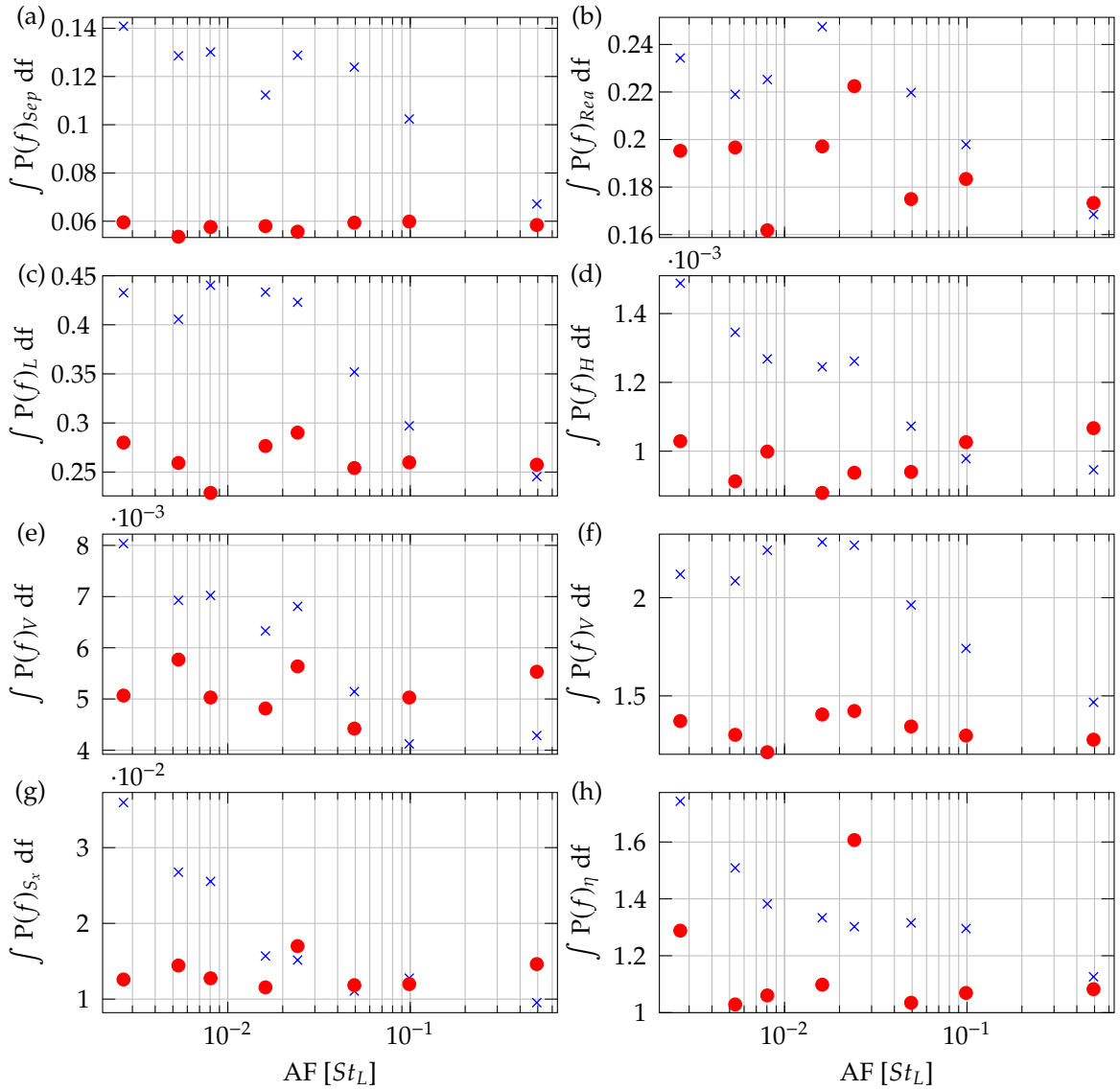


Figure 3.8: Total PSD power for AF variation for Group 2 × and Group 3 ●: (a) x_{sep}, (b) x_{rea}, (c) L_{sep}, (d) H_{sep}, (e) V_{sep}, (f) ASR, (g) S_x and (h) η.

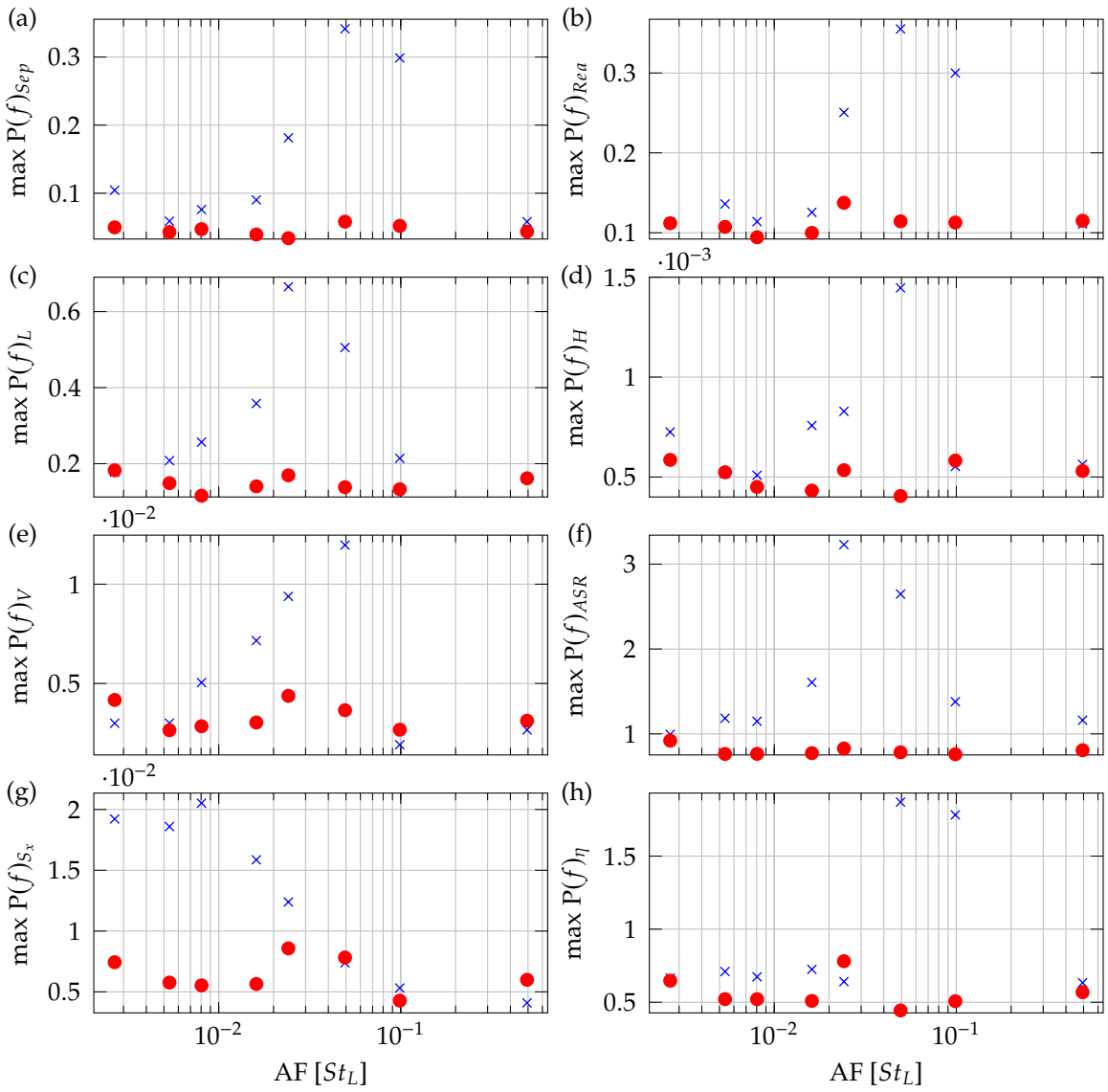


Figure 3.9: Peak PSD for AF variation for Group 2 × and Group 3 ●: (a) x_{sep}, (b) x_{rea}, (c) L_{sep}, (d) H_{sep}, (e) V_{sep}, (f) ASR, (g) S_x and (h) η.

3.5. Case selection

As mentioned in the introduction of this chapter, the results from the parametric study, which have been discussed in the previous sections, are used to select several cases which are simulated on a finer mesh. The selected cases and reasoning for this are given in this section. During the selection process, the selection has mostly been based on the influence different control cases have had on the spatial characteristics of the separation bubble. The reason for this is two-fold, firstly the influence on the spectral characteristics is more difficult to determine as a limited sample rate and simulation time will only provide a limited insight in the spectral behavior, especially the low frequency behavior. Secondly the techniques that have been applied to analyze the low-frequency behavior do not paint a clear and decisive picture on which the decision should be made. Additionally it is more difficult to determine whether or not it is beneficial to add significant power to certain frequencies and what consequences this might have on the flow behavior without doing a much deeper analysis of the flow, which is out of the scope of this project.

Since the location has a greater influence on the reduction in spatial characteristics than the frequency as has been shown in subsection 3.3.1, the decision was made to test at the optimal location, and at two locations within the separation bubble. Testing at this optimal location also has the benefit that it can be compared to previous experimental studies [33, 38]. Then the second and third locations are within the separation bubble, near the middle and near reattachment respectively. The second location is chosen because the parametric study showed that moving the actuator to far towards the reattachment point severely limits its ability to influence the separation bubble in terms of its spatial characteristics, but to be well within the bubble, the location should be around the middle. Even though the parametric study shows that the reduction in size is limited at reattachment, the third location is chosen to be close to reattachment. The reason for this is that this has not been tested numerically and recent studies indicate that this might be possible [67]. Additionally these locations could provide further insight into the driving mechanisms of forcing.

The selected frequencies are 0.0988 St_L and 0.0161 St_L. 0.0988 St_L as this is the most effective while still being a realistic number. And 0.0161 St_L because the parametric study results showed that tests at lower frequencies could still be effective. Additionally it was deemed interesting to use an actuator frequency close to the natural frequency of the separation region.

This results in 3 selected locations and 2 frequencies, for a total of 6 cases, of which the settings are given in Table 3.3. The cases locations are indicated by the high frequency case names in Figure 3.10

Table 3.3: Selected Cases.

Case Name	Sim Name	NA [−]	AD $[mm]$	IV $[m/s]$	AL $[(x - x_{imp})/\delta_0]$	AL $[x/\delta_0]$	AF $[St]$	AF $[kHz]$
LSFHp	JA18	4	4.0	250.0	−4.3146	25.0000	0.0988	3.6834
LSFLp	JA6	4	4.0	250.0	−4.3146	25.0000	0.0161	0.6000
LMFHp	JA71	4	4.0	250.0	−1.8570	40.0000	0.0988	3.6834
LMFLp	JA61	4	4.0	250.0	−1.8570	40.0000	0.0161	0.6000
LRFHp	JA74	4	4.0	250.0	−0.8739	46.0000	0.0988	3.6834
LRFLp	JA64	4	4.0	250.0	−0.8739	46.0000	0.0161	0.6000

For more insight into the spectral behavior and to provide reference data for the production cases, the results of the peak power and corresponding frequency, the power per frequency range and the coherence plots are provided below for the selected cases.

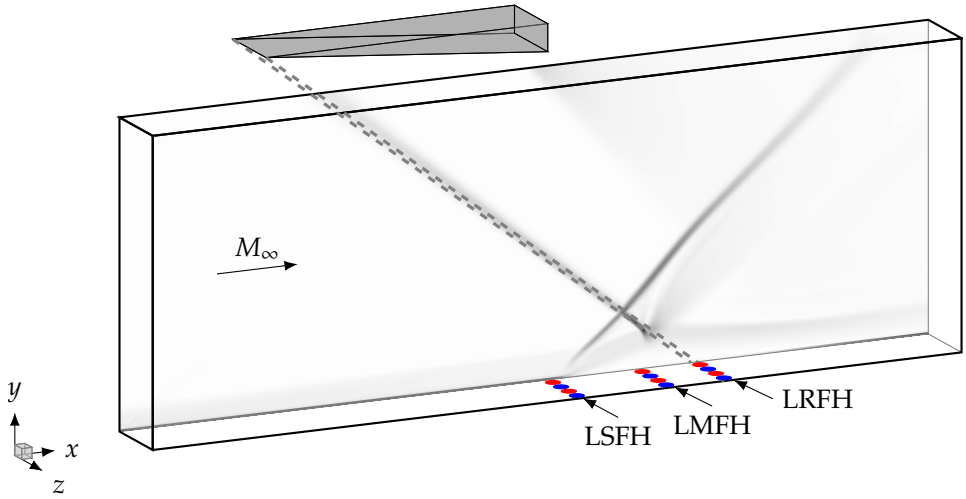


Figure 3.10: Schematic for the placement of the actuators for the different control cases.

3.5.1. Peak power and frequency for selected cases

Similar to the peak and total PSD power which was computed for the bubble metrics in the previous sections, these values can also be computed for the wall pressure fluctuations (p'_w) of each probe along the centerline. The results of the peak PSD power of and its corresponding frequency are shown in Figure 3.11, it shows how the SWBLI system responds to forcing at frequency and how this forcing is carried through the domain. The behavior seen for LSFHp, in Figure 3.11b, can be observed to a lesser degree for all the high-frequency cases. The dominant frequency, which is the actuator frequency, is shown throughout the bubble and even downstream of it. For cases LMFHp and LRFHp, the dominant frequency fluctuates around the actuator frequency but remains quite close. For the low-frequency cases, no dominant frequency throughout the domain can be observed. However the dominant frequency at separation is the same as the actuator frequency, indicating that the low-frequency cases might be able to control the separation shock motion even when the actuator is placed on the other side of the bubble. Another interesting observation is the amount of energy during the separation, which is much higher for the low-frequency cases than for the high-frequency cases.

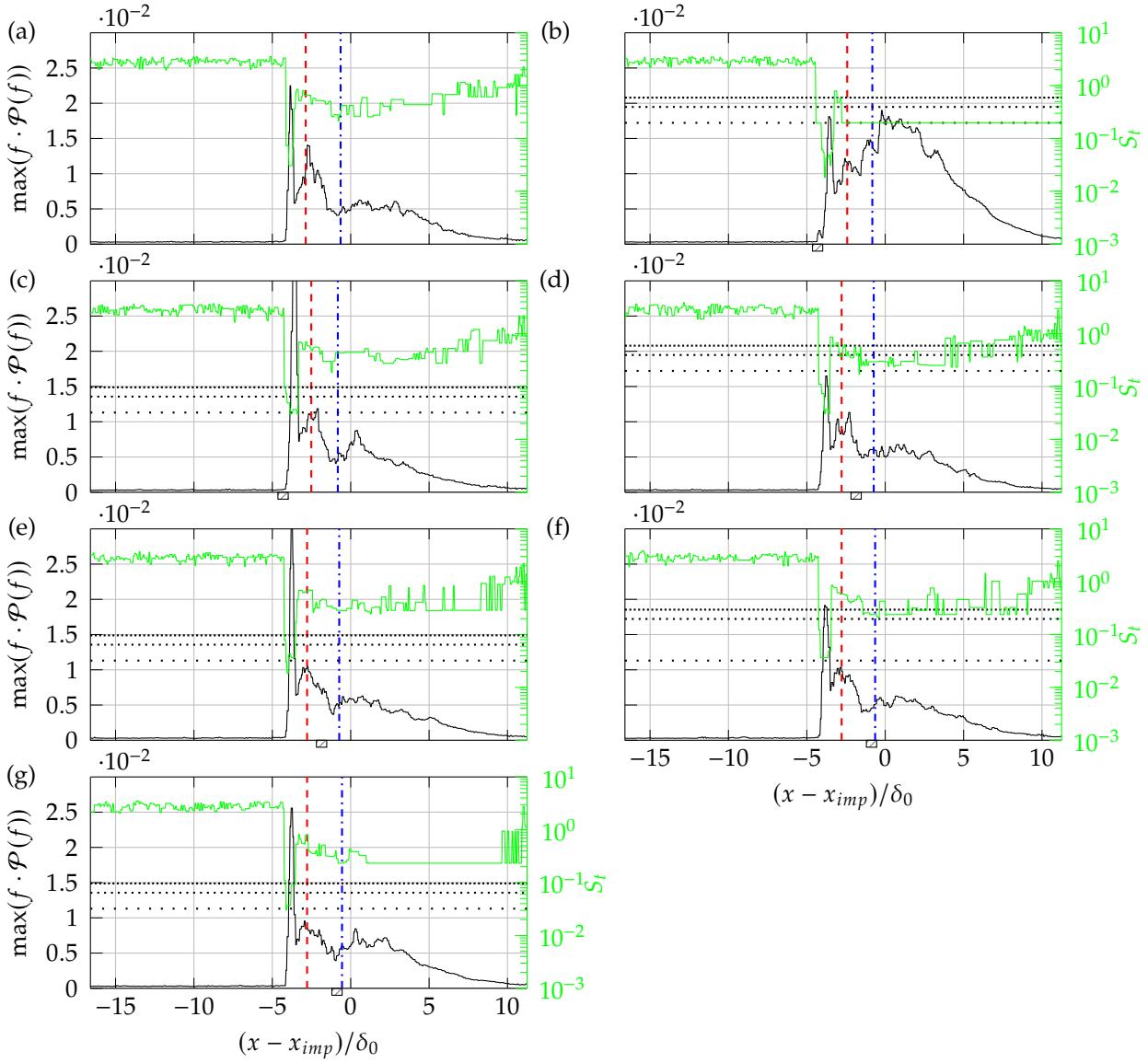


Figure 3.11: Peak PSD power and corresponding frequency of p'_w for all coarse cases. The vertical red dashed line indicates the statistical separation point, the vertical blue dashed-dotted line indicates the statistical reattachment point. The horizontal dashed lines indicate the first, second and third harmonics of the AF. The AL is indicated by ▨.

3.5.2. Power per range for selected cases

For all the selected cases, the power per frequency range closely resembles the Referencep case, with a peak of all the ranges near separation and then the medium and low fequency powers drop away, while the high frequency range rises and then drops over the bubble, to finally drop once again after reattachment. There are some difference between the Referencep case and the control cases, such as the shift from the medium range being dominant during separation to the low range being dominant for case LSFHp, a shift also observed for case LMFHp. Both of these shifts are counter intuitive as one would expect a shift towards the high frequency range for these cases. This shift is not observed for case LRFHp indicating that certain combinations of actuator location and frequency might show significantly different results. Rather than a shift, an increase in medium frequency range power can be observed for cases LSFLp, LMFLp and LRFLp can be observed.

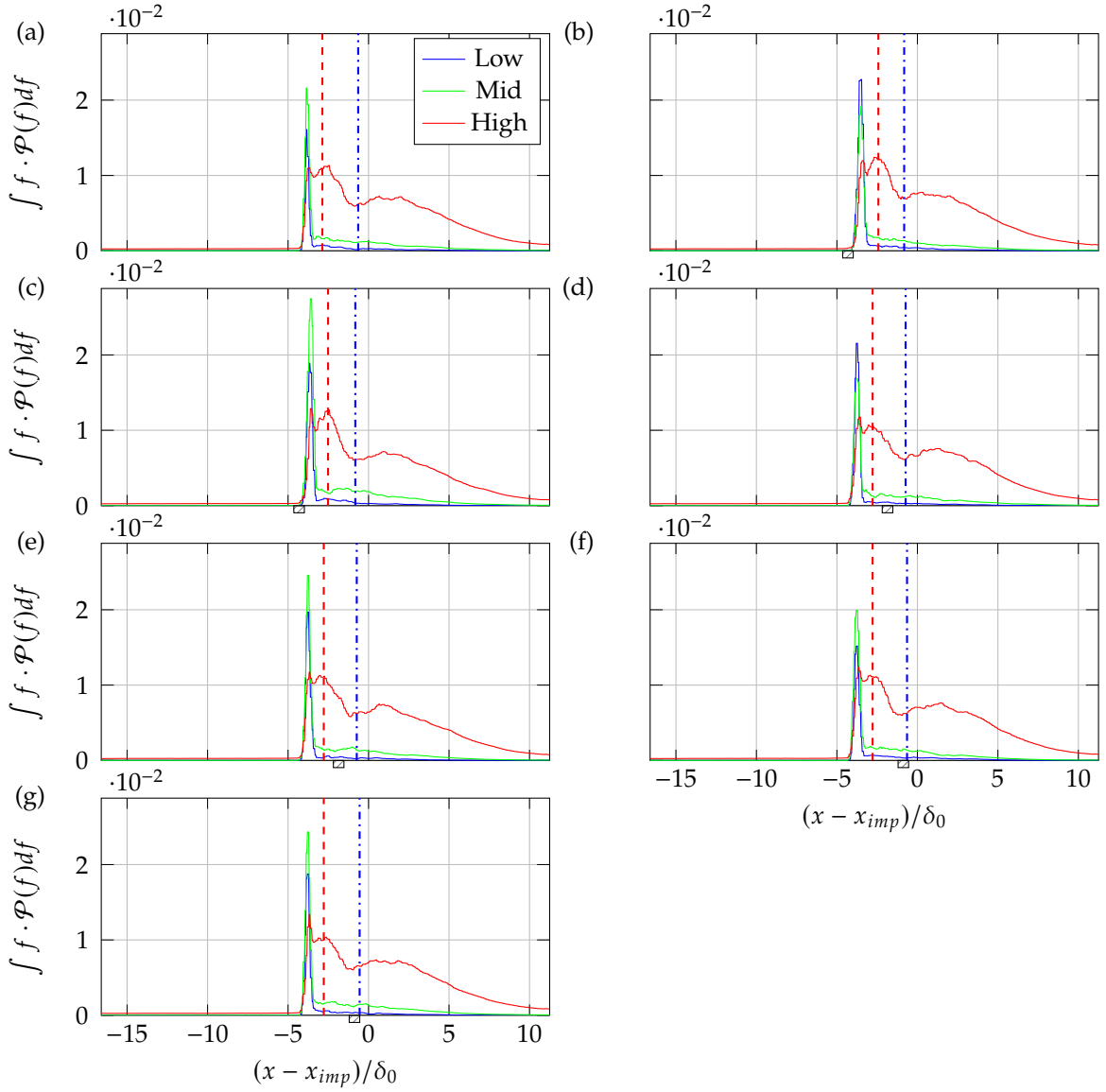


Figure 3.12: Power per frequency range for p'_w for all coarse cases. The vertical red dashed line indicates the statistical separation point, the vertical blue dashed-dotted line indicates the statistical reattachment point. The AL is indicated by ▨.

3.5.3. Coherence with injection velocity for selected cases

Similar to the observation made for the frequency range shifts, the coherence plots show that the effectiveness of the control method is depending on the actuator location and frequency. While both cases LSFHp and LSFLp show significant coherence between IV and the other metrics, the cases where the actuator is placed in the middle: cases LMFHp and LMFL show significantly less coherence at the actuator frequency. And case LRFLp does not show coherence at all. This lead to the conclusion that based on the parametric results, it is unlikely to see much influence on the separation bubble from the cases near reattachment.

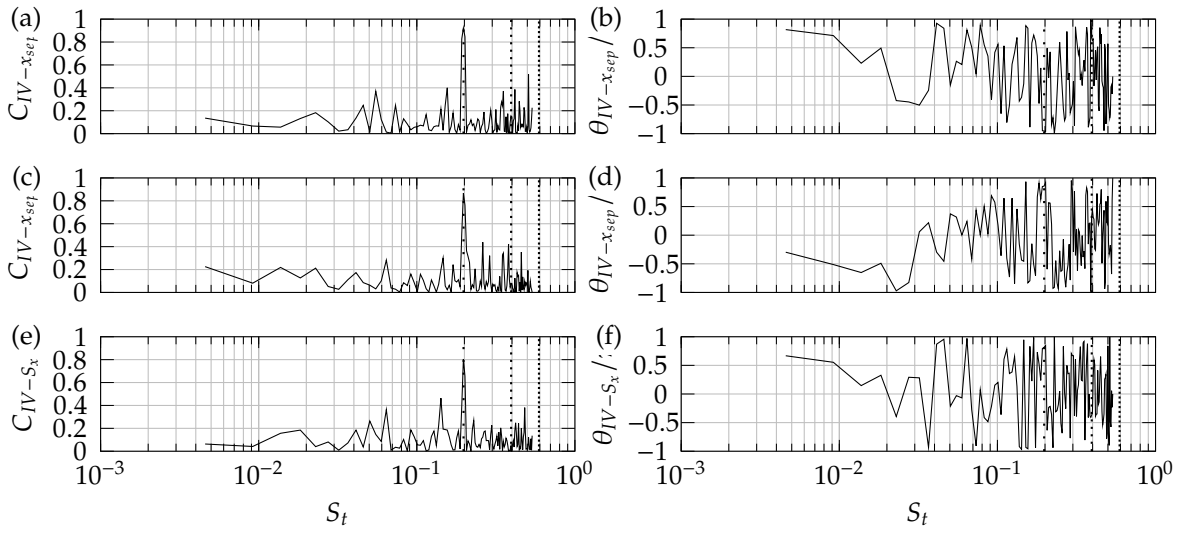


Figure 3.13: Coherence and phase between bubble motion and injection velocity for case LSFHp. (a) Coherence and (b) Phase, between x_{sep} and IV, (c) Coherence and (d) Phase, between x_{rea} and IV. The vertical dashed lines indicate the first, second and third harmonics of the AF.

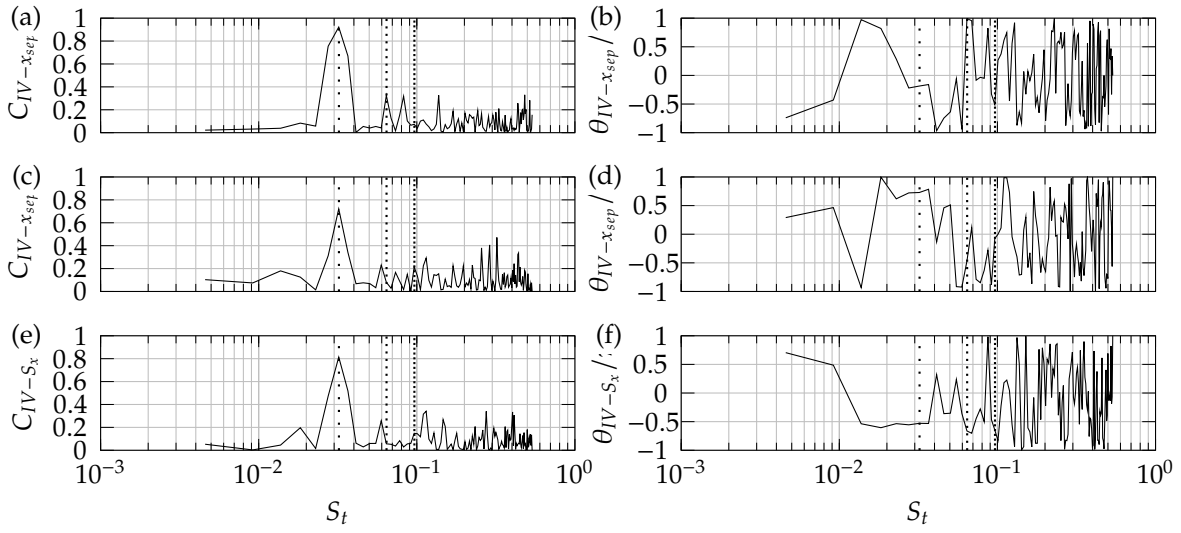


Figure 3.14: Coherence and phase between bubble motion and injection velocity for case LSFLp. (a) Coherence and (b) Phase, between x_{sep} and IV, (c) Coherence and (d) Phase, between x_{rea} and IV. The vertical dashed lines indicate the first, second and third harmonics of the AF.

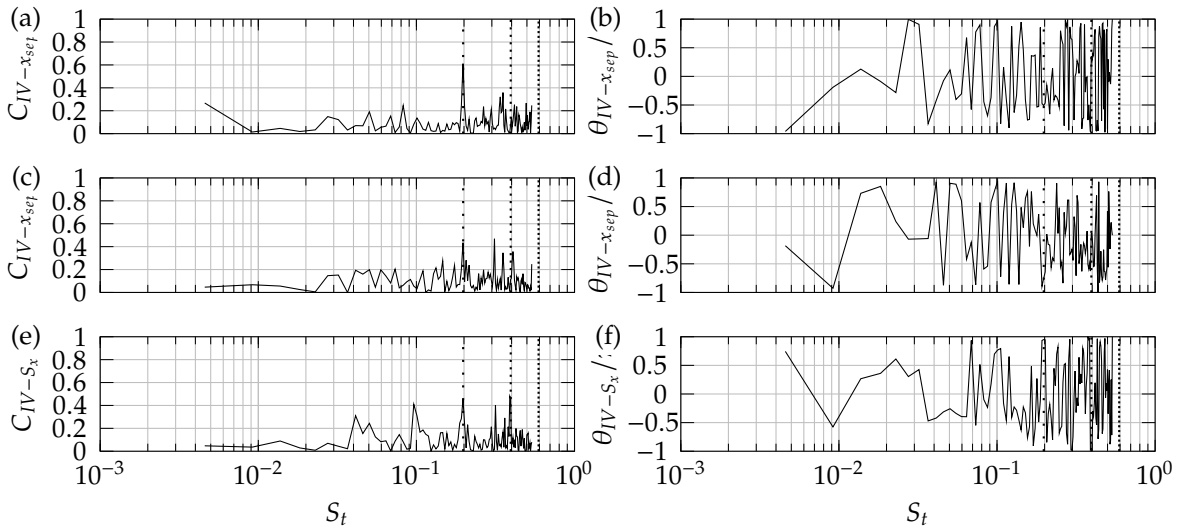


Figure 3.15: Coherence and phase between bubble motion and injection velocity for case LMFHp. (a) Coherence and (b) Phase, between x_{sep} and IV, (c) Coherence and (d) Phase, between x_{rea} and IV. The vertical dashed lines indicate the first, second and third harmonics of the AF.

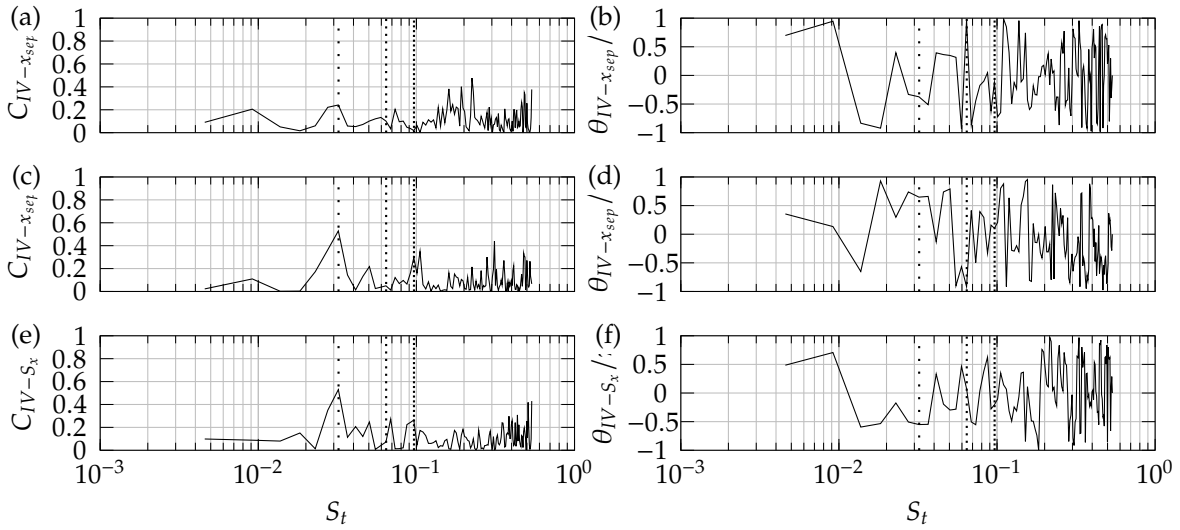


Figure 3.16: Coherence and phase between bubble motion and injection velocity for case LMFLp. (a) Coherence and (b) Phase, between x_{sep} and IV, (c) Coherence and (d) Phase, between x_{rea} and IV. The vertical dashed lines indicate the first, second and third harmonics of the AF.

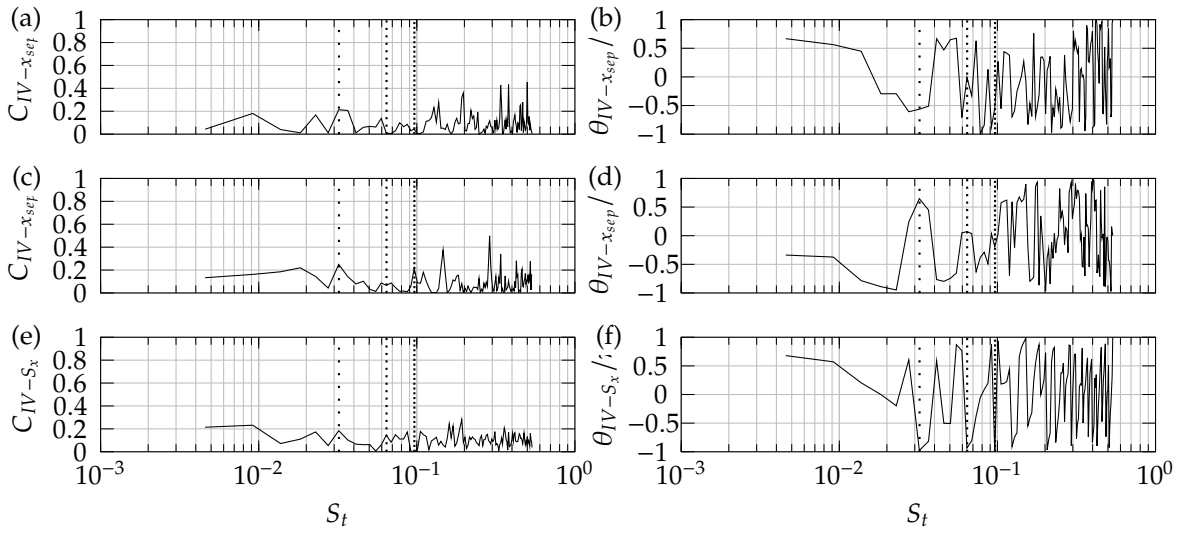


Figure 3.17: Coherence and phase between bubble motion and injection velocity for case LRFLp. (a) Coherence and (b) Phase, between x_{sep} and IV, (c) Coherence and (d) Phase, between x_{rea} and IV. The vertical dashed lines indicate the first, second and third harmonics of the AF.

4

Results

The results of the parametric study, given in chapter 3, show that the location of the actuators has a large impact on the size of the separation bubble. Actuators placed far upstream show a small reduction in the bubble size and this reduction increases as the actuators are placed closer to the reference separation point, up to an optimal location, around 1.5 δ_0 before separation. Downstream of the optimal point the reduction drops off slightly. Inside the bubble the effectiveness of the reduction in bubble size decreases as the actuators are moved downstream towards separation. At separation and downstream of the bubble, there is very little to no difference compared to the reference case.

While the variation of the actuator location showed large differences, the variation of the frequency showed a smaller influence. The results show that low frequency injection is slightly more effective in the reduction of the separation bubble size and the displacement of the separation shock. Additionally there seem to be two distinct peaks of effectiveness for actuator locations for low and high frequencies, where the low frequency seems to be effective from further upstream than the high frequency cases. Within the separation bubble, the effectiveness of both high and low frequency drops, as seen in the location variation results, and there is no clear difference between high and low frequency cases.

4.1. Control case settings

The settings used for the control cases for the production simulations are given in Table 4.1. These settings are converted from the parametric study cases as given in section 3.5 because the Reference case changes on the finer mesh. As mentioned before three ALs are used and two AFs to get a total of 6 cases.

Table 4.1: Production Case Settings.

Case	NA [−]	AD $[mm]$	IV $[m/s]$	IP $[p_\infty]$	IT $[T_\infty]$	AL $[(x - x_{imp})/\delta_0]$	AL $[x/\delta_0]$	AF $[St]$	AF $[kHz]$	Line Style
Reference	×	×	×	×	×	×	×	×	×	—
LSFH	4	4.0	250.0	2.0023	1.7993	−6.9167	9.1462	0.0988	1.3116	—
LSFL	4	4.0	250.0	2.0023	1.7993	−6.9167	9.1462	0.0161	0.2137	- - -
LMFH	4	4.0	250.0	2.0023	1.7993	−2.5884	35.2141	0.0988	1.3116	—
LMFL	4	4.0	250.0	2.0023	1.7993	−2.5884	35.2141	0.0161	0.2137	- - -
LRFH	4	4.0	250.0	2.0023	1.7993	0.2220	52.0634	0.0988	1.3116	—
LRFL	4	4.0	250.0	2.0023	1.7993	0.2220	52.0634	0.0161	0.2137	- - -

4.2. Results I: Jet actuation effects on SWBLI organization

The results obtained from the statistics, given in Table 4.2 show that both the location and frequency have different influences on the separation bubble. This table provides the spacial characteristics obtained using the method described in Appendix A.

The use of actuators has a larger influence on the movement of x_{sep} than on the movement of x_{rea} even when the actuator is placed very close to the reattachment location as done for cases LRFH and LRFL. For all cases x_{rea} moves upstream. A result that stands out is case LSFL, for which statistics indicate that

Table 4.2: Relevant interaction topology parameters obtained from the time-spanwise averaged results for the investigated cases.

Case	x_{sep} - x_{imp} [δ_0]	x_{rea} - x_{imp} [δ_0]	L_{sep} [δ_0]	V_{sep} [A/δ_0]	H_{sep} [δ_0]	S_x - x_{imp} [δ_0]	η [$^\circ$]
Reference	−5.4654	0.8780	6.3434	1.0302	0.3191	−6.5866	39.5903
LSFH	−7.7797	0.5100	8.2897	0.8454	0.3022	−8.5975	41.0926
LSFL	−3.9593	0.0054	3.9646	0.4115	0.1905	−8.7873	40.8987
LMFH	−6.2691	0.5789	6.8480	0.9128	0.2557	−7.3731	39.4527
LMFL	−6.1249	0.2185	6.3434	0.6196	0.2279	−7.3896	39.0358
LRFH	−6.0421	0.0851	6.1272	1.3349	0.3945	−7.1421	39.5862
LRFL	−6.1142	0.0130	6.1272	1.3457	0.3844	−7.0780	40.3425

x_{sep} has moved downstream compared to the Reference case, whereas all the other control cases x_{sep} moved upstream. Additionally x_{rea} moved upstream more than any other case, giving it the shortest L_{sep}, a reduction of 37.5% with respect to the Reference case. A similar volume reduction is seen for case LSFL.

L_{sep} increases for the high-frequency cases where the actuator is placed at separation or in the middle. The separation length is exactly the same for the case LMFL as it is for the Reference case. Cases LRFH and LRFL reduce L_{sep} slightly while case LSFL shows a significant reduction. The reason for the differences will be discussed in further detail in subsection 4.2.2. For the control cases located near separation and in the middle of the bubble, V_{sep} decreases compared to the Reference case. For these locations the lower actuator frequency is more effective in reducing the volume than the high-frequencies. The same pattern can be observed for H_{sep}. However for H_{sep}, the lower frequency is slightly more effective at reattachment too, although the bubble height is still larger than the Reference case.

Interestingly there is a large difference, almost 5 δ_0 between x_{sep} and S_x for case LSFL, while for most cases the difference between these two points is about 1 δ_0. This is an effect of the method of computation and the fact that the statistics were spanwise averaged.

One significant difference between the parametric study results and the production results is the upstream movement of the separation shock. In the parametric study, most cases moved the separation location downstream and reduced the separation size and volume significantly. The production cases did not move the separation point downstream, it actually moved upstream. It is true that the production cases did not have actuators placed well upstream of the separation location as the forward movement of the separation bubble was anticipated but not to this extend, placing the actuator at separation rather than upstream.

Table 4.3: Results of the snapshot averages for production cases.

Case	x_{sep} - x_{imp} [δ_0]	x_{rea} - x_{imp} [δ_0]	L_{sep} [δ_0]	V_{sep} [A/δ_0]	H_{sep} [δ_0]	S_x - x_{imp} [δ_0]	η [$^\circ$]
Reference	−6.1846	2.9374	9.1221	1.4262	0.3718	−6.6012	39.5703
LSFH	−8.1383	3.0395	11.1778	1.6643	0.3850	−8.6089	39.6332
LSFL	−8.1460	2.8048	10.9508	1.5055	0.3086	−8.5375	39.9064
LMFH	−6.9473	2.9226	9.8699	1.5270	0.3734	−7.3585	39.6239
LMFL	−6.8963	2.8534	9.7497	1.4655	0.3532	−7.3086	39.6347
LRFH	−6.7262	2.9351	9.6613	1.7177	0.4340	−7.1240	39.7945
LRFL	−6.7289	2.9390	9.6679	1.7335	0.4365	−7.1274	39.7909

Similar to statistical results of Table 4.2, the snapshot averaged results in Table 4.3 show that both the location and frequency have different influences on the separation bubble. For all control cases x_{sep} moves upstream, especially for the cases where the actuator is placed before the separation point of the Reference case, LSFH and LSFL, the separation location moves significantly further upstream than for the other cases, moving as much as 1.9 δ_0 for LSFL.

While most trends are similar between Tables 4.2 and 4.3, the values can differ significantly. Especially the bubble height is much higher for the snapshot averages because of the method used for the computation of the bubble height. The snapshots use the highest cell of the bubble while the statistics, spanwise average and then average over time, which reduces the outliers.

Another significant difference between Tables 4.2 and 4.3 are the values of LSFL. The time-averaged results show a reduction in the bubble size while the snapshot averages show an increase. This is due to the different sampling methods used, while the statistics obtain data after a set number of iterations, the snapshots are taken at a simulation time interval. The sampling rate at peak injection velocity was slightly slower thus slightly over representing the situation at peak injection velocity.

The difference between cases LSFH and LSFL could be due to the pulsing length, which is much longer for the low-frequency cases, due to the way the actuators are modeled. This will be further investigated in the instantaneous flow organization.

The frequencies used in the production cases of this study were based on a combination of the results of the parametric study and the frequencies used by literature such as Narayanaswamy et al. [33], Webb et al. [67] and Greene et al. [38]. Even though Webb et al. concluded that there was no optimal frequency when actuators are placed upstream of the separation region, both Narayanaswamy et al. and Greene et al. concluded that there was an optimal frequency. For Greene et al. this was at 3200 Hz or a Strouhal number of 0.018. The results in Table 4.2, are in agreement with Narayanaswamy et al. and Greene et al. that the more optimal frequency is around a Strouhal number of 0.0161 however the modeling of the actuators might be the cause here rather than the frequency alone. This will be discussed further in this chapter.

4.2.1. Instantaneous flow organization

Despite the instantaneous results not providing much insight in the spectral characteristics for the system, as the flow organization can vary significantly between snapshots especially for cases where control is applied, they can provide insight into the internal mechanics causing the differences observed between time- and spanwise-averaged and the snapshot averaged results. To obtain this insight the situation which provides the most contrast to the Reference case is examined which is the snapshot at peak injection velocity. As a lot of data is collected and snapshots of different angles and variables are taken, not all instantaneous fields are included. Ones that are not shown in this chapter are provided in section C.1.

First the separation shock is examined, which can be observed in the numerical Schlieren shown in Figure 4.1 but can also be observed in the instantaneous temperature and pressure, shown in Figures C.4 and C.5 respectively. These figures show that the separation shock emanates from deep within the boundary layer for all production cases. More importantly the figures show that there is a significant difference in the location of the separation shock, especially for cases LSFH and LSFL the separation shock is moved upstream significantly compared to the other control cases where it moves upstream less. The upstream movement of the separation shock consequently also causes the intersection between the two shocks to move upstream and away from the wall.

For both the Reference and the control cases the expansion fan created by the interaction between the impinging shock and the shear layer is clearly visible in Figure 4.1. However there are some differences between the control cases, in which the total width of the expansion fan can changes depending on the location of the actuator. For cases LSFH and LSFL the expansion fan extends till $(x - x_{imp}) = 2\ \delta_0$ while for the other cases it expands till past $(x - x_{imp}) = 3\ \delta_0$. Additionally, for these two cases, the presence of the actuator can be observed just below the separation shock. The presence of the actuator can be observed for LRFL in a similar manner.

While the strength of the separation shock seems to be very similar for all production cases in Figure 4.1, Figure C.4 shows that the separation shock does not behave the same in all cases. In case LSFH the initial separation shock angle gets reduced slightly towards the intersection point. For cases LSFH and LSFL there is a slight decrease in temperature after the shock, which could be caused by the actuator. For cases LSFH and LSFL there seems to be a strong first shock, which is the separation shock which is followed by a weaker shock, created by the actuators. This can be observed in Figure 4.1b-c. This result is similar to observations made by Narayanaswamy et al. [33], who clearly observed the shocks created by the actuators using Schlieren imagery. The method of extracting S_x from the data will not be able to distinguish these two shocks so close together and will have tracked the strongest shock. This means that the data for S_x and η is not completely reliable for cases LSFH and LSFL for the instantaneous, time-averaged and time series of this data.

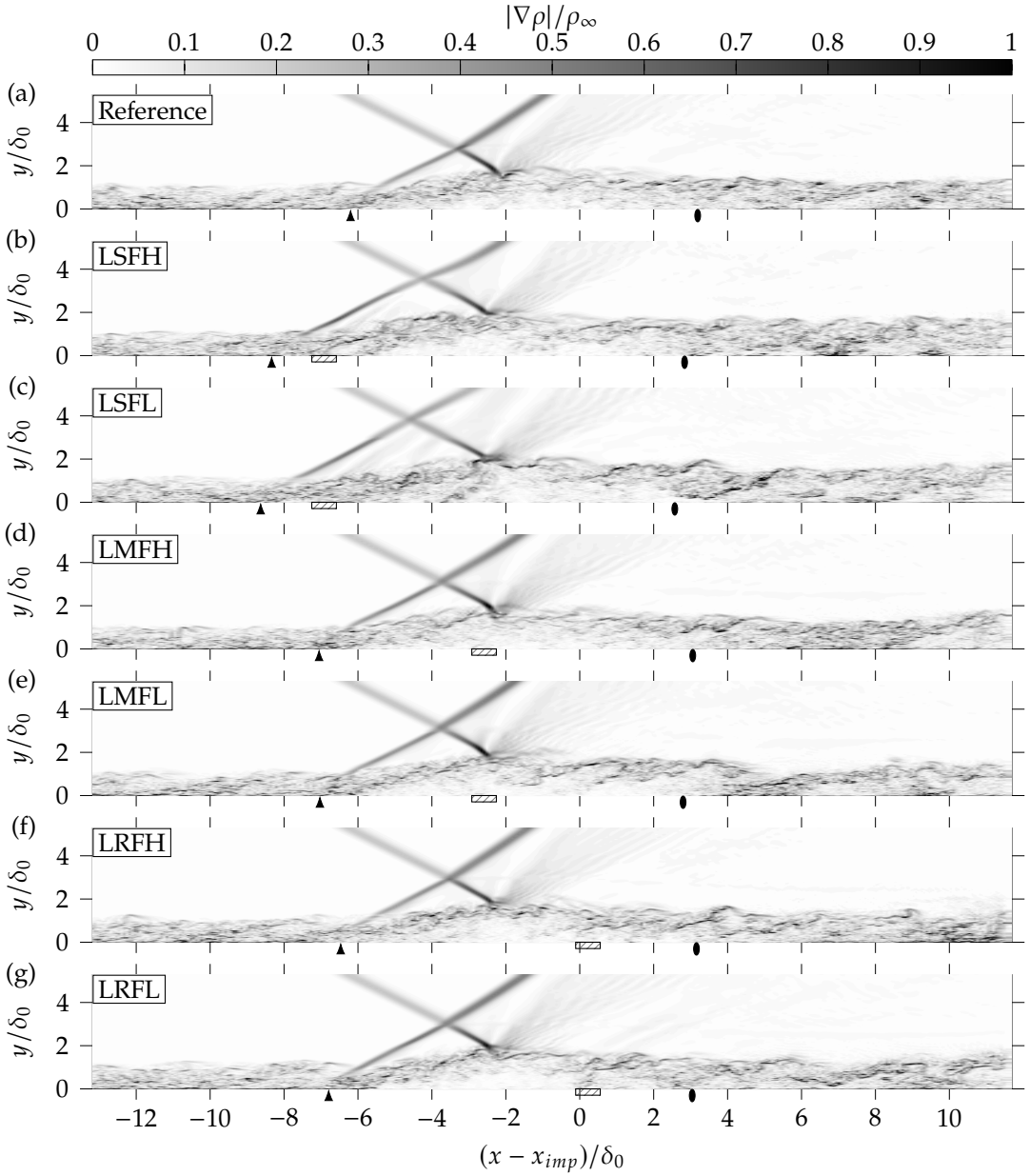


Figure 4.1: Instantaneous numerical Schlieren comparison for: (a) Reference case, (b) case LSFH, (c) case LSFL, (d) case LMFH, (e) case LMFL, (f) case LRFH, and (g) case LRFL. The instantaneous separation and reattachment points are indicated by ▲ and ⬮ respectively. The AL is indicated by ▨.

Evaluating variables such as temperature and pressure at the wall provides insight in the functioning of the actuator. Velocity at the wall is 0 as per the no-slip condition, except when the actuators are active in which case a wall velocity is set, which can be observed in Figure C.8. Pressure at the wall is shown in Figure C.10.

The placement of the actuators at separation causes local excessive heat buildup at separation. This is shown in Figure 4.2 for cases LSFH and LSFL. Especially for case LSFH there is a significant region of increased temperature. The actuators seem to cool the flow when placed at separation while they clearly heat the flow when placed at the other locations, as they can be easily spotted for the other control cases in Figure 4.2d-g. The reason for this is because the actuators use a reference temperature, which is set, however during the simulations the actual temperature of the actuators is calculated based on Riemann invariants. Case LRFH seems to be much cooler after the separation region but this could just be just this snapshot. Also cases LMFH and LMFL show very similar patterns around reattachment.

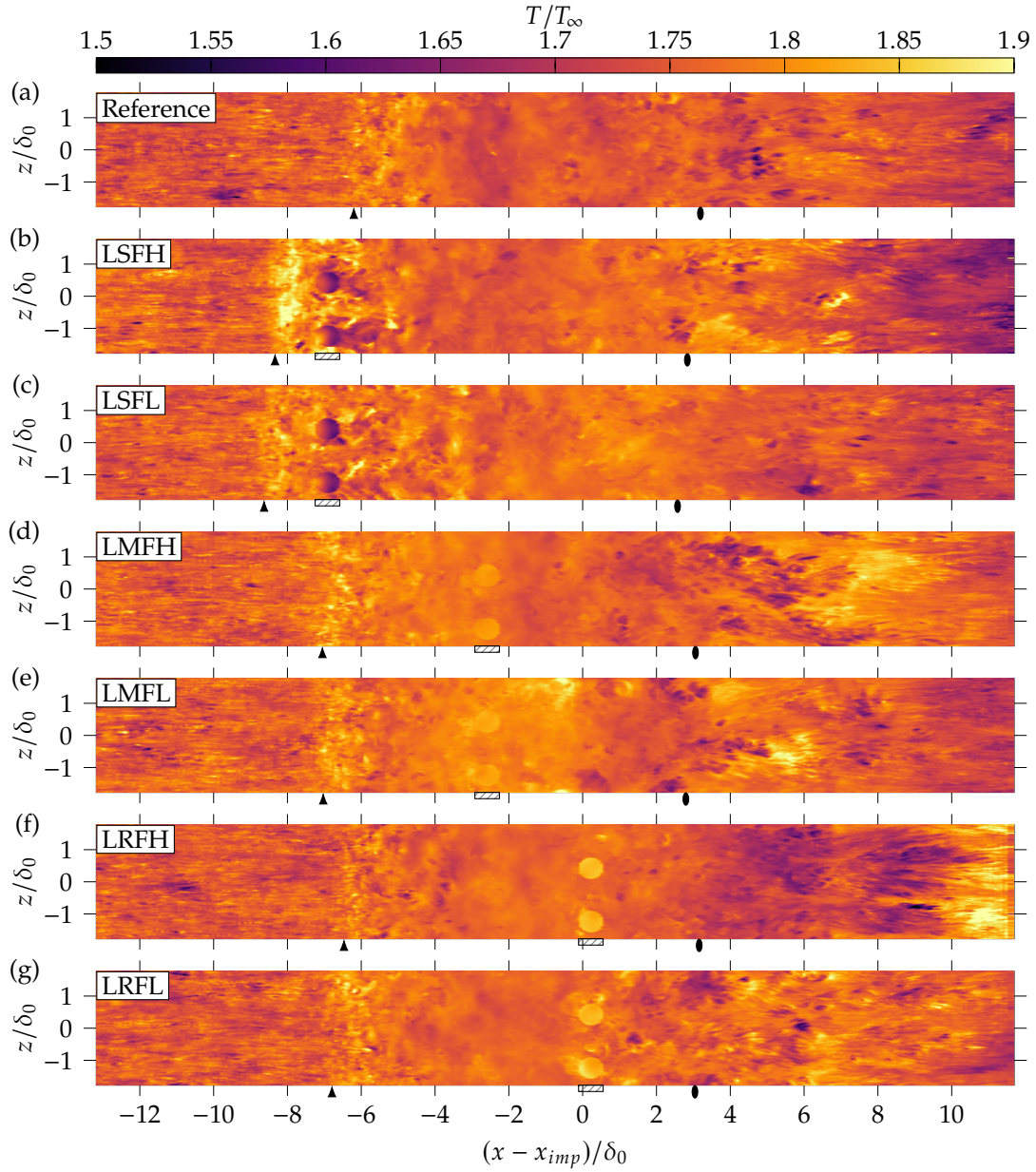


Figure 4.2: Instantaneous wall temperature comparison for: (a) Reference case, (b) case LSFH, (c) case LSFL, (d) case LMFH, (e) case LMFL, (f) case LRFH, and (g) case LRFL. The instantaneous separation and reattachment points are indicated by ▲ and ⬮ respectively. The AL is indicated by ▨.

The region downstream of the actuators seems to be cooler and the region between two actuators relatively hotter for cases LSFH and LSFL. These streaks of hotter and cooler air along the wall are present for quite a significant distance. These streaks could indicate the presence of vortical structures which trap hot air, emanating from the separation region, close to the wall. The reason for not seeing this in cases LMFH, LMFL is that the air inside the separation bubble simply moves too slow to create these vortical structures. Finally for cases LRFH and LRFL there seems to be no source of heat close enough from which hot air can be trapped and taken along the wall. There are indicators of vortical structures along the wall created by the actuators, for example in Figure C.7 and Figure C.9, even if they are not as pronounced as the ones created in cases LSFH and LSFL.

Similar to the streaks observed in the temperature for cases LSFH and LSFL, the instantaneous skin friction coefficient (C_f), as shown in Figure 4.3, shows streaks of higher of higher skin friction between and downstream of active actuators, when placed in the separation region. These streaks of higher skin

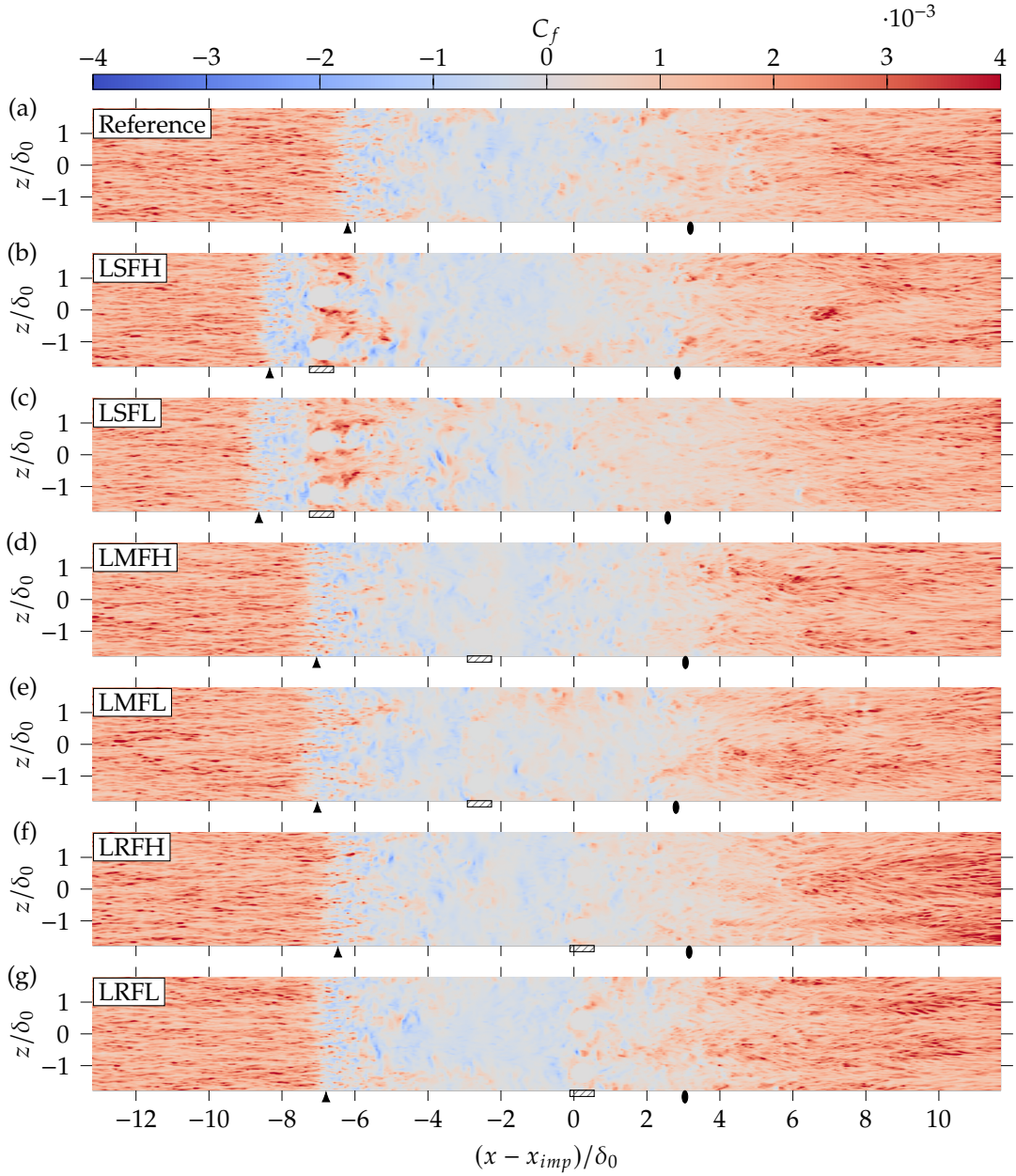


Figure 4.3: Instantaneous C_f comparison for: (a) Reference case, (b) case LSFH, (c) case LSFL, (d) case LMFH, (e) case LMFL, (f) case LRFH, and (g) case LRFL. The instantaneous separation and reattachment points are indicated by ▲ and ⬮ respectively. The AL is indicated by ▨.

friction can also be observed for case LRFL. Higher skin friction would indicate that the flow has not separated at that location. The streaks emanating from the actuators at separation, extend significantly into the separation bubble, well past the separation location of the Reference case. The skin friction just before the actuators is lower for case LSFH than for case LSFL. Despite the bubble front being highly corrugated and non-uniform in the spanwise direction, even for the Reference case, the streaks are an indication that separation has been delayed in between the actuators for cases LSFH and LSFL.

As the results in Figure 4.3 show, the spanwise averaged separation point is pushed downstream due to the vortices created by the actuators, something which has also been found experimentally [33, 38]. However this only occurs when the actuators are active, when they are not, the separation bubble returns to its original location. Additionally the instantaneous results suggest that there is a slight difference in the length of the vortices and thus the penetration into the separation bubble between

cases LSFH and LSFL. Although this is not directly clear from Figure 4.2 or Figure 4.3, it is clearly shown in Figure 4.6. Additionally this is supported by Figures C.7 and C.9, where the streaks emanating from the actuators are longer for case LSFL than for case LSFH. A reason for this could be the longer actuation time, allowing for a longer vortex to develop before the source of the vortex disappears. This could contribute to the differences in separation locations and volumes between the two cases for the time-averaged results.

To examine the creation of vortical structures by the actuators more thoroughly, they have been visualized with the λ_{ci} criterion at the last peak injection in Figure 4.4. The snapshot used for the Reference case is the last snapshot available. Because only one snapshot is used, there is a lot of noise and small scale structures which make it difficult to discern large scale structures, yet they are visible. Cases LSFH and LSFL show large scale structures emanating around and especially in wake of the actuators, indicating that the actuators cause the vortices as posed by Narayanaswamy et al. [33] and by Greene et al. [38]. And while there are some large scale strucutes visible near reattachment for both cases LMFH and LMFL, these are not observed for cases LRFH and LRFL. This could mean that the actuators only create large scale vortical structures when placed near separation or in the middle, but this needs to be investigated further using phase-averaged data as this will reduce the noise. The phase-averaged results will be discussed in subsection 4.2.6. Phase averging can also resolve the difference between case LRFH and the other cases, as this case shows very little vortical structures which is just a consequence of selecting a single snapshot and using the same iso-value for all cases.

The vortices created by the actuators when placed near separation, can be visualized by span-wise slices of v, as is done for case LSFL in Figure 4.5, and for all cases separately in section C.6. The slices show that there is a region of significant negative v velocity in between the actuators, which starts small and close to the actuators and increases in size when moving downstream. The flow towards the wall brings high energy flow near the wall, preventing separation or even reattaching the flow, which can be observed by the shape of the bubble, indicated by the yellow lines in Figure 4.5. This shows that the bubble gets split in the steamwise direction, where the bubble mainly forms directly behind the actuators and is reduced or completely removed in between the actuators. Additionally the bubble is not necesarily connected from wall to the peak of the bubble as shown in the fourth slice.

It should be noted that there is a difference between cases LSFL and LSFH shown in Figure 4.5 and Figure C.70 respectively, which is the magnitude of v and the shape of the bubble in the 4th slice. There is both a higher positive and negative v velocity for case LSFL and the bubble is shaped as two narrow columns where the bubble shape for case LSFH is much wider. This indicates that, at this location, there is still a vortex, created by the actuators, which is not present for case LSFH. As there is only a difference in actuation time, this suggests that the vortices created by the low-frequency case are longer in the streamwise direction those created by the high-frequency case.

Further exploration into the difference actuation time makes, with respect to the penetration of the vortices inside the bubble, is done using the 3D visualization of the bubble as shown in Figure 4.6. The isometric view of the instantaneous separation bubble is given in Figure C.15. As the snapshots are both at peak injection, the main difference between low- and high-frequency cases is the actuation time.

From Figure 4.6b-c it is clear that the vortices penetrate into the bubble much further for case LSFL than for case LSFH. In fact the vortex almost penetrates the entire bubble length for case LSFL, while it only manages to penetrate a quarter of the length for case LSFH. Both cases show a region of separation just upstream of the actuators, which is a result of an increase in the pressure near the wall due to the active actuators. As the actuator partially block the airflow, forcing it through a narrow channel, a region of slow moving, sometimes even recirculating, air builds up just before the actuators. This is confirmed by the velocity at the wall shown in Figure C.7. Although the other cases also move the separation point upstream, the blockage causes the upstream movement to be the largest for cases LSFH and LSFL.

Cases LMFH and LMFL do no show the splitting of the bubble that is observed for cases LSFH and LSFL. Although case LMFL does seem to show a significant reduction in the bubble after the actuators, but this could be contributed to this specific snapshot. The same can be said for cases LRFH and LRFL which seem to show a reduction of the bubble in between the actuators yet this could be the snapshot. Just as for the vortical structures of Figure 4.4, phase-averaging the results will provide an answer, and these results are given in Figure 4.14 and Figure C.18 for the isometric and top views respectively.

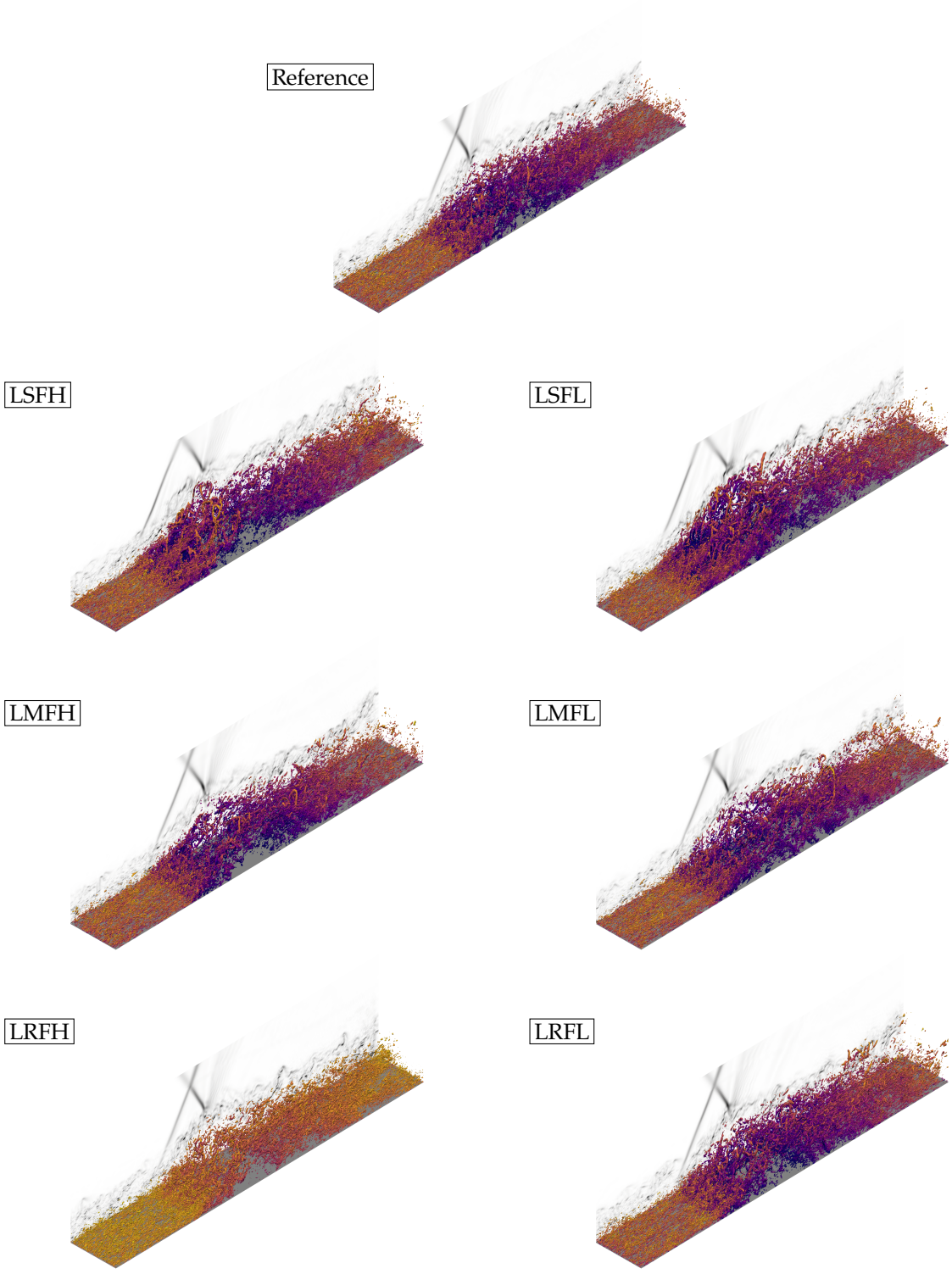


Figure 4.4: Instantaneous vortical structures visualized with the $\lambda_{ci}/u_\infty = 0.35$ criterion and colored by the local streamwise velocity.A numerical schlieren is shown in the background slice for each case.

Due to the high corrugation of the bubbles separation and reattachment lines and vortical structures created by the actuators, it is debatable whether the assumption that spanwise averaging data and then using this to do spectral analysis is valid. However, there are few alternatives and looking at, for example, the instantaneous C_f, as shown in Figure 4.3, the separation point seems to be quite stable

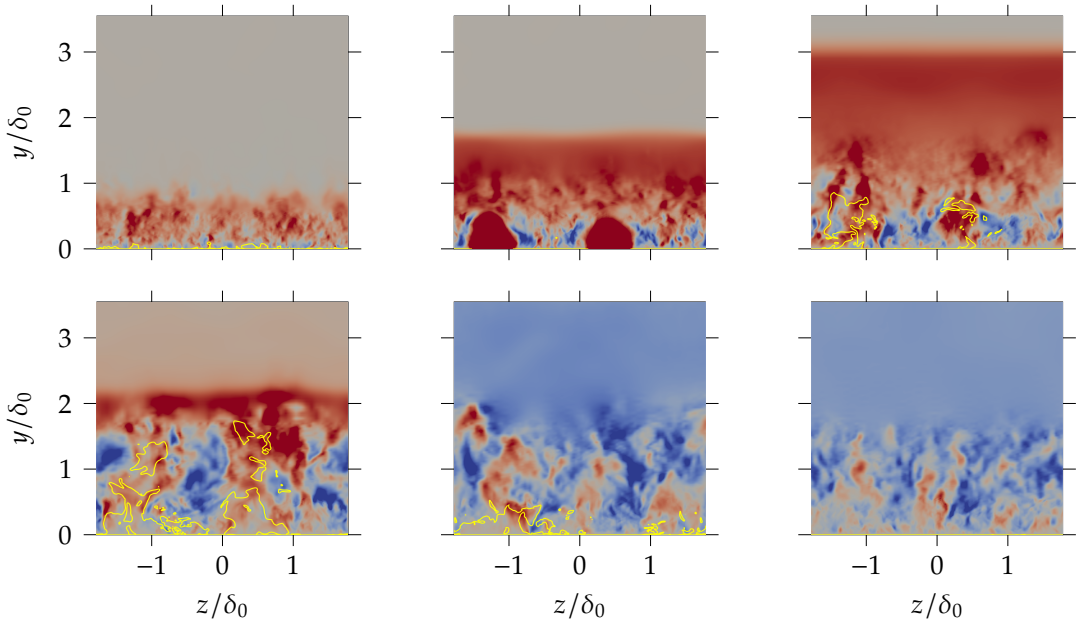


Figure 4.5: Span-wise slices of v velocity at peak injection for case LSFL. The yellow line indicates the contour of the separation bubble.

over the span. This is actually not the case. Greene et al. [38] actually shows why spanwise averaging might not be fair. The active actuators cause local upstream movement of the separation line, while the vortices created by the actuators push the separation point downstream, as shown by the bubble in Figure 4.6. Therefore spanwise averaging does not always correctly show the actual point of separation.

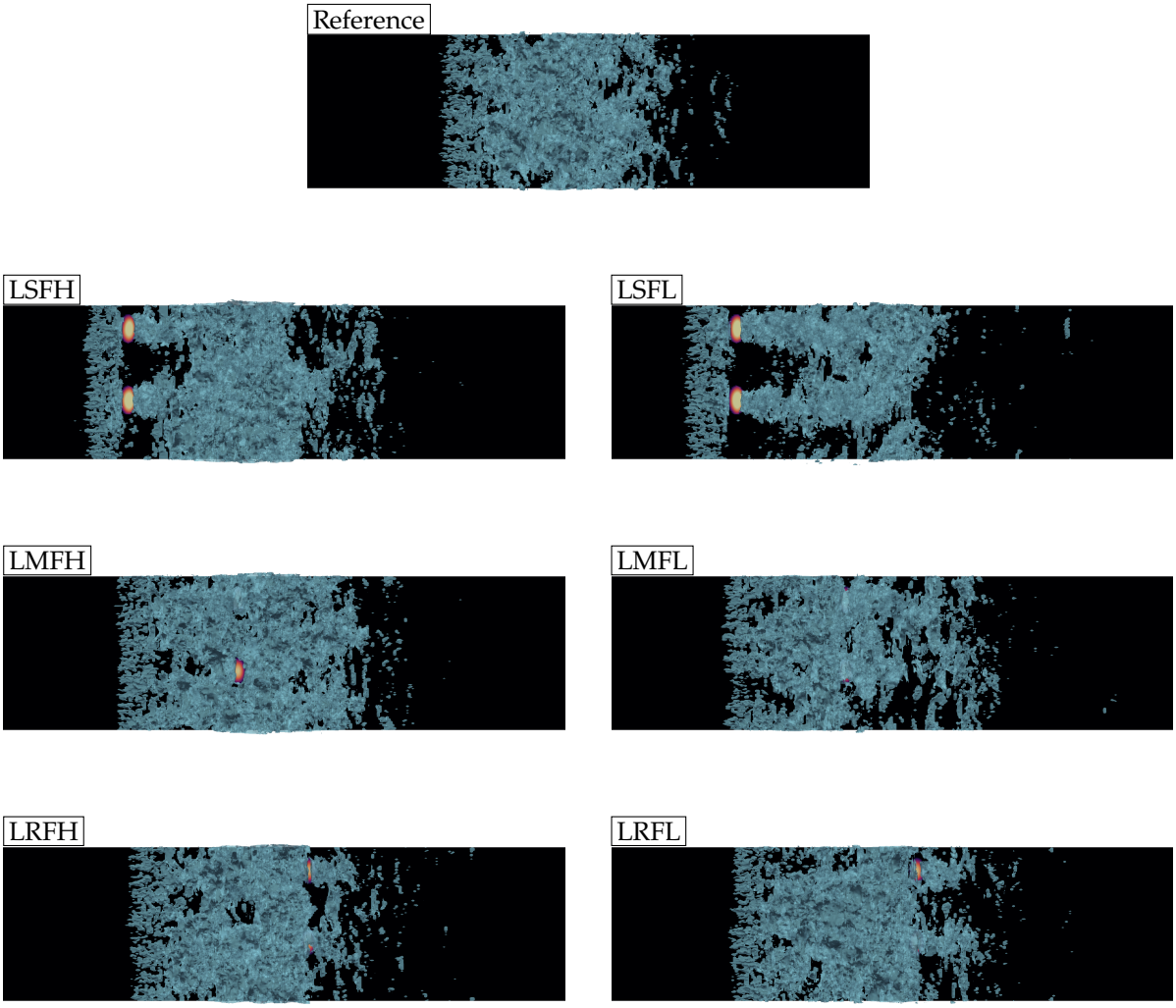


Figure 4.6: Instantaneous bubble shape visualized with the iso-contour of $u = 0$, viewed from above.

4.2.2. Skin friction comparison

The instantaneous skin friction from Figure 4.3 gives clues to what causes the difference between cases LSFH and LSFL, it is only a snapshot which provides limited information. Even if the vortical structures do not make the spanwise averaging completely valid, it does show why the x_{sep} is vastly different between the two cases. By time- and spanwise-averaging the skin friction, as done in Figure 4.7, it shows the impact the actuators have on the separation behavior.

In all cases the use of actuators causes a drop in skin friction just before the actuator location. After the actuator C_f actually increases again and even overshoots the Reference case, then slowly getting back closer to the Reference case. For cases LSFL and LRFL, the point at which C_f starts to drop is slightly before the high frequency case at the same location. However all low frequency cases decline slightly slower than the high frequency cases. And in all low frequency cases the C_f is higher after the rebound. Thus by placing the actuators in the correct location, the drop and rebound can be placed so that C_f does not become zero, and thus delaying separation. This is the difference between cases LSFH and

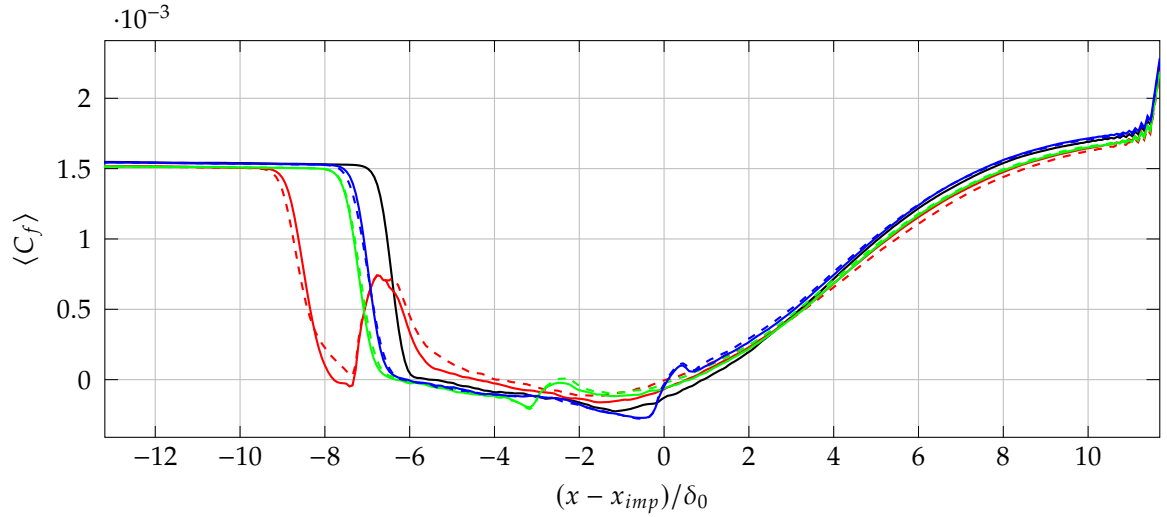


Figure 4.7: Time- and spanwise-averaged skin friction compared. For line legend see Table 4.1.

LSFL and the reason why x_{sep} is further upstream for case LSFL. Although as mentioned, this is mainly an effect present because of the spanwise averaging, this result is not shown by averaging the snapshots, as shown in Table 4.3.

4.2.3. Probe and statistical wall data compared

Time-averaging the wall data obtained by the probes might provide similar insight into the certain flow features as the averaging of C_f did. The results of this are shown in Figure 4.8.

The wall pressure (p_w) normalized by the p_∞ shown in Figure 4.8a shows little differences between the cases except for cases LSFH and LSFL as these are placed before the initial pressure rise of the Reference case. A small pressure drop can be observed for cases LRFH and LRFL near reattachment, which is due to the pressure of the actuators being lower than the pressure in the bubble, something that can be observed directly in Figure C.10. This could be one of the reasons for the lower effectiveness of the actuators when placed inside the bubble. The pressure inside the bubble is significantly higher than the pressure of the actuator, which reduces the effectiveness of the pressure disruption the actuators can achieve.

Even with the reference value of IP set to 2 p_∞, with the computation of the Riemann invariants, the actual pressure is lower, just above 1.5 p_∞. This can be observed in Figure 4.8a for cases LSFH and LSFL. Additionally this can be observed for case LSFL in Figure 4.29 for the probe at the actuator location. Similarly the reference value of IT is also not reached as shown in Figure 4.8d.

For all control cases the initial rise in p_w is moved upstream compared to the Reference case. While up- and downstream of the bubble, the time-averaged values are the same, the peak values are not. The peak wall pressure occurs at roughly the same location for all cases, yet the Reference case has a observably higher peak. At separation, both cases show the same peak value, which is noticeably lower than the peaks observed in the middle and at reattachment, where no significant differences are present. Therefore it seems that the upstream movement of the initial separation reduces the peak pressure inside the bubble, and the longer the bubble is stretched, the lower the peak value in p_w.

Perhaps the most interesting result of the probe data is the RMS of the p'_w shown in Figure 4.8b. These results show large differences between control cases and the Reference case but also between low- and high-frequency cases. There is naturally an increase in pressure variance ($p'p'$) near separation, but for all control cases this rise is moved upstream, in line with the upstream movement of the rise in p_w. All the low-frequency cases show a distinct and significantly higher peak in $p'p'$ during separation compared to the high-frequency cases in the same locations. This is somewhat expected for case LSFL, however this increase is also clearly visible for cases LMFL and LRFL. This increase could be an indication that the separation shock, which is located here, has increased in its low-frequency unsteadiness. While case

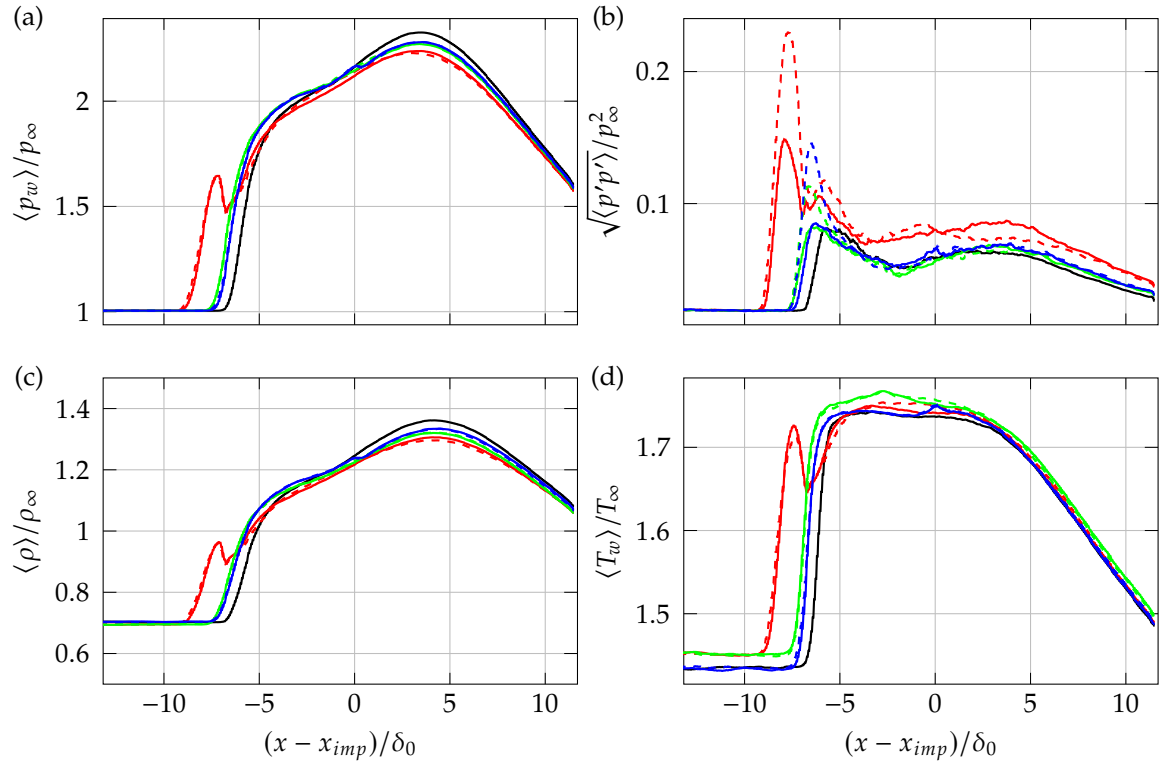


Figure 4.8: Comparison of temporally averaged probe data for the production cases: (a) $\langle p_w \rangle / p_\infty$, (b) RMS of the p'_w, (c) $\langle \rho \rangle / \rho_\infty$, (d) $\langle T_w \rangle / T_\infty$. For line legend see Table 4.1.

LSFH shows a significantly higher peak compared to the Reference case, cases LMFH and LRFH show only a small increase. Additionally while there is an increase in $p'p'$ near the reattachment point for all cases, this increase starts much earlier for cases LSFH and LSFL and is carried downstream of the bubble, indicating that the pressure disruptions are present throughout the entire domain.

A sharp rise in T_w just before the actuator can be observed for cases LSFH and LSFL as shown in Figure 4.8d. As both the IP and IT are computed based on the Riemann invariants, the temperature in the injector is not exactly the reference value given in Table 4.1, similar to what was observed for the IP in Figure 4.8a. However this does not explain why it is just in front of the actuator. This can also be observed in Figure C.4b-c, Figure 4.2b-c and Figure C.37b-c. This buildup is caused by the actuator blockage which was also observed for Figure 4.6.

4.2.4. Time-averaged flow organization

The upstream movement of the separation bubble and shock, which was already indicated by the results of Table 4.2, Figure 4.7 and the instantaneous snapshots, due to the actuators can also be observed in the time- and spanwise-averaged streamwise velocity field u, as shown in Figure 4.9. This translation is especially apparent in for cases LSFH and LSFL, Figure 4.9b-c, in which it is clear that the separation shock moves upstream significantly. Placement of the actuators just upstream of the separation location of the Reference case leads to translation of the separation location to just upstream of the actuators. The other cases also move the separation point and separation shock upstream, however this difference is not as significant.

The application of control seems to weaken the shock strength of the separation shock for cases LSFH and LSFL. This is can be observed in the more gradual ρ gradient shown in Figure 4.10. This weaker gradient could indicate that the shock strength has decreased, however as the inflow velocity and the wedge angle are constant this is unlikely. The gradual gradient is an indication of a larger range of motion of the separation shock. The low-frequency cases all show a weaker shock compared to the high-frequency cases and the Reference case, suggesting that the separation shock of the low-frequency cases has a larger excursion range.

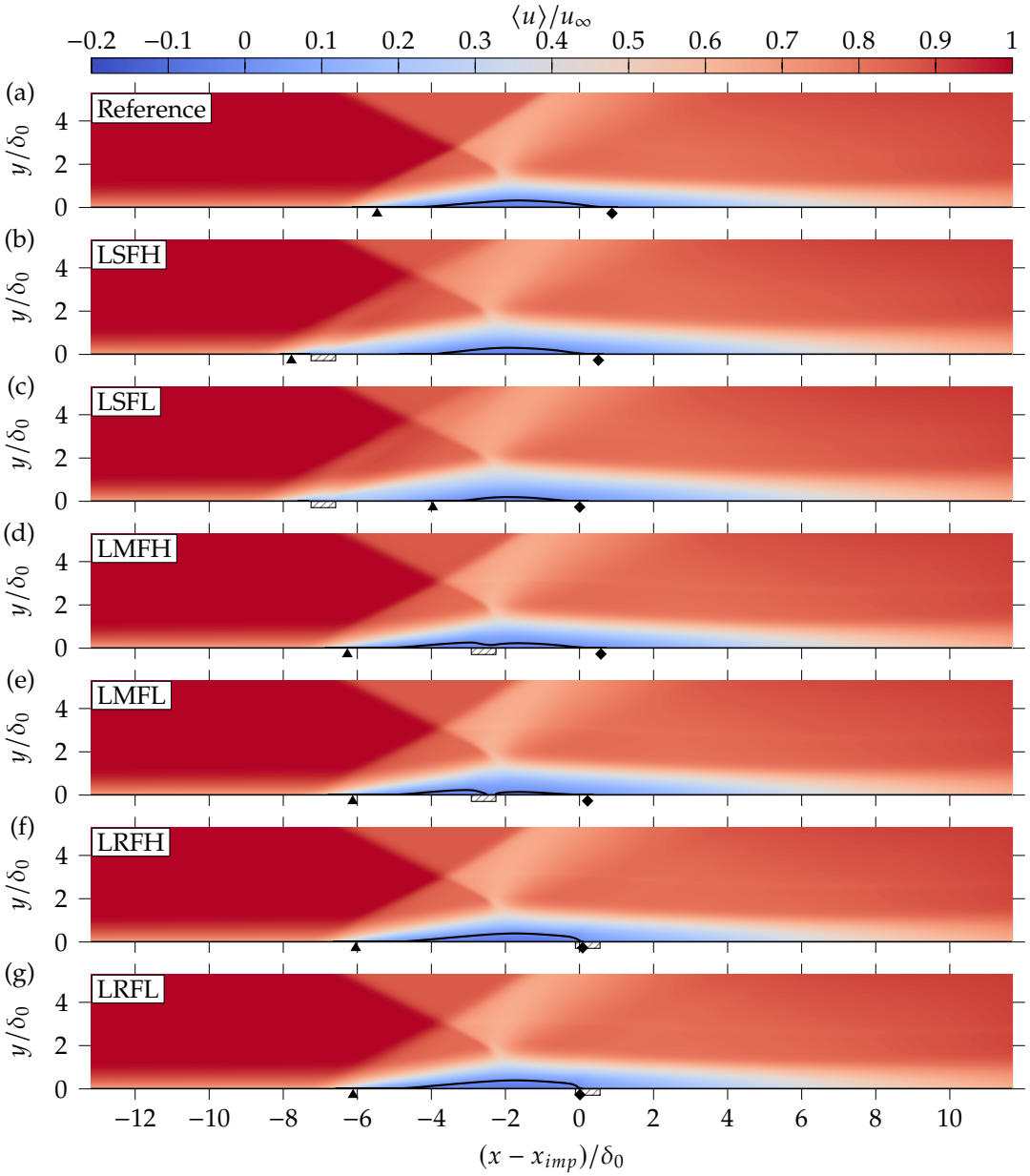


Figure 4.9: Time- and spanwise-averaged streamwise velocity comparison for: (a) Reference case, (b) case LSFH, (c) case LSFL, (d) case LMFH, (e) case LMFL, (f) case LRFH, and (g) case LRFL. The solid black line indicates the statistical isocontour of $u = 0$.The statistical separation and reattachment points are indicated by ▲ and ◆ respectively. The AL is indicated by ▨.

Similar to what was observed for the instantaneous results in Figure 4.1, the expansion fan, created by the interaction between the impinging shock and the shear layer, is clearly visible for all cases in Figure 4.10. While the instantaneous results showed slight differences in the angle of the fan between the cases, this is not really observed for the time- and spanwise-averaged results.

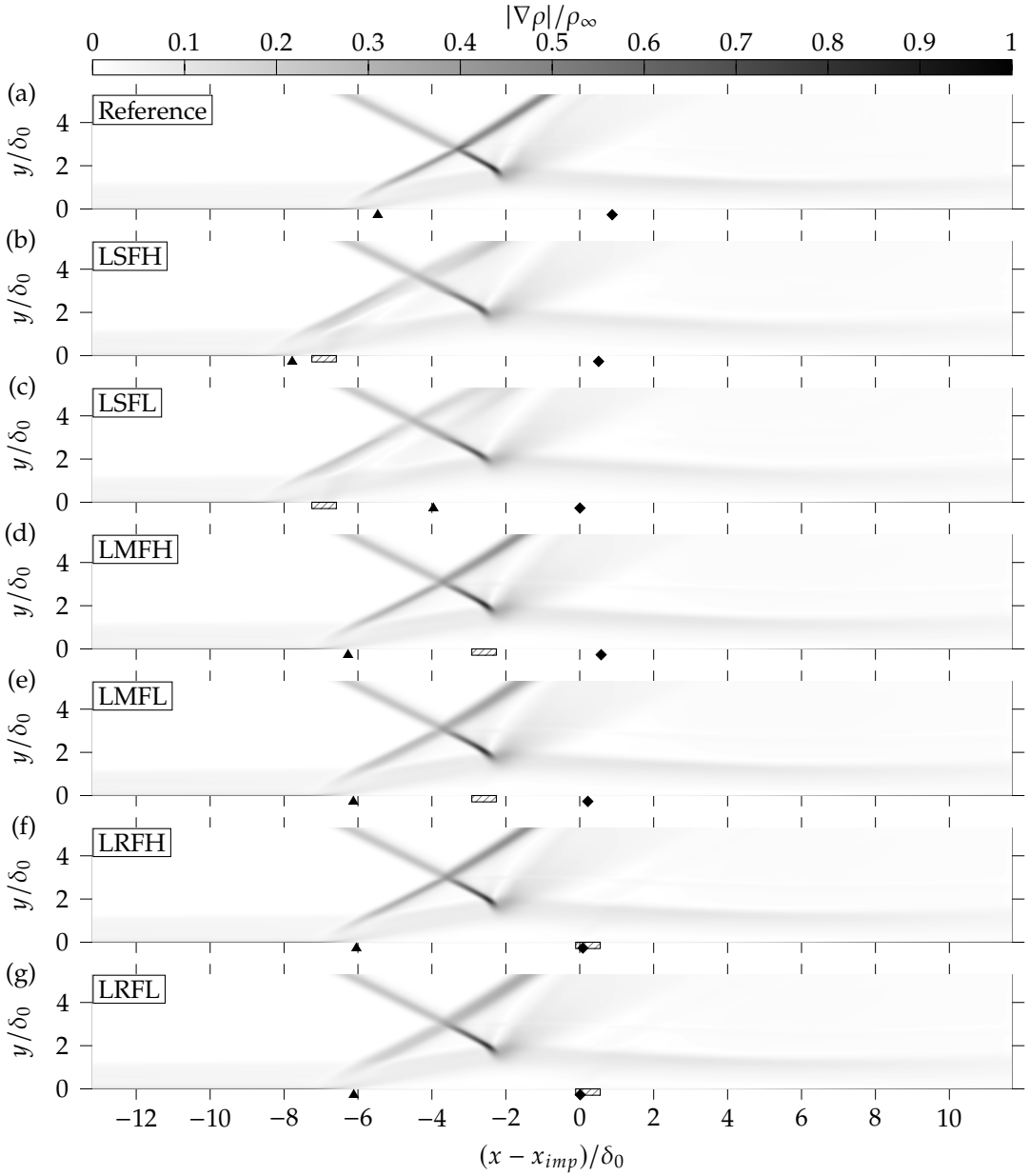


Figure 4.10: Numerical Schlieren based on time- and spanwise-averaged ρ comparison for: (a) Reference case, (b) case LSFH, (c) case LSFL, (d) case LMFH, (e) case LMFL, (f) case LRFH, and (g) case LRFL. The statistical separation and reattachment points are indicated by ▲ and ◆ respectively. The AL is indicated by ▨.

4.2.5. Bubble shape

The placement and frequency of the actuators significantly influence the volume and shape of the statistical separation bubble as shown in Figure 4.11, which shows a zoomed in version of the isocontours of $\langle u \rangle = 0$ in Figure 4.9. Beware of the vertical axis which is not scaled the same as the horizontal axis. Showing these separately allows for an easier comparison regarding the volume and shape of the separation bubble. While metrics such as the L_{sep}, H_{sep} and V_{sep} from Table 4.2 do provide some insight on the bubble topology, additional metrics for the analysis of the bubble topology are given in Table 4.4.

The previously made suggestion that the actuators act as a temporary barrier, causing a buildup of slow moving and sometimes even separating flow, seems to be corroborated by the results of Figure 4.11. This causes the small bulge just before the actuators for cases LSFH and LSFL . It is also the cause why the bubble is much fuller and steeper for the cases at reattachment, and why the actuators in the middle have the same separation point as the cases near reattachment and the same reattachment point as the

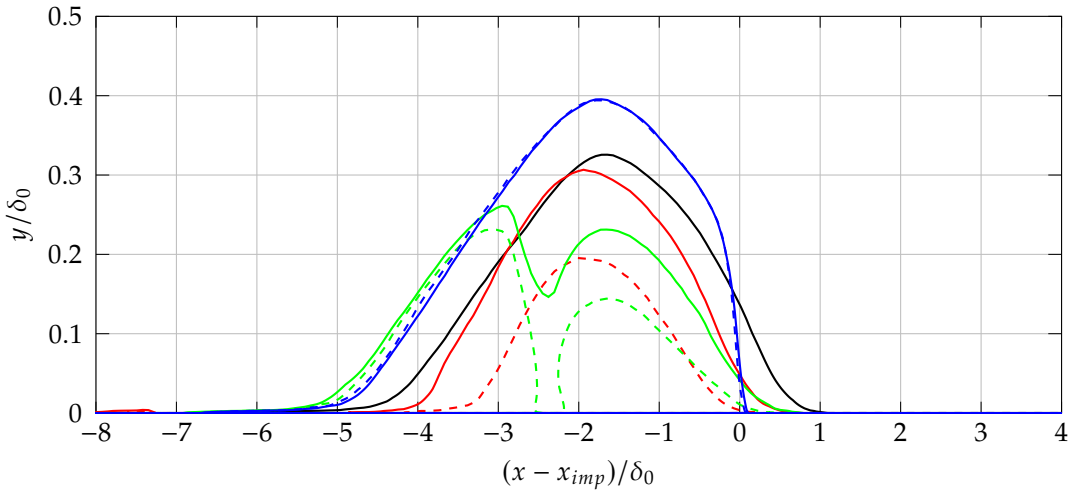


Figure 4.11: Isocontours of $\langle u \rangle = 0$ for production cases. For line legend see Table 4.1.

cases near separation. The results also show why spanwise averaged results do not tell the full story as Figure 4.6 and even Figure 4.14 clearly show that there is a bubble present but in when spanwise averaged it is not visible.

Visually the volumes shown align with the data given in Table 4.2. Cases where the actuator is placed at separation or in the middle of the separation bubble show a reduction of volume compared to the Reference case. The low frequency cases show a significantly larger reduction in total volume compared to high frequency cases at the same AL. Cases LRFH and LRFL on the other hand show a significant increase in the bubble volume and here there is little difference between between these two cases.

The apex point (x_a) is less effected by the variation of frequency than it is influenced by the variation of injection location. The apex location is the same for cases LSFH and LSFL and it is the same for cases LRFH and LRFL. Cases LMFH and LMFL have a different location because the actuator has changed the bubble shape so much that there are two apex points. Although visually they seem to be very close still.

Table 4.4: Topological properties of the separation bubble.

Case	x_a - x_{imp} [δ_0]	$\frac{H_{sep}}{L_{sep}}$ [-]	$\frac{V_{sep}}{\frac{1}{2}H_{sep}L_{sep}}$ [-]	$\frac{L_a}{L_{sep}}$ [-]	$\frac{V_a}{V_{sep}}$ [-]
Reference	−1.6797	0.0408	0.8410	0.5682	0.3538
LSFH	−1.9634	0.0344	0.7734	0.6957	0.2533
LSFL	−1.9649	0.0282	0.8909	0.4727	0.2341
LMFH	−2.3192	0.0378	0.8287	0.4737	0.3146
LMFL	−2.4297	0.0362	0.8511	0.4659	0.3044
LRFH	−1.7904	0.0449	0.8194	0.6941	0.4077
LRFL	−1.8104	0.0451	0.8216	0.6706	0.4033

The shape of the bubble for the Reference case is quite symmetric with the leading side being more concave and the trailing side slightly being convex. The triangular compliance ($\frac{V_{sep}}{\frac{1}{2}H_{sep}L_{sep}}$) is close to 1 and the leading side is slightly longer than the trailing side. However due to the convexity of the trailing side the leading side is slightly less voluminous than the trailing side. From visual assessment case LSFH and case LSFL are very similar however for case LSFH there is a small portion of the bubble between -8 and -7 which gives dissimilar results in Table 4.2. The movement of the separation point upstream leads to a drop in aspect ratio and triangular compliance and an increase in the leading to total separation length ratio. In this case the volumetric ratio shows that the bubble is symmetrically similar to the Reference case with the trailing side having a higher volume than the leading side.

The height, length and volume of case LSFL are significantly lower than the Reference while visually

having a similar shape, although there are some distinct differences. The apex is much rounder, the apex location is before the halfway point of the separation length and the bulging of the trailing side is higher.

The effect of an abrupt reduction in height of the bubble as can clearly be seen in cases LMFH and LMFL which show a shape unlike any of the other cases. The injection causes the isocontour line to be drawn towards the wall, in case LMFL the effect of the actuators is strong enough to divide the separation region into two zones. The actuators seem to have ejected the recirculation region directly above pushing the entire bubble forward and one could argue that there are now two apex points.

The effect of the injection is also seen in cases LRFH and LRFL, due to the AL for these cases being near the reattachment point of the Reference case, there is an abrupt ending of the bubble. This is the bulging effect which was observed for cases LSFH and LSFL in Figure 4.6. This results in an increase in the volumetric ratio, where the ratio of LRFH is actually above 0.5, meaning that the leading volume is larger than the trailing volume. The abrupt ending of the bubble also has implications on the length and thus triangular compliance. The reason for the bubble not being present above the actuator in the time- and spanwise-averaged isocontour is that the actuators cover more than half the domain and the injection velocity is so high that u is no longer negative.

The effect the presence of actuator has on the mean shape of the separation bubble can be compared to the effect observed by Pasquariello et al. [8]. The difference is that Pasquariello et al. used a duct to effectively do suction inside the bubble and inject this mass upstream of the separation bubble, which impacts the shape of the bubble. The similar effect is observed in the way that the separation bubble completely disappears directly above the the method of control.

Based on the data shown in this section it can be concluded that the bubble shape is predominantly influenced by the actuator location rather than the frequency. The metrics presented in Table 4.4 indicate that the elements related to bubble shape, such as triangular compliance and the volumetric ratio, exhibit comparable patterns across cases where the actuator is placed in the same location. On the other hand, as deduced by the data in Table 4.2 and from visual inspection of Figure 4.11, frequency is the a significant influencing factor when it comes to the size of the bubble.

Even though the snapshot averages showed only a marginal reduction in the separation bubble size, the time- and spanwise-averaged bubble size and shape shows that both the location and frequency are of significant influence. The larger reduction at separation is conform the results found by Narayanaswamy et al. [33] and Greene et al. [38], which showed reductions of the separation bubble close to 40%. These studies also found minimum to no reduction with the actuators placed inside the bubble.

4.2.6. Phase-averaged flow organization

Rather than time- and spanwise-averaged data which loses a lot of details and does not distinguish between the actuators being active or not, the instantaneous snapshots can also be used for phase averaging. The periodically pulsing motion of the actuators allows for averaging at the same injection phase, indicated by θ_p which ranges from 0 to 1, resulting in an isolation of the effect of this phase. Arguably the most interesting phase is at peak injection or $\theta_p = 0.5$. The phase is averaged using the snapshot at peak injection, and for the low-frequency cases two additional snapshots are taken before and after the peak snapshot. Where the data in Figure 4.4 is noisy which makes it hard to distinguish large scale coherent structures, the phase-averaged data clearly shows these large scale structures around the actuators. Additionally injection-phase-averaged results are shown for cases LSFH and LSFL in which 4 phases of the injection, $\theta_p = [0, 0.25, 0.5, 0.75]$, are are averaged. For brevity only a selected number of phase-averaged figures is shown in this section, the top views and injection-phase-averages of the remaining cases are shown in section C.3.

4.2.6.1 Peak-phase-averaged

The vortical structures visualized by the λ_{ci} criterion for the peak-phase-averaged data, as shown in Figure 4.12, indicate that at peak injection the cases at separation create a significant amount of large scale vortical structures in the shear layer. These large scale structures remain present till the peak of the bubble after which they are no longer clearly apparent. At the peak of the bubble, where the impinging shock interacts with the shear layer, a large amount of vortical structures is created,

independent of actuator location or frequency. Comparing this to the start of the injection phase, as shown in Figures C.19 and 4.15 for $\theta_p = 0$, there seems to be a larger amount of vortices created at this interaction location.

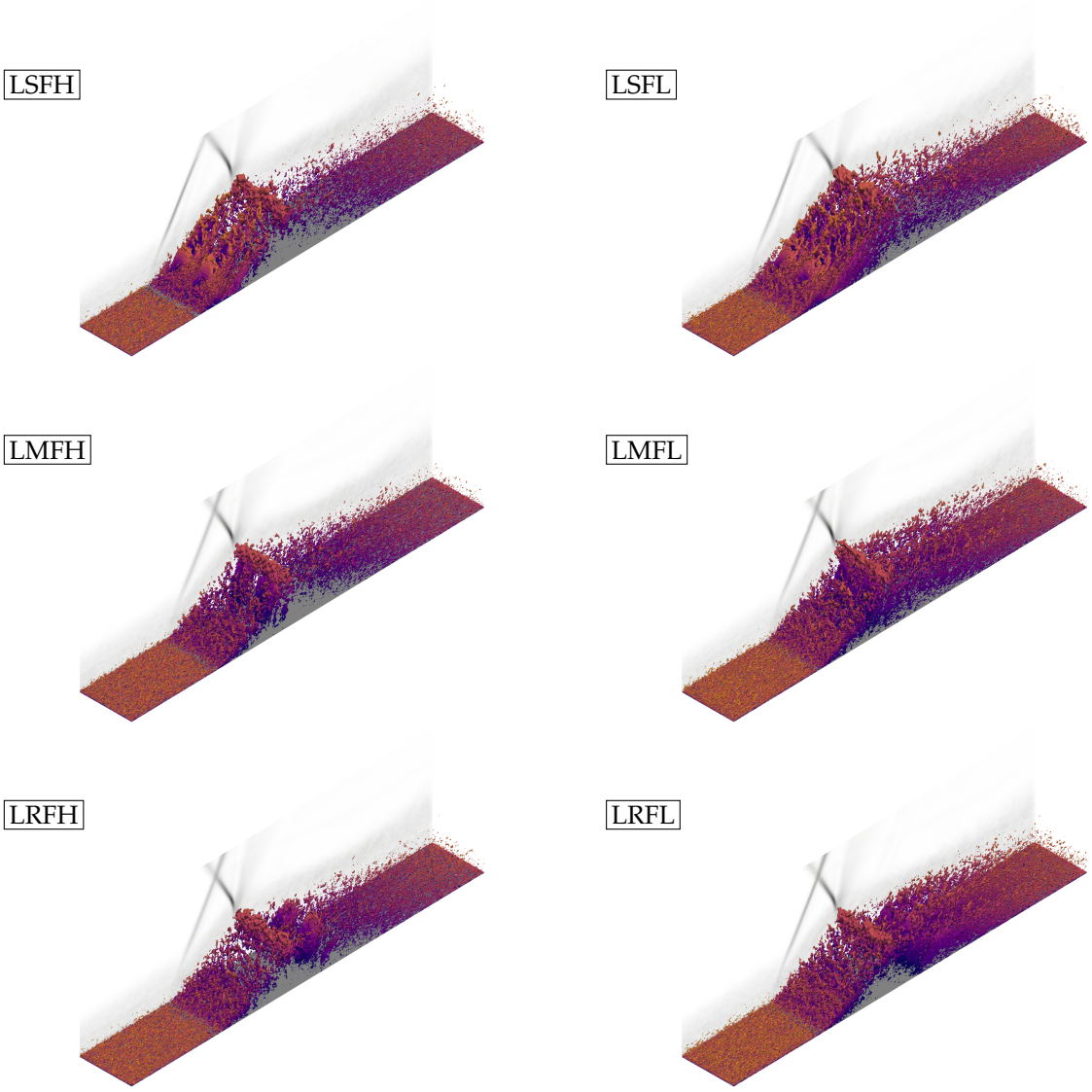


Figure 4.12: Peak-phase-averaged vortical structures visualized with the λ_{ci} criterion and colored by the local streamwise velocity. An isovalue of $\lambda_{ci}/u_\infty = 0.0583$ is used. A phase-averaged numerical Schlieren is shown in the background.

The iso-contours of the streamwise vorticity component (ω_x) at peak injection, shown in Figure 4.13, clearly show the difference in length of the vortices created by the actuators at separation. While the vortices of LSFH only reach several until around the peak of the bubble, the vortices of LSFL are twice as long and almost reach the point of reattachment, which can be recognized by the reappearance of larger iso-surfaces at the wall.

The results in Figure 4.13 also show how the location of the actuator influences the vertical iso-surfaces created by the actuators, which are at the origin of the large scale vortical structures. At separation these are angled sharply downstream, as they are positioned virtually in the freestream flow. In the middle of the bubble they are largely unaffected by the streamwise velocity as they appear nearly vertical. Finally at reattachment they are oriented in the downstream direction yet not as severely as those placed at separation. This is because of the difference in steamwise velocity between the three locations. This means that only the actuators placed at separation really create longer streamwise vortical structures

which penetrate the bubble.

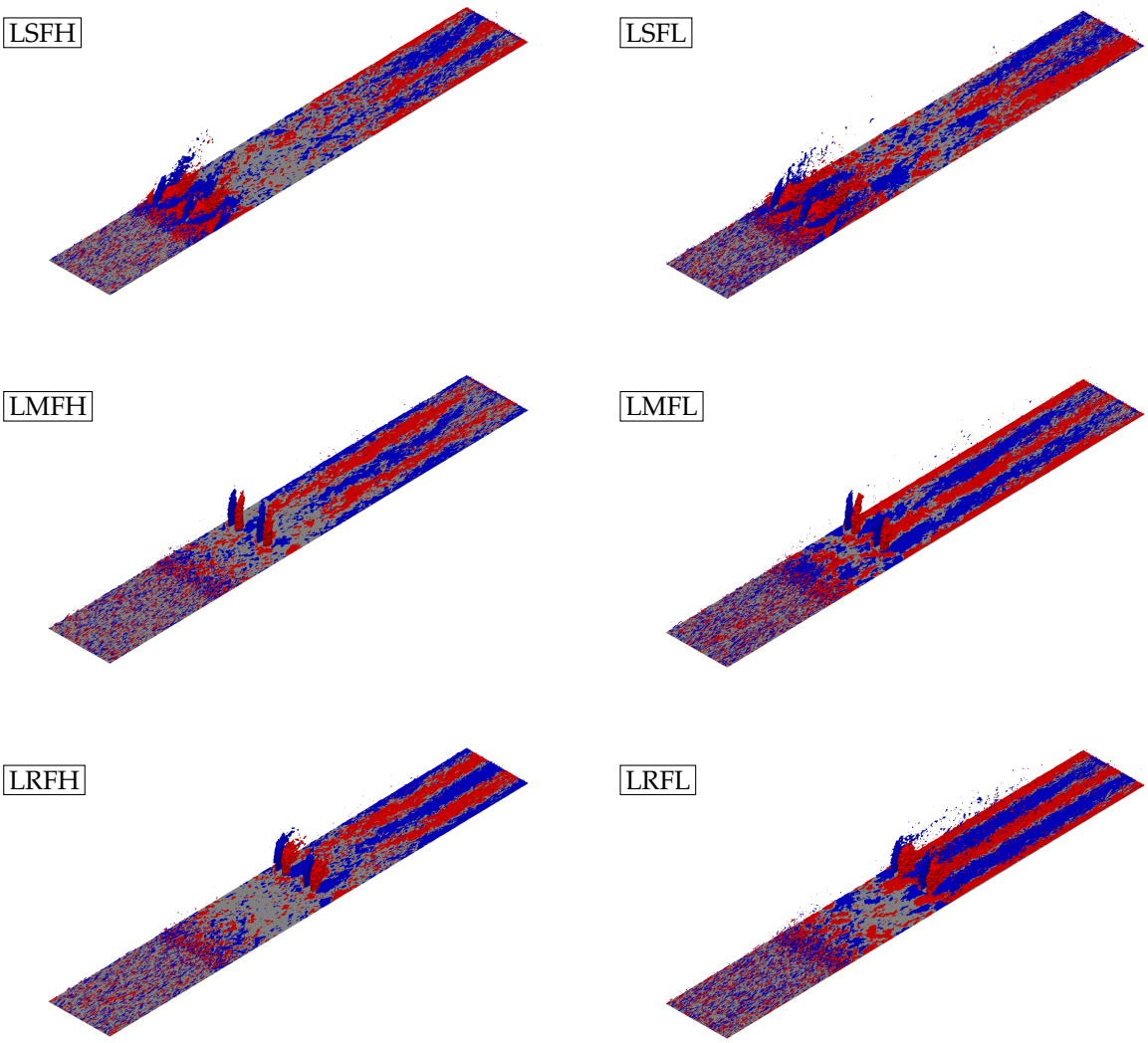


Figure 4.13: Peak-phase-averaged vorticity visualized by an isocontour ω_x, where red is ω_x = 0.2 and blue is ω_x = -0.2.

While instantaneous results such as the v velocity slices and the bubble shape at peak injection, as shown in Figure 4.6, hinted at a difference in behavior with respect to actuation time, this is clearly observed in the phase-averaged bubble shape shown in Figure 4.14. The actuation time for the low-frequency cases makes a significant difference in the length of the vortices which are present. For case LSFH, in between the actuators the bubble is split, but the penetration into the bubble, which reduces the overall bubble size, is limited and a full but shortened bubble is still visible. In contrast to case LSFL which shows that the vortices almost stretch the full length of the separation bubble. Cases LMFL, LRFH and LRFL also show the splitting of the bubble in between the actuators.

All control cases show a region of separation on the wall directly behind the actuators, which is caused by the slow moving air directly behind the active actuators. Additionally there is a plume emanating from the actuators that is not connected to the separated region at the wall, which was also observed in Figure 4.5. This plume is the reason for the bubble shape in Figure 4.11 for cases LMFH and LMFL.

The shape of the bubble in Figure 4.14 seems to be closely related to the presence of ω_x at the wall in Figure 4.13. If the isosurfaces are present at the wall, meaning that rotational flow has come close to the

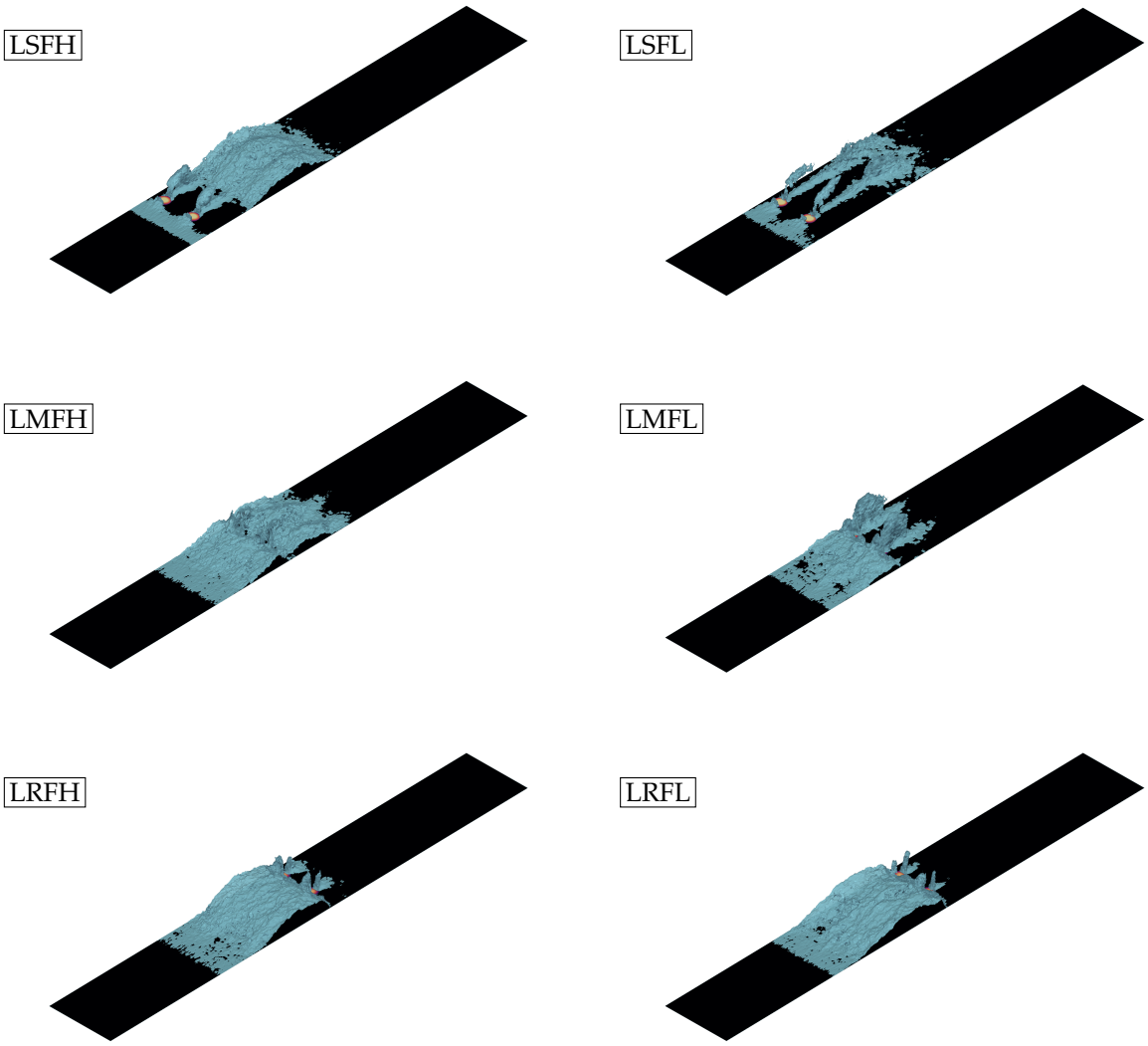


Figure 4.14: Peak-phase-averaged bubble shape visualized with the iso-contour of $u = 0$.

wall, and thus there is no reverse flow present. This can be observed best for cases LSFH and LMFL, where the isosurfaces of ω_x are present shortly downstream of the actuators and then disappear until reattachment, which coincides with the presence of the bubble at these locations.

4.2.6.2 Injection-phase-averaged

To get a grasp of how the bubble responds to the different phases of injection, the λ_{ci} criterion is shown for case LSFH in Figure 4.15. At the start of the injection phase, the actuators have not yet created any large scale vortical structures. At $\theta_p = 0.25$ the influence of the actuators is already visible, although the amount of vortical structures is still small, they are starting to move up along the shear layer and there is already an increase in large scale structures at the point of interaction between the shear layer and the impinging shock. At $\theta_p = 0.5$, the vortical structures created by the actuators have reached the peak of the bubble, potentially increasing the interaction between the impinging shock and the shear layer. During this phase the amount of vortices created by the actuators is largest, additionally the separation shock, visualized by the numerical Schlieren, is appears to be the strongest compared to the other phases. At $\theta_p = 0.75$ the strong vortices created during $\theta_p = 0.5$ have reached and gone past the bubble apex, increasing the vortices in the aft side of the bubble. The creation of new vortices by

the actuator has decreased and seems about the same level as for $\theta_p = 0.25$. The other cases, shown in Figures C.19 to C.23, show a similar pattern: the actuators cause a significant increase in vortices, which are carried downstream by the shear layer, as soon as they interact with it.

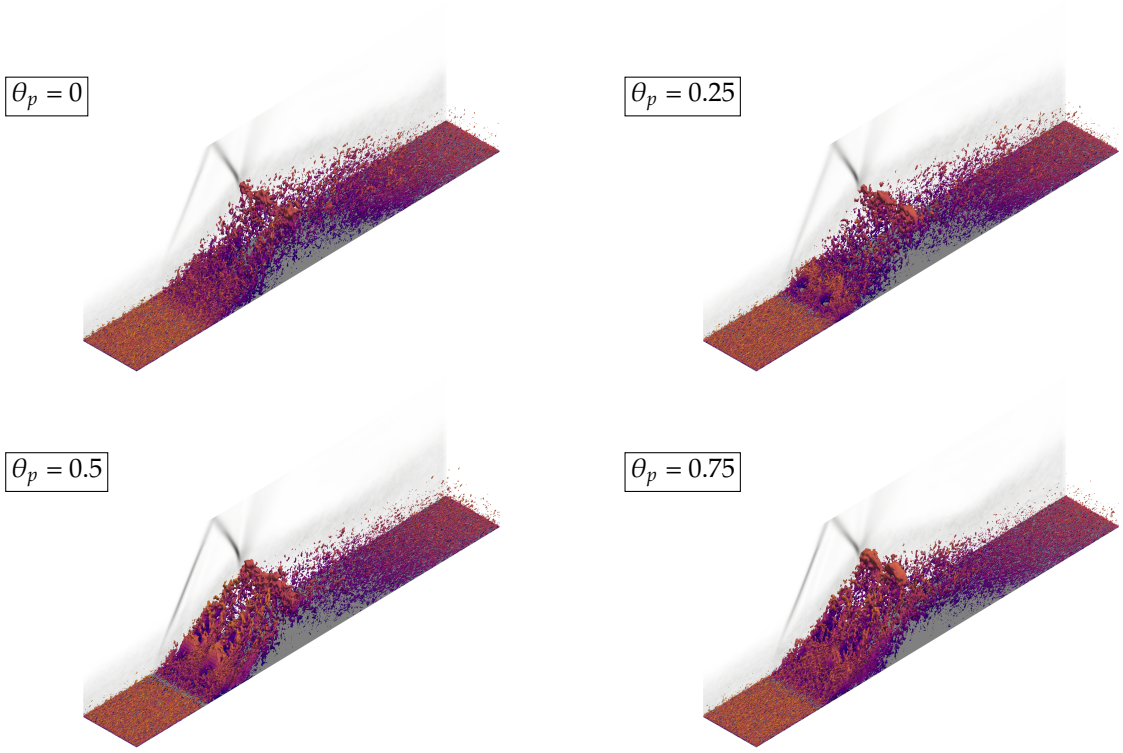


Figure 4.15: Injection-phase-averaged vortical structures visualized with the λ_{ci} criterion and colored by the local streamwise velocity case LSFH. An isovalue of $\lambda_{ci}/u_\infty = 0.0583$ is used. A phase-averaged numerical Schlieren is shown in the background.

Additional evidence of the working principle of the actuators is provided by Figure 4.16, which shows that as the actuators are activated, vortices are created around the edges of the actuators.

Figure 4.17 provides additional evidence for the claim that the longer actuation time of the low-frequency case at separation creates longer streamwise vortices compared the high-frequency case. The iso-surfaces of ω_x in Figure 4.17 stretch much further into the bubble at $\theta_p = 0.5$ in Figure 4.17 than in Figure 4.16.

The orientation of ω_x in wake of the bubble is flipped between as the odd actuators are becoming active after the even actuators have been shut off. This is faintly visible in the flip in red to blue at the boundaries and in the middle, between $\theta_p = 0$ and $\theta_p = 0.75$ in Figure 4.16. This is easier to observe for the other cases in the middle of the bubble and at reattachment, as shown in Figures C.24 to C.27.

The difference in actuation time and therefore the difference in time between the injections is clearly illustrated in the differences between Figures C.28 and C.29, where case LSFL shows a bubble that has almost returned to the Reference case position, while the bubble for case LSFH is still split. This causes the bubble in between the actuators to move back and forth.

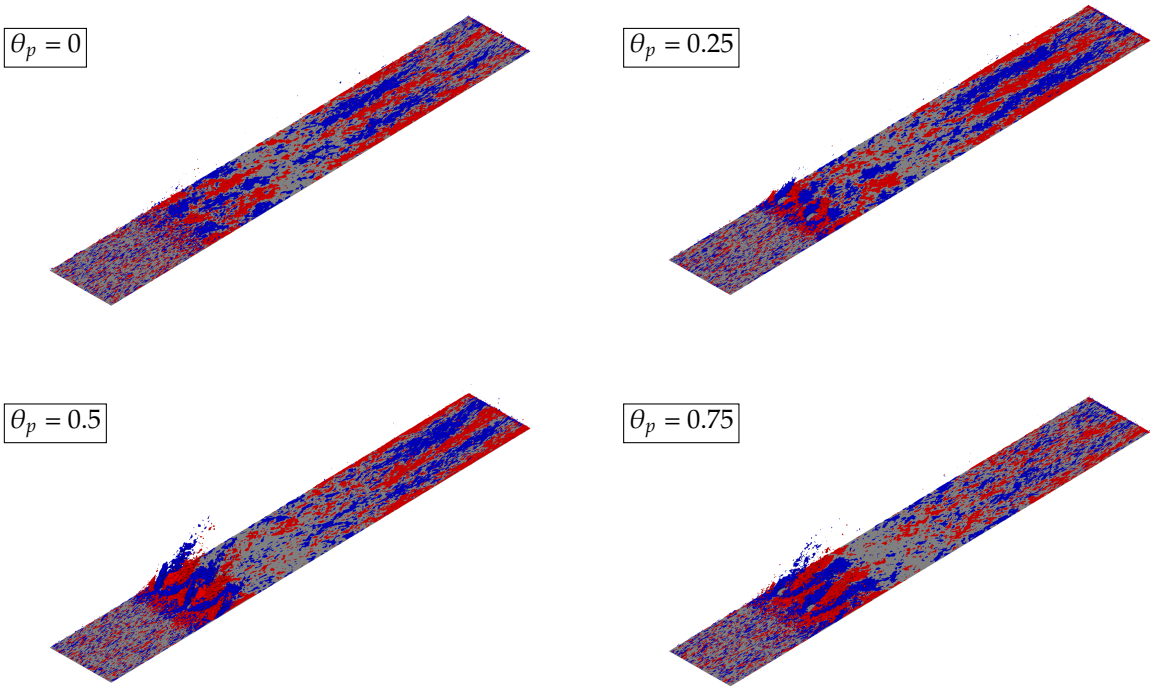


Figure 4.16: Injection-phase-averaged iso-contours of ω_x for case LSFH, where red is ω_x = 0.2 and blue is ω_x = -0.2.

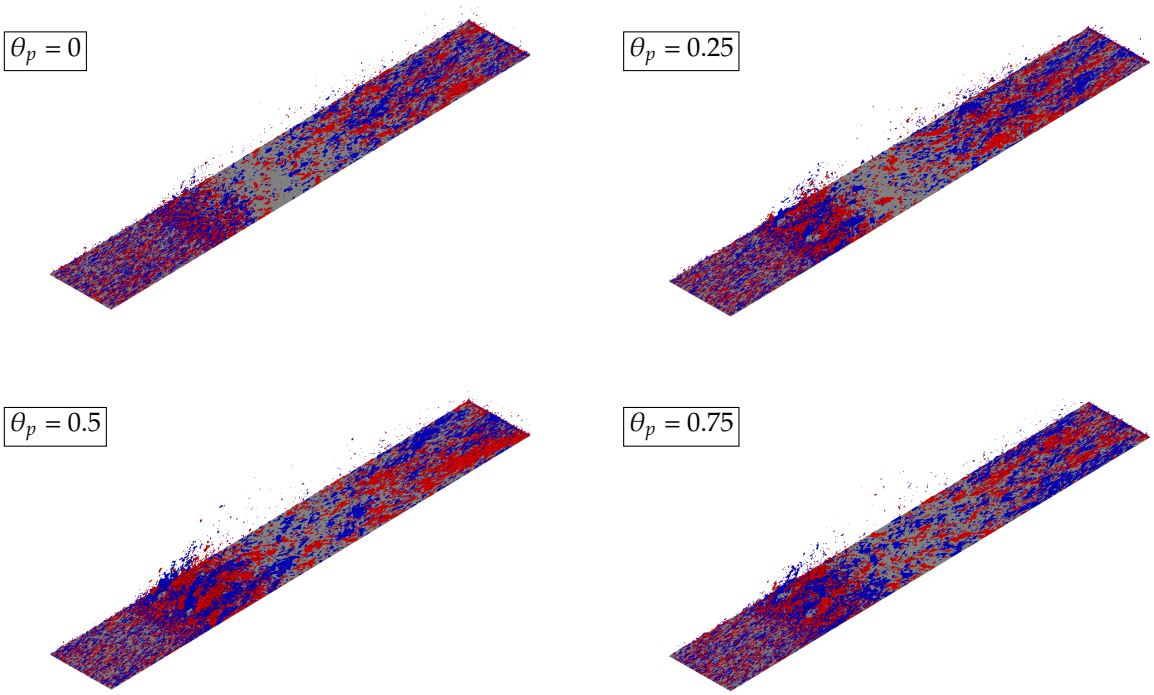


Figure 4.17: Injection-phase-averaged iso-contours of streamwise vorticity case LSFL, where red is ω_x = 0.4 and blue is ω_x = -0.4.

4.2.7. Reynolds stresses

The phase-averaged results in subsection 4.2.6 have shown that the actuators effect the flow in different ways during the injection. It also showed that there is a significant creation of vortical structures when the actuators are active. However the exact mechanism for the creation of these is not clear yet. As these vortical structures create velocity fluctuations in the system, the Reynolds stresses could provide additional insight.

The influence of the actuators on the creation of turbulence in the shear layer is apparent from the comparison of the streamwise Reynolds stress ($u'u'$), shown in Figure 4.18, which shows a clear difference between the actuator placed in the separating region and the Reference case. With an increase in stresses just before the actuator and in the separating region, even though the stresses directly above the actuator are slightly lower than the region surrounding the actuator. Similarly in the other control cases the actuator actually reduces the $u'u'$ stresses directly above the actuator, which can be observed in Figure 4.18d-e by the small indent just above the actuator and in Figure 4.18f-g where the wake is split in two by a region of low stresses. An explanation for this is that the injection velocity has just the wall normal velocity component, v, which introduces large wall-normal velocity fluctuations (v'), however no fluctuations in the streamwise or spanwise direction are generated, therefore reducing the fluctuations in the region directly above. However as the injected flow interacts with the incoming flow, an increase in fluctuations is expected. So directly above there should be a decrease and surrounding the actuator the should be an increase in fluctuations. And this also seems to be the case for spanwise Reynolds stress ($w'w'$), as shown in Figure C.39.

The control cases also show a slight increase in stresses in the separation shock, where the low-frequency cases show a wider and stronger region of stress. This could indicate that the movement of the separation shock has increased for the control cases and this excursion range is larger for the low-frequency cases. A similar observation to the one made in Figure 4.10.

Similar to the $u'u'$ stress, the impact of the actuators on the wall-normal Reynolds stress ($v'v'$) stress is mostly local. Contrary to what is shown in Figure 4.18, the $v'v'$ stress, as shown in Figure 4.19, the actuator causes a large local increase. This is a logical result as the actuator sets the v which will influence the stresses in the same direction. Also similar to Figures 4.18 and 4.19 shows an increase in stress in the separation shock and the low-frequency cases show a larger increase. The low-frequency cases also show a slightly larger region of influence for cases at separation and reattachment, as the wake shows a larger region of increased stress. Even though the stress in the separation shock increase, there seems to be little to no difference in the stresses upstream of the actuator.

As expected $v'v'$, as shown in Figure 4.19, increase significantly directly above and in the wake of the actuator. This figure also indicates the slow stream-wise velocity within the separation bubble which is observed by comparing the plume shape of the injector from Figure 4.19d-e, which shows the plume moving straight upwards, whereas the other control cases show the plume at a much larger downstream angle, something that can also be observed in Figure C.41. The slightly increased intensity of $v'v'$ where the impinging shock interacts with the shear layer is observable in Figure 4.19b-c but perhaps better observable in Figure C.41b-c. This can also be observed in Figure 4.18 and Figure C.34. It can be observed for the other control cases but is most pronounced for cases LSFH and LSFL.

For all cases $v'v'$ produced by the separation shock is observable, however there are clear differences between control cases and the Reference case. Cases LSFH and LSFL show the largest range of motion for the separation shock, indicated by the larger area of the separation shock and the area of increased intensity between the separation shock and the shear layer, which is higher for these two particular cases than for any of the other control cases. This is perhaps clearer in Figure C.41. Additionally there is a clear distinction between low- and high-frequency cases, where the low-frequency cases show a higher turbulence intensity in the separation shock. Additionally the region of increased intensity is also larger, suggesting a larger range of motion of the separation shock.

The increases in $v'v'$ in the separation shock, where the increase is larger for the low-frequency cases compared to the high-frequency cases, is also observed in Reynolds shear stress ($u'v'$), shown in Figure 4.20. The shear stress created in the separation shock, by the cases at separation, is significantly higher than for the other control cases. Additionally the actuators placed at separation create a large amount of stress in the upstream side of the bubble while the other cases only show an increase at

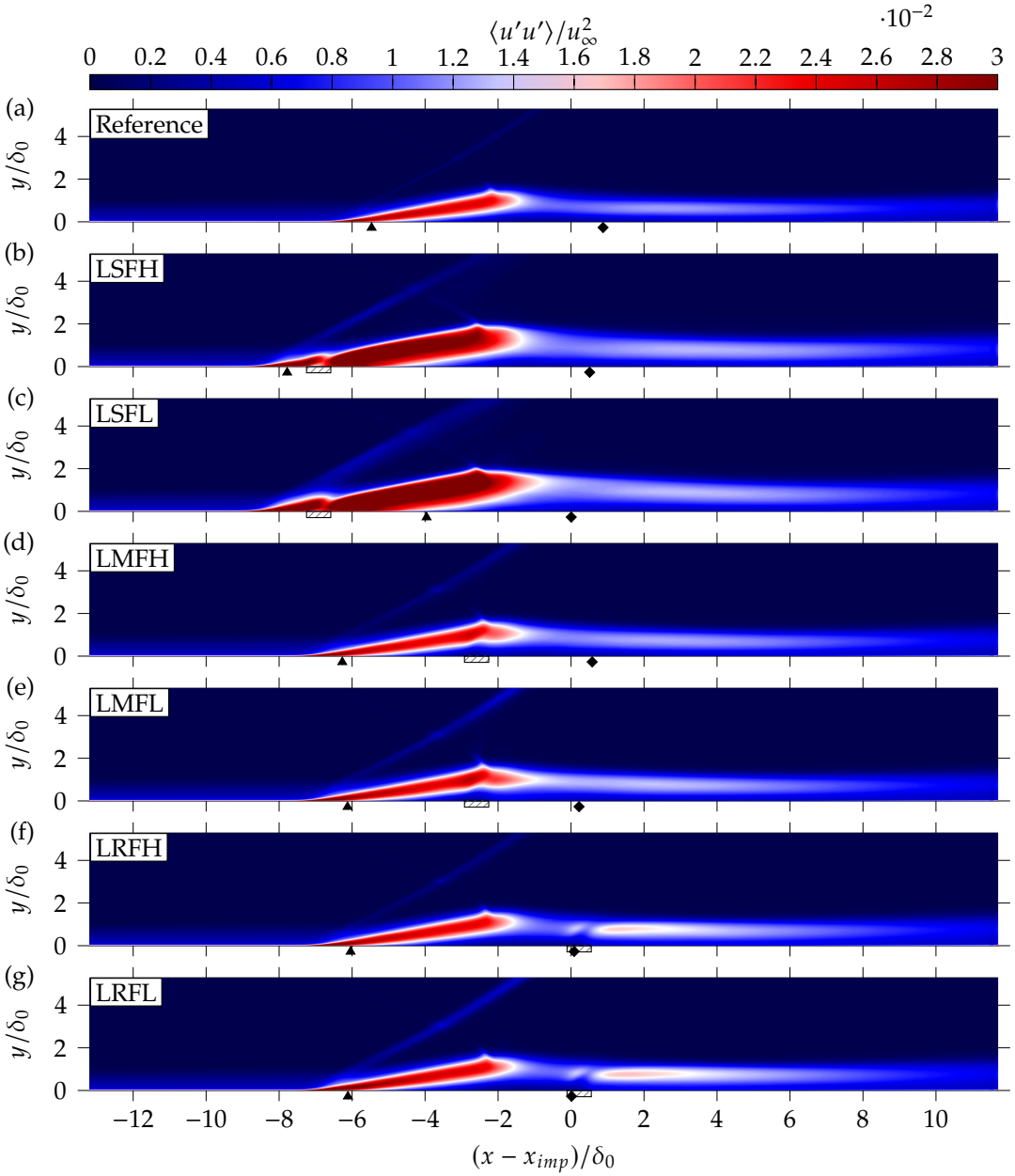


Figure 4.18: Time- and spanwise-averaged streamwise Reynolds stress $u'u'$ comparison for: (a) Reference case, (b) case LSFH, (c) case LSFL, (d) case LMFH, (e) case LMFL, (f) case LRFH, and (g) case LRFL. The statistical separation and reattachment points are indicated by ▲ and ◆ respectively. The AL is indicated by ▨.

the separation shock foot and in the shock itself. A difference between the cases at separation and the other control cases is that the shear stress in the separation shock is highest before it interacts with the impinging shock, while for the cases at reattachment the intensity is the same and the cases in the middle show an increase in intensity.

The shear stress intensity in the wake of the bubble is similar in all cases, except for the cases where the actuators are placed at reattachment where there is a large increase, however way downstream of reattachment the intensity seems to be similar. One additional difference in the shear stress in the wake of the bubble is the thickness of the region, which appears much thicker for cases LSFH and LSFL.

Although it is harder to distinguish, there is an increase in shear stress, at the interaction location between the impinging shock and the shear layer, for the control cases. It is best seen in Figure 4.20b-c but can also be observed for cases LMFL and LRFL.

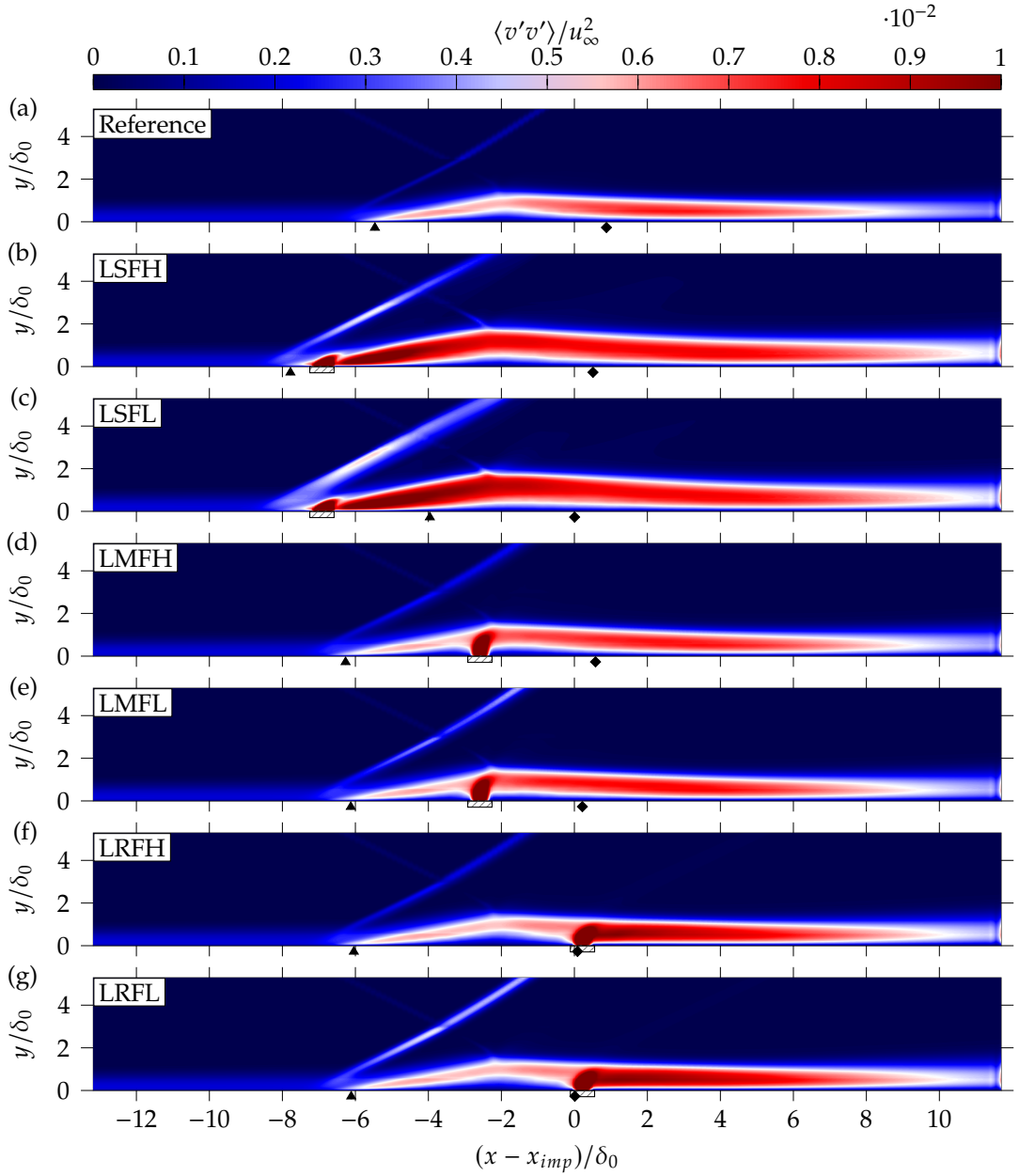


Figure 4.19: Time- and spanwise-averaged wall-normal Reynolds stress $v'v'$ comparison for: (a) Reference case, (b) case LSFH, (c) case LSFL, (d) case LMFH, (e) case LMFL, (f) case LRFH, and (g) case LRFL. The statistical separation and reattachment points are indicated by ▲ and ◆ respectively. The AL is indicated by ▨.

The different placements of the actuators also show how the injection interacts with the shear layer, as the actuators at separation create shear stress at the wall, while for the actuators at reattachment there is a small gap just above the actuators before shear stress creation starts. For the actuators in the middle this gap is even larger. Another interesting result is the splitting of the shear stress layer for cases LMFH and LMFL, just upstream of the creation of shear stress directly above the actuators, shown in Figure 4.20d-e, there is a small region where there is little to no shear stress. This is also observed at the wall in Figure 4.20b-c. This could be evidence of the blockage caused by the actuators, which was observed in the bubble shape in Figure 4.11.

The RMS of $u'u'$, $v'v'$ and $w'w'$ are given in Figures C.40 to C.42.

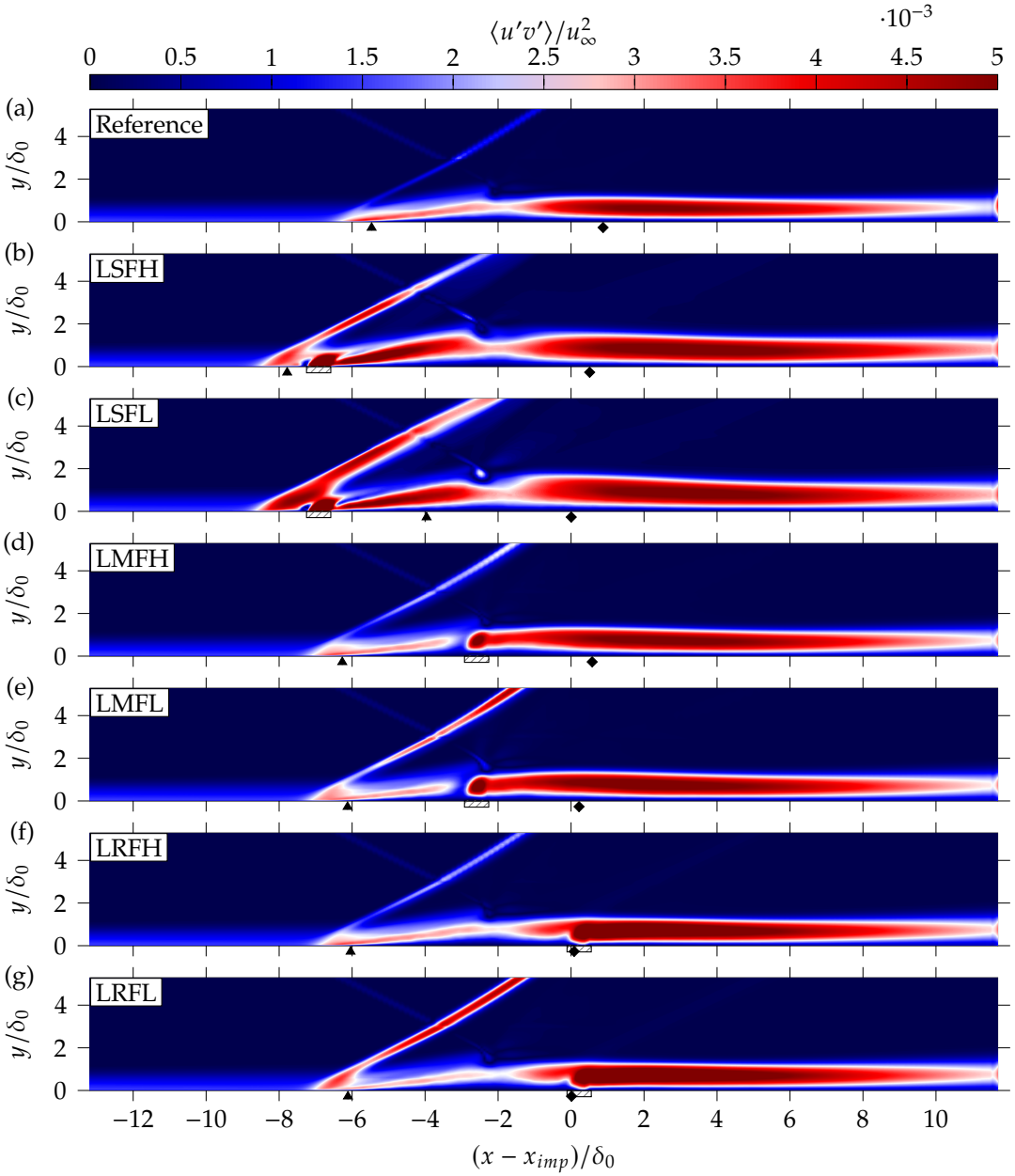


Figure 4.20: Time- and spanwise-averaged Reynolds shear stress $u'v'$ comparison. for: (a) Reference case, (b) case LSFH, (c) case LSFL, (d) case LMFH, (e) case LMFL, (f) case LRFH, and (g) case LRFL.The statistical separation and reattachment points are indicated by ▲ and ◆ respectively. The AL is indicated by ▨.

4.2.8. Pressure variance

The use of actuators significantly effects the low-frequency behavior of the system. The larger intensity of velocity fluctuations observed around the separation shock in Figure 4.19 can also be observed the pressure variance as shown in Figure 4.21 which gives results for substitution of p for u in Equation A.11.

The actuator location has large implications on the low-frequency response of the whole system. Case LSFH and LSFL show an increase in the pressure variance around the separation shock, indicating an increase in low-frequency shock oscillation. Not only is there an increase in the strength of the pressure variance, there is also a much larger area where the pressure variance has increased indicating a larger excursion range of the separation shock, additional evidence for this is provided in Sections 4.3.2 and 4.3.3. This region even extends beyond the separation shock-impinging shock interaction which is also an indication of a larger excursion range of the separation shock.

Whereas the increased unsteadiness of the separation shock is expected for cases LSFH and LSFL, as the actuators interfere with the separation shock, it is also observed for the cases where the actuators are placed in the middle or near the reattachment point of the separation bubble. This is the an important indication that the actuators do influence the motion of the separation shock, even if they are not located close.

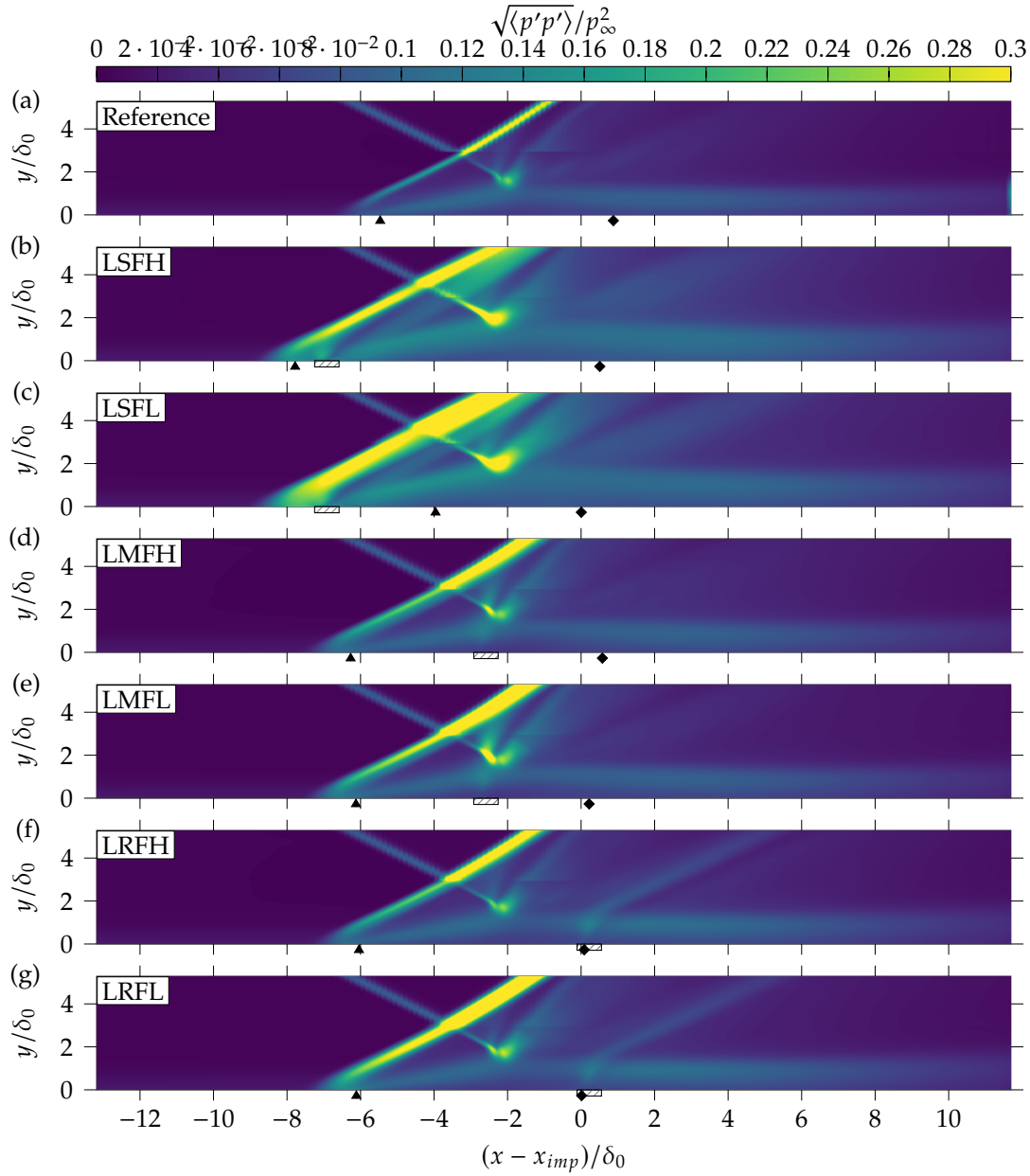


Figure 4.21: Time- and spanwise-averaged $p'p'$ comparison for: (a) Reference case, (b) case LSFH, (c) case LSFL, (d) case LMFH, (e) case LMFL, (f) case LRFH, and (g) case LRFL. The statistical separation and reattachment points are indicated by ▲ and ◆ respectively. The AL is indicated by ▨.

Once again, similarly to the results for $u'u'$, the results for $p'p'$ show a region of low intensity emanating from the actuator. Except for cases LRFH and LRFL, where the actuator seems to form a weak shock. The results of $p'p'$ provide additional evidence that there is a link between actuator frequency and the low-frequency motion of the shocks, the shock-shock interaction and the shock-shear layer interaction.

Similar to results observed in Figure 4.10, the pressure variance clearly indicates the expansion fan caused by the reflection of the impinging shock of the shear layer. This could indicate that there is more

turbulence in the shear layer, that there is more motion in the shear layer, causing a larger range of motion of the expansion fan, or it can be caused by the flapping motion of the incident-transmitted shock. The last option is most likely as the cases where a larger range of motion of the separation shock is observed, creating a larger range of motion of the incident-transmitted shock, increasing the pressure fluctuations at the bubble apex, thus resulting in more pressure variance in the expansion fan. This is supported by the observable increase in pressure fluctuations of the incident-transmitted shock near the bubble apex. This location also coincides with the creation of the vortical structures shown in Figure 4.12.

While the wall pressure data from the probes shown in Figure 4.8 already indicated an increase in p'_w, Figure 4.21 shows that this does not only occur at the wall, but throughout the entire separation shock, even after the interaction with the impinging shock. The separation-transmitted shock of control cases shows a significant increase in pressure variance compared to the Reference case, which is another indicator of the larger excursion range of the separation shock. Where the results for $u'u'$, $v'v'$ and $w'w'$ did not indicate a significant difference between the intensity of the fluctuations of the separation shock before and after interacting with the impinging shock, the results of pressure variance clearly show a significant increase in intensity after the interaction, suggesting an amplification of the variance due to the interaction. This is in contrast to the results for $u'v'$ which showed a dependency of the actuator location on the intensity before or after the interaction.

4.3. Results II: Jet actuation effects on SWBLI unsteadiness

While the vortical structures observed in subsection 4.2.1 provide an explanation for the reduction in bubble volume for cases LSFH and LSFL, they do not provide an explanation for the observed increase in both velocity and pressure fluctuations. This increase in fluctuations indicate a potential alteration of the SWBLI unsteadiness which will be the focus of this section.

4.3.1. PSD maps

While the results of the time- and spanwise-averaged $p'p'$, shown in Figure 4.21, indicate there could be a change in the spectral behavior of the bubble, time-averaging does not show the motion. Therefore the probe data is used to create the PSD maps of p'_w which can provide a broader insight over the most energetic frequencies experienced at the wall during the simulation. Beware that the PSD maps in Figure 4.22 are given in a logarithmic scale.

For cases LSFH and LSFL a vertical band of low power just after separation, which is best visible at $St_L = 0.2$, is caused by the actuator. This vertical band seems to be there for the other control cases but is more difficult to discern. The reduction in energy of the pressure fluctuations above the actuator is in line with the observations made in subsection 4.2.4, that the air above the actuator gets a significant reduction in fluctuations, except in the wall-normal direction, due to them not being present in the actuator. This effect was also observed by Pasquariello et al. [8], although it is more pronounced in their study as they used an actual hole at this location which would greatly reduce the energy towards the wall.

Even though Pasquariello et al. [8] used passive suction within the bubble and blowing upstream of the bubble, the varying of the control location does show similarities on the PSD maps for p'_w. For both studies, there is a shift in the dominant frequency for Pasquariello et al. this was an increase frequency and for this study the shift depended on the actuator frequency. As Pasquariello et al. used a passive method there is not difference in frequency of the blowing, there is a difference in the acoustic feedback frequency, which becomes lower as the suction location is moved further downstream, which results in a similarly lowering dominant frequency. Secondly for both studies, when control is applied in the reattachment region, there is a significant reduction in the energy at separation when compared to the other control cases.

What the PSD maps clearly show is that the injection at the high-frequency causes a clear dominant frequency in the separating region, and throughout the bubble. For case LSFH, as shown in Figure 4.22b, the harmonics of the actuator frequency, which were also observed in the PSDs of certain metrics, can even be observed. As indicated by the PSDs these harmonics are less energetic and thus dissipate more quickly than the actuator frequency. The second harmonic is still visible after the separation bubble, but

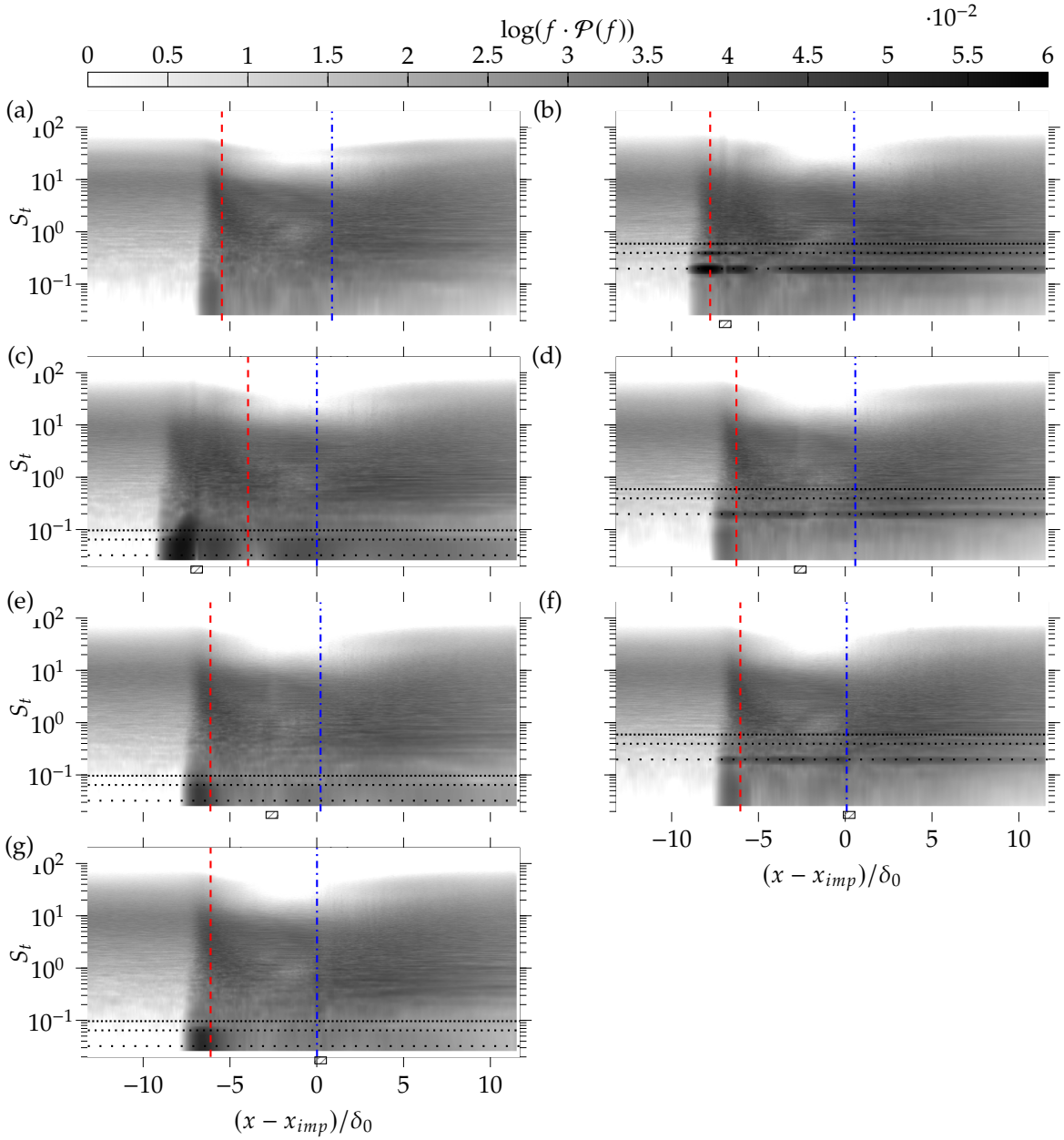


Figure 4.22: Log scaled PSD map of p'_w at the center line for: (a) Reference case, (b) case LSFH, (c) case LSFL, (d) case LMFH, (e) case LMFL, (f) case LRFH, and (g) case LRFL. The vertical red dashed line indicates the statistical separation point, the vertical blue dashed-dotted line indicates the statistical reattachment point. The horizontal dashed lines indicate the first, second and third harmonics of the AF. The AL is indicated by ▨.

the third seems to have dissipated. These harmonics are also faintly visible for case LMFH, shown in Figure 4.22d. Interestingly these results were also observed by Laguarda et al. [73] even though they did not use actuators, rather they used a flexible panel. Despite their setup matching the one used in this study very closely, the dominant frequencies they found were lower as they were linked to the bending frequency of the panel. Another difference is the maximum energy, which is much higher for the results in this study, which is why the results are given on a logarithmic scale.

The clearly dominant frequency throughout the domain which is present for the high-frequency cases is not present for the low-frequency cases and neither are the harmonics. As seen in Figure 4.8b, the low-frequency cases show an increase in energy just before reattachment, which is best observed in Figure 4.22c but also clearly visible in Figure 4.22e.

The dominant frequencies in the PSD maps, give an indication that pressure disturbances created by the actuators might be the driving control mechanism. As these are present throughout the domain, up to the separation shock. And the fact that the disturbances are clearly at the actuator frequency indicates that pressure is of significant influence.

4.3.2. Bubble motions compared

The energetic frequencies in the PSD maps require further investigation to examine these dominant pressure fluctuation frequencies, which seem to propagate throughout the domain, also influence the large scale bubble behavior. The results obtained from the snapshots plotted as time series are shown in Figure 4.23. However showing these results in a single figure might be unclear due to the number of cases and data points shown for each data set. So for clarity the results are also given separately in section C.6.

The time series data shows the equilibrium state is not reached immediately after the actuators are first activated. It takes a time interval of 300 to 600 u_∞/δ_0 before the system settles into large scale periodic motion. This is best observed in the movement of S_x as shown in Figure 4.23g, where all control cases start at the same location as the Reference case and then drop.

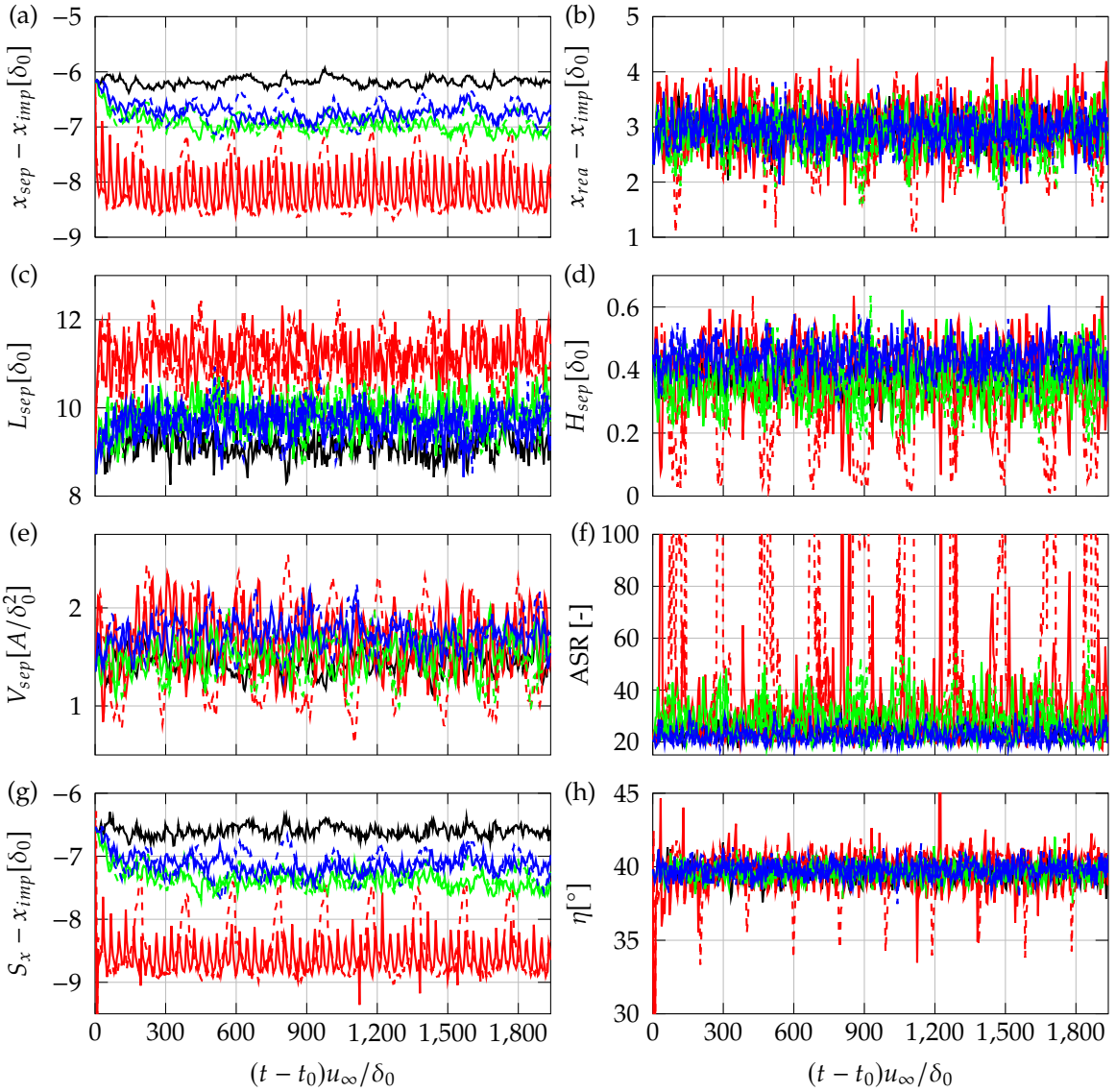


Figure 4.23: Bubble motion cases compared of: (a) x_{sep}, (b) x_{rea}, (c) L_{sep}, (d) H_{sep}, (e) V_{sep}, (f) ASR, (g) S_x and (h) η. For line legend see Table 4.1.

Narayanaswamy et al. [33] found that the motion of the separation shock was characterized by an initial rapid upstream movement and a slower recovery motion when the actuators were turned off. This motion of the separation shock has also been observed in this study, however this motion is not just observed for the separation shock, it is also observed in other metrics such as x_{sep}, V_{sep} and η. Additionally there is a significant difference in the movement speed between the low- and high-frequency cases. The low-frequency cases show a much slower movement of the bubble.

The combination of S_x and η provides insight into the movement of the separation shock. Which is pushed forward along the wall during the initial phase of the actuators being active. This causes the separation shock to have a smaller angle compared to the wall, which will recover slowly. During the downstream movement of the separation shock the angle of the separation shock remains quite constant. This motion is best observed in Figure C.72.

As alluded to in subsection 4.2.8, the results show a large increase in the range of motion for the separation shock when the actuators were placed at separation. This increase is much smaller when the actuators were placed in the middle or at reattachment. The upstream movement of the separation shock ranged from 0.2 to 0.6 δ_0 for Narayanaswamy et al. [33], one δ_0 for Webb et al. [67]. The movement was also observed by Greene et al. [38] when the actuators were placed upstream of separation shock. Both Narayanaswamy et al. and Greene et al. observed the movement of the separation shock when the actuators were placed inside the separation bubble, although this movement was much smaller than when placed upstream. Additionally both studies noted that the range of motion decreased for higher frequencies, which is in agreement with the results shown. This is because the bubble does not get as much time to relax between pulses for the high-frequency cases, which limits the range of motion.

4.3.3. PDFs of bubble motion

While the data given in Table 4.3 provides insight into the averages, it does not provide insight into the variability of the metrics. As the data in Figure 4.23 indicates, some metrics have a larger range of motion for similar average values, which is why the PDFs of the metrics are investigated.

Similar to the time-averaged results, x_{sep} is greatly influenced by the actuators. Not only does the mean value move upstream compared to the Reference case, the range of motion also varies significantly. All control cases, especially cases LSFH and LSFL, show a larger range of motion, although the range of motion of cases LMFH, LMFL and LRFH is not much higher than the Reference case. While the range of motion of cases LMFH and LMFL is comparable, the range of motion of case LRFL is significantly larger than of case LRFH.

The larger range of motion for the low-frequency case compared to the high-frequency case also holds for L_{sep}, V_{sep} and S_x. Except for the cases in the middle of the bubble, where the range of motion is quite constant across the low and high-frequency cases for all metrics.

The PDF of x_{rea} show that the separation point is quite stable and is not influenced nearly as much as x_{sep}. One could expect that the range of motion would be larger for the cases where the actuators are placed near the reattachment location, but this is not the case. The range of motion of x_{rea} for cases LRFH and LRFL is actually most similar to the Reference case out of all control cases.

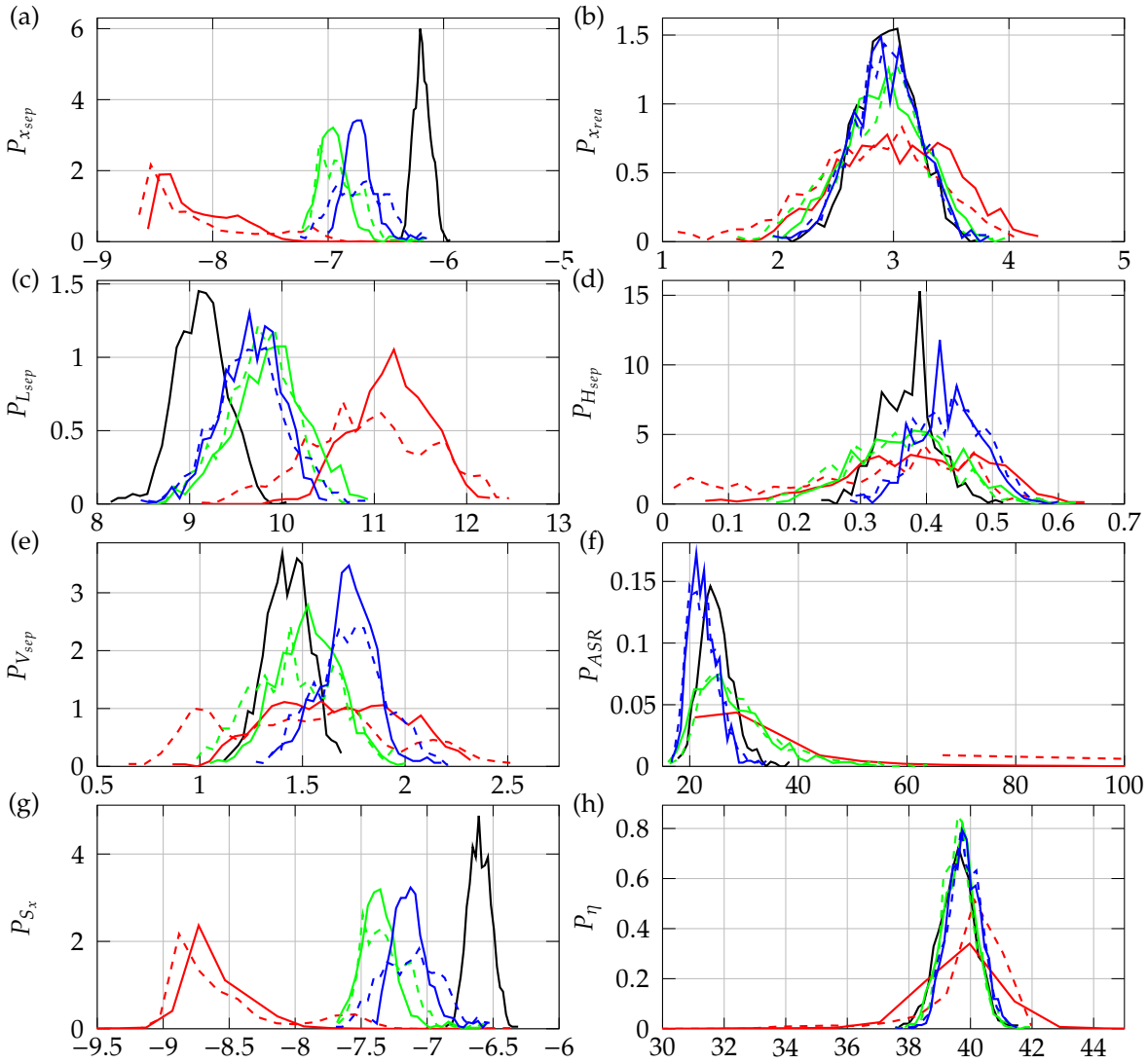


Figure 4.24: Bubble motion PDFs cases compared: (a) x_{sep}, (b) x_{rea}, (c) L_{sep}, (d) H_{sep}, (e) V_{sep}, (f) ASR, (g) S_x and (h) η. The horizontal labels correspond to the vertical labels of Figure 4.23. For line legend see Table 4.1.

4.3.4. PSDs of the bubble motion

The significant deviations and increased ranges of motion compared to the Reference case, shown in Figure 4.24, indicate that the actuators are able to change the behavior of the bubble with statistical significance. However it does not show if the actuators are able to modulate the movement of the bubble, as some of the results of Figure 4.23 suggest, to confirm this the PSD of the bubble characteristics are analyzed and shown in Figure 4.25. Beware that the results here are shown on a logarithmic scale, thus any peaks are potentially orders of magnitude higher.

Something that becomes immediately apparent from the results in Figure 4.25, is a close correlation between the most energetic frequencies and the actuator frequency. For both the high- and low-frequency cases it shows that the most energetic frequency is at the actuator frequency, which indicates that the actuators actually modulate the motion of the bubble with the same periodicity.

For cases LSFH and LSFL the PSD values are slightly to significantly higher than for the other cases. Especially the metrics which are focused around the separation, x_{sep}, S_x and η, show much more energy throughout the entire spectrum, except for the very low-frequency of x_{sep} and S_x for case LSFH.

The PSD results for the ASR for case LSFL as shown in Figure 4.25f are orders of magnitude larger than the other results. The definition of ASR, as given by Equation A.22, results in near infinite values

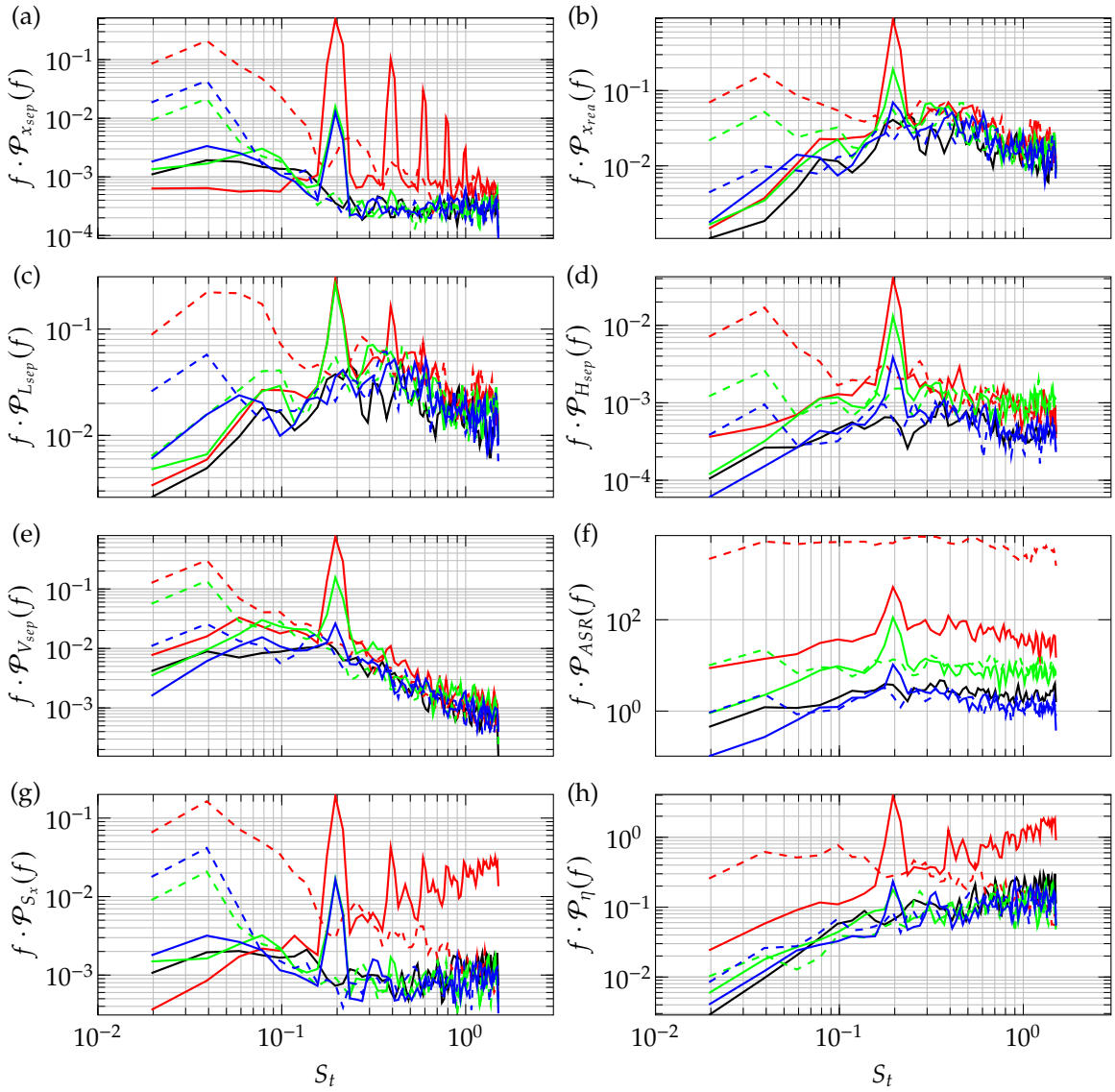


Figure 4.25: PSDs of the production cases motion compared of: (a) x_{sep}, (b) x_{rea}, (c) L_{sep}, (d) H_{sep}, (e) V_{sep}, (f) ASR, (g) S_x and (h) η. For line legend see Table 4.1.

when the H_{sep} approaches zero. The large fluctuations in ASR make the magnitude of the PSD is not representative of the systems behavior. These results are in line with the results shown for the PDF of this metric.

One emerging pattern from Figure 4.25 is the ordering of the peaks. For most metrics, the cases at separation are the highest peak at their respective actuator frequencies. Then if there is a clear order for example: LSFL, LMFL, LRFL at the low-frequency then the order at the high-frequency will be LSFH, LMFH, LRFH as can be seen in Figure 4.25b,d-f. For some metrics the peaks are too close.

The use of control makes the entire spectrum more energized, the black line representing the Reference is at or close to the lowest value throughout the domain for practically every result, especially in the low- to medium-frequency range.

A notable detail in the PSD for the V_{sep} is how the energy diminishes for the higher frequencies. For the other metrics the power stays at approximately the same level. An exception to this are peaks at harmonic frequencies of AF as observed x_{sep} andS_x, these can be orders of magnitude larger than the noise levels.

Unfortunately, neither Narayanaswamy et al. [33] nor Greene et al. [38], computed the PSD of S_x which could have provided more insight into the ability to modulate the separation shock movement. However Narayanaswamy et al. do come to the conclusion that the separation shock is locked to the pulsing frequency of the actuator, something that can also be concluded from the results such as Figure 4.25 and can be observed from results such as Figures 4.23 and 4.26. Locking of the separation shock, and to an extend the entire SWBLI flow, to the control method was also shown by Laguarda et al. [73], where the whole system would resonate with the first bending frequency of the flexible panel. The PSD of S_x in their study showed the most powerful peak at the first bending mode but it is not clear if second peak corresponds to the second mode.

For the high-frequency cases there are peaks at certain frequencies which are at harmonics of the actuator frequency, best visible for Cases LSFH in Figure 4.25a, c,g. A notable difference between the cases is that these harmonics are not visible for the low-frequency cases, however this might be due to the low-frequency resolution. These harmonics could be a result of the pulsing motion of the actuator. As the injection velocity of the actuators is not a purely sinusoidal waveform, some harmonics are expected, however if this was the only mechanism, they should show up for all cases. Additionally they were also observed in the PSD maps of subsection 4.3.1, indicating that the non-linear behavior of the separation bubble might be an amplifier of the harmonics created. Another reason why these are not visible is that the movement of the shock is much slower for the low-frequency cases, thus the secondary harmonics are not picked up due to the smaller rate of change.

The harmonics observed for x_{sep}, L_{sep} and S_x for case LSFH are not observed in the other metrics. The reason these are present for L_{sep} is a logical consequence of these being present in x_{sep}. The harmonics observed for S_x yet here they are less pronounced. In combination with the results observed for the PSD maps, which also showed harmonics for case LSFH, this suggest that there is some driving force. These harmonics usually just appear in flexible or closed systems, so that the pressure waves can be reflected, as was the case for Laguarda et al. [73] with a flexible panel, or any other systems where waves can reflect off the boundaries. The origin of the first harmonics are caused by the actuators. While the second harmonics could be a response to the actuators turning off if this is done quickly enough, this change or the effect this has on the separation shock could propagated through the bubble, which would explain why the p'_w can be observed throughout the domain.

4.3.5. Injection velocity response

So for all locations and at both the high- and low-frequencies, a peak in the PSD signals are observed at the actuator frequency, which would indicate that the actuator is able to modulate the spectral characteristics of the bubble. To further investigate this, the relation between the IV and x_{sep}, x_{rea} and S_x is examined.

The locations of x_{sep} and x_{rea} are dependent on the IV as is shown in Figure 4.26. x_{sep} is moved upstream immediately when the actuator is activated. While the injection velocity reaches it's peak amplitude, the separation points gets pushed further upstream until it reaches it's maximum point at maximum injection velocity, after which the point moves downstream. When the actuator turns off, the separation point moves back to the original location almost instantly.

However the relation between IV and x_{rea} is not as clear. The back and forth motion of the reattachment point is not as clearly related to the injection velocity, seemingly moving upstream during at peak injection, remaining there for a short period and then slowly returning to the original location. Still these signals could be closely related with the signals being out of phase, which will be examined using coherence results.

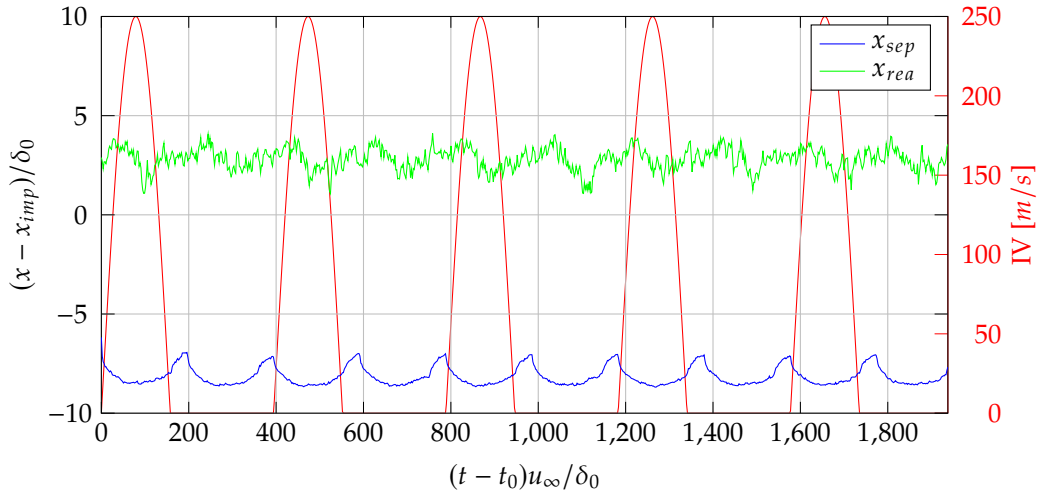


Figure 4.26: x_{sep}, x_{rea} and IV over the simulation time for case LSFL.

4.3.6. Coherence comparison

The coherence between IV and x_{sep}, x_{rea} and S_x is given in Figure 4.27. As was done for other results, results are separated by case in section C.6. Similar to the PSD results shown in Figure 4.25, the coherence results also do not have a high resolution in the low-frequency range due to the simulation time.

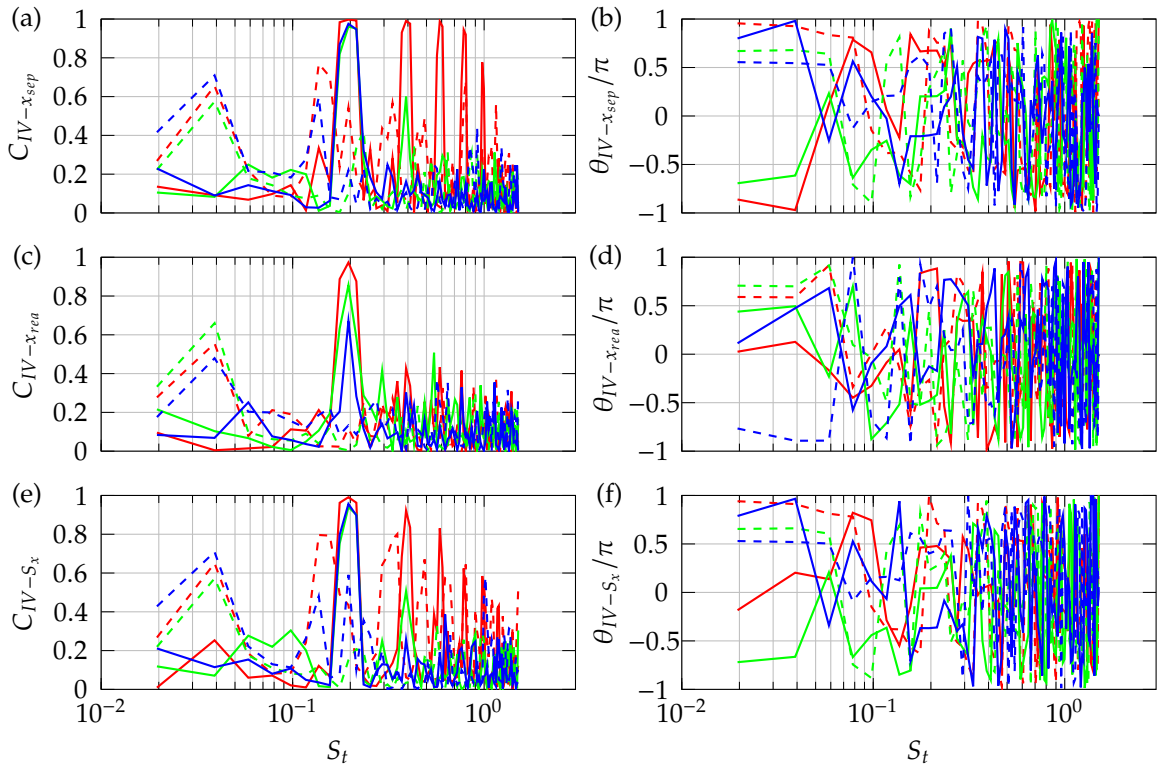


Figure 4.27: Coherence and phase between bubble motion and injection velocity for all control cases. (a) Coherence and (b) Phase, between IV and x_{sep}, (c) Coherence and (d) Phase, between IV and x_{rea}, (e) Coherence and (f) Phase, between IV and S_x.

There is strong coherence between the IV and x_{sep} at the actuator frequency for cases LSFH, LMFH, LRFH. For cases LSFL, LMFL and LRFL there is a peak of coherence at the actuator frequency which reaches around 0.6. For case LSFH the harmonics which were observed for the PSD of x_{sep} and S_x, are also represented by the coherence data. In contrast to the PSD results, the coherence between IV and

x_{rea} does show a second harmonic for case LRFH. Similarly there is a small peak of coherence between IV and x_{sep} for LMFH at the second harmonic frequency which reaches 0.6.

The harmonics found in the coherence between IV and x_{sep} are also present for the coherence between IV and S_x. However there is a difference, for case LSFH, the harmonics are present up to a much higher St_L. They can even be observed for case LSFL, which is not the case for any of the other low-frequency cases. This is likely due to the automatic recognition method of S_x, which can pick the shock created by the actuators rather than the separation shock.

Even though the phase results, Figure 4.27b, d,f seem to be incoherent, some patterns emerge upon closer inspection. There is a shift in the phase between IV and x_{sep} for the actuator frequency when AL changes. From leading almost a full phase for case LSFH to leading half a phase for case LMFH to almost being in phase for case LRFH. For the low-frequency cases, something similar happens, a decrease in leading phase between IV and x_{sep} at the actuator frequency, although the difference is much smaller, spanning less than half a phase difference between all three cases. Additionally the leading phase of IV is considered to be flipped because of the modulation of phase between $-\pi$ and π. A similar pattern is observed for the phase shift for the coherence of IV and S_x, the difference being a slight downwards shift for all cases. The phase shift is also observed for the coherence between IV and x_{rea} and between IV and S_x. The phase shift IV and x_{rea} is flipped from the results observed for the coherence between IV and x_{sep} as the actuators at reattachment is now leading. Half a phase lower is the actuator in the middle of the separation bubble and again half a phase lower it the actuator at separation. For the low-frequency cases, the order has also flipped and the phase difference between locations is close to the one observed for IV and x_{sep}.

While Figure 4.27 shows the coherence and phase between IV and three points: x_{sep}, x_{rea} and S_x while Figure 4.28 shows the coherence and phase between several points. These results are also given separately in section C.6. Similar to the results observed in Figure 4.27, the coherence results of Figure 4.28 show very strong coherence between all the selected metrics at the actuator frequency for the high-frequency cases. For the low-frequency cases the coherence is strong for most metrics for cases LSFL and LMFL, however for case LRFL, in several metrics, no discernible coherence is observed at the control frequency.

As there is no injection velocity for the Reference case, Figure 4.27 does not include the reference data, but Figure 4.28 does. This shows that unlike the control cases there is no frequency where the coherence between two metrics is high. Except for coherence between x_{sep} and S_x at low-frequency, which is to be expected as these are very closely related. This is yet another indicator that the actuators do modulate the movement of the separation bubble, especially at the actuator frequency.

The phase shifts observed in Figure 4.27 are present in some metrics such as Figure 4.28b, d,h. Something that does stand out is that similar to the phase results of Figure 4.27, the phase around the actuator frequency plateaus for the high-frequency cases.

The simulations of the parametric study were over a longer simulation period, combined with a smaller separation bubble, which increased the low-frequency resolution of the PSD figures and consequently the coherence figures. This is why the low-frequency dynamics are better captured by the parametric study. Nonetheless, the peaks in coherence observed for the production cases was predicted with the results of the parametric study. Although the parametric study did not predict the high coherence at the actuator frequency for the cases where the actuator was not placed at separation. This could be because the parametric study was performed using an actuator model which did not set a pressure at the wall, therefore not causing pressure waves which would drive the pulsating movement of the bubble.

So there is strong coherence between the velocity of the injection and x_{sep},x_{rea} and S_x, additionally the leading or lagging of these points is dependent on the location of the actuators. This provides better insight into the refined control of the separation bubble, allowing for better prediction of the bubble behavior. The coherence between certain metrics shows that it is not just the x_{sep} and x_{rea} points which are influenced by the actuators but the entire bubble motion is affected.

The difference in phase could be another indicator that the pressure disturbances could be the driving factor of the control mechanism. As the distance is changed, so does the phase, as the waves have

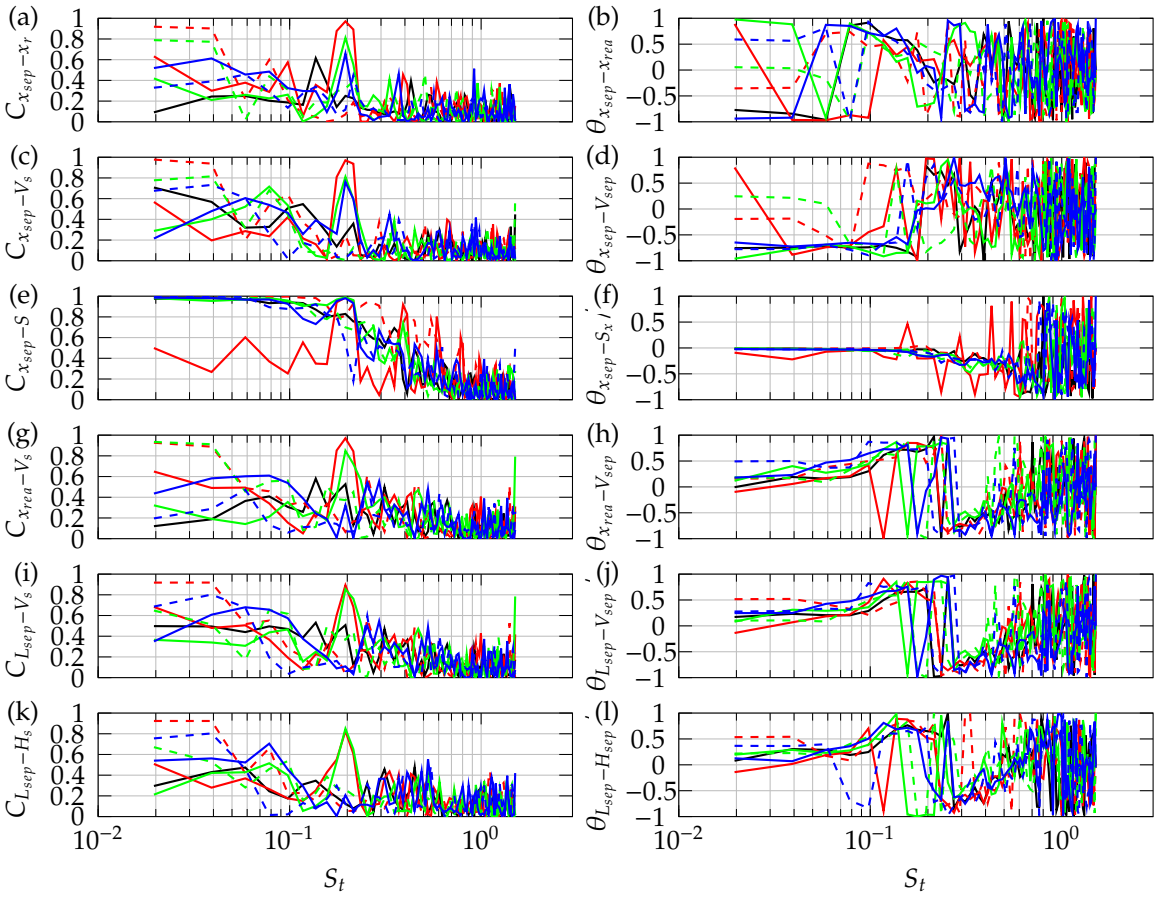


Figure 4.28: Coherence and phase of bubble motion for production cases.

different travel times, but not the coherence. The much weaker shock caused by the low-frequency cases could be reasoned from the closer phase difference.

According to Narayanaswamy et al. [33] the motion of the separation shock is a direct indication of the SWBLI unsteadiness and thus if the motion of the separation shock can be controlled, then the motion of the bubble is modified similarly. This research does agree that the separation shock motion is very closely related to the movement of the entire system as shown in coherence results such as presented in Figure 4.27 and Figure 4.28. So even though the effects are diminished for the cases where control is applied from the middle or near the reattachment region of the separation bubble, motion of the bubble can be modified from these locations.

4.3.7. Probe pressure signals

The motion of the bubble is clearly influence by the actuators, however the driving mechanism behind this is not clear. As pressure has been one of the proposed mechanisms this is further investigated by analysis of the pressure signals of probes at selected locations, which are shown for case LSFL in Figure 4.29. The probes have been placed at 8 locations, way upstream of separation, way downstream of reattachment, under the separation shock, at reattachment, at the actuator location, and then at a quarter, halfway and at three-quarters inside the bubble. These probe locations have been sorted in a downstream manner, for the probe at the actuator location refer to Table 4.1. Where Figure 4.8a, showed the time-averaged data of the probe pressure, Figure 4.29 shows the time series of several probe locations, allowing for analysis of the pressure differences as a consequence of the active jets. The pressure signals for the other cases are given in section C.6.

The signal at $(x - x_{imp})/\delta_0$ = -6.92, which is the actuator location, shows the behavior of the actuator, where the pressure is raised till around 1.5 p_w/p_∞, which is significantly lower than the reference value

of IP, which is explained by the method of computation of IV, IP and IT. As mentioned in subsection 4.2.3, the injection pressure is only higher than the flow directly above it for the actuators placed at separation. The wall pressure below the separation shock, shown by the probe at $(x - x_{imp})/\delta_0$ = -7.74, shows that there is a small delay in the response to the increase in pressure when the actuator is active. Where the response of the probe at $(x - x_{imp})/\delta_0$ = -6.92 is a sharp rise, as soon as the actuator is activated, and a slower return when the actuators are not active, the response of the pressure at $(x - x_{imp})/\delta_0$ = -7.74 is much slower especially during the pressure rise. This suggest that the motion of the separation shock, could be driven by the increase in pressure but has a limited travel speed.

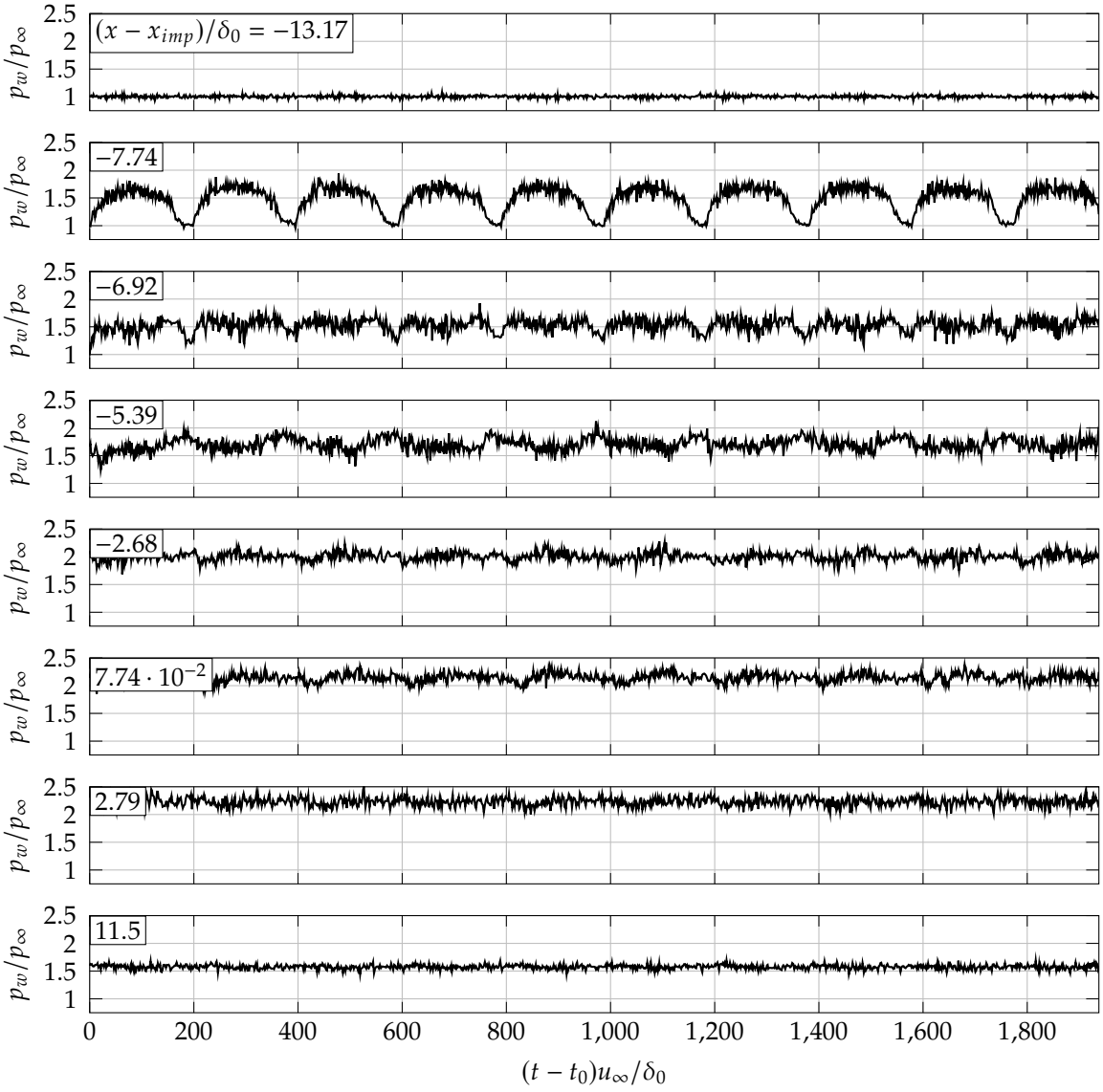


Figure 4.29: Wall-pressure for case LSFL obtained by probes placed at locations indicated in the top left corner of each plot.

The increase in pressure at $(x - x_{imp})/\delta_0$ = -5.39, which occurs before the new injection, just before $(t - t_0)u_\infty/\delta_0 = 200$, is not caused by the actuator. It most likely shows the increase in pressure because of the separation shock moving back to its original position. The actuator only is activated shortly afterwards, and it does not happen at $(t - t_0)u_\infty/\delta_0 = 0$ meaning that it is not an effect of the actuator activating, but rather of the actuator deactivating.

The coherence results of subsection 4.3.6 indicated that there is a phase difference between the injection velocity and other metrics and this phase difference depending on the actuator location. This results of Figure 4.29 seem to be in agreement with this. As the low-frequency pressure differences are observed

for all probes downstream of $(x - x_{imp})/\delta_0$ = -7.74. Although this might not be immediately apparent, it can be observed from the dip in pressure caused by the actuator deactivating. When focusing on the deactivation just before $(t - t_0)u_\infty/\delta_0$ = 800 or 1600, the data shows this same dip but slightly more delayed as the probes move further downstream.

The delay is also directly observed by the difference in the pressure at the separation shock between cases LSFL and LRFL, shown in Figures C.113 and 4.29 respectively. Case LRFL shows a delay in the response while the response of LSFL is nearly instantaneous. This difference is caused because the greater distance the pressure disturbances emanating from the actuators have to travel before interacting with the separation shock.

4.3.8. Cross-correlation comparison

The response of x_{sep} and x_{rea} to IV, shown in Figure 4.26 already seemed to show a lagging of the response. The coherence results in subsection 4.3.6 and the probe pressure data in subsection 4.3.7 further substantiated the lagging behavior, yet data does not provide clear evidence for this. In order to find more compelling evidence, the cross-correlations between several metrics of the separation bubble have been examined. Additional cross-correlations between metrics and pressure signals from probes are given in section C.5.

Results for the cross-correlation between IV and the three points: x_{sep}, x_{rea} and S_x are shown in Figure 4.30 for the high-frequency cases and in Figure C.46 for the low-frequency cases. These are separated into two figures for clarity.

Figure 4.30 confirms that the lag is dependent on the actuator location and thus that the disturbance has a certain travel time. This is observed by the order of the peaks, which is the same for the cross-correlation between IV and x_{sep} and between IV and S_x, while the order is flipped for IV and x_{rea}. Additionally the lag between the three cases is quite constant, even if it is flipped for IV and x_{rea}. Similar observations can be made for the low-frequency cases shown in Figure C.46.

Results such as Figure C.49 show the acoustic propagation of the pressure disturbance by the actuator moving through the bubble. This is observed by the difference in peak lags, where the case at separation, all the peaks are increasing in lag, for the middle, the two upstream probes lag, the one very close only lags a little bit, and then the downstream peaks lag increasingly. And the same is observed for the case at reattachment, where the actuator probe is close to the 5th probe shown, the one downstream peak lags slightly, the upstream peak lags, and moving further upstream the lag increases.

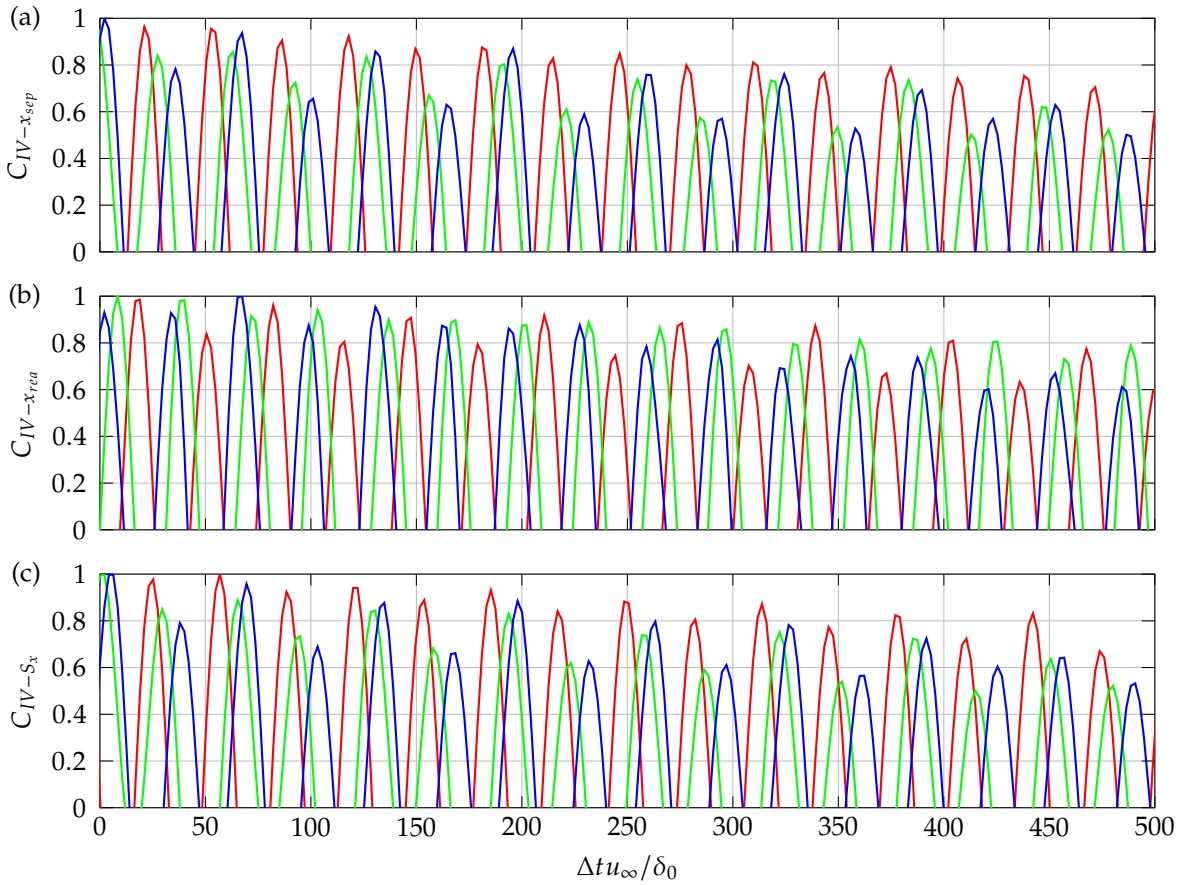


Figure 4.30: Cross-correlation with injection velocity for the high-frequency production cases.

4.3.9. Power per frequency range

The PSD maps, from subsection 4.3.1, provided a good initial insight into the development of dominant frequencies of p'_w throughout the domain. This change in dominant frequency and energy is further explored by integrating the PSD of the p'_w over three different frequency ranges for each probe as explained in section A.5. This provides numerical data on the shifts in frequency that occur throughout the domain.

Initially the results in Figure 4.31 seem to show that for all the cases where low-frequency injection is used, there is a significant increase in low-frequency energy. Now comparing cases LSFH and LSFL, it looks like the medium-frequency is replaced by the low-frequency. However when looking at LMFH and LMFL, there seems to be a significant increase in low-frequency while the high-frequency remains. The same holds when comparing LRFH to LRFL. The high-frequency peak observed for case LRFH, Figure 4.31f, still remains, peaking at $(x - x_{imp})/\delta_0 = -6$ with a value of around 0.0045 which is still there for case LRFL.

The total energy from the wall pressure fluctuations at separation is dependent on the actuator location. Similar to the Reference case, as shown in Figure 4.31 , the high-frequency peak coincides exactly with the point of separation for cases LMFH, LMFL, LRFH and LRFL. This could be because of the proximity to both the separation shock and the shear layer, which are both able to create vortices, adding to the total energy in p'_w. Additionally the order of the peaks, the most upstream peak is the low-frequency range, then the high-frequency range and finally the medium-frequency range. For all the cases LMFH, LMFL, LRFH, LRFL the peak amplitude of the high-frequency is at $(x - x_{imp})/\delta_0 = -6$, while the low-frequency peak is at around at $(x - x_{imp})/\delta_0 = -7$.

The power per frequency range figures show that the total power of the pressure fluctuations is dependent on both the actuator location and the actuator frequency. Where the low-frequency cases

almost double the power of p'_w compared to the high-frequency cases. And the actuator placed in the middle of the domain has the least amount of energy in the pressure fluctuations.

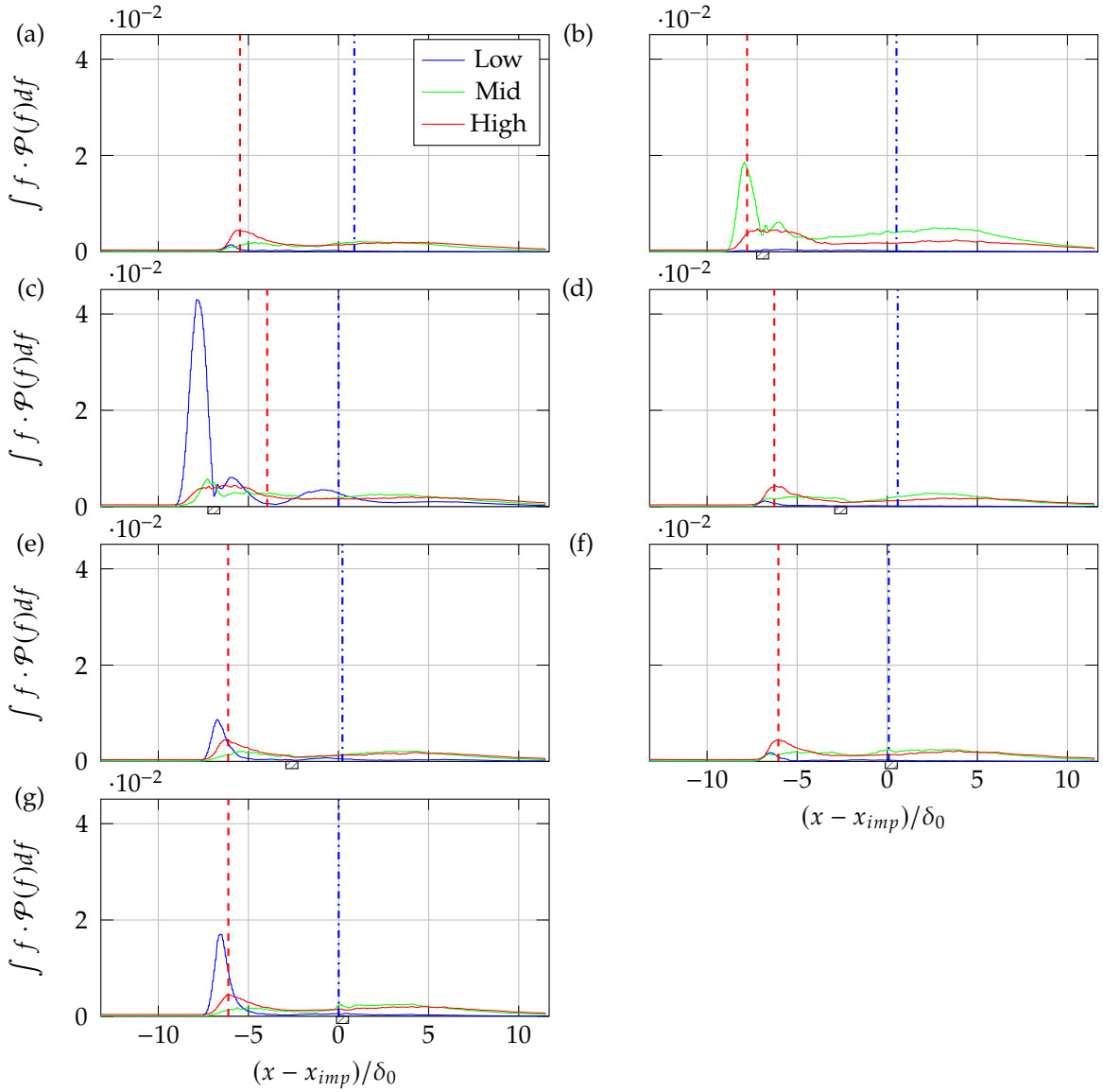


Figure 4.31: Power per frequency range for p'_w for all production cases. The vertical red dashed line indicates the statistical separation point, the vertical blue dashed-dotted line indicates the statistical reattachment point. The AL is indicated by ▨.

The integrated range of the p'_w PSD of the parametric study cases, as shown in subsection 3.5.2, is slightly different compared to the production cases, shown in subsection 4.3.9. As the parametric study used a longer simulation time and a shorter separation bubble length, the ranges of Low, Mid and High were slightly different, making the shifts shown in Figure 4.31 not one on one comparable to the parametric study results. However for both the production cases and the parametric study cases, the actuator frequency falls in the dominant frequency range. So for low-frequency cases, the dominant frequency range would be the Low range.

The shape of the medium-frequency range of case LSFH is very similar to that of the low-frequency range of case LSFL. The medium-frequency peak of case LSFH is close to $(x - x_{imp})/\delta_0 = -8$, while there is no discernible peak for either the low- or high-frequency ranges. For case LSFL there is a clear peak in the same location as the medium-frequency range peak for case LSFH. Then a steep drop which first bottoms out exactly above the actuator, before rising shortly, dropping slightly and then rising once more, reaching the second highest peak for that frequency range. One difference between the two is

the spanwise length of the last bump, which is much shorter for the low-frequency case. However this seems to be just a result of the low-frequency signal which gets a small bump just before reattachment.

An increase in medium-frequency range energy can be observed, which starts around $(x - x_{imp})/\delta_0 = -4$ for LSFH and around$(x - x_{imp})/\delta_0 = -2$ for cases LMFH-LRFL and lasts up to 2 to 4 δ_0 after reattachment. For the low-frequency cases this increase is less noticeable as the peak power of the low-frequency cases is around twice as high compared to the medium- or high-frequency range peaks for the high-frequency cases. This initial increase can also be observed for the Reference case, however for the Reference case the peak of this increase is at reattachment and not well after. For both the control simulations and the Reference case the increase starts at the location of the bubble apex. So as the bubble becomes smaller, the medium-frequency wall pressure fluctuations increase. This combined with the observation that for both case LRFH and case LRFL there is a very sharp increase just before the actuator, which is where the bubble abruptly ends, suggests that at least the medium-frequency fluctuations are linked to the height of the bubble at that location. Which could suggest that as the bubble shrinks more energy is transfered from the shear layer to the wall.

4.3.10. Peak power and frequency

The shift in power seen in subsection 4.3.9, shows that the actuators are able to control the low-frequency throughout the entire bubble. To see at what frequency the wall pressure fluctuations are most dominant, the peak power and corresponding frequency are shown. The methodology for this is given in section A.5.

The figures in this section seem to show that the high-frequency injector causes a sharp drop in the most energetic frequency in the injectors even though they are not placed at the center line. This can be seen from the sharp drop shown in Figure 4.32b, d,f. The reason for this is that the pressure is set at the actuators and therefore there are less fluctuations. This can also be observed in the PSD maps in Figure 4.22b, d,f where a vertical band of little to no pressure fluctuations can be observed.

The drop in both peak frequency and power for actuators placed in the same spanwise location as the actuators, which can be observed for cases LSFH and LSFL, was also observed in the PSD maps in Figure 4.22b-c.

Similar to what was observed in subsection 4.3.1, the high-frequency cases clearly set the dominant frequency of the p'_w throughout most of the separation bubble. The location of the actuator determines how strictly the most dominant frequency adheres to the actuator frequency. When placed at separation the most energetic frequency is the control frequency from the moment there is an increase in energy, increasing slightly just after separation but then being the control frequency throughout the rest of the domain where probes were placed. For case LMFH the start is the same, but around separation the most energetic frequency is slightly higher before returning to the actuator frequency. This extends till well after reattachment, however at 6 δ_0 the frequency starts to flip between higher values and the control frequency. For case LRFH the most energetic frequency is the actuator frequency during the separating phase and throughout the separation bubble from -4 δ_0 up to reattachment, after which it is no longer the dominant frequency.

The evolution of the dominant frequency of the p'_w PSD spectra, shown in Figure A.28, is consistent with the findings of Narayanaswamy et al. [33], i.e. that the dominant frequency is higher within the separated region, peaking around the separation shock, and progressively decreases throughout the bubble and even beyond reattachment. Narayanaswamy et al. also found that certain locations do not show signs of forcing by the actuators, something which is consistent with the results of the streamwise probes such as given in Figure C.67. However as the results from Figure C.68 show, the exact same case with different probe locations can give very different results. This was already confirmed by studies such as Pasquariello et al. [8] and Hu et al. [13, 40].

This behavior is not observed for the low-frequency cases, for which the most dominant frequency is usually observed around S_x. However the region for which the most energetic frequency is the actuator frequency, is wider around the shock foot for the low-frequency cases. This once again is an indication of the wider range of motion of the separation shock for the low-frequency cases.

While Webb et al. [67], who conducted experiments with localized arc filament plasma actuators,

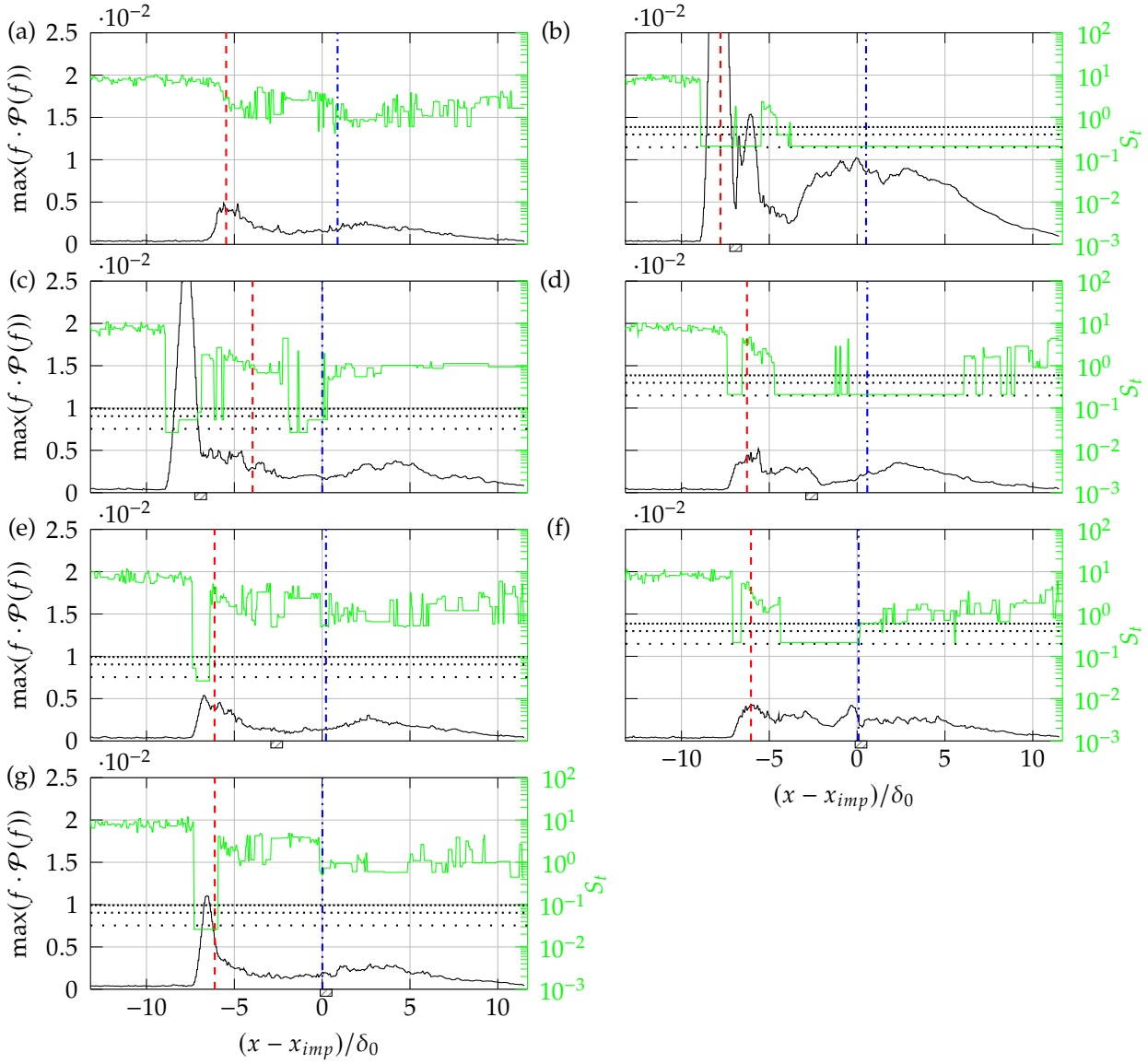


Figure 4.32: Peak PSD power and corresponding frequency of p'_w for all production cases. The vertical red dashed line indicates the statistical separation point, the vertical blue dashed-dotted line indicates the statistical reattachment point. The horizontal dashed lines indicate the first, second and third harmonics of the AF. The AL is indicated by ▨.

concluded that the main control authority of the actuators was the addition of heat, this study shows that this is not necessarily the case. The actuators show significant control authority over the low-frequency unsteadiness even though no heat is added. Webb et al. did come to this conclusion based on the actuators placed in upstream of the separation bubble. However they suggested that actuators placed near the reattachment region could manipulate the instabilities of SWBLI, something that this study has proven to be correct.

Despite some discrepancies, there are some insights obtained by the parametric study which did transfer to the production cases. For example the dominant PSD frequency is similar in shape between the selected cases from the parametric results and the production cases. The prediction that the dominant frequency would remain constant at the second harmonic frequency throughout the domain is consistent between the LSFHp and LSFH from the parametric study and the production results respectively. The frequency being less dominant when the actuator is placed in the middle of the bubble or at reattachment is also observed in both the parametric study and the production cases. Similarly, the fact that the

dominant frequency is only prevalent in the high-frequency cases is clear in both the parametric study and the production cases. The dominant frequency peak during separation is clearly visible for both the parametric study and the production cases with low actuator frequency. Where the parametric study also shows a clear dominant peak during initial separation for high-frequency cases, the production cases do not show this.

4.4. Results summary

The results shown in this chapter provide answers to the research question, but also provide some insight into the mechanisms that might be at play.

There is a significant difference between the time- and spanwise-averaged results and the results obtained from time-averaging the instantaneous snapshots, caused by the method of obtaining the data. Where the time- and spanwise-averaged data shows that a reduction in both length and volume can be achieved, the snapshot averages show that this is not the case.

However the instantaneous results show that the size of the bubble can be reduced, albeit temporarily, when the actuators are active and are placed near the separation point of the bubble. Active actuators near the separation point cause vortices which bring high energy flow near the wall, delaying or even preventing separation. Slices of v and visualization of the 3D bubble shape show that the actuation time plays a role in the streamwise length of these vortices, where the longer actuation time causes longer vortices.

The results also show that the large scale motion of the bubble can be modulated at different frequencies and from all three locations tested. However the location of the actuator does influence the effectiveness of change in the bubble motion. The modulation of the large scale motion is also clearly observed in the pressure signals at the wall.

5

Discussion

This research aimed to asses whether control using jet actuators from within the separation bubble of a SWBLI system is possible, and if so, how effective this method is. To asses the effectiveness of control two metrics were considered: reduction of the bubble size and the modulation of its the low-frequency motion. Due to computational constraints, only a limited number of high-fidelity simulations could be performed. To select the settings which showed effective control, a lower-fidelity parametric study was conducted. In the parametric study the location of the actuators was varied from way upstream of the separation to just after reattachment and the injection frequency was varied from $2.681 \cdot 10^{-3}$ to 0.4938 St_L.

Based on the time- and spanwise-averaged averaged results, it was found that a significant reduction in the size of the separation bubble was only achieved when actuators were placed near separation and could not be achieved from within the separation bubble. This finding agrees with the experimental work of Narayanaswamy et al. [33] and Greene et al. [38], who observed that actuators had to be placed upstream for effective size reduction.

The rationale of using jet actuators upstream of the separation bubble, is that these can generate counter-rotating vortices which transport high-momentum flow closer to the wall, delaying or even preventing separation, as was posed by by Narayanaswamy et al. [33] and Greene et al. [38]. Due to the upstream movement of the separation bubble the actuators were not placed in the optimal location for size reduction, compared to the results of Greene et al. [38] and the parametric study results. Still streamwise vortices were observed cases LSFH and LSFL especially in peak-phase-averaged results, Figure 4.13. The results also show streamwise vortical structures for the control cases in the middle of the bubble and at reattachment, yet these do not bring high-momentum flow closer to the wall as the the steamwise velocity at these locations is insufficient. This observation is also supported by Figures C.7, C.9 and 4.3. Finally these results show that the longer actuation time of the low-frequency cases creates longer vortices, penetrating deeper into the bubble thus being more effective in the reduction of the bubble size, which can be observed in both the instantaneous and phase-averaged bubble shape results in Figures 4.6 and 4.14.

Webb at al. [67], similarly observed an increase in displacement of the separation shock with increased arc times and increased frequencies, which they attribute to the reduced relaxation time of the separation shock. However the longer arc time has a significantly greater impact on the displacement than the frequency does. The results for the cases near separation in Figures 4.23 and 4.24 agree with a larger range of motion of the separation shock for longer actuation time, while the maximum displacement was similar for both frequencies. However the shorter relaxation time would not explain the lower minimum bubble volume for the low-frequency at separation, this has to be attributed to the longer actuation time. How the separation shock is pushed forward with quick consecutive injections can clearly be observed in Figures C.63 and 4.23, yet the same can be achieved by longer, lower frequency pulses.

Although heating can be a control mechanism as Webb et al. [67] investigated, the results do not show

that this is the primary mechanism. Even though some heat was added by the actuators when inside the bubble, as shown in Figures 4.2 and 4.8, the actuators at separation did not. The actuators near separation resemble MVG, introducing a blockage effect that can shift the separation upstreamm further than for the other control cases, which can be observed in the instantaneous bubble shape, Figure 4.6, but also in the time- and spanwise-averaged and phase-averaged bubble shape in Figure 4.11 and Figure 4.14 respectively. This blockage causes a buildup of heat as shown in Figure 4.2 and Figure 4.8d, which would increase the energy of the vortices created by the actuators, but this effect is not the primary mechanism of the separation reduction.

The analogy of the jet actuators functioning similarly to MVG is useful to understand why there is little to no reduction in the bubble size when actuators are placed in the middle of the bubble. In order for MVG to create vortical structures fast moving air is required, which is not present inside the separation bubble. Thus this mechanism will not work for a reduction in size of the bubble. Actually the blockage seen for cases LSFH and LSFL is also present for cases LRFH and LRFL and here it has an adverse effect on the bubble size. The blockage causes a swelling of the bubble, as seen in Figures 4.11 and 4.14, which creates a very asymmetrical bubble.

In cases LMFH and LMFL, the time- and spanwise averaged reduction in volume is achieved by ejection of the bubble above the actuator rather than through the use of vortices. This is supported by Figures 4.11 and 4.13 where is shown that the bubble is split and the vortices created by the actuator do are not present at the wall, thus the flow remains separated. Although the results of Figures C.31 and 4.14 do indicate that the longer actuator time do create some vortices, these are not very effective as they only occur around peak injection. The fact that the bubble reduction only occurs above the actuator makes this an inefficient method of reducing the size. However this could be used when angling the actuators upstream and placing them near reattachment. Angling the actuators in the middle did not provide a significant reduction as shown by Narayanaswamy et al. [33].

While the blockage by the actuators for cases LSFH and LSFL causes the separation shock to move upstream significantly, the other cases also show this upstream movement of the separation shock. One of the suggested reasons behind this is the increased pressure within the separation bubble, increasing its size. As the reattachment point is mainly determined by the incident shock and the expansion fan generated by the trailing edge of the shock generator, the bubble can mostly expand upstream, thus the separation point moves upstream. Because previous research done by Narayanaswamy et al. [33] and Greene et al. [38] did not include extensive results where actuators were placed inside the bubble, the corresponding driving mechanism will be compared to other control methods. Pasquariello et al. [8] showed delayed separation under reduced bubble pressure. Laguarda et al. [73] used a flexible panel, thus not altering the pressure inside the bubble and found no significant upstream movement of the bubble. Even though the IP of the actuators is insufficient to overcome the pressure inside the bubble, as shown in Figure 4.8a, these results also show that there is an increased pressure compared to the Reference case. And while instantaneous pressure snapshots, as shown in Figures C.5 and C.10, do not show a large pressure front emanating from the actuators, large pressure disturbances can be observed which are not present for the Referencecase. This leads to the conclusion that the pressure influenced by the actuators is the driving factor for the upstream movement of the separation shock.

While the reduction in size of the bubble has proven difficult when the actuators are placed within the bubble or at reattachment, the results indicate that the modulation of the low-frequency dynamics of the SWBLI system is possible. Once again the proposed mechanism for this is the pressure disturbances created by the actuators causing the expanding and contrasting motion of the bubble which is locked to the frequency of the actuators. Without a significant size reduction of the separation bubble, the low-frequency back and forward movement can be controlled.

Based on the present LES results, the following observations can be made regarding the pressure disturbances: firstly the influence of these is be confined to within the separation bubble, as these are absorbed by the shock, changing its location, but they do not cross the shock. This can be observed in the PSD maps of Figure 4.22, where the increase in p'_w does not travel further upstream than the separation shock.

Secondly, as these disturbances propagate through the bubble, energy dissipation is expected, resulting in diminished influence on the shock movement for actuators placed further downstream of the

separation shock. This is reflected in the data of the separation shock movement in Figure 4.23 and Figure 4.24. The difference in energy is seen in the total displacement of the separation shock, but also in the travel velocity of the shock. Even though the coherence between the IV and x_{sep} is the same for all high-frequency cases and similar for all low-frequency cases. Energy dissipation could be the reason for these differences, another could be the IP to local wall-pressure ratio, which decreases as the actuators are moved towards reattachment.

Finally, these pressure disturbances can only travel at a certain wave speed, depending on the conditions within the separation bubble. Therefore the separation-shock movement, as a response to activation of actuators, takes longer for the actuators at reattachment than those placed in the middle and the response to those placed at separation should take even less time. This can be observed in the phase changes in Figure 4.28 but is even clearer from the cross-correlation shown in Figures C.46 and 4.30. It can even be observed directly when comparing the wall-pressure signals of case LSFL in Figure 4.29 to case the signals of case LRFL in Figure C.113. Where the pressure response of case LSFL is virtually instantaneous while the response of case LRFL, has a certain delay.

The movement of the separation shock has consequences for pressure disturbances at the wall. When the actuators deactivate, the separation shock moves downstream causing pressure disturbances, which show up as harmonics in wall-pressure signals. For this to happen the movement velocity of the separation shock has to be sufficient to create strong pressure fluctuations. This is why the harmonics are clearly visible for near separation for case LSFH and not for case LSFL, as the low-frequency injection lets the separation shock move upstream more gradually. The same holds for the other control cases, as the movement of the separation shock is not enough to cause clearly visible pressure fluctuations at the wall.

The second harmonic of the actuator frequency can be observed in the pressure fluctuations for all the high-frequency cases near reattachment. This is because the separation shock motion causes shear-layer vortices convected downstream, causing the second harmonic of the pressure fluctuations. Because the shear layer is closer to the wall, thus the travel distance for the pressure fluctuations is small, these can be observed in the PSD maps in Figure 4.22, and why they are not visible in the middle of the bubble for LSFH. Additionally they may not be observed for the low-frequency cases as the shear layer vortices occur at a higher frequency, ($St_L \approx 0.5$) [9].

The possibility that pressure disturbances are either reflected or caused by the shear layer, thus causing an increase in p'_w would be supported by the results given in subsection 4.3.9. All high-frequency cases show an increase in pressure fluctuations in the medium range, which is the range where the high actuator frequency is in, as the shear layer comes closer to the wall near reattachment, thus increasing the energy as the pressure waves have to travel a smaller distance. For the low-frequency cases, this increase is not present, instead an increase in the low-frequency range can be observed, except for case LRFL. This can be due to scaling or the placement of the actuator.

Pressure disturbances as a driving factor for instability could even be an explanation for the results of Pasquariello et al. [8], where the pressure disturbances could be dependent on the length of the tube, although this is difficult to discern as the mass removed from inside the bubble is injected upstream which could also influence the incoming boundary layer unsteadiness. It could also be a suitable explanation for the behavior in the flexible panel study done by Laguarda et al. [73], where the fluctuations in the panel cause an expansion and retraction of the bubble and the separation shock. This separation shock movement will, similarly to the results of this study, cause pressure disturbances to be felt by the panel, where the natural frequency of the panel gets amplified, causing a positive feedback loop.

While there is good coherence at the actuator frequency between the IV and x_{sep}, x_{rea} and S_x for basically all production control cases, the selected cases of the parametric study show a lack of coherence when the actuators were placed inside the bubble. Aside the fidelity, the main difference between the production cases and the parametric study is that the parametric study did not set a pressure in the actuator, and thus the primary control mechanism is not present.

If the actuator velocity was the driving factor of the control system then one would expect an increase in velocity fluctuations inside the separation bubble and at the separation shock and shear layer. However the time-averaged results in subsection 4.2.7 do not reflect this. Since the injection velocity is only in

the wall-normal direction, an increase of $v'v'$ would be expected, yet Figures C.41 and 4.19 show that the influence of the actuator on these fluctuations is mainly local and moving downstream. There is an increase in fluctuations in the separation shock, however this can be attributed to the larger range of motion of the shock. Additionally there is no indication of a mechanism that allows for significant upstream movement of the flow which would carry these perturbations.

A similar argument could be made against pressure being the primary control mechanism, as direct evidence of the pressure disturbances created by the actuators is expected in the instantaneous snapshots, shown in Figures C.5 and C.10 respectively. And while the pressure from the actuator can be seen for cases LSFH and LSFL and faintly for cases LMFH and LMFL due to the high pressure inside the bubble, it is not visible in the middle of the actuator. Additionally the snapshots are taken at peak injection, which is not the point at which the pressure gradient at the actuators is the largest, which would be at the start and end of the injection, as shown in Figure 4.29.

Besides the faint signs of the pressure disturbances created by the actuators, if the pressure fluctuations are examined, there is an increase in $p'p'$ in the separation shock and the shear layer. The increase in pressure fluctuations in the separation shock can be mostly attributed to the increased low-frequency range of motion of the separation shock. And the small increase in $p'p'$ the shear layer could be a result of an increase in shear layer vortices.

While there is no direct, conclusive evidence of pressure being the mechanism used for control, the circumstantial evidence does support this. Other analysis techniques such as Dynamic Mode Decomposition (DMD) or Spectral Proper Orthogonal Decomposition (SPOD) could provide more insight into the inner workings. Direct evidence could perhaps be obtained by phase averaging pressure similar to what is in the results given. Additional improvements of the analysis would include 3D statistics, as the ones used here are spanwise averaged and for the snapshots the initial transient should be removed. However because the simulated time was limited in this case, it was decided to not remove this transient to preserve more data points.

Greene et al. [38] suggested moving the jets further upstream to reduce the strength of the separation shock and possibly reduce the distortion in the downstream boundary layer. However the suggestion based on the results would be to place the actuators inside the bubble. The data shows that the energy of the wall-pressure fluctuations can be reduced significantly, the dominant frequency can be modulated, potentially reducing the risk of getting bubbles vibrating at the natural frequency of certain parts. Or a variation in frequency could distribute the energy over a frequency spectrum. Additionally, Greene et al. remarked that reducing the size of the separation bubble could have counterproductive effects if the goal is to minimize the flow distortion downstream of the SWBLI, which is not something that is in the order when placing the actuators inside the bubble.

Even though the parametric study was performed with a different actuator model which did not set the pressure and temperature at the wall, it did show results which are quite comparable to the production cases. It showed similar behavior for the differences in high- and low-frequency activation, especially upstream of the separation point, where the low-frequency cases showed to be more effective at reducing the separation-bubble size. In some areas there are differences as expected. There is an especially large difference in the prediction of the size of the bubble, which can be attributed to the much coarser grid in the wall region, which under-resolves the near-wall turbulence. The spectral results of the parametric study only seem to be valid up to a certain extend as it did fail to find coherence for cases inside the separation bubble. The dominant frequency shape is also quite similar between the parametric results and the production results for LSFH and LSFL. However the power of the dominant frequency is significantly lower for the production cases where the actuators are placed in the middle or at reattachment. This can be attributed to the parametric study using a different actuator model.

With the current actuator model it is difficult to determine what optimal control frequency when controlling from within the separation bubble. Using just the results in this study the use of a lower frequency would be the best option. It provides slightly better results in the reduction in volume and length of the bubble while not getting pressure fluctuation harmonics which could be detrimental for structures. While the much higher pressure fluctuations at the separation shock could be a drawback, it is one of the only negatives compared to the high-frequency cases. However this is all based on the results where the pulse of the low-frequency cases was much longer than the pulse of the high-frequency

cases. If the actuation time is the same, just the period between pulses varies, then controlling at higher frequencies is preferable as the variation of the bubble size would be smaller, possibly making the downstream flow behavior more stable and predictable. Additionally the shorter pulses could show harmonics for the low-frequency cases which would negate the benefit it is now showing to have as these short pulses cause a faster motion of the separation shock.

Finally the effective modulation of the low-frequency by pressure disturbances could hint at the origin of the intrinsic unsteadiness of the SWBLI system. Vortical unsteady structures emanating near the separation shock, which are transported by the unsteady shear layer cause the reattachment point to be unstable, which feeds back to the reattachment point and the separation shock, which in turn show unsteady behavior, keeping this process going. By altering the pressure within the separation bubble, the frequency of the bubble can be modulated from any location inside the bubble. Therefore it would seem that the low-frequency unsteadiness is an intrinsic property of the SWBLI system and not merely a consequence of amplified upstream perturbations, as the actuators do not influence these perturbations.

6

Conclusion

This research investigated the ability to control a SWBLI system using jet actuators. With previous research focusing on injection upstream of the separation bubble, this research focused on injection from within. In order to find suitable locations and frequencies, a parametric study was conducted for locations ranging from far upstream to just after reattachment and frequencies ranging from low to high. From this parametric study 6 cases were selected and simulated using wall-resolved LES. While the parametric study offered preliminary insights, results mainly focus on the production cases as these provide higher-fidelity results. The setup for both the parametric study and the production cases has been used in previously published research. The ability to control was split into two aspects: reducing the separation bubble and modulation of unsteadiness.

The first aspect has been shown to be possible using actuators placed at separation and to a smaller extend when placed in the middle. As the main control mechanism of the size reduction is the creation of vortical structures, also shown by [33, 38], similar to MVG, a flow velocity is required which is not sufficient in the middle or near the reattachment region of the bubble. However the actuators located in the middle of the bubble did reduce the bubble volume by ejection of the recirculation region directly above the actuator, which is a very localized effect and does not provide a feasible solution to efficiently reduce the bubble size. The actuators at reattachment showed an increase in bubble volume.

The shape of the bubble was mainly determined by the actuator location, as the placement either created vortices which reduced the size but not influenced the shape much, caused the bubble to split or, similar to MVG the active actuators showed blockage of the flow, creating a bulging of the separation bubble when placed at reattachment.

While the shape was determined by the actuator location, the volume is related to the actuation frequency. At locations that did show a reduction in size of the bubble, low-frequency actuation was more effective, although this is due to the actuator model, where it is active for longer for the low-frequency cases. Nonetheless for actuators near separation, this longer activation period created vortices which penetrated the separation bubble much further, significantly reducing the separation volume.

The second aspect of the control ability, to modulate the unsteadiness of the bubble, was shown to be possible independent of the control location or frequency. Even with limited low-frequency resolution in the spectral analysis, the ability to control the dominant frequency of the bubble motion was shown for both the low and high-frequency cases at all locations. Although low-frequency actuation did show a less energetic control authority over the bubble motion, it still modulated it.

As the ability of modulation was independent of location and frequency, a method which is the driving factor behind this modulation is proposed. The data in this research supports the claim that pressure disturbances emanating from the actuators are the driving factor behind the modulation of the unsteadiness. The fact that there is a dominant frequency throughout the domain for the high-frequency cases, which have a stronger pressure disturbances, is a good indication of this. The fact that the control

authority of the separation shock decreases with an increase in distance to the actuators further supports this. Finally differences in response time, shown in cross-correlation and probe pressure signals, show that the response time is dependent on the location of actuation, which would also fit this proposed method.

The driving mechanism behind the actuator potentially provided more insight into the unsteadiness of the SWBLI system. By modulating the pressure inside the system, the unsteadiness could be modulated effectively, indicating that pressure fluctuations within the separation bubble could be the cause of the unsteadiness.

So while control from within the separation bubble is possible, it should not be used to reduce the size of the bubble. Not only is the possibility to do this very limited, it is also ineffective. It is more effective to modulate the low-frequency unsteadiness as this can likely be set to a range of different frequencies, without the downside of creating unwanted unsteadiness downstream of the bubble.

6.0.1. Future Recommendations

To further investigate the driving mechanism behind the actuators, a new actuator model should be implemented, perhaps based on an analytical model such as those proposed in recent works [45, 81, 82, 83]. This model should not use the actuator frequency to determine the pulse length, rather the pulse length should either be set or calculated based on inputs. This would either confirm or reject the claim that the absence of secondary harmonics in the PSD maps for the low-frequency cases, is because of the weaker shock. A revised actuator model would also change the bubble motion significantly as the bubble would return to its original location sooner. Thus the expectation is that the difference between the low-frequency cases and the Reference will be smaller than between the high-frequency cases and the Reference.

After implementation of a better actuator model, the parametric study could be redone as the current a model did not accurately predict the coherence found between the injection velocity and the bubble motion. While other factors such as the under-prediction of near-wall turbulence could also be a cause of this, ensuring that the injection pressure is correct can exclude that as a reason for the differences. To prove the correct implementation of the actuator model, the results should be experimentally validated and results from previous studies should be recreated, see e.g. [33, 38, 67, 86]. Finally with a correct implementation of the actuator model, additional design variables such as injection angle and sweep could be tested which could provide further insight into the reduction and modulation of the separation bubble.

Improving the actuator model could result in slightly different outcomes, but this is a worthwhile effort. This would also allow verification of results with the previously performed experimental studies performed by Narayanaswamy et al. [33] and Greene et al. [38].

In future research, 3D statistics, which should also start after the initial transient and could be taken at specific phases of the injection rather than from snapshots, will be able to better isolate the effects of the actuators. Because even with phase-averaging applied, the low-frequency simulations show quite a bit of noise simply because the number of snapshots used is not very large, only 50. The low-frequency simulations are more affected by the simulation time because there are fewer pulses than for the high-frequency cases. This could be solved by increasing the simulation time or using predetermined time steps for phase-averaging. Additionally phase averaging different variables such as pressure and temperature, could provide further insight into the influence of the actuators, especially inside the bubble.

Further examination of the data using tools like DMD and SPOD could provide further insight into the driving mechanism of the actuators. Similarly a more extensive analysis of phase-averaged data using different variables such as temperature and pressure could provide this. Additional analysis of the cross-correlation of the pressure signals might show that disturbances travel at the acoustic propagation speed and cross-correlation between the pressure signals and the motion of the bubble might provide further evidence of the primary control mechanism of the bubble.

Even with the comparatively low injection pressure, when injecting inside the bubble, the pressure disturbances enacting the modulation are visible. However the effective control was less as the distance

increased, which has mainly been attributed to the larger travel distance of the disturbances. Future simulations could feature injection pressures above the local wall pressure inside the bubble based on the baseline interaction, to see if modulation is stronger.

References

[1] David S. Dolling. "Fifty years of shock-wave/boundary-layer interaction research: What next?" In: *AIAA Journal* 39 (8 2001), pp. 1517–1531. DOI: 10.2514/2.1476.

[2] K. Stewartson. "On the interaction between shock waves and boundary layers". In: *Mathematical Proceedings of the Cambridge Philosophical Society* 47 (3 1951), pp. 545–553. DOI: 10.1017/S0305004100026943.

[3] Matthew J. Schwartz, Datta V. Gaitonde, and John W. Slater. "Uncertainty and Sensitivity Analysis of Bleed Modeling in Shock/Turbulent Interactions". In: *Journal of Propulsion and Power* 39 (1 Jan. 2023), pp. 106–120. ISSN: 15333876. DOI: 10.2514/1.B38785.

[4] M. K. Fukuda, Eli Roshotko, and W. R. Hingst. *Control of shock-wave boundary-layer interactions by bleed in supersonic mixed compression inlets*. Sept. 1975. DOI: 10.2514/6.1975-1182.

[5] Kazuyasu Matsuo, Yoshiaki Miyazato, and Heuy Dong Kim. "Shock train and pseudo-shock phenomena in internal gas flows". In: *Progress in Aerospace Sciences* 35 (1 Jan. 1999), pp. 33–100. ISSN: 0376-0421. DOI: 10.1016/S0376-0421(98)00011-6.

[6] Z. Seifollahi Moghadam and A. Jahangirian. "Flow control of transonic airfoils using optimum suction and injection parameters". In: *Journal of Applied Fluid Mechanics* 10 (1 2017), pp. 103–115. ISSN: 17353645. DOI: 10.18869/acadpub.jafm.73.238.26201.

[7] Michael Amitay et al. "Aerodynamic flow control over an unconventional airfoil using synthetic jet actuators". In: *AIAA journal* 39 (3 2001), pp. 361–370. ISSN: 00011452. DOI: 10.2514/2.1323.

[8] Vito Pasquariello et al. "Large-eddy simulation of passive shock-wave/boundary-layer interaction control". In: *International Journal of Heat and Fluid Flow* 49 (C 2014), pp. 116–127. ISSN: 0142727X. DOI: 10.1016/j.ijheatfluidflow.2014.04.005.

[9] Vito Pasquariello, Stefan Hickel, and Nikolaus A. Adams. "Unsteady effects of strong shock-wave/boundary-layer interaction at high Reynolds number". In: *Journal of Fluid Mechanics* 823 (July 2017), pp. 617–657. ISSN: 14697645. DOI: 10.1017/jfm.2017.308.

[10] Todd S.C. Davidson and Holger Babinsky. "Influence of boundary-layer state on development downstream of normal shock interactions". In: *AIAA Journal* 56 (6 2018), pp. 2298–2307. ISSN: 00011452. DOI: 10.2514/1.J056567.

[11] Tamal Jana and Mrinal Kaushik. "Survey of control techniques to alleviate repercussions of shock-wave and boundary-layer interactions". In: *Advances in Aerodynamics* 4 (1 2022). DOI: 10.1186/s42774-022-00119-9.

[12] Feng Yuan Zuo, Ming Yu, and Sergio Pirozzoli. "Modal Analysis of Separation Bubble Unsteadiness in Conical Shock Wave/Turbulent Boundary Layer Interaction". In: *AIAA Journal* 60 (9 2022), pp. 5123–5135. ISSN: 1533385X. DOI: 10.2514/1.J061855.

[13] Weibo Hu, Stefan Hickel, and Bas W. van Oudheusden. "Unsteady mechanisms in shock wave and boundary layer interactions over a forward-facing step". In: *Journal of Fluid Mechanics* 949 (Oct. 2022). ISSN: 14697645. DOI: 10.1017/jfm.2022.737.

[14] Muzio Grilli et al. "Analysis of unsteady behaviour in shockwave turbulent boundary layer interaction". In: *Journal of Fluid Mechanics* 700 (June 2012), pp. 16–28. ISSN: 14697645. DOI: 10.1017/jfm.2012.37.

[15] Sébastien E.M. Niessen et al. "Convective instabilities in a laminar shock-wave/boundary-layer interaction". In: *Physics of Fluids* 35 (2 Feb. 2023), p. 024101. ISSN: 10897666. DOI: 10.1063/5.0135590.

[16] Alessandro Ceci et al. "On low-frequency unsteadiness in swept shock wave–boundary layer interactions". In: *Journal of Fluid Mechanics* 956 (Feb. 2023). ISSN: 0022-1120. DOI: 10.1017/jfm.2023.2.

[17] Jean Paul Dussauge, Pierre Dupont, and Jean François Debiève. "Unsteadiness in shock wave boundary layer interactions with separation". In: *Aerospace Science and Technology* 10 (2 Mar. 2006), pp. 85–91. ISSN: 12709638. DOI: 10.1016/j.ast.2005.09.006.

[18] Stephan Priebe and M. Pino Martín. "Low-frequency unsteadiness in shock wave-turbulent boundary layer interaction". In: *Journal of Fluid Mechanics* 699 (May 2012), pp. 1–49. ISSN: 14697645. DOI: 10.1017/jfm.2011.560.

[19] Noel T. Clemens and Venkateswaran Narayanaswamy. "Low-frequency unsteadiness of shock wave/turbulent boundary layer interactions". In: *Annual Review of Fluid Mechanics* 46 (Jan. 2014), pp. 469–492. ISSN: 00664189. DOI: 10.1146/annurev-fluid-010313-141346.

[20] Datta V. Gaitonde. "Progress in shock wave/boundary layer interactions". In: *Progress in Aerospace Sciences* 72 (Jan. 2015), pp. 80–99. ISSN: 03760421. DOI: 10.1016/j.paerosci.2014.09.002.

[21] S. Priebe et al. "Low-frequency dynamics in a shock-induced separated flow". In: *Journal of Fluid Mechanics* 807 (2016), pp. 441–477. DOI: 10.1017/jfm.2016.557.

[22] Jean M. Délery. "Shock wave/turbulent boundary layer interaction and its control". In: *Progress in Aerospace Sciences* 22 (4 1985), pp. 209–280. ISSN: 03760421. DOI: 10.1016/0376-0421(85)90001-6.

[23] Wesley L. Goodman and E. Leon Morrisette. "Passive control plate for shock-boundary layer interactions". In: American Institute of Aeronautics and Astronautics Inc, AIAA, 1988. DOI: 10.2514/6.1988-3537.

[24] Ru Bing Liu et al. "Experimental study on airfoil flow separation control via an air-supplement plasma synthetic jet". In: *Advances in Aerodynamics* 4 (1 Dec. 2022). ISSN: 25246992. DOI: 10.1186/s42774-022-00126-w.

[25] Aniruddha Ajay Kane, Ravi K. Peetala, and Vinayak Kulkarni. "Investigation of pressure feedback technique to control ramp based SWBLI". In: *Acta Astronautica* 201 (Dec. 2022), pp. 482–495. ISSN: 00945765. DOI: 10.1016/j.actaastro.2022.09.057.

[26] Hao Xu et al. "Control of shock wave/boundary layer interaction induced by the microjet configuration". In: *Acta Astronautica* 201 (Dec. 2022), pp. 111–128. ISSN: 00945765. DOI: 10.1016/j.actaastro.2022.09.010.

[27] Jin Young Shin, Hyung Jin Kim, and Kyu Hong Kim. "Development of one-dimensional analytical model for a SparkJet actuator". In: *AIAA Journal* 59 (3 2021), pp. 1055–1074. ISSN: 1533385X. DOI: 10.2514/1.J059619.

[28] Shintaro Sato, Tomoki Enokido, and Naofumi Ohnishi. "Fabrication of a multi-stage plasma synthetic jet actuator using printed electronics". In: *AIP Advances* 11 (4 Apr. 2021). ISSN: 21583226. DOI: 10.1063/5.0047709.

[29] Vilas J. Shinde, Jack J. McNamara, and Datta V. Gaitonde. "Control of transitional shock wave boundary layer interaction using structurally constrained surface morphing". In: *Aerospace Science and Technology* 96 (2020). DOI: 10.1016/j.ast.2019.105545.

[30] Argyris G. Panaras and Frank K. Lu. "Micro-vortex generators for shock wave/boundary layer interactions". In: *Progress in Aerospace Sciences* 74 (2015), pp. 16–47. DOI: 10.1016/j.paerosci.2014.12.006.

[31] Han Wu et al. "Study of the streamwise location of a micro vortex generator for a separation-control mechanism in supersonic flow". In: *Physics of Fluids* 34 (11 Nov. 2022), p. 116115. ISSN: 10897666. DOI: 10.1063/5.0123541.

[32] Holger Babinsky, Y. Li, and Charles W.Pitt Ford. "Microramp control of supersonic oblique shock-wave/boundary-layer interactions". In: *AIAA Journal* 47 (3 2009), pp. 668–675. DOI: 10.2514/1.38022.

[33] Venkateswaran Narayanaswamy, Laxminarayan L. Raja, and Noel T. Clemens. "Control of unsteadiness of a shock wave/turbulent boundary layer interaction by using a pulsed-plasma-jet actuator". In: *Physics of Fluids* 24 (7 July 2012), p. 076101. ISSN: 1070-6631. DOI: 10.1063/1.4731292.

[34] Xin Li et al. "Görtler vortices behavior and prediction in dual-incident shock-wave/turbulent-boundary-layer interactions". In: *Physics of Fluids* 34 (10 Oct. 2022). ISSN: 10897666. DOI: 10.1063/5.0100718.

[35] B. Bugeat et al. “Low-frequency resolvent analysis of the laminar oblique shock wave/boundary layer interaction”. In: *Journal of Fluid Mechanics* 942 (July 2022). ISSN: 14697645. DOI: 10.1017/jfm.2022.390.

[36] Matteo Bernardini et al. “Unsteadiness characterisation of shock wave/turbulent boundary-layer interaction at moderate Reynolds number”. In: *Journal of Fluid Mechanics* 954 (Jan. 2023). ISSN: 14697645. DOI: 10.1017/jfm.2022.1038.

[37] Nathaniel Hildebrand et al. “Sensitivity analysis for the control of oblique shock wave/laminar boundary layer interactions at Mach 5.92”. In: *47th AIAA Fluid Dynamics Conference, 2017* (2017). DOI: 10.2514/6.2017-4312.

[38] Benton Robb Greene et al. “Control of mean separation in shock boundary layer interaction using pulsed plasma jets”. In: *Shock Waves* 25 (5 Sept. 2015), pp. 495–505. ISSN: 09381287. DOI: 10.1007/s00193-014-0524-5.

[39] Jingchang Shi and Hong Yan. “Turbulence amplification in the shock wave/turbulent boundary layer interaction over compression ramp by the flux reconstruction method”. In: *Physics of Fluids* 35 (1 Jan. 2023), p. 016122. ISSN: 1070-6631. DOI: 10.1063/5.0134222.

[40] Weibo Hu, Stefan Hickel, and Bas W. Van Oudheusden. “Low-frequency unsteadiness mechanisms in shock wave/turbulent boundary layer interactions over a backward-facing step”. In: *Journal of Fluid Mechanics* 915 (2021). ISSN: 14697645. DOI: 10.1017/jfm.2021.95.

[41] E.E. Zukoski. “Turbulent boundary-layer separation in front of a forward-facing step”. In: *AIAA Journal* 5 (10 1967), pp. 1746–1753. DOI: 10.2514/3.4299.

[42] Yong Yi Zhou et al. “Evolution characteristics of streamwise vortex of crossing shock wave/-turbulent boundary layer interaction”. In: *Physics of Fluids* 35 (1 Jan. 2023). ISSN: 10897666. DOI: 10.1063/5.0135680.

[43] Ke Zhu, Wei Dong Liu, and Ming Bo Sun. “Impacts of periodic disturbances on shock wave/-turbulent boundary layer interaction”. In: *Acta Astronautica* 182 (May 2021), pp. 230–239. ISSN: 00945765. DOI: 10.1016/j.actaastro.2021.02.017.

[44] Hao Jiang et al. “Hypersonic flow control of shock wave/turbulent boundary layer interactions using magnetohydrodynamic plasma actuators”. In: *Journal of Zhejiang University: Science A* 21 (9 Sept. 2020), pp. 745–760. ISSN: 18621775. DOI: 10.1631/jzus.A2000025.

[45] Kiyoshi Kinefuchi, Andrey Y. Starikovskiy, and Richard B. Miles. “Numerical investigation of nanosecond pulsed plasma actuators for control of shock-wave/boundary-layer separation”. In: *Physics of Fluids* 30 (10 Oct. 2018). ISSN: 10897666. DOI: 10.1063/1.5051823.

[46] Vilas J. Shinde, Datta V. Gaitonde, and Jack J. McNamara. “Control of shock wave turbulent boundary layer interaction using structurally constrained active surface morphing”. In: *AIAA Scitech 2020 Forum* (Jan. 2020), pp. 1–18. DOI: 10.2514/6.2020-0038.

[47] Louis J. Souverein et al. “Effect of Interaction Strength on Unsteadiness in Shock-Wave-Induced Separations”. In: *AIAA Journal* 48 (7 Apr. 2010), pp. 1480–1493. ISSN: 00011452. DOI: 10.2514/1.J050093.

[48] Louis J. Souverein and Jean François Debiève. “Effect of air jet vortex generators on a shock wave boundary layer interaction”. In: *Experiments in Fluids* 49 (5 2010), pp. 1053–1064. DOI: 10.1007/s00348-010-0854-8.

[49] Luis Laguarda. “Shock interaction phenomena”. Delft University of Technology, May 2024. ISBN: 978-94-6366-874-3. DOI: 10.4233/uuid:9bedea88-5e93-4261-84a0-04e1fb35cf22. URL: https://doi.org/10.4233/uuid:9bedea88-5e93-4261-84a0-04e1fb35cf22.

[50] Sergio Pirozzoli and Matteo Bernardini. “Turbulence in supersonic boundary layers at moderate Reynolds number”. In: *Journal of Fluid Mechanics* 688 (2011), pp. 120–168. DOI: 10.1017/jfm.2011.368.

[51] Luis Laguarda et al. “Assessment of Reynolds number effects in supersonic turbulent boundary layers”. In: *International Journal of Heat and Fluid Flow* 105 (2024). DOI: 10.1016/j.ijheatfluidflow.2023.109234.

[52] Louis J. Souverein, P.G. Bakker, and Pierre Dupont. "A scaling analysis for turbulent shock-wave/boundary-layer interactions". In: *Journal of Fluid Mechanics* 714 (2013), pp. 505–535. DOI: 10.1017/jfm.2012.495.

[53] Hugo F.S. Lui et al. "Mach number effects on shock-boundary layer interactions over curved surfaces of supersonic turbine cascades". In: *Theoretical and Computational Fluid Dynamics* 38 (4 Aug. 2024), pp. 451–478. ISSN: 14322250. DOI: 10.1007/s00162-024-00712-2.

[54] Y. Yao et al. "The effect of Mach number on unstable disturbances in shock/boundary-layer interactions". In: *Physics of Fluids* 19 (5 2007). DOI: 10.1063/1.2720831.

[55] Erich Schülein, Christian Schnepf, and Sebastian Weiss. "Concave Bump for Impinging-Shock Control in Supersonic Flows". In: *AIAA Journal* 60 (5 2022), pp. 2749–2766. ISSN: 1533385X. DOI: 10.2514/1.J060799.

[56] John D. Anderson. *Fundamentals of aerodynamics.* 1984. ISBN: 9780070016569.

[57] Surya Prakash Baskaran and T. M. Muruganandam. "A study on shock-wave/boundary-layer interaction with varying flow deflection angle". In: *Physics of Fluids* 36 (5 May 2024). ISSN: 10897666. DOI: 10.1063/5.0198982.

[58] Sunyoung Lee and Andreas Gross. "Numerical Investigation of Turbulent Shock-Wave Boundary Layer Interaction for Two Different Shock Strengths". In: American Institute of Aeronautics and Astronautics Inc, AIAA, 2022. ISBN: 9781624106354. DOI: 10.2514/6.2022-3988.

[59] Pierre Dupont, C. Haddad, and Jean François Debiève. "Space and time organization in a shock-induced separated boundary layer". In: *Journal of Fluid Mechanics* 559 (2006), pp. 255–277. DOI: 10.1017/S0022112006000267.

[60] Matteo Bernardini et al. "Heat transfer and wall temperature effects in shock wave turbulent boundary layer interactions". In: *Physical Review Fluids* 1 (8 2016). DOI: 10.1103/PhysRevFluids.1.084403.

[61] M. Cogo et al. "Assessment of heat transfer and Mach number effects on high-speed turbulent boundary layers". In: *Journal of Fluid Mechanics* 974 (2023). DOI: 10.1017/jfm.2023.791.

[62] R. Sriram and G. Jagadeesh. "Shock tunnel experiments on control of shock induced large separation bubble using boundary layer bleed". In: *Aerospace Science and Technology* 36 (2014), pp. 87–93. ISSN: 12709638. DOI: 10.1016/j.ast.2014.04.003.

[63] Bao-hu Zhang, Yu-xin Zhao, and Jun Liu. "Effects of bleed hole size on supersonic boundary layer bleed mass flow rate". In: *Journal of Zhejiang University: Science A* 21 (8 2020), pp. 652–662. DOI: 10.1631/jzus.A1900507.

[64] P.J.K. Bruce and S.P. Colliss. "Review of research into shock control bumps". In: *Shock Waves* 25 (5 2015), pp. 451–471. DOI: 10.1007/s00193-014-0533-4.

[65] Jonathan S. Couldrick et al. "Active control of normal shock wave/turbulent boundary layer interaction using "Smart" piezoelectric flap actuators". In: *2nd AIAA Flow Control Conference* 109 (1101 2004), pp. 577–583. DOI: 10.2514/6.2004-2701.

[66] Jonathan S. Couldrick et al. "Investigation of unswept normal shock wave/turbulent-boundary-layer interaction control". In: *Journal of Aircraft* 46 (5 2009), pp. 1634–1641. ISSN: 15333868. DOI: 10.2514/1.42104.

[67] Nathan Webb, C. Clifford, and M. Samimy. "Control of oblique shock wave/boundary layer interactions using plasma actuators". In: *Experiments in Fluids* 54 (6 June 2013). ISSN: 07234864. DOI: 10.1007/s00348-013-1545-z.

[68] Guoqing Zhao, Qijun Zhao, and Xi Chen. "Wind-tunnel tests of synthetic jet control effects on airfoil flow separation". In: *Scientific Reports* 12 (1 Dec. 2022). ISSN: 20452322. DOI: 10.1038/s41598-022-19642-2.

[69] Zhijie Zhao et al. "Effects of dual synthetic jets on longitudinal aerodynamic characteristics of a flying wing layout". In: *Aerospace Science and Technology* 132 (Jan. 2023). ISSN: 12709638. DOI: 10.1016/j.ast.2022.108043.

[70] Wei Yi Su, Xin Yu Chang, and Kun Yuan Zhang. "Effects of magnetohydrodynamic interaction-zone position on shock-wave/boundary-layer interaction". In: *Journal of Propulsion and Power* 26 (5 2010), pp. 1053–1058. ISSN: 15333876. DOI: 10.2514/1.49838.

[71] Deepak Prem Ramaswamy and Anne Marie Schreyer. "Control of shock-induced separation of a turbulent boundary layer using air-jet vortex generators". In: *AIAA Journal* 59 (3 2021), pp. 927–939. ISSN: 1533385X. DOI: 10.2514/1.J059674.

[72] J.C. Lin. "Review of research on low-profile vortex generators to control boundary-layer separation". In: *Progress in Aerospace Sciences* 38 (4-5 2002), pp. 389–420. DOI: 10.1016/S0376-0421(02)00010-6.

[73] Luis Laguarda et al. "Shock-wave/turbulent boundary-layer interaction over a flexible panel". In: American Institute of Aeronautics and Astronautics Inc, AIAA, 2023. ISBN: 9781624107047. DOI: 10.2514/6.2023-3884.

[74] Venkateswaran Narayanaswamy, Laxminarayan L. Raja, and Noel T. Clemens. "Characterization of a high-frequency pulsed-plasma jet actuator for supersonic flow control". In: *AIAA Journal* 48 (2 Feb. 2010), pp. 297–305. ISSN: 00011452. DOI: 10.2514/1.41352.

[75] Stefan Hickel, Nikolaus A. Adams, and J. Andrzej Domaradzki. "An adaptive local deconvolution method for implicit LES". In: *Journal of Computational Physics* 213 (1 Mar. 2006), pp. 413–436. ISSN: 10902716. DOI: 10.1016/j.jcp.2005.08.017.

[76] Stefan Hickel, Christian P. Egerer, and Johan Larsson. "Subgrid-scale modeling for implicit large eddy simulation of compressible flows and shock-turbulence interaction". In: *Physics of Fluids* 26 (10 Oct. 2014), p. 106101. ISSN: 10897666. DOI: 10.1063/1.4898641.

[77] Stefan Hickel. *Welcome to the world of Inca!* URL: https://www.inca-cfd.com/.

[78] *Delft High Performance Computing Centre (DHPC)*. 2024. URL: https://www.tudelft.nl/dhpc/ark:/44463/DelftBluePhase2.

[79] Luis Laguarda and Stefan Hickel. "Analysis of improved digital filter inflow generation methods for compressible turbulent boundary layers". In: *Computers and Fluids* 268 (2024). DOI: 10.1016/j.compfluid.2023.106105.

[80] Haohua Zong and Marios Kotsonis. "Characterisation of plasma synthetic jet actuators in quiescent flow". In: *Journal of Physics D: Applied Physics* 49 (33 July 2016). ISSN: 13616463. DOI: 10.1088/0022-3727/49/33/335202.

[81] Sarah H. Popkin, Trent M. Taylor, and Bohdan Z. Cybyk. "Development and application of the Sparkjet actuator for high-speed flow control". In: *Johns Hopkins APL Technical Digest (Applied Physics Laboratory)* 32 (1 2013), pp. 404–418.

[82] Hao hua Zong et al. "Analytic model and frequency characteristics of plasma synthetic jet actuator". In: *Physics of Fluids* 27 (2 Feb. 2015). ISSN: 10897666. DOI: 10.1063/1.4908071.

[83] H. Zong et al. "Plasma synthetic jet actuators for active flow control". In: *Actuators* 7 (4 2018). DOI: 10.3390/act7040077.

[84] Luis Laguarda et al. "Reynolds number effects in shock-wave/turbulent boundary-layer interactions". In: *Journal of Fluid Mechanics* 989 (2024). DOI: 10.1017/jfm.2024.361.

[85] H. Xu et al. "Influences of microjet pressure and number of microjets on the control of shock wave/boundary layer interaction". In: *Aerospace Science and Technology* 138 (2023). DOI: 10.1016/j.ast.2023.108345.

[86] Edgar Caraballo et al. "Supersonic inlet flow control using plasma actuators". In: 2009. DOI: 10.2514/6.2009-924.

[87] Peter D Welch. "The Use of Fast Fourier Transform for the Estimation of Power Spectra: A Method Based on Time Averaging Over Short, Modified Periodograms". In: *IEEE Transactions on Audio and Electroacoustics* 15 (2 1967), pp. 70–73. DOI: 10.1109/TAU.1967.1161901.

A

Data Analysis

This section will discuss how data obtained from simulations has been analyzed. The data analysis script used has been the same for every simulation. The order of this section is similar to that of the script. It will first discuss how data obtained from the simulations is non-dimensionalized, then it will discuss the statistics followed by the analysis of snapshots.

The software version control is done both within scripts as well as via GitHub. For a more detail explanation see Appendix B.

A.1. Non-Dimensionalization

The data of the different simulations has been normalized so that the comparison between simulations in this project, literature and experimental data is valid without having to make conversions. The normalization is based on the statistics data for the case where control has not been applied which is discussed in more detail in section A.2.

All spatial data is normalized by the δ_0, which is computed by finding the height where the value of the stream-wise velocity component of the boundary layer is 0.99 u_∞. In Figure A.1 the boundary layer profile is shown which is used to compute the δ_0 which in this case is 6.0183 mm. This non-dimensionalization is mainly used when referencing dimensions of the domain.

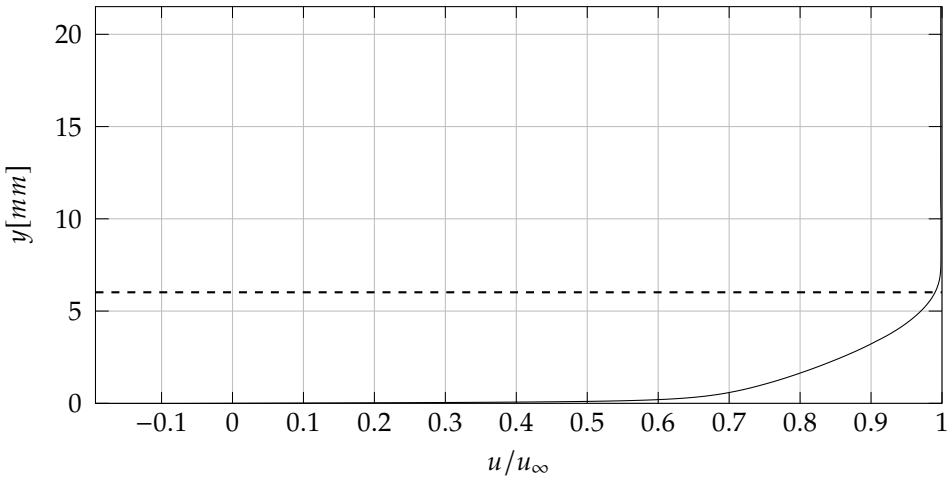


Figure A.1: Statistical boundary layer profile for reference production case. $0.99u_\infty$is indicated by **- - -**.

When figures are show the steamwise domain length, the domain is normalized by x_{imp}, making the results of different studies comparable irrespective of the domain size used. The resulting normalization

is as given in Equation A.1.

$$(x - x_{imp})/\delta_0 \tag{A.1}$$

Temporal data is also non-dimensionalized using δ_0 by Equation A.2.

$$\frac{(t - t_0)u_\infty}{\delta_0} \tag{A.2}$$

In which t is the simulation time and t_0 is the moment at which the gathering of snapshots and statistics starts, in the simulations for this research the scale of t is in milliseconds. t_0 in this study is 7 milliseconds.

Spectral dimensions will be normalized by the St_L number given by equation Equation A.3.

$$St_L = \frac{fL_{Sep}}{u_\infty} \tag{A.3}$$

Where f is the characteristic frequency, in this case the frequency obtained from the computation of the PSD of L_{sep} of the reference case which will be discussed in subsection A.3.1.

As mentioned previously in chapter 1, the Reynolds number has a significant influence on SWBLI and it is computed using Equation A.4.

$$Re = \frac{uL}{\nu} = \frac{\rho uL}{\mu} \tag{A.4}$$

A.2. Statistics

The simulation provides several outputs as discussed in section 2.7. Among these is the statistical data which is gathered and a running average is computed for every time step. It can also be set to compute the span-wise average which was used in the simulations. Thus the statistics data provides the temporal and span-wise averages for selected variables such as the u, v and w. Reynolds decomposition can be used for each of these variables as done in Equation A.5.

$$u = \langle u \rangle + u' \tag{A.5}$$

Where u is an instantaneous value, $\langle u \rangle$ is the temporally averaged value u' is the deviation from $\langle u \rangle$, also known as fluctuations. The statistics obtained from INCA are temporally averaged variables thus for u, v and w these are $\langle u \rangle$, $\langle v \rangle$ and $\langle w \rangle$. These velocity flow fields as shown in Figure A.2.

The Görtler number, computed using Equation A.6 is used to check for the possibility of the presence of Görtler vortices.

$$G_t = \frac{\theta^{\frac{3}{2}}}{0.18\delta^*|R|^2} \tag{A.6}$$

In which δ^* is boundary layer displacement, θ is boundary layer momentum and R is the radius of the curvature of the streamline. Which can be computed with Equation A.7, Equation A.8 and Equation A.9 respectively.

$$\delta^* = \int_0^{\delta_0} \left(1 - \frac{\rho u}{\rho_\infty u_\infty}\right) dy \tag{A.7}$$

$$\theta = \int_0^{\delta_0} \frac{\rho u}{\rho_\infty u_\infty} \left(1 - \frac{u}{u_\infty}\right) dy \tag{A.8}$$

$$R = \frac{\left(1 + \frac{dy}{dx}^2\right)^{\frac{3}{2}}}{\frac{d^2y}{dx^2}} \tag{A.9}$$

θ and δ^*, are also used in the determination of the shape factor (H) as given in Equation A.10.

$$H_{12} = \frac{\delta^*}{\theta} \tag{A.10}$$

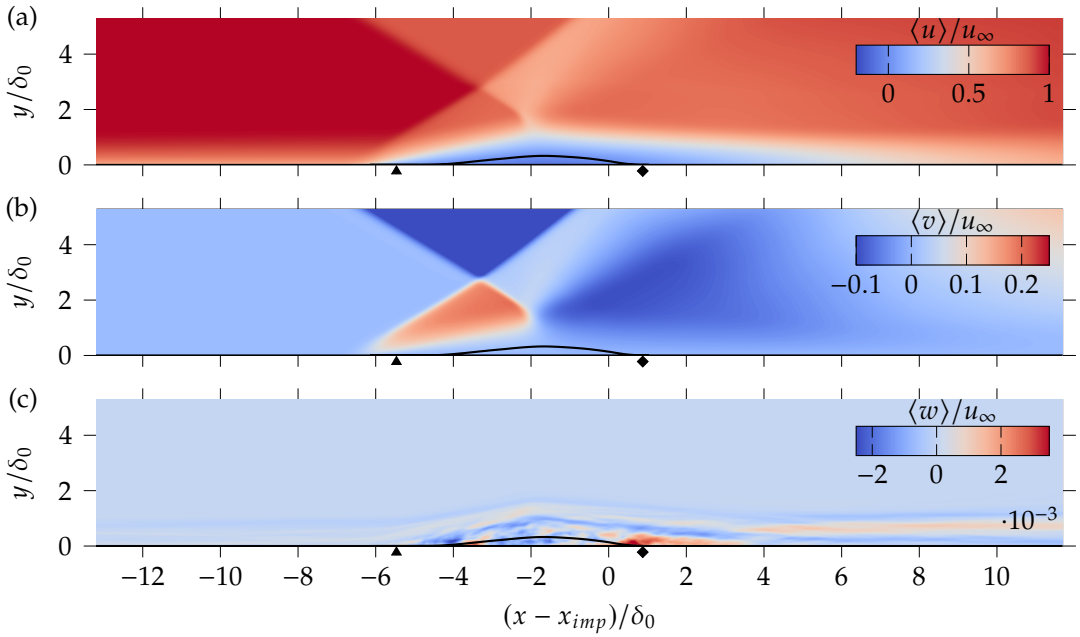


Figure A.2: Time- and spanwise-averaged velocity fields: (a) $\langle u \rangle$, (b) $\langle v \rangle$ and (c) $\langle w \rangle$. The solid black line indicates the statistical isocontour of $u = 0$.The statistical separation and reattachment points are indicated by ▲ and ◆ respectively.

Using the u and v from Figure A.2a-b allows for the computation of a streamline. Selecting a point above the wall, in this case at $y = 0.125\ \delta_0$ and then using the 4^{th} order Runge-Kutta method to obtain the x and y coordinates, which will then be used to find u and v at this location, allowing for the computation of the next point. By interpolating the resulting streamline, the radius of the curvature can be computed using Equation A.9.

The statistical data also provides the double correlations such as $\langle uu \rangle$, $\langle vv \rangle$ and $\langle ww \rangle$ from which the Reynolds stresses: $u'u'$, $v'v'$ and $w'w'$, can be computed using Equation A.11.

$$\langle u'u' \rangle = \langle uu \rangle - \langle u \rangle \langle u \rangle \tag{A.11}$$

In Equation A.11 v or w can be substituted for u to obtain the other Reynolds stresses or cross stresses. Equation A.12 is used to compute the RMS of the fluctuations, the results of this are shown in Figure A.5.

$$\langle u'u' \rangle_{RMS} = \sqrt{\langle u'u' \rangle} \tag{A.12}$$

The T, ρ and p fields as shown in Figure A.3a-c respectively. These statistical fields are mainly used for the visualization of shocks, while instantaneous fields show more.

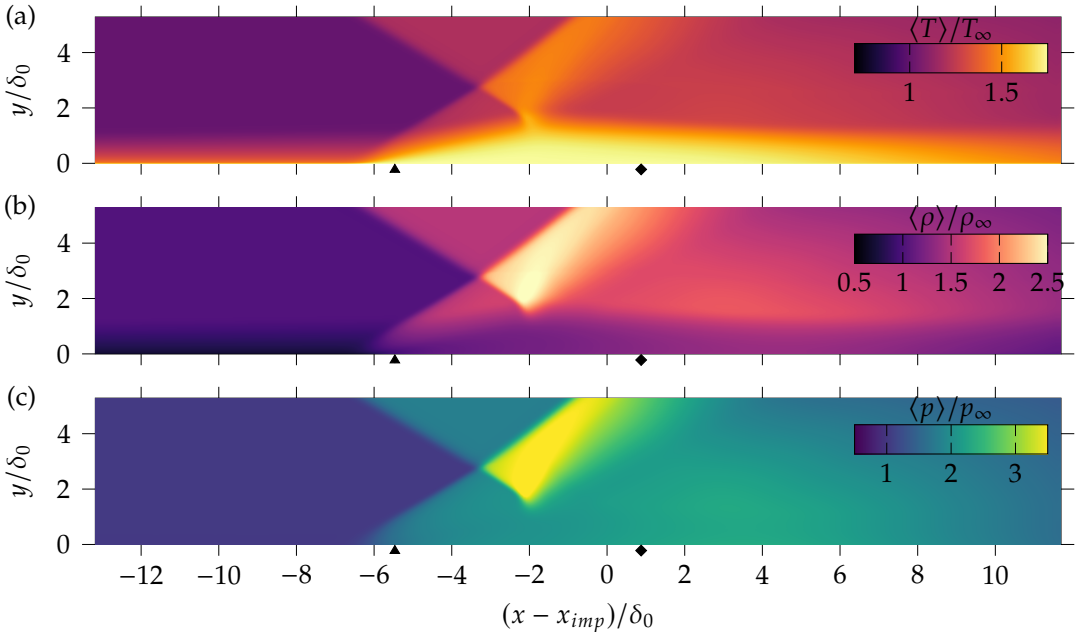


Figure A.3: Time- and spanwise-averaged flow fields: (a) $\langle T\rangle$ (b) $\langle\rho\rangle$ and (c) $\langle p\rangle$. The solid black line indicates the statistical isocontour of $u = 0$.The statistical separation and reattachment points are indicated by ▲ and ◆ respectively.

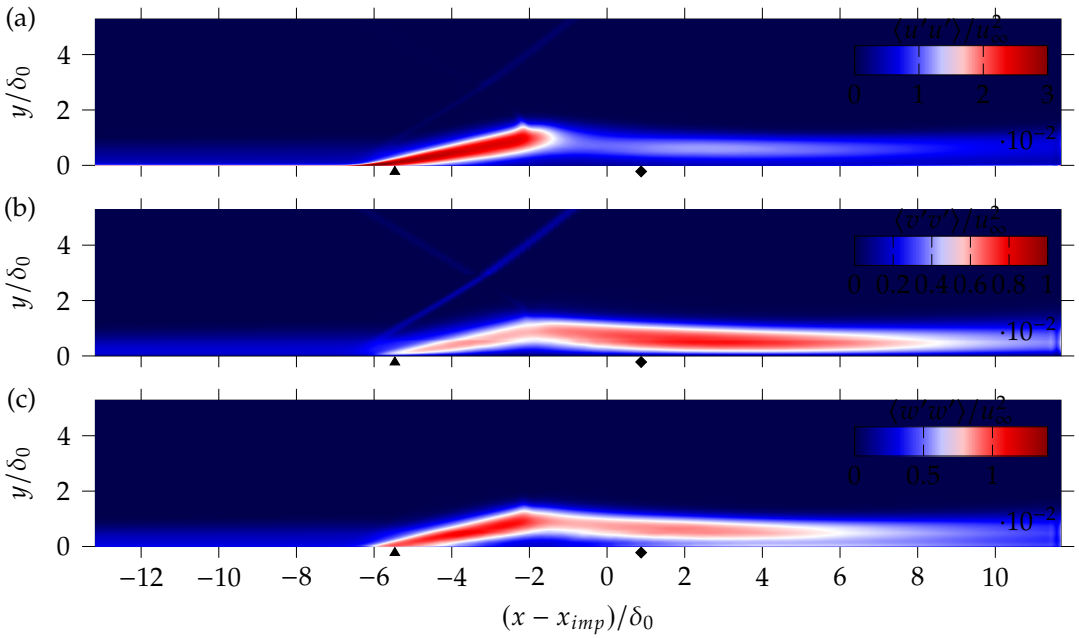


Figure A.4: Time- and spanwise-averaged Reynolds stresses: (a) $\langle u'u'\rangle$, (b) $\langle v'v'\rangle$, (c) $\langle w'w'\rangle$. The solid black line indicates the statistical isocontour of $u = 0$.The statistical separation and reattachment points are indicated by ▲ and ◆ respectively.

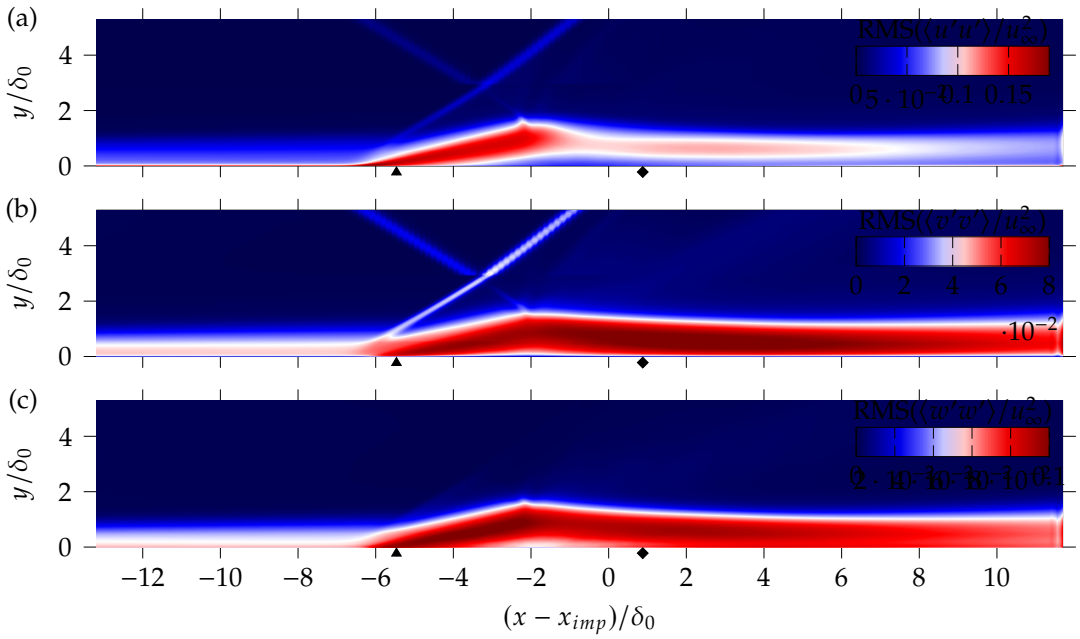


Figure A.5: RMS of the time- and spanwise-averaged velocity fluctuations: (a) $\sqrt{\langle u'u' \rangle}$, (b) $\sqrt{\langle v'v' \rangle}$, (c) $\sqrt{\langle w'w' \rangle}$ The solid black line indicates the statistical isocontour of $u = 0$.The statistical separation and reattachment points are indicated by ▲ and ◆ respectively.

A.3. Instantaneous

This section will discuss how the snapshots obtained from INCA are analyzed, how the different physical aspects of the separation bubble are determined and how the evolution of these physical aspects over time can be analyzed in a spectral manner all to gather a comprehensive picture of the bubble behavior.

A.3.1. Spatial Characteristics Analysis

The analysis of the physical attributes of the separation bubble mainly relies on the analysis of the stream-wise velocity field, u. In contrast to the statistics data, the data obtained from snapshots is instantaneous an example of this is given in Figure A.6 which shows the three velocity components, u, v and w, of a snapshot.

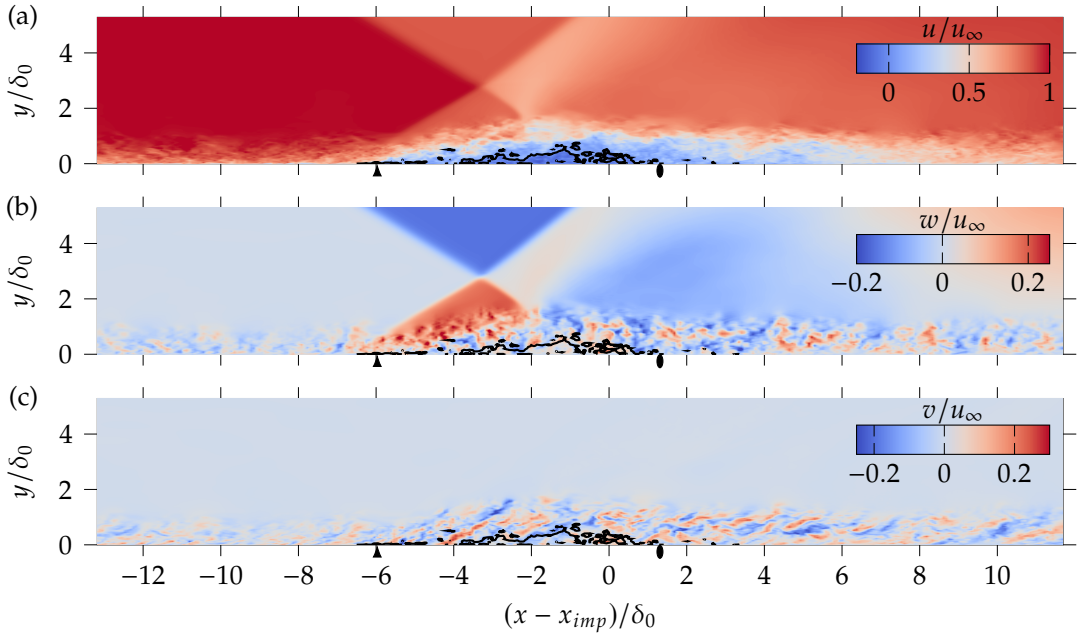


Figure A.6: Instantaneous span-wise velocity fields normalized by u_∞: (a) u, (b) v and (c) w. The solid black line indicates the instantaneous isocontour of $u = 0$.The instantaneous separation and reattachment points are indicated by ▲ and ⬮ respectively.

The instantaneous velocity at the wall is shown in Figure A.7. The instantaneous pressure at the wall is shown in Figure A.9.

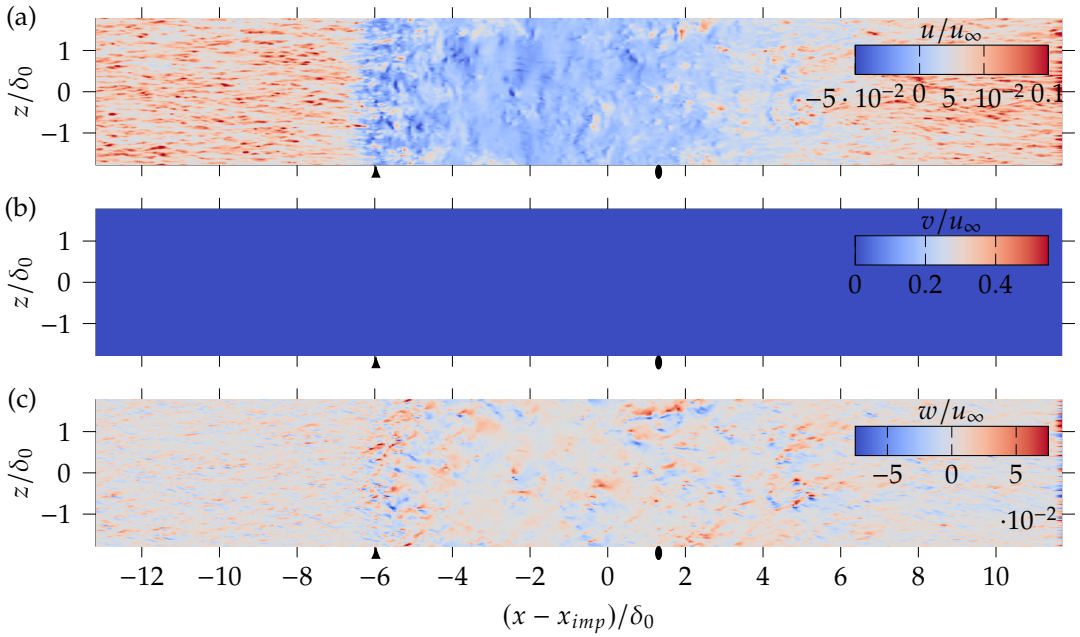


Figure A.7: Instantaneous wall velocity fields normalized by u_∞: (a) u, (b) v and (c) w. The solid black line indicates the instantaneous isocontour of $u = 0$.The instantaneous separation and reattachment points are indicated by ▲ and ⬮ respectively.

A.3.2. Vorticity

The grid size is used to take obtain the spatial derivatives for all three velocity components. Using a central difference scheme. This gives 9 derivatives.

The vorticity vector ($\vec{\omega}$) given in Equation A.13 is composed of three vorticity components: the ω_x, the wall-normal vorticity component (ω_y) and spanwise vorticity component (ω_z).

$$\vec{\omega} = \begin{pmatrix} \omega_x \\ \omega_y \\ \omega_z \end{pmatrix} \tag{A.13}$$

These three components are computed using Equations (A.14) to (A.16).

$$\omega_x = \left(\frac{\partial w}{\partial y} - \frac{\partial v}{\partial z} \right) \tag{A.14}$$

$$\omega_y = \left(\frac{\partial u}{\partial z} - \frac{\partial w}{\partial x} \right) \tag{A.15}$$

$$\omega_z = \left(\frac{\partial v}{\partial x} - \frac{\partial u}{\partial y} \right) \tag{A.16}$$

Equations (A.14) to (A.16) are used to compute the vorticity magnitude ($|\omega|$).

$$|\vec{\omega}| = \sqrt{\omega_x^2 + \omega_y^2 + \omega_z^2} \tag{A.17}$$

The spatial derivatives are also used to compute the Q-criterion using Equation A.18.

$$Q = 0.5 \left(\frac{\partial u}{\partial x}\frac{\partial u}{\partial x} + \frac{\partial v}{\partial x}\frac{\partial u}{\partial y} + \frac{\partial w}{\partial x}\frac{\partial u}{\partial z} + \frac{\partial u}{\partial y}\frac{\partial v}{\partial x} + \frac{\partial v}{\partial y}\frac{\partial v}{\partial y} + \frac{\partial w}{\partial y}\frac{\partial v}{\partial z} + \frac{\partial u}{\partial z}\frac{\partial w}{\partial x} + \frac{\partial v}{\partial z}\frac{\partial w}{\partial y} + \frac{\partial w}{\partial z}\frac{\partial w}{\partial z} \right) \tag{A.18}$$

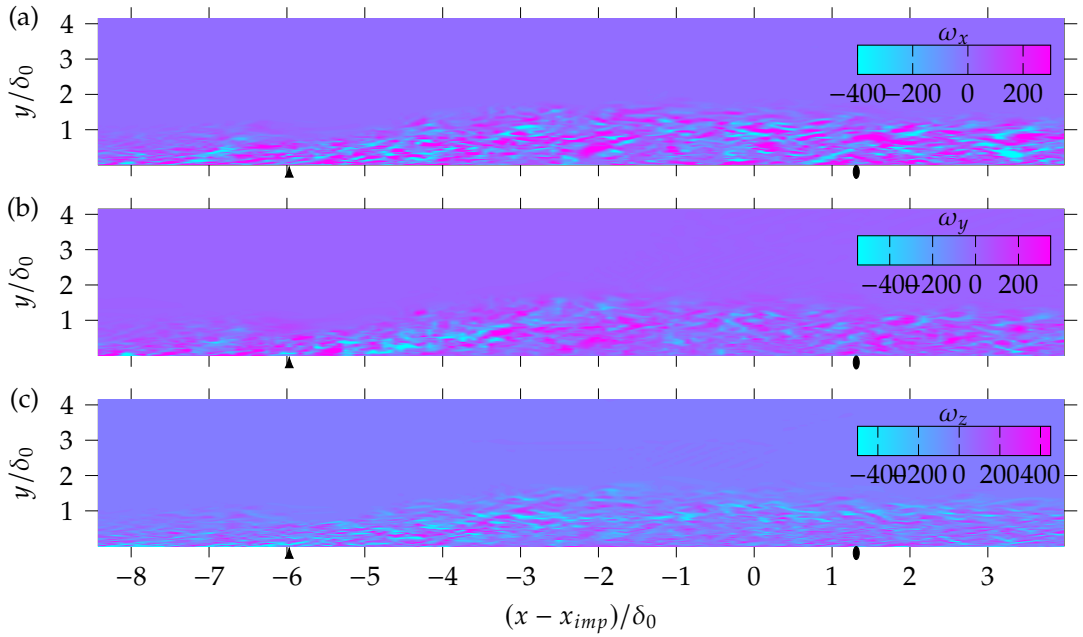


Figure A.8: Instantaneous span-wise vorticity fields in the middle of the domain: (a) ω_x, (b) ω_y and (c) ω_z. The solid black line indicates the instantaneous isocontour of $u = 0$.The instantaneous separation and reattachment points are indicated by ▲ and ⬮ respectively.

A.3.3. Pressure and Temperature

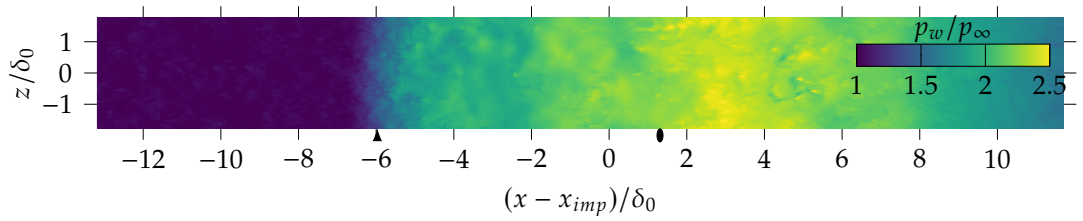


Figure A.9: Instantaneous normalized wall pressure at the wall. The instantaneous separation and reattachment points are indicated by ▲ and ⬮ respectively.

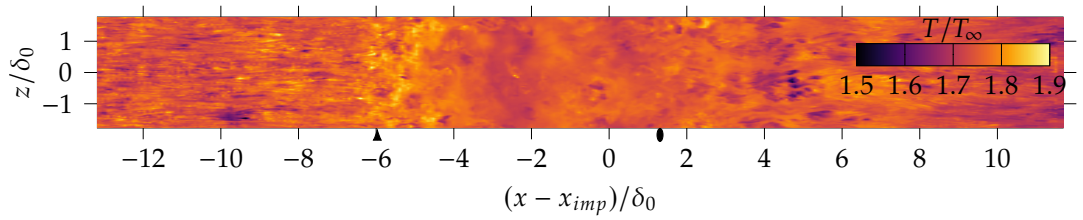


Figure A.10: Instantaneous normalized wall temperature at the wall. The instantaneous separation and reattachment points are indicated by ▲ and ⬮ respectively.

In Figure A.9 and Figure A.10 the point of separation can be observed quite easily. In Figure A.9 there is a sharp rise in the pressure and in Figure A.10 there is a sharp increase in the temperature. The point of reattachment is much harder to obtain, especially from the wall temperature. Additionally neither of these can be used to define the exact point of separation. In order to do this the velocity is needed.

A.3.4. Skin Friction

Of the three fields in Figure A.6, u from Figure A.6a,is used in the computation of the x_{sep} and x_{rea}. Separation is defined as the region in which C_f is negative. By definition the x_{sep} is the first occurrence of negative skin-friction and the x_{rea} is the last occurrence, even it the skin-friction coefficient becomes

positive in between these two locations. C_f is computed using Equation A.19.

$$C_f = \frac{\tau_w}{\frac{1}{2}\rho u_\infty} \tag{A.19}$$

In which τ_w is the wall shear stress which is computed using Equation A.20.

$$\tau_w = \mu \frac{\partial u}{\partial y}\bigg|_{y=0} \tag{A.20}$$

In which μ is the dynamic viscosity and $\frac{\partial u}{\partial y}\Big|_{y=0}$ is the gradient of the flow velocity towards the wall, evaluated at the wall. Since the simulation has a grid which possibly overlaps the wall, $y = 0$ does not necessarily exist at an exact cell center therefore the wall shear stress is computed by dividing the stream-wise velocity one cell above the wall by the cell center height.

Computing the C_f for all the cells above the wall for a single snapshot results in Figure A.11a. Computing the span-wise average C_f for every snapshot and averaging this gives Figure A.11b. As statistics data is span-wise averaged, a figure similar to Figure A.11b can be obtained from the statistics data, however Figure A.11a can not be obtained. Which is why the statistical separation and reattachment locations are computed from a figure similar to Figure A.11b. However because the bubble front is highly corrugated, the separation and reattachment points are computed for each streamwise row of cells first and these are then spanwise averaged. These values are used for further analysis.

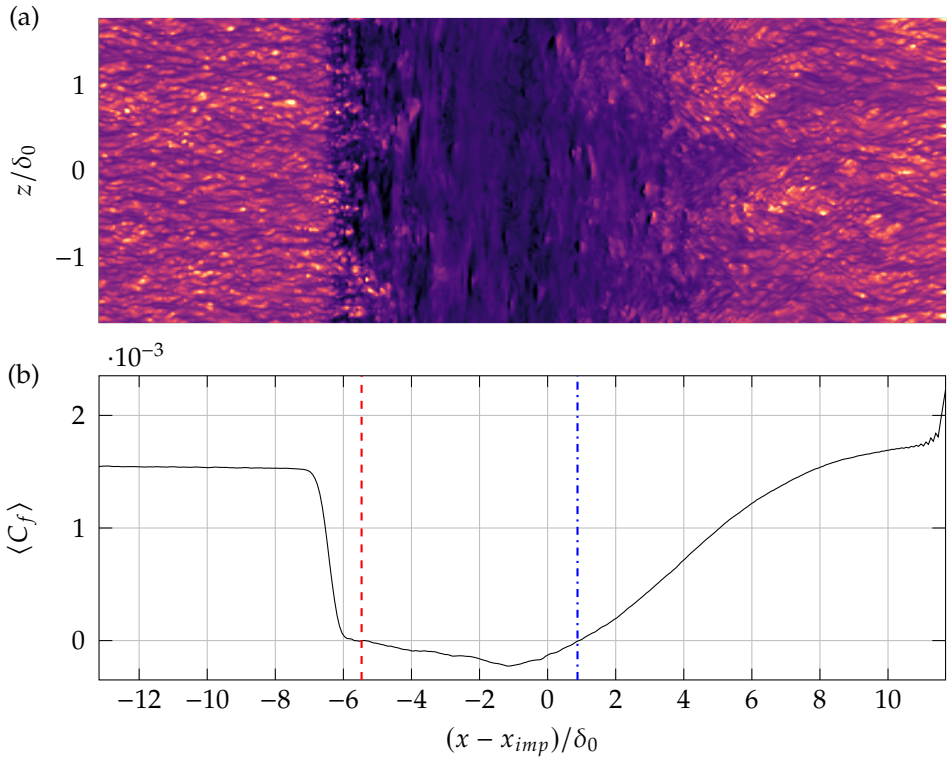


Figure A.11: Instantaneous skin friction computation. (a) Snapshot of C_f where the instantaneous, span-wise averaged and statistical separation and reattachment locations are indicated. (b) Span-wise averaged C_f. The statistical separation and reattachment points are indicated by - - - and -·-·- respectively.

After obtaining x_{sep} and x_{rea} from Figure A.11, L_{sep} can be computed using Equation A.21.

$$L_{sep} = x_{rea} - x_{sep} \tag{A.21}$$

The H_{sep} is obtained from the height of the highest cell center above the wall for which the span-wise averaged, stream-wise velocity component is negative. The V_{sep} is obtained by summation of all the

cell volumes of which u is negative. This summation is divided by the span-wise length of the domain to make the value irrespective of the domain size. For the statistics, which are only two dimensional, the volume is computed using the first cell of the grid and multiplying this by the number of cells in the span-wise direction before dividing this by the span-wise length of the domain. This does mean that there is a difference between the snapshots and statistics which is that the snapshot volumes are instantaneous take into account every single cell while the statistics show a span-wise averaged result.

L_{sep} is diveded by H_{sep} and V_{sep} is divided by the L_{sep} as is done in Equation A.22 and Equation A.23 to obtain the ASR and Volumetric Ratio (VR) respectively.

$$ASR = \frac{L_{sep}}{H_{sep}} \tag{A.22}$$

$$VR = \frac{V_{sep}}{L_{sep}} \tag{A.23}$$

The x_a is defined as the highest point of the separation bubble. The distance that measuring from the start of the separation bubble up to x_a is separation to apex length (L_a). The volume of the bubble from the separation point up to the apex point is bubble volume before the apex point (V_a). These three values are used to gage the symmetry of the separation bubble.

The computation of the S_x and the η is done using the p fields rather than the velocity fields because shocks better detectable in pressure fields than velocity fields. Figure A.12 shows an instantaneous p field which is still quite noisy, the noise can be significantly reduced by spanwise averaging the results as done for Figure A.13.

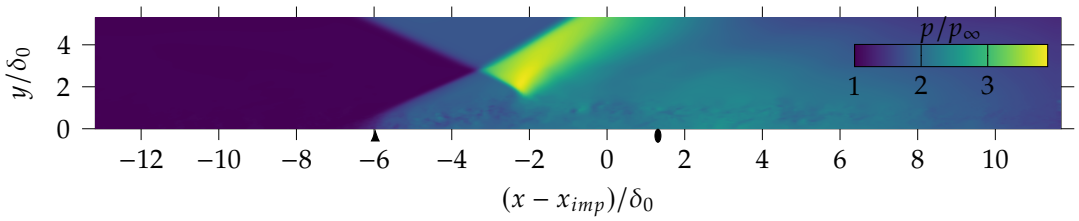


Figure A.12: Instantaneous pressure field.

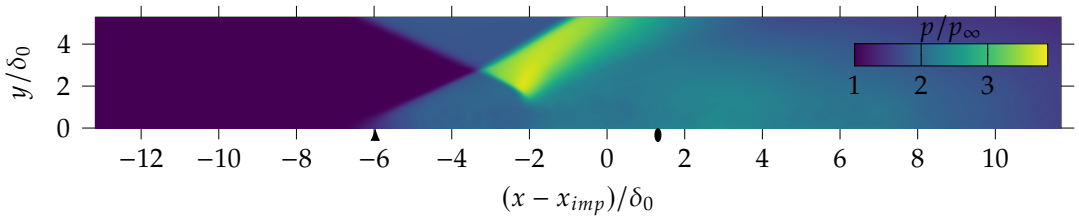


Figure A.13: Instantaneous span-wise averaged pressure field.

The spanwise averaged pressure field in Figure A.13 is then used to compute pressure gradient (∇p), the result of which is given in Figure A.14. From the obtained ∇p, the isocontours can be computed by selecting a pressure gradient ratio. As a shock wave, by definition, has a significant pressure gradient, they stand out against other possibly present pressure fluctuations. For each shock a separate smaller domain is created so that only the desired shock is found. For the impinging shock, which is computed first, this domain is relatively stable. As the impinging shock is created by a wedge, the location of this shock is relatively stable and therefore easy to recognize. Secondly the separation shock after interaction is identified in the region after the separation. As this shock is also relatively stable, the domain where it should appear can be set with little trail and error. The impinging shock and separation shock after interaction are used to compute a point of intersection which is used to create a smaller domain in which the separation shock is obtained, from which the angle is computed with respect to the wall

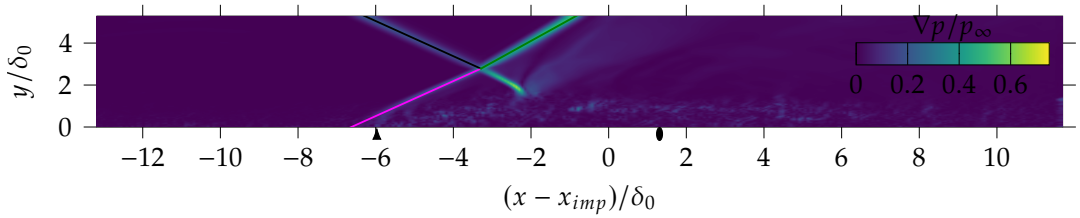


Figure A.14: Instantaneous span-wise averaged pressure gradient where —— indicates the impinging shock, —— indicates the separation shock after interaction and —— indicates the separation shock

which gives η. The location where the shock would intersect with the wall is also computed which gives S_x. Together these values give a general idea of the shock motion, however this method is not precise, especially not on a coarse grid as used in the parametric study results.

Finally the instantaneous field of the T is shown in Figure A.15. This field could provide additional information on the internal mechanisms of the control method.

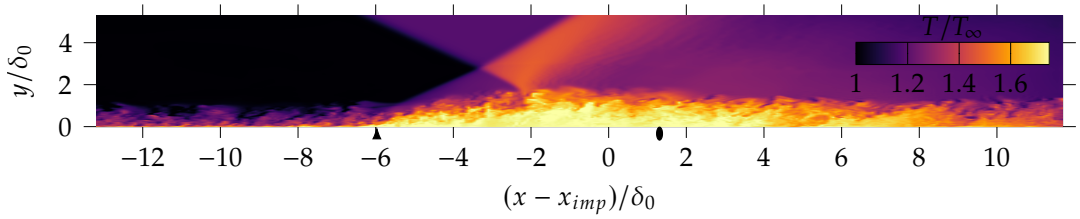


Figure A.15: Instantaneous T field.

Now all the values; x_{sep}, x_{rea}, L_{sep}, H_{sep}, V_{sep}, ASR, S_x and η are computed for every snapshot. As the snapshot data also includes the simulation time, the movement of the bubble can be plotted as a time series as shown in Figure A.16. From this figure several things are clear, there is much more variance in the x_{rea} than x_{sep}, which will be discussed further in subsection A.4.2. x_{sep}, x_{rea}, by extension L_{sep} and η seem to be moving at a higher frequency than V_{sep}, while S_x is moving in a slow motion with a significant amount of small fluctuations This will be further substantiated in subsection A.4.1.

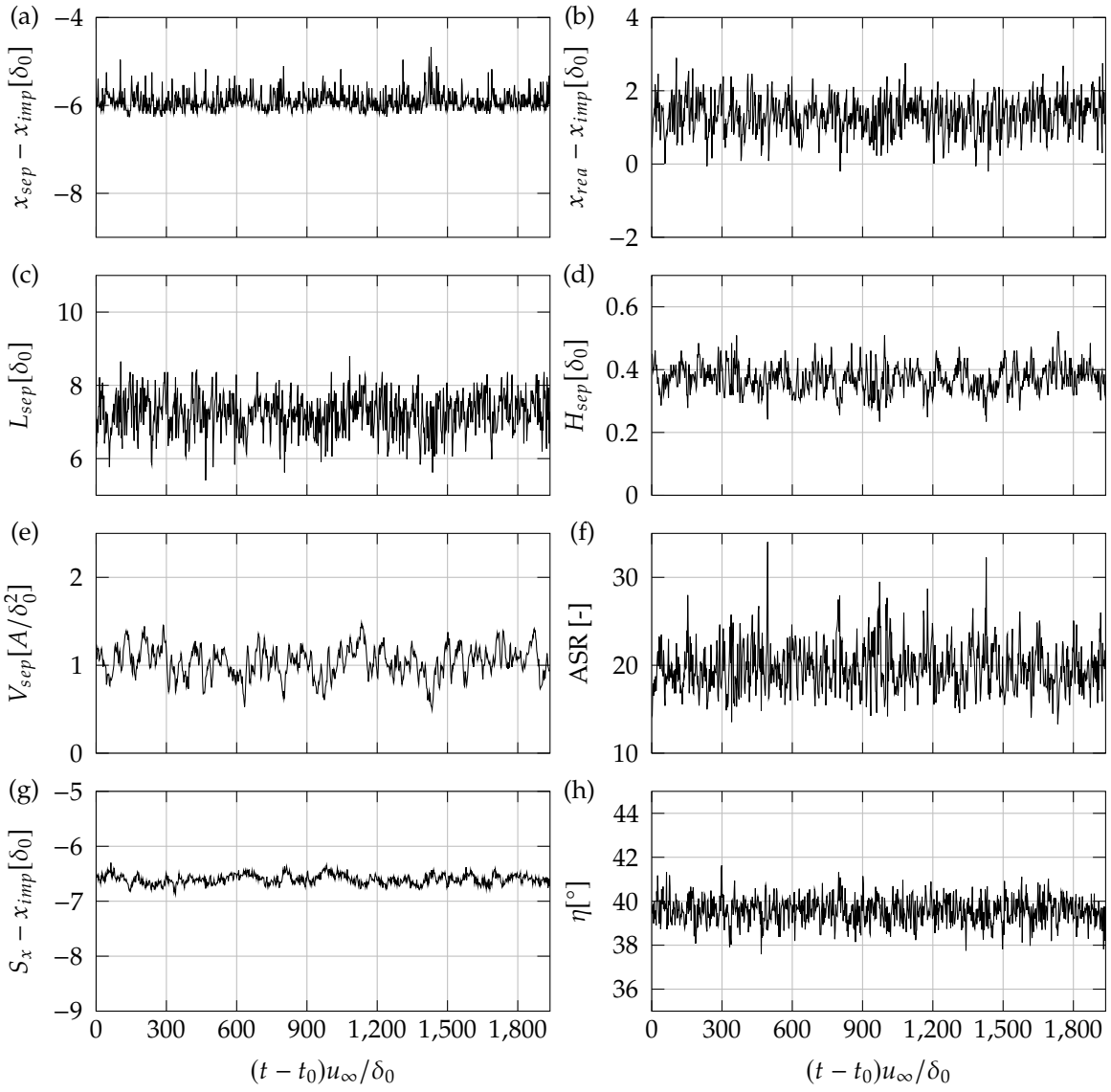


Figure A.16: Bubble motion for the Reference case: (a) x_{sep}, (b) x_{rea}, (c) L_{sep}, (d) H_{sep}, (e) V_{sep}, (f) ASR, (g) S_x and (h) η. **Add Averages back in**

A.4. Spectral Characteristics Analysis

For the analysis of the spectral characteristics several analysis techniques are used. First the usage of PSDs is discussed which give better insight into the the prominence of certain frequencies of the bubble motion. Secondly the variance of the bubble motion is investigated using PDFs. Finally a DMD analysis will be given which will provide insight into different motion scales of the flow.

A.4.1. Power Spectral Density

Signal analysis using Power Spectral Density (PSD) spectra is a commonly used technique in unsteady flow phenomena. It reperesents the power per unit frequency for a given signal, which can be used to obtain information on the dominant frequencies of a complex signal. The PSD spectra in this research are computed using Welch's algorithm [87], with 8 Hamming windows and a 70% overlap.

Computing the PSDs for the bubble motion signals is done using the following method. Firstly the time series or signal is divided into overlapping segments of length N. Each of these segments is multiplied with a windowing function $w(n)$. The discrete Fourier Transform is then computed for each windowed segment using Equation A.24.

$$X_k(m) = \sum_{n=0}^{N-1} x_m(n) w(n) e^{-j2\pi kn/N}, \quad k = 0, 1, \ldots, N-1. \tag{A.24}$$

The power spectrum per window segment (P_m) is then computed with .

$$P_m(f) = \frac{1}{U} |X_k(m)|^2 \tag{A.25}$$

Where U, given by Equation A.26, is the normalization factor for a window function's energy.

$$U = \sum_{n=0}^{N-1} w^2(n). \tag{A.26}$$

The final PSD estimate is obtained by averaging over the number of segments M using Equation A.27.

$$\mathcal{P}_{xx}(f) = \frac{1}{M} \sum_{m=1}^{M} P_m(f). \tag{A.27}$$

The results of using this method on the signals of the bubble motion are given in Figure A.17.

The reason peak of the PSD do not always align perfectly with the actuator frequency or a harmonic of the frequency is the number of windows used. Currently the number is 8, but if this is decreased to 4, they do align. Doubling the number of segments to 16 gives shorter segments and thus reduces the frequency resolution, this does filter out more noise, yet some spectral features are lost. Increasing the overlap comes with a higher computational cost but is better at reducing variance, but this is a reduced benefit system, where increasing the overlap is not linearly scaled with the increased reduction of variance.

The computation of the PSD for the time series of the bubble motion, allows for the identification of dominant and energetic frequencies. As previously mentioned in subsection A.3.1, the different signals of the bubble motion shown in Figure A.16 seem to have different frequencies of motion and this is confirmed by Figure A.17. Both the x_{sep} and x_{rea} signals do not show a pronounced peak in the low-frequency domain. For the V_{sep} and S_x there is a clear peak at just above 0.03 St_L. This same peak can also be observed in a diminished form for H_{sep}. For L_{sep}, ASR and η there is a peak at just above 0.05 St_L.

Pasquariello et al. [9] shows a method of integrating the power of a PSD signal while their method is applied to wall-pressure fluctuations, this same method can be used to separate the contribution of low-, mid- and high-frequencies of a certain power spectrum. The Integrated PSD power per frequency range (IPPR) for a certain variable can be obtained using Equation A.28.

$$IPPR = \int_{f_1}^{f_2} f \cdot \mathcal{P}(f) df \tag{A.28}$$

Where f_1 and f_2 are the lower and upper frequency bounds of the range respectively and $P(f)$ the PSD power of a given signal. The results of integrating all the powers in the different ranges, which are given in Table A.1, are given in Figure A.18. This shows the what frequency range is more dominant for certain bubble characteristics.

$$E^2_{f_1-f_2} = \int_{f_1}^{f_2} f \cdot \mathcal{PSD}(f) d(log f) \tag{A.29}$$

The computation of the PSD also allows for the computation coherence coherence between two PSD signals (C_{xy}), which is a measure of correlation between two signals across their frequency spectra.

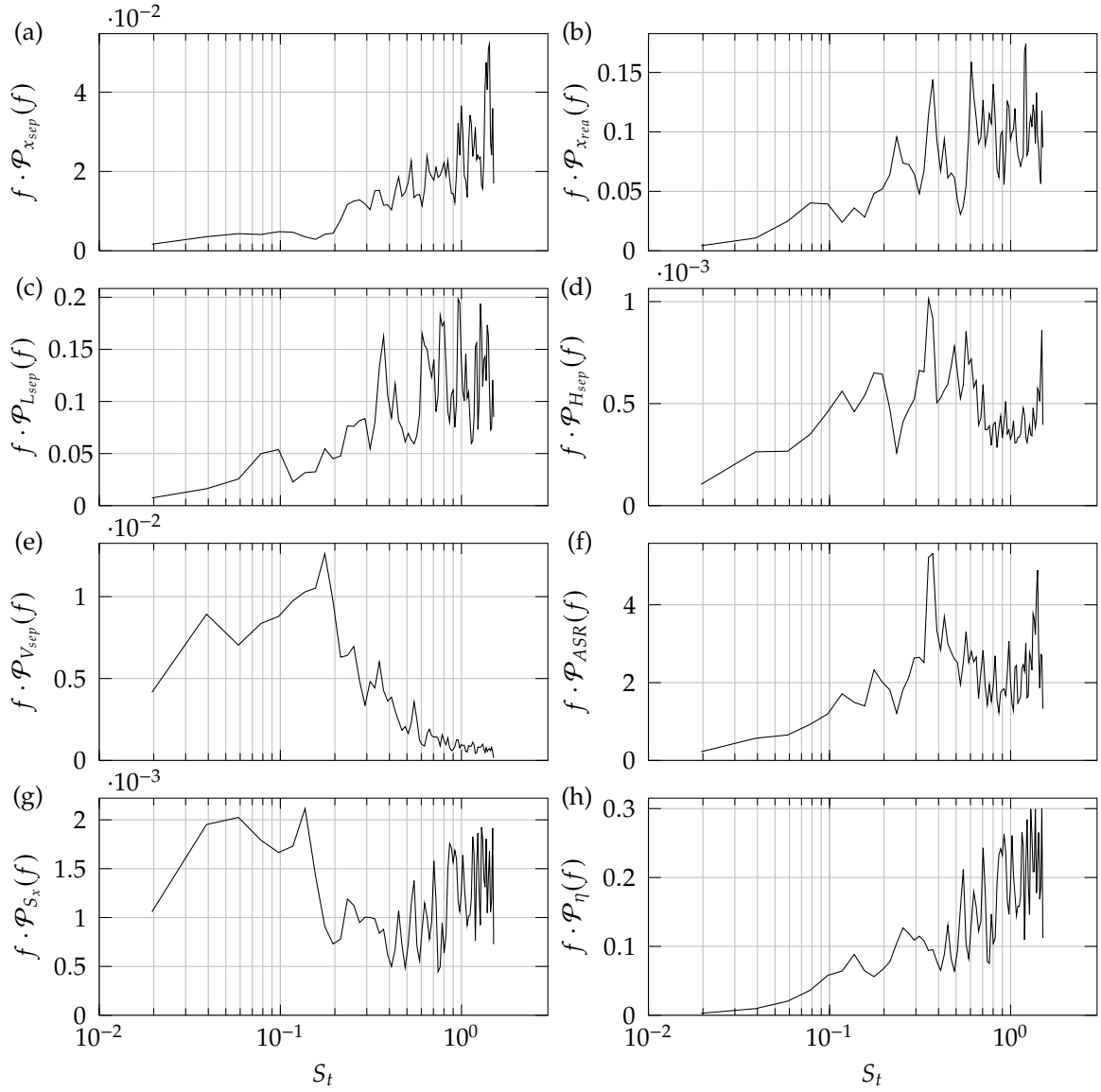


Figure A.17: PSDs of the production reference case motions of: (a) x_{sep}, (b) x_{rea}, (c) L_{sep}, (d) H_{sep}, (e) V_{sep}, (f) ASR, (g) S_x and (h) η.

Table A.1: Production frequency ranges.

Range	Frequencies
Low	$St_L < 0.1$
Mid	$0.1 \leq St_L \leq 1.0$
High	$1.0 < St_L$

So two signals might be closely correlated at specific frequencies and not correlate at all at others. Coherence is calculated using Equation A.30.

$$C_{xy}(f) = \frac{|P_{xy}(f)|^2}{P_{xx}(f)P_{yy}(f)}, 0 \leq C_{xy} \leq 1 \tag{A.30}$$

Where P_{xx} is the PSD of the first signal, P_{yy} the PSD of the second signal and P_{xy} is the cross-PSD between the two signals. P_{xy} can also be used to compute the phase between two PSD signals (θ_{xy}) as is

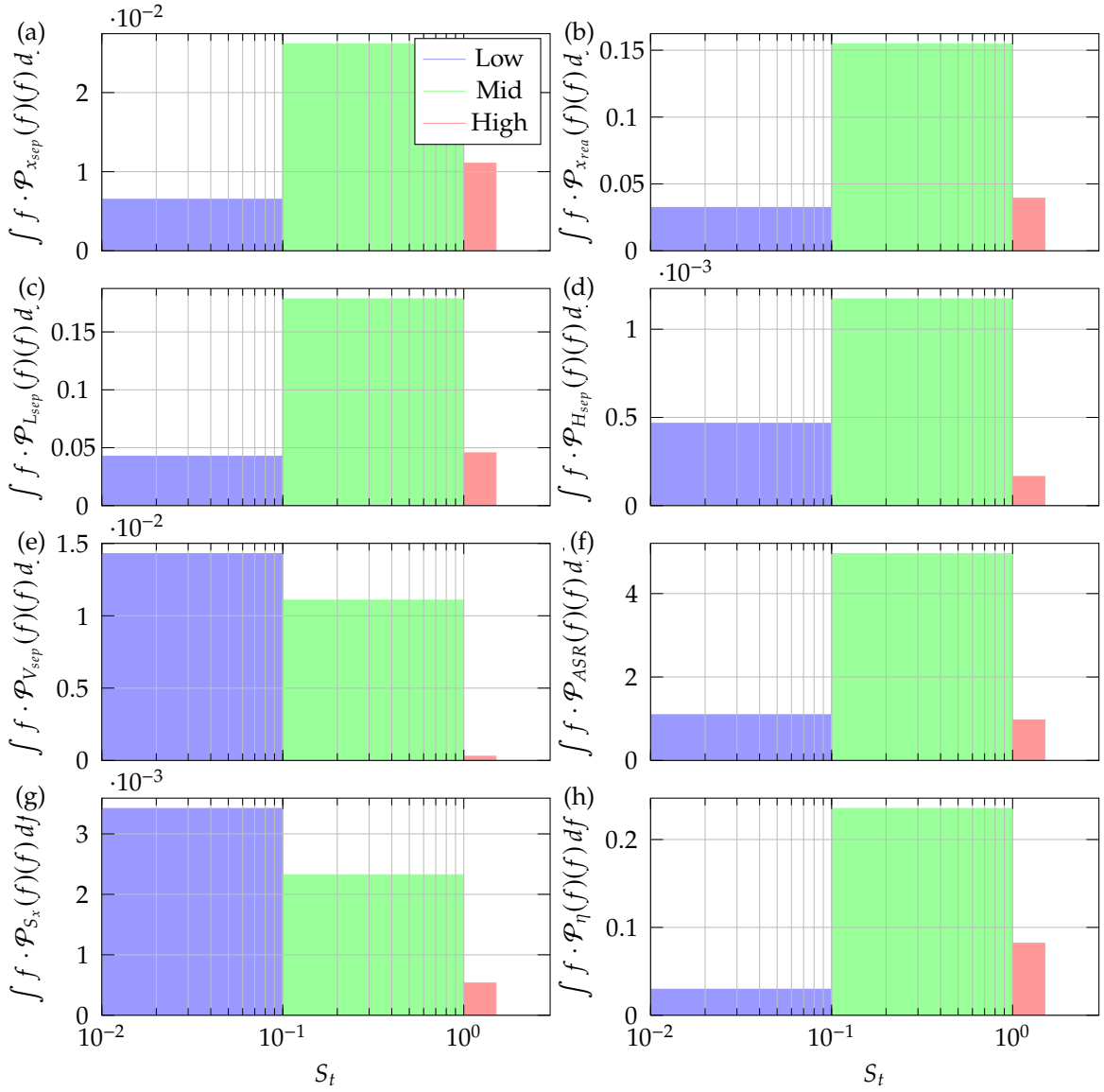


Figure A.18: Power per frequency range of bubble motion for the reference production simulation: (a) x_{sep}, (b) x_{rea}, (c) L_{sep}, (d) H_{sep}, (e) V_{sep}, (f) ASR, (g) S_x and (h) η.

done using Equation A.31.

$$\theta_{xy}(f) = \frac{\Im(P_{xy}(f))}{\Re(P_{xy}(f))}, -\pi < \theta_{xy} \leq \pi \tag{A.31}$$

The C_{xy} between two signals should be interpertated in the following manner: if $C_{xy} = 0$ then the two signals are completely unrelated, if $C_{xy} = 1$ then there is a direct linear relationship between the two signals. At every value in between there is a certain degree of noise between the two signals or the relationship is simply not linear. This interpretation should be done at every frequency of the signal as the coherence can change for every frequency. The C_{xy} and θ_{xy} between several different signals is given in Figure A.19.

The coherence between the control frequency and specifically the injection velocity and the bubble motions can also be computed. This is used in the parametric study to see if the pulsing frequency is corresponding to the separation and reattachment points. As coupling might occur.

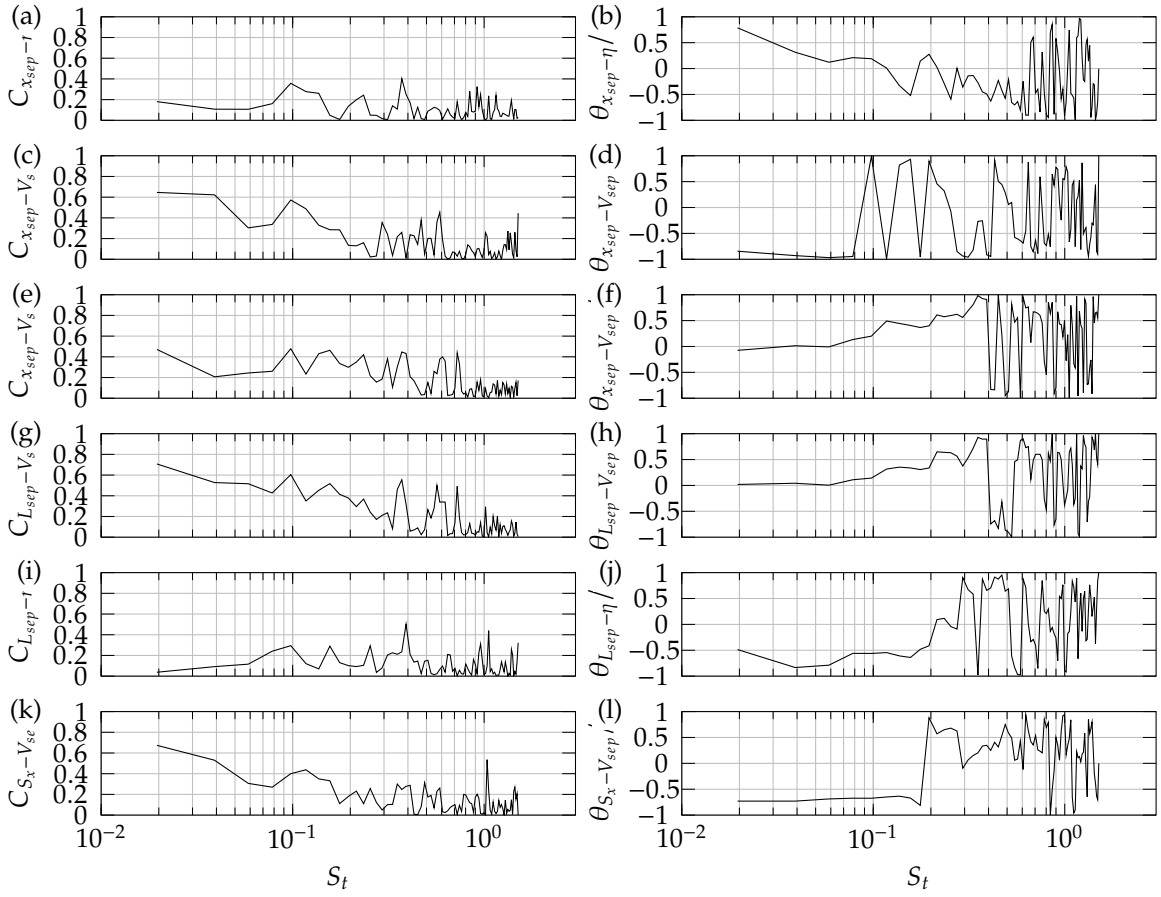


Figure A.19: Coherence and phase of bubble motion for the Reference case.

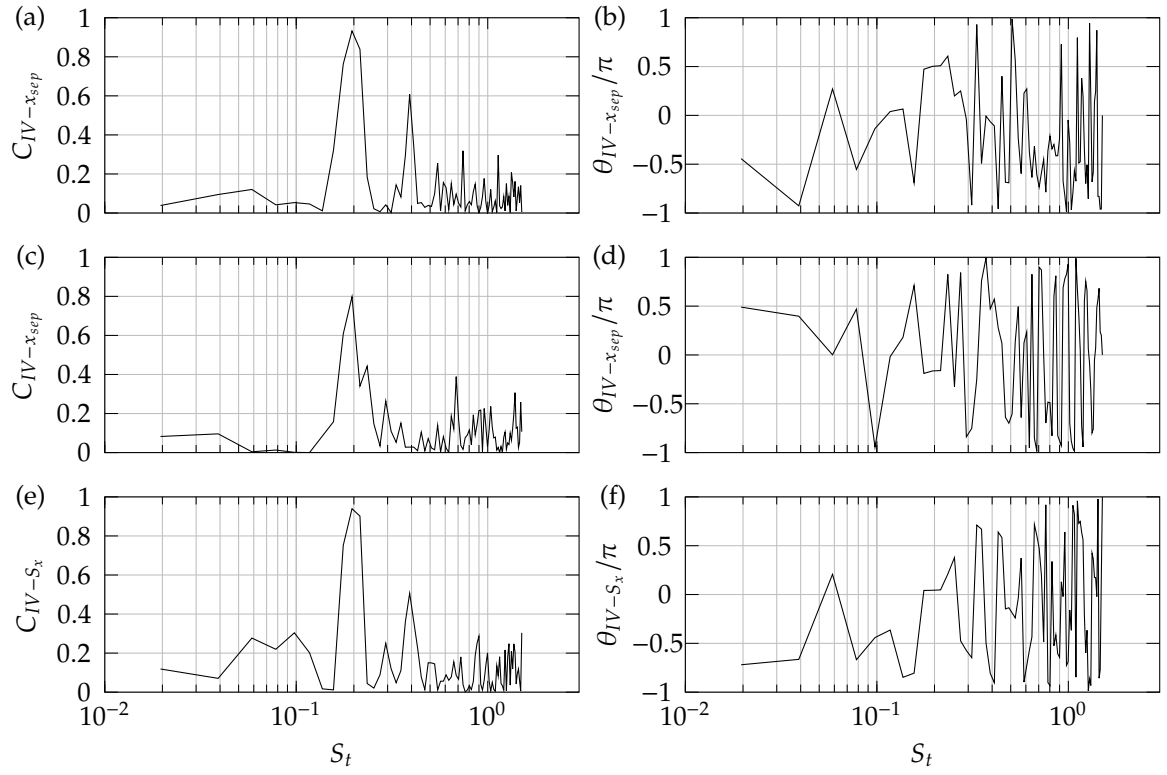


Figure A.20: Coherence and phase between bubble motion and injection velocity for case LMFH.

A.4.2. Probability Density Function

A Probability Density Function (PDF) is used to define the probability of a certain variable to have a certain value. By giving representing it as a distribution it can be used to check if a variable deviates from the mean value with statistical significance or not. Similar to the computation of the PSD of a signal, a PDF of a signal uses the time series of a certain metric, however here it is used to determine the likelihood of a metric having a certain value.

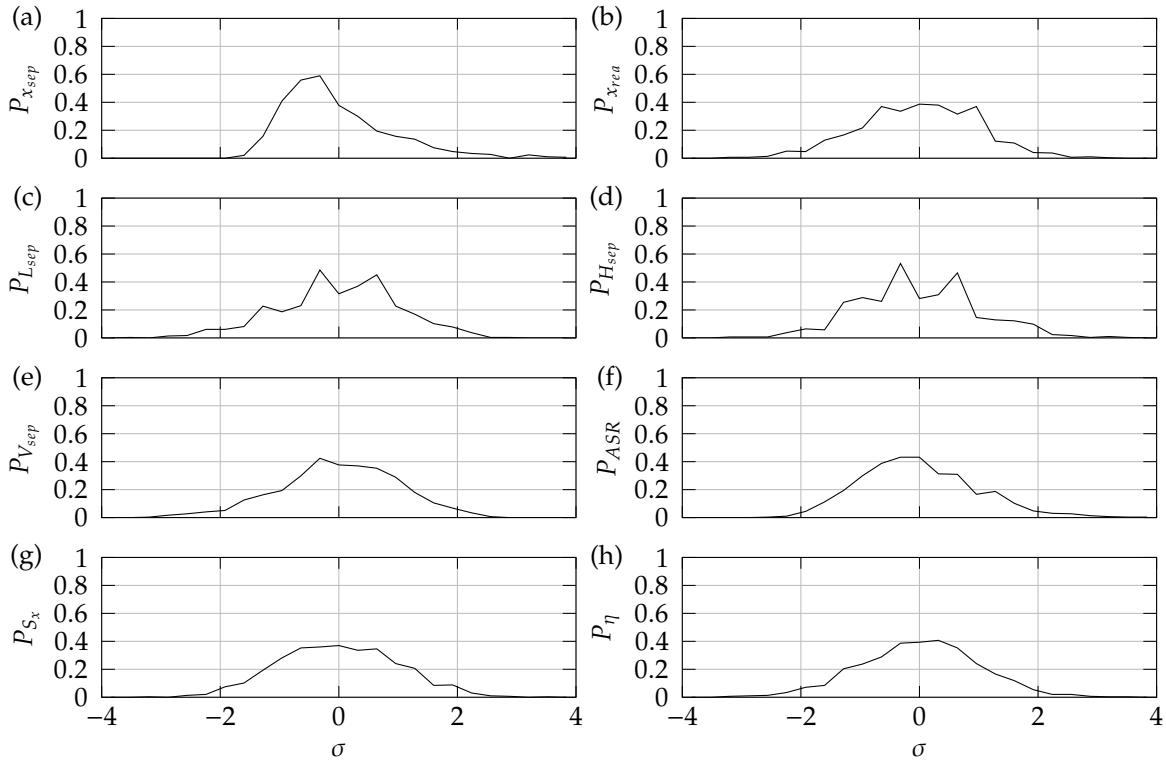


Figure A.21: PDFs of the bubble motion for the Reference case: (a) x_{sep}, (b) x_{rea}, (c) L_{sep}, (d) H_{sep}, (e) V_{sep}, (f) ASR, (g) S_x and (h) η.

A.5. Probe Analysis

As explained in section 2.7 the simulation outputs data for the placed probes. As the data recording of these probes causes little overhead it is computationally cheap to place a large number which allows for the accurate capture of p_w and T_w signals. The probe data is used in the following ways, the temporal averages of the p_w and T_w of each individual probe is computed which is normalized by the p_∞, T_∞ respectively. The p'_w are computed by rearranging Equation A.5 to Equation A.32.

$$p'_w = p_w - \langle p_w \rangle \tag{A.32}$$

The RMS of these fluctuations is then computed using Equation A.12. And finally the variance (σ^2) of the p'_w is computed using Equation A.33

$$\sigma^2 = \frac{\sum_{i=1}^{N} (p'_i)^2}{N} \tag{A.33}$$

All of these outcomes, $\langle p_w \rangle$, RMS of the p'_w, σ^2 of the p'_w, $\langle T_w \rangle$ are shown in Figure A.22a-d respectively.

The placement of all the probes along the centerline of the domain allows for the data shown in Figure A.22. However some locations are more interesting than others which is why a selection is made from all the possible locations. There are two groups of selected locations called independent and common. The independent group is computed for each simulation separately and does not take into

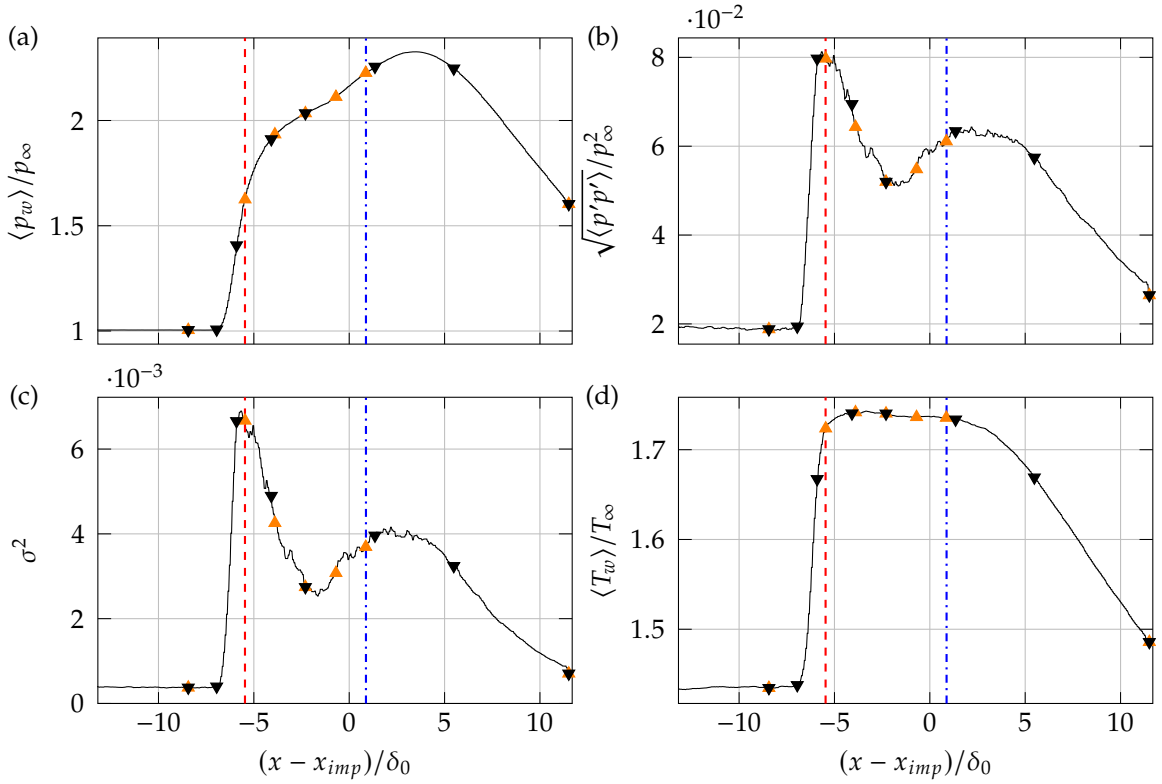


Figure A.22: Temporally averaged probe data for the reference production simulation: (a) $\langle p_w \rangle$, (b) RMS of the p'_w, (c) σ^2 of the p'_w, (d) $\langle T_w \rangle$. Common probe locations are indicated by ▲ and selected probe locations are indicated by ▼.

account the results of other simulations. The locations of this group are purely based on the separation and reattachment locations of this particular simulation. The locations of the common group are shared amongst all simulations and are based on the separation region of the reference simulation. This differentiation is made because the separation region changes between different control simulations. Common probe locations are indicated by ▲ and selected probe locations are indicated by ▼.

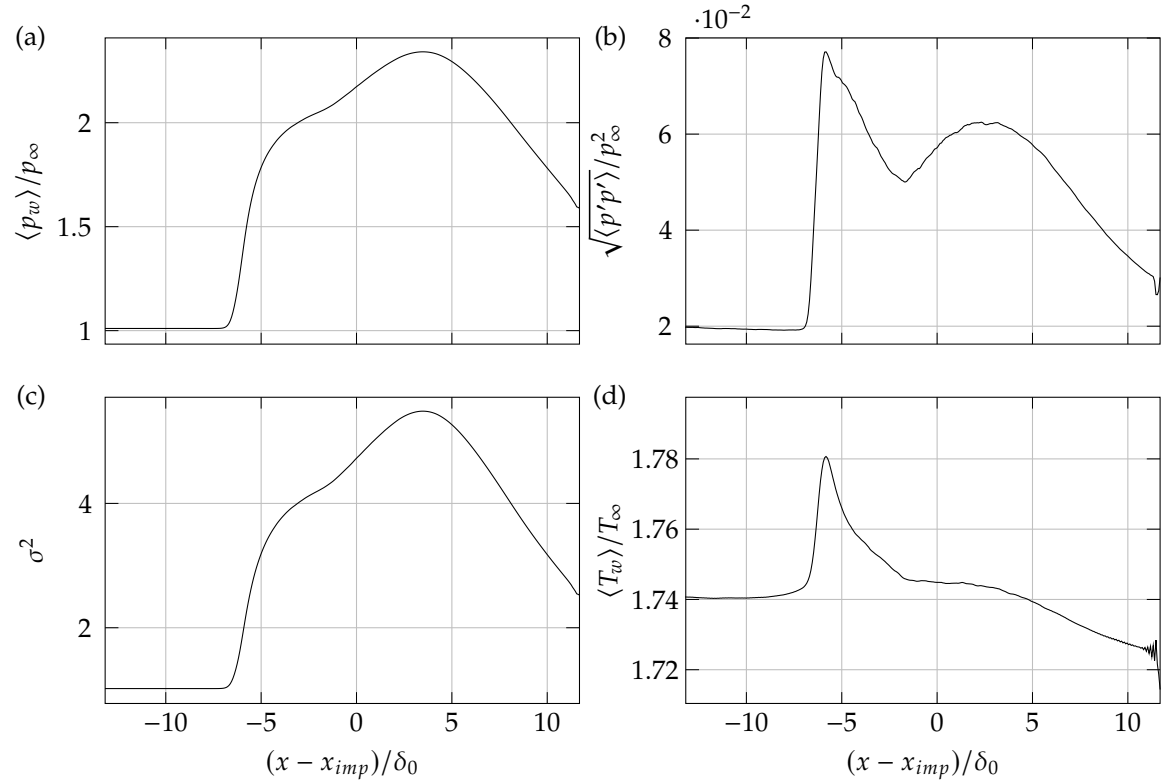


Figure A.23: Statistical wall data along the centerline for the reference production simulation: (a) $\langle p_w \rangle$, (b) RMS of the p'_w, (c) σ^2 of the p'_w, (d) $\langle T_w \rangle$.

A.5.1. Probe PSD

The p'_w obtained from Equation A.32 are used to compute the PSD spectra for each probe. Similarly to what has been done in Figure A.18, the power per frequency range can be computed for each probe and plotted over the stream-wise domain giving Figure A.27. This gives an indication of what frequency range dominates the wall pressure fluctuations along the centerline.

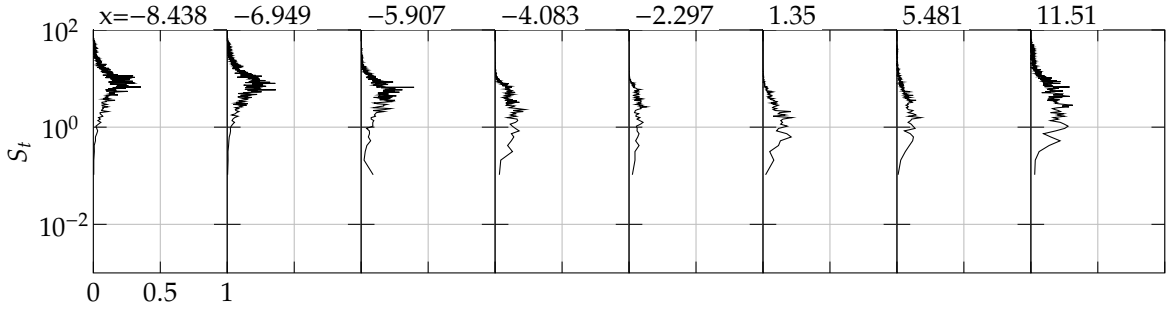


Figure A.24: PSDs of p'_w for the reference production simulation at selected locations, indicated with ▼ in Figure A.22.

The PSDs of the p'_w in the common group are given in Figure A.25.

Instead of showing the PSDs of the p'_w for a selected group of probes, they can also be shown for all probes at once. By plotting the streamwise location of a probe and using the PSD data to make a contour map a PSD map is made as shown in Figure A.26. Notice here that the scaling of the contours is logarithmic, meaning the logarithmic value is taken for the result of Equation A.27 which are computed for each probe.

Once again this can be integrated for a set frequency range to obtain the IPPR. Plotting these values for each probe location will give Figure A.27. This clearly shows that the low and middle frequency

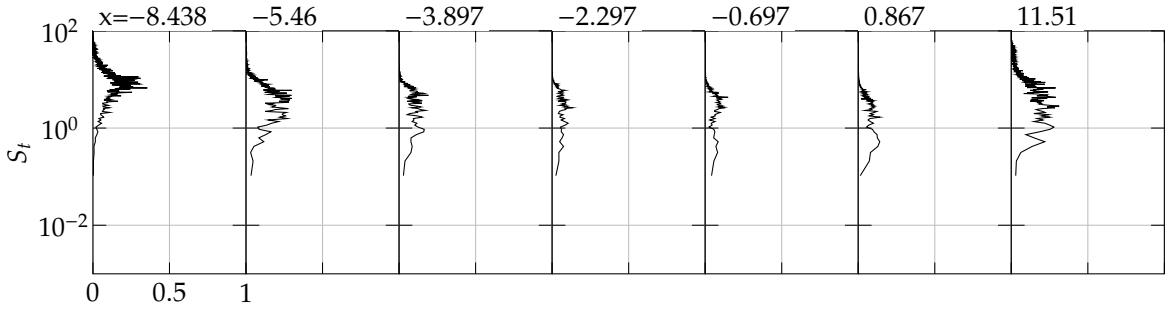


Figure A.25: PSDs of p'_w for the reference production simulation at common locations, indicated with ▲ in Figure A.22.

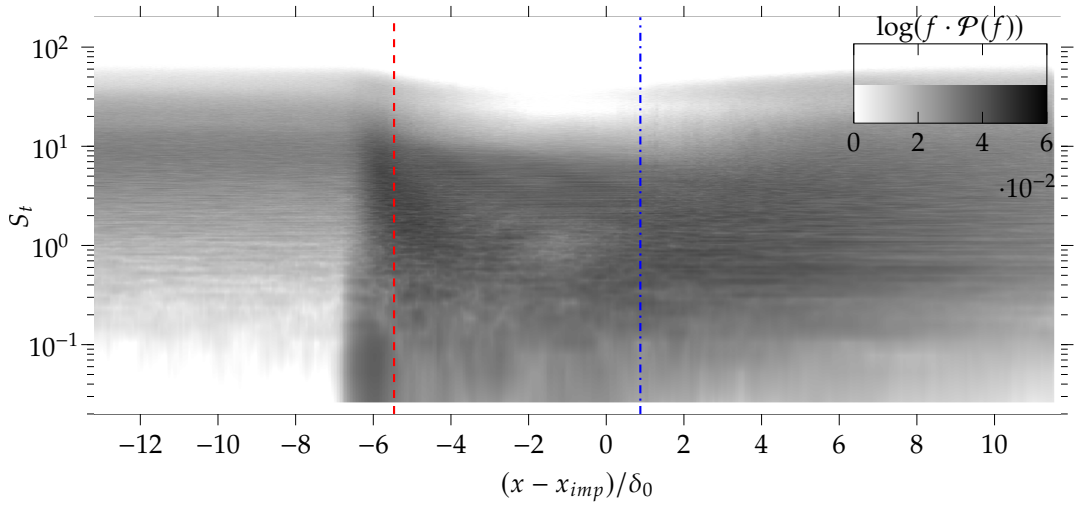


Figure A.26: Log scaled PSD map of wall-pressure at the center line for the Reference case.

ranges dominate the separating region, the region just before the actual separation. However the low and middle ranges only dominate in this region after which they quickly reduce to a small portion of the high-frequency fluctuations. The high-frequency range also gets an significant increase during the separating region, then it drops inside the actual separation bubble, before it slightly increases after reattachment after which it decays again.

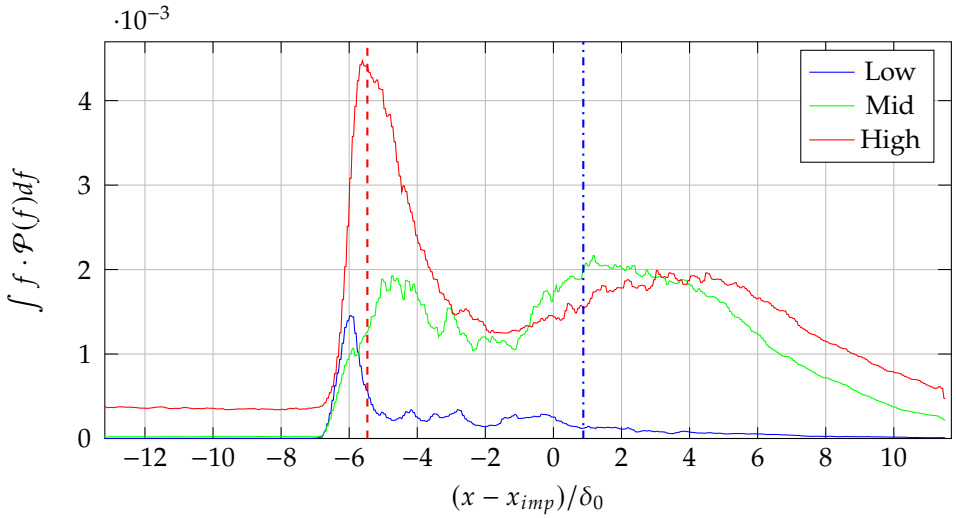


Figure A.27: Power per frequency range for p'_w.

Rather than integrating to obtain the IPPR the PSD signal with the highest energy and the corresponding frequency can be extracted. Again visualizing this along the domain gives Figure A.28. This visualization is used during the analysis of the parametric study results.

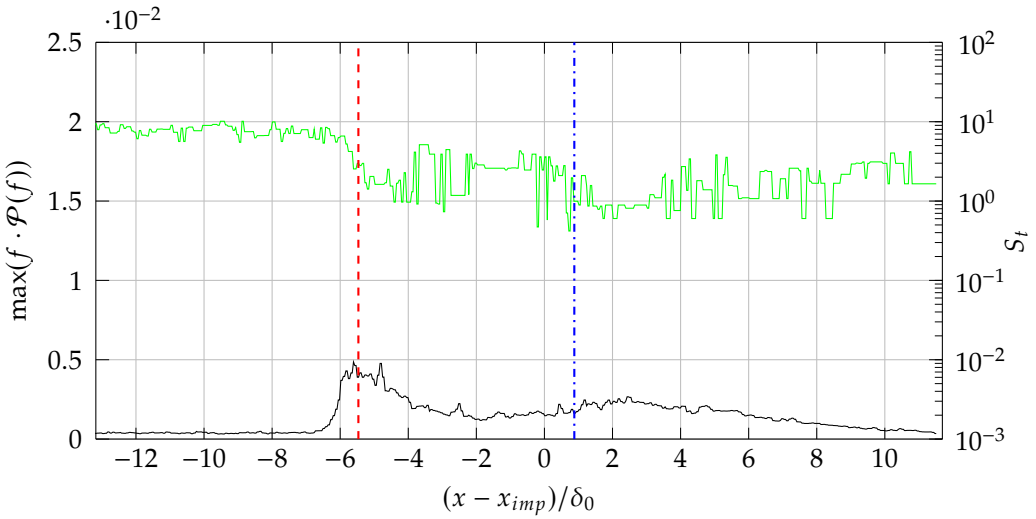


Figure A.28: Power of dominant p'_w PSD with corresponding frequency for probes along the centerline for the Referencecase.

A.5.2. Probe PDF

The PDFs of the p'_w for the independent group are given in Figure A.29.

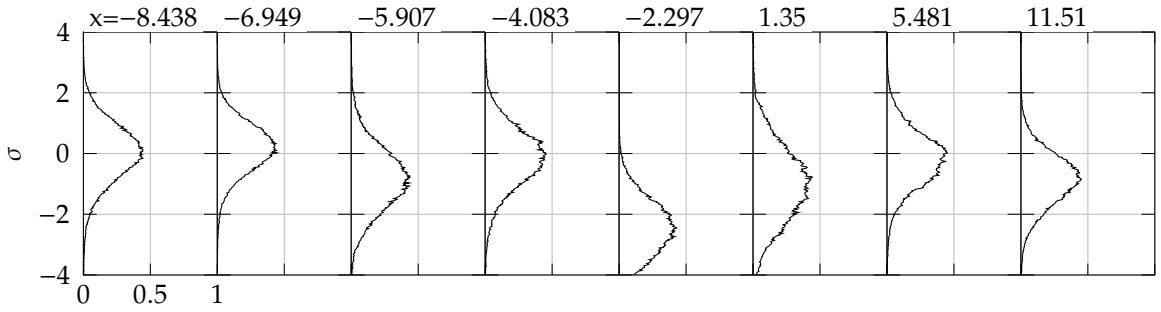


Figure A.29: PDFs of p'_w for the reference production simulation at selected locations, indicated with ▼ in Figure A.22.

B

Analysis Software Tips

B.1. Software version control

Python version control is done with conda. This allows for the creation of an evironment which includes all the required libraries and packages. This environment can be transfered between different systems and ensures that scripts are compatible.

The python scripts were uploaded to a GitHub repository, so that the scripts can be made and tested before they are used on an HPC system. Git allows for the easy syncing of changes and version control.

B.2. Computational resource management

As the data set in this research was about 1.5 Tb per simulation one should be careful not to keep analyzing and extracting the data. In order to prevent this the script was split up into three parts. The first part extracted the raw data from the simulation snapshots and saved this in a separate files. The second part would then use this raw data and analyze it, or it would load it if it had been extracted before. The analyzed data would then be saved in a new object, much smaller than the raw data, only about 1 Gb. Additionally some data for animations could be exported to separated objects if desired. Finally the making of figures can take quite a significant amount of time while it is not computationally expensive. Therefore doing this on the same machine as running the extraction and analysis is a waste of resources and should be done on a lighter system.

B.3. HPC usage

By using the argspars module in python, the script can be run from external inputs. This is useful when using a bash script as this allows the user to set the inputs. Inputs to the script include the simulation data folder, the processed data folder, the image directory and some settings used for processing such as the number of cores and whether or not the script should output figures.

B.4. Figure updating

All figures were made with tikz, and were possible directly from data exported by python. And all tikz pictures were externalized so that they only had to be made once. To automatically converte the tikz output to a png figure which can be used in presentations use ghostscript. This line should then be included in latex: \tikzsetexternal/system call=pdflatex \tikzexternalcheck-shellescape -halt-on-error -interaction=batchmode -jobname "\image" "\texsource" && "C:/Program Files/gs/gs9.56.1/bin/gswin64.exe" -q -dSAFER -dBATCH -dNOPAUSE -sDEVICE=pngalpha -r300 -sOutputFile="\image.png" "\image.pdf"

C

Production Result Figures

C.1. Instantaneous

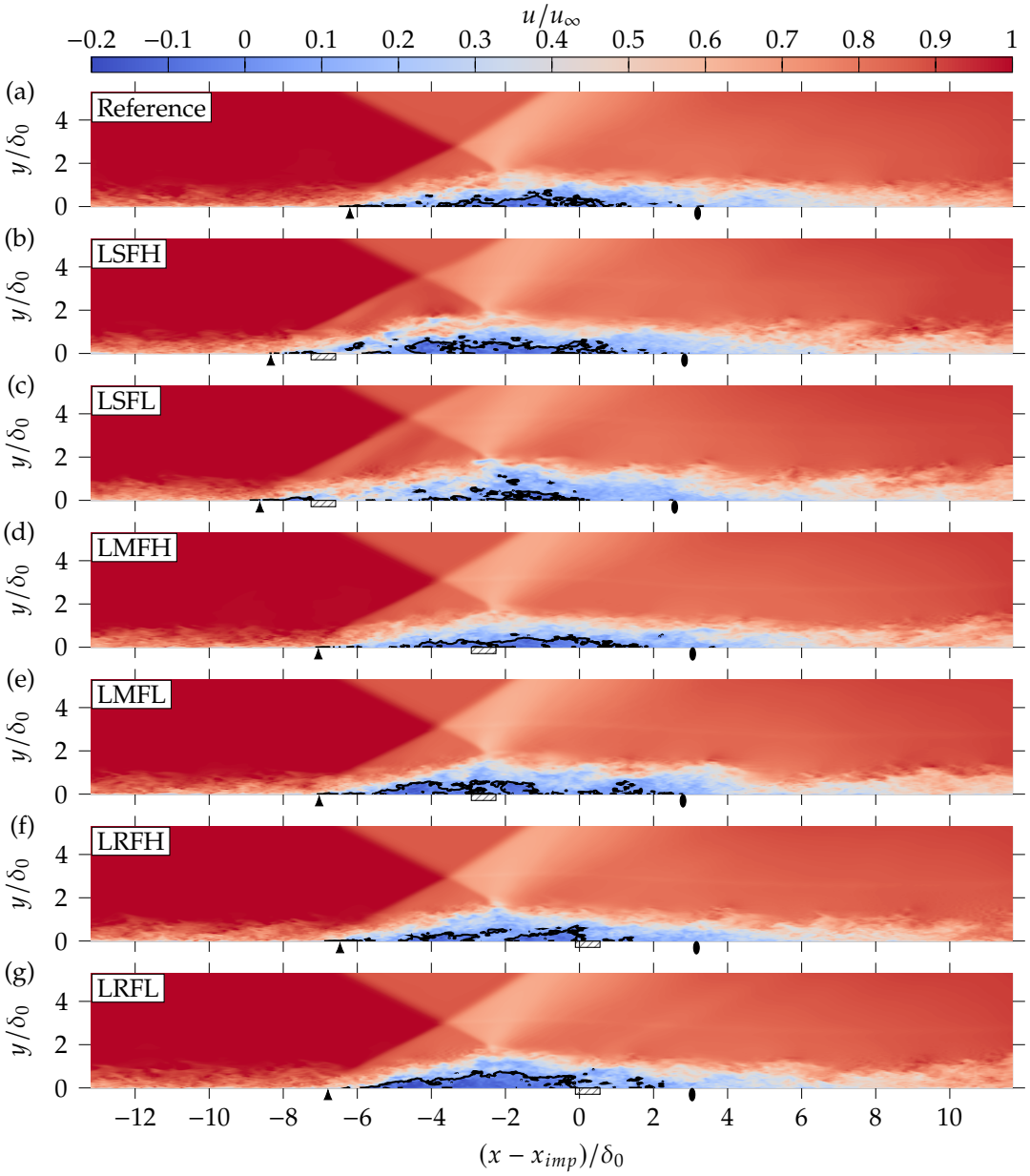


Figure C.1: Instantaneous u field comparison for: (a) Reference case, (b) case LSFH, (c) case LSFL, (d) case LMFH, (e) case LMFL, (f) case LRFH, and (g) case LRFL. The instantaneous separation and reattachment points are indicated by ▲ and ⬮ respectively. The AL is indicated by ▨.

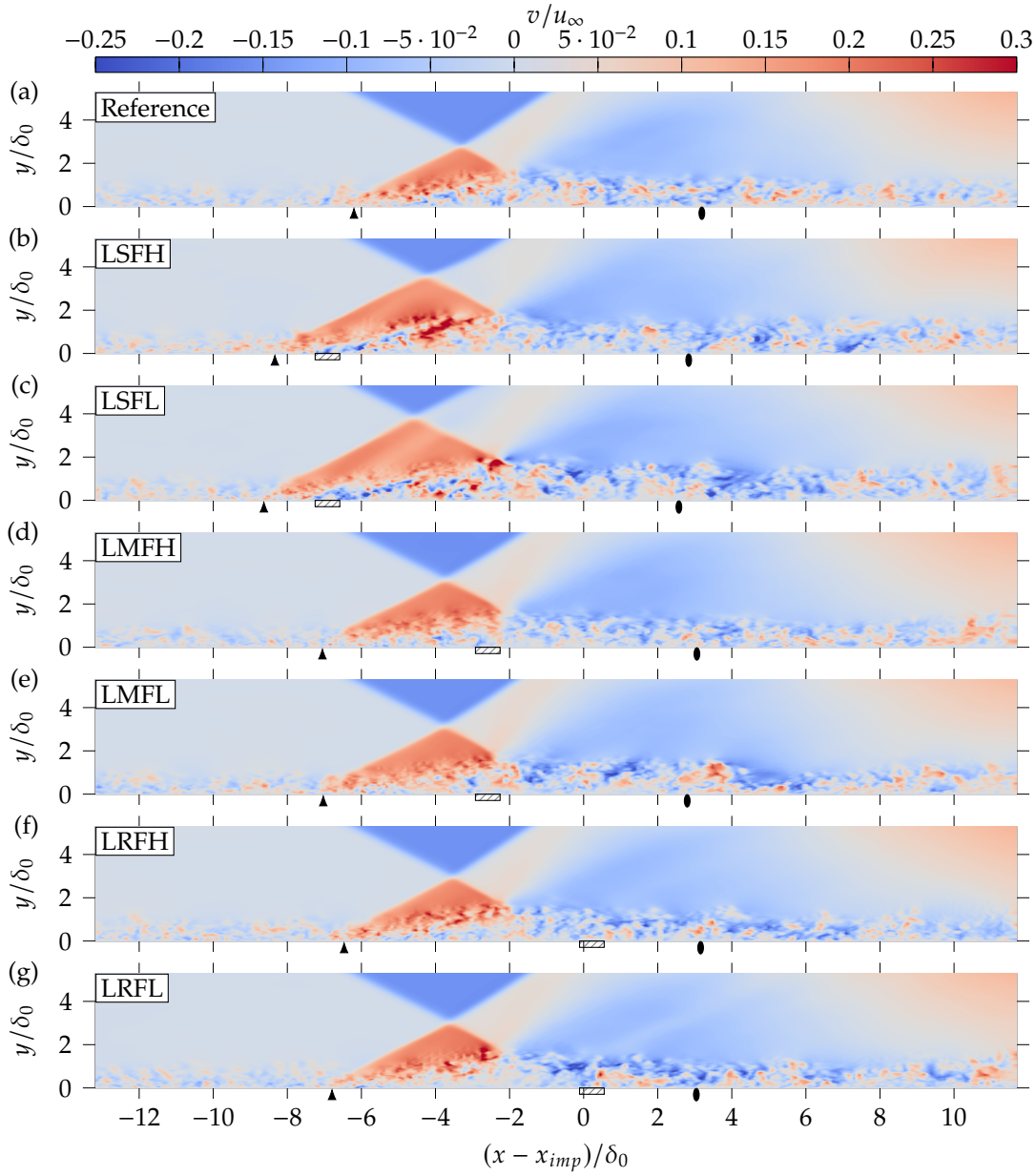


Figure C.2: Instantaneous v field comparison for: (a) Reference case, (b) case LSFH, (c) case LSFL, (d) case LMFH, (e) case LMFL, (f) case LRFH, and (g) case LRFL. The instantaneous separation and reattachment points are indicated by ▲ and ⬮ respectively. The AL is indicated by ▨.

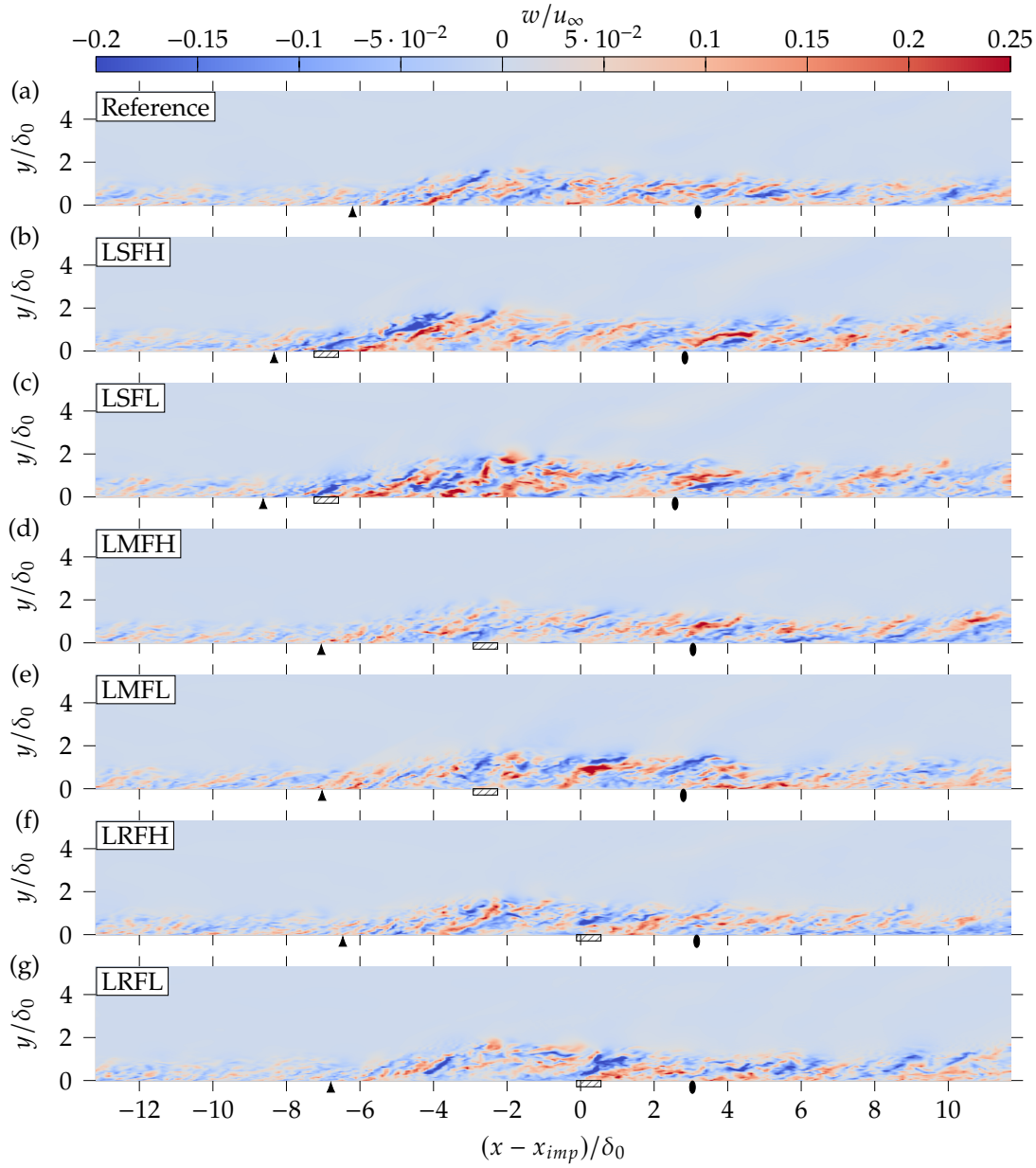


Figure C.3: Instantaneous w field comparison for: (a) Reference case, (b) case LSFH, (c) case LSFL, (d) case LMFH, (e) case LMFL, (f) case LRFH, and (g) case LRFL. The instantaneous separation and reattachment points are indicated by ▲ and ⬮ respectively. The AL is indicated by ▨.

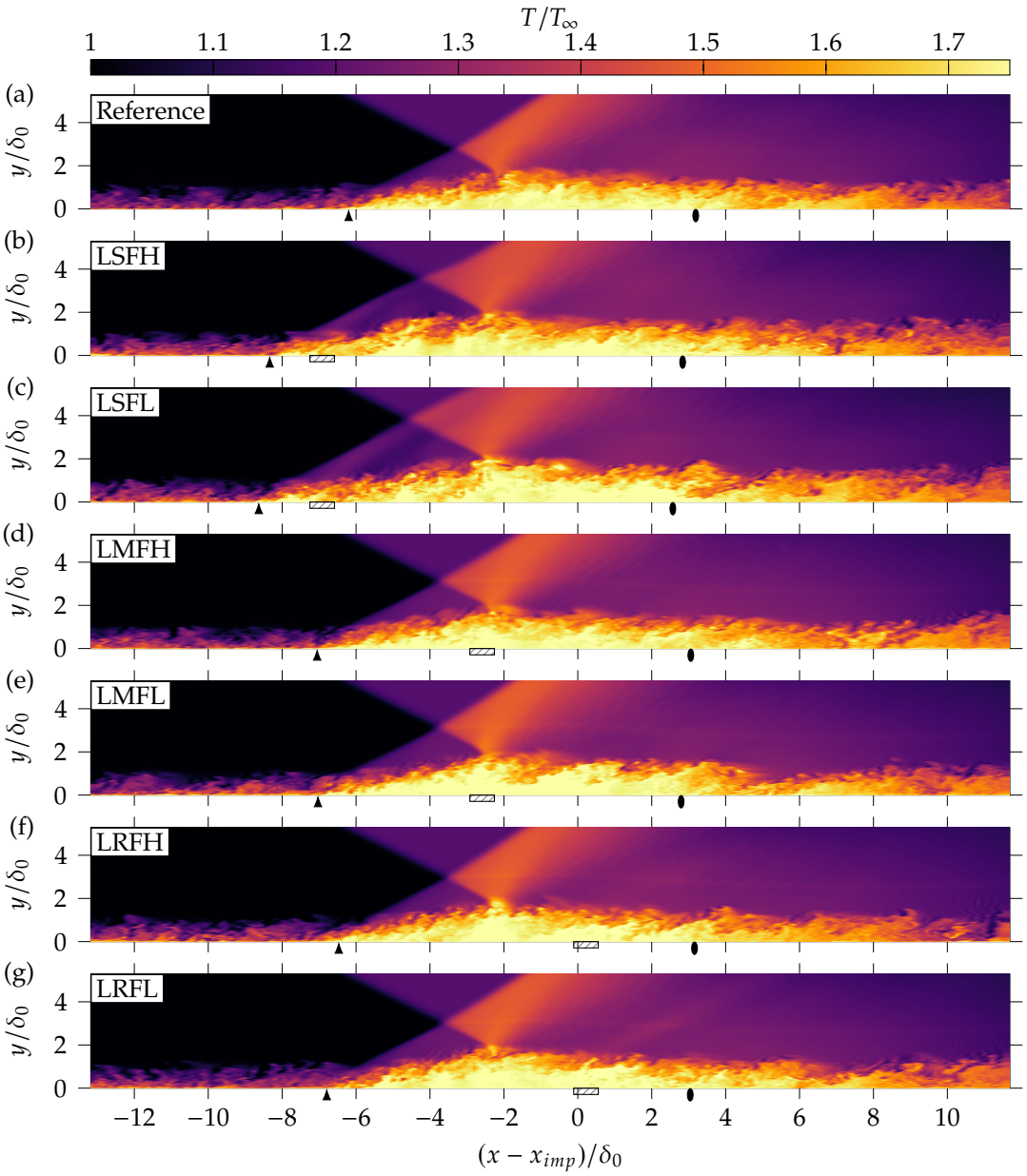


Figure C.4: Instantaneous span-wise temperature comparison for: (a) Reference case, (b) case LSFH, (c) case LSFL, (d) case LMFH, (e) case LMFL, (f) case LRFH, and (g) case LRFL. The instantaneous separation and reattachment points are indicated by ▲ and ⬮ respectively. The AL is indicated by ▨.

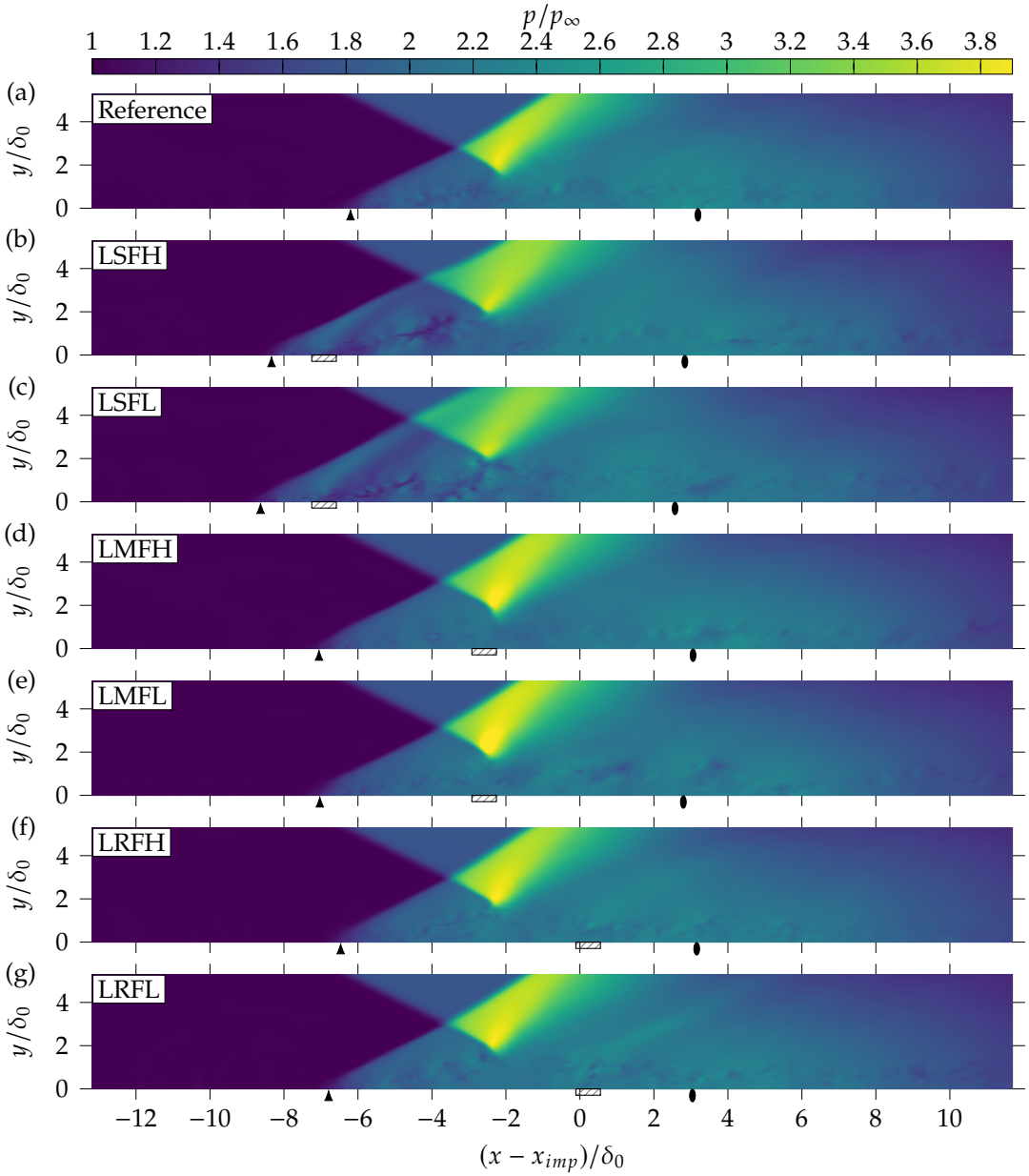


Figure C.5: Instantaneous p field in the middle of the span comparison for: (a) Reference case, (b) case LSFH, (c) case LSFL, (d) case LMFH, (e) case LMFL, (f) case LRFH, and (g) case LRFL. The instantaneous separation and reattachment points are indicated by ▲ and ⬮ respectively. The AL is indicated by ▨.

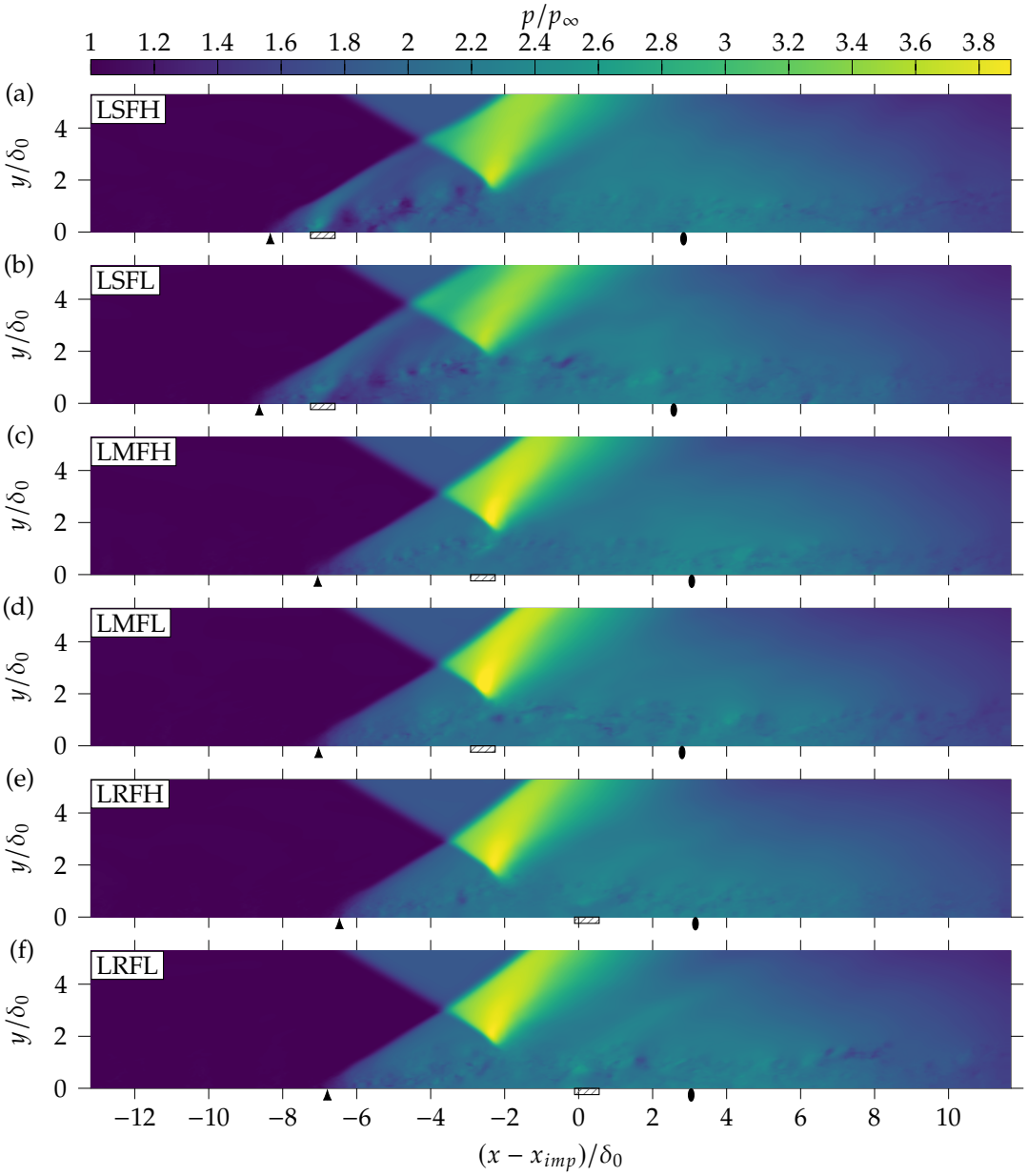


Figure C.6: Instantaneous p field through actuator comparison for: (a) case LSFH, (b) case LSFL, (c) case LMFH, (d) case LMFL, (e) case LRFH, and (f) case LRFL. The instantaneous separation and reattachment points are indicated by ▲ and ⬮ respectively. The AL is indicated by ▨.

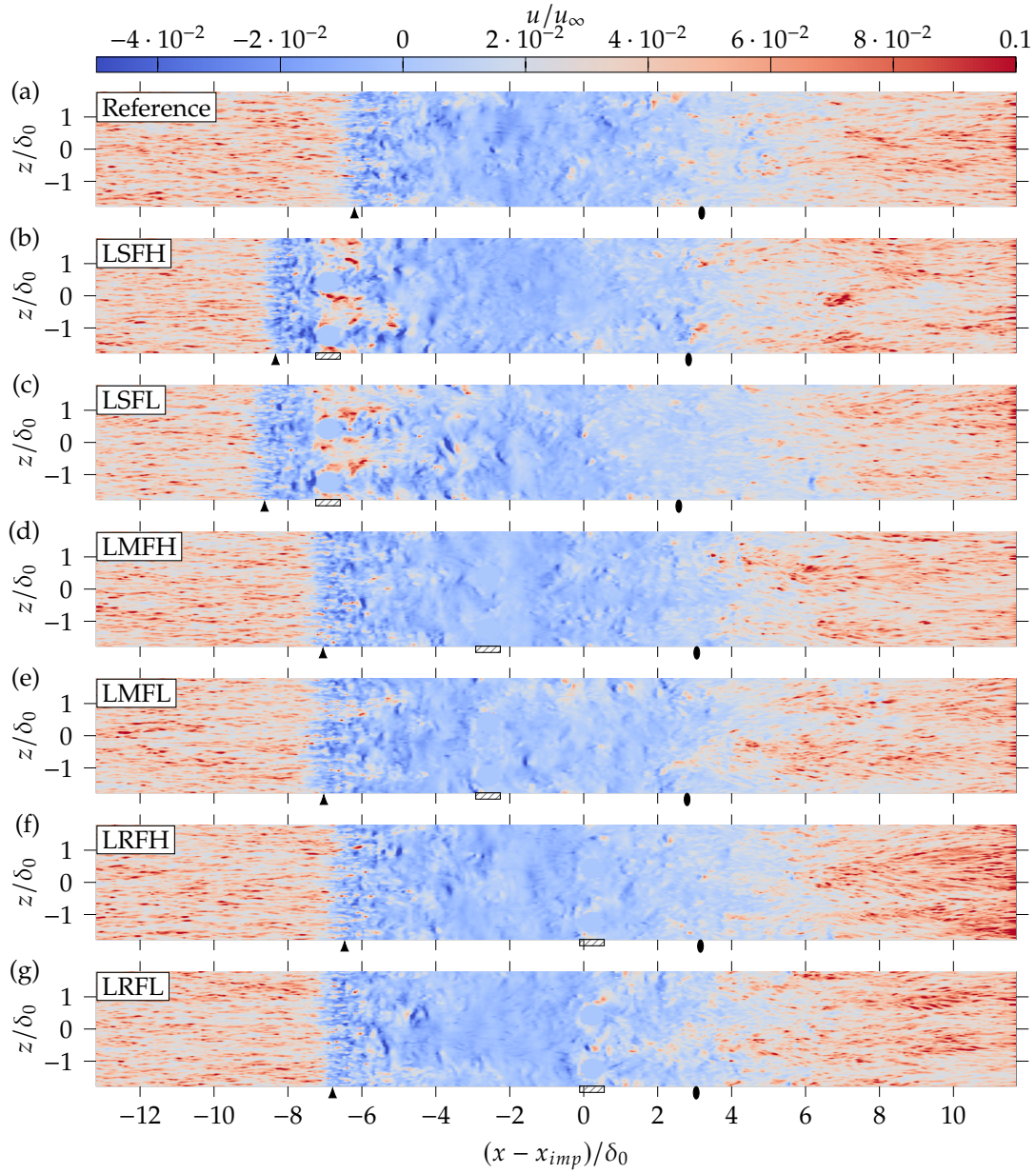


Figure C.7: Instantaneous u velocity at the wall comparison for: (a) Reference case, (b) case LSFH, (c) case LSFL, (d) case LMFH, (e) case LMFL, (f) case LRFH, and (g) case LRFL. The instantaneous separation and reattachment points are indicated by ▲ and ⬮ respectively. The AL is indicated by ▨.

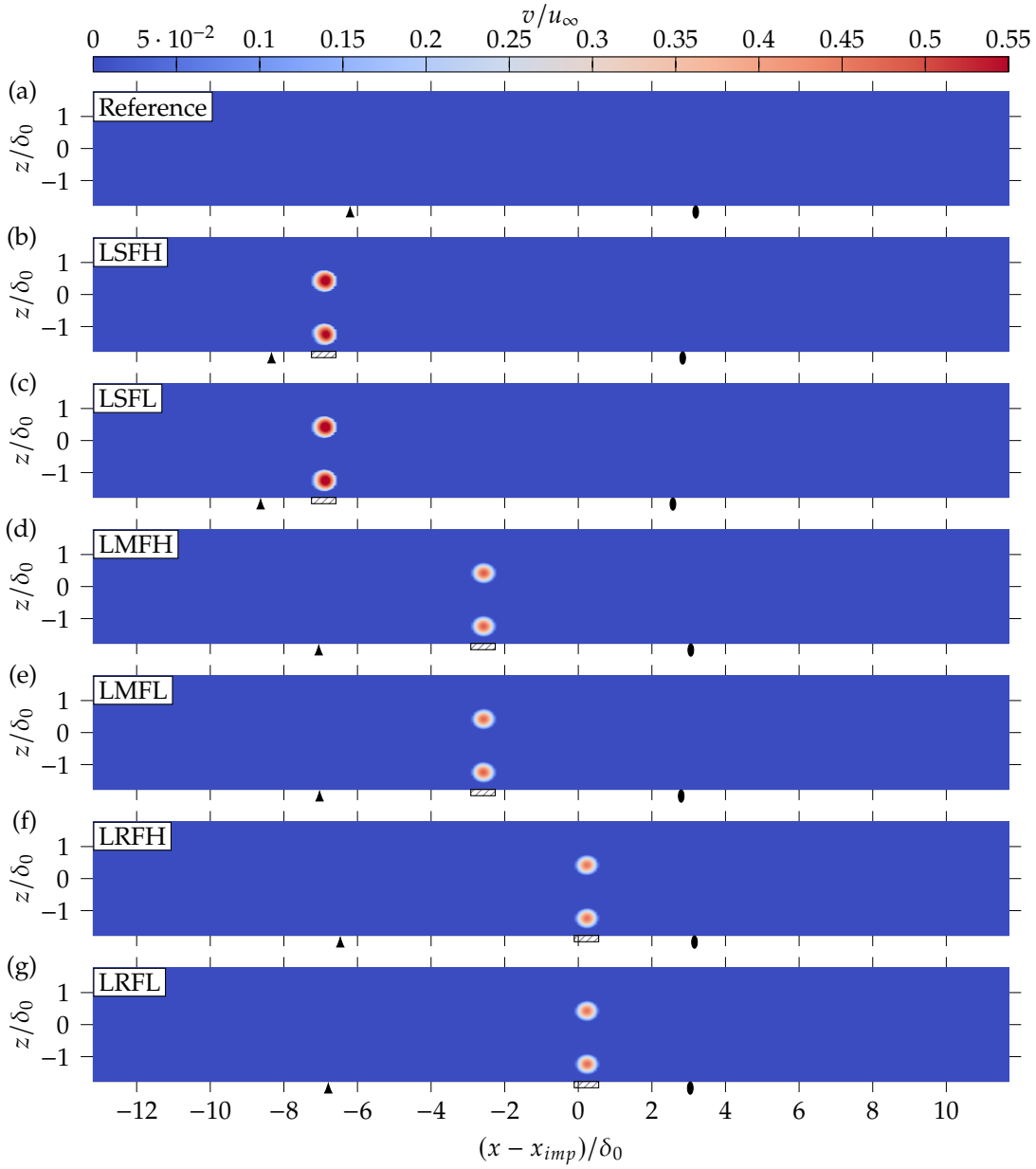


Figure C.8: Instantaneous v velocity at the wall comparison for: (a) Reference case, (b) case LSFH, (c) case LSFL, (d) case LMFH, (e) case LMFL, (f) case LRFH, and (g) case LRFL. The instantaneous separation and reattachment points are indicated by ▲ and ⬮ respectively. The AL is indicated by ▨.

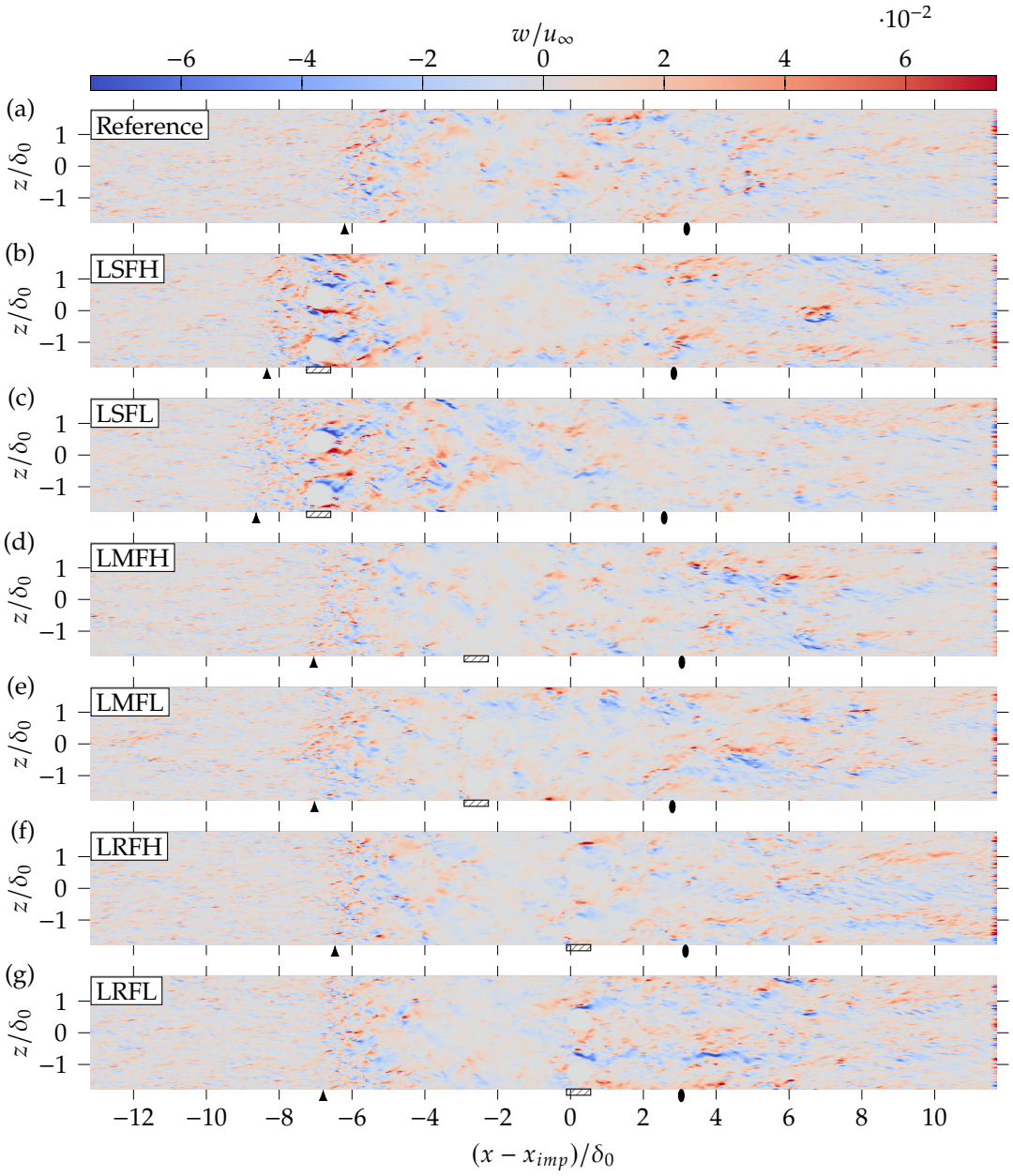


Figure C.9: Instantaneous w velocity at the wall comparison for: (a) Reference case, (b) case LSFH, (c) case LSFL, (d) case LMFH, (e) case LMFL, (f) case LRFH, and (g) case LRFL. The instantaneous separation and reattachment points are indicated by ▲ and ⬮ respectively. The AL is indicated by ▨.

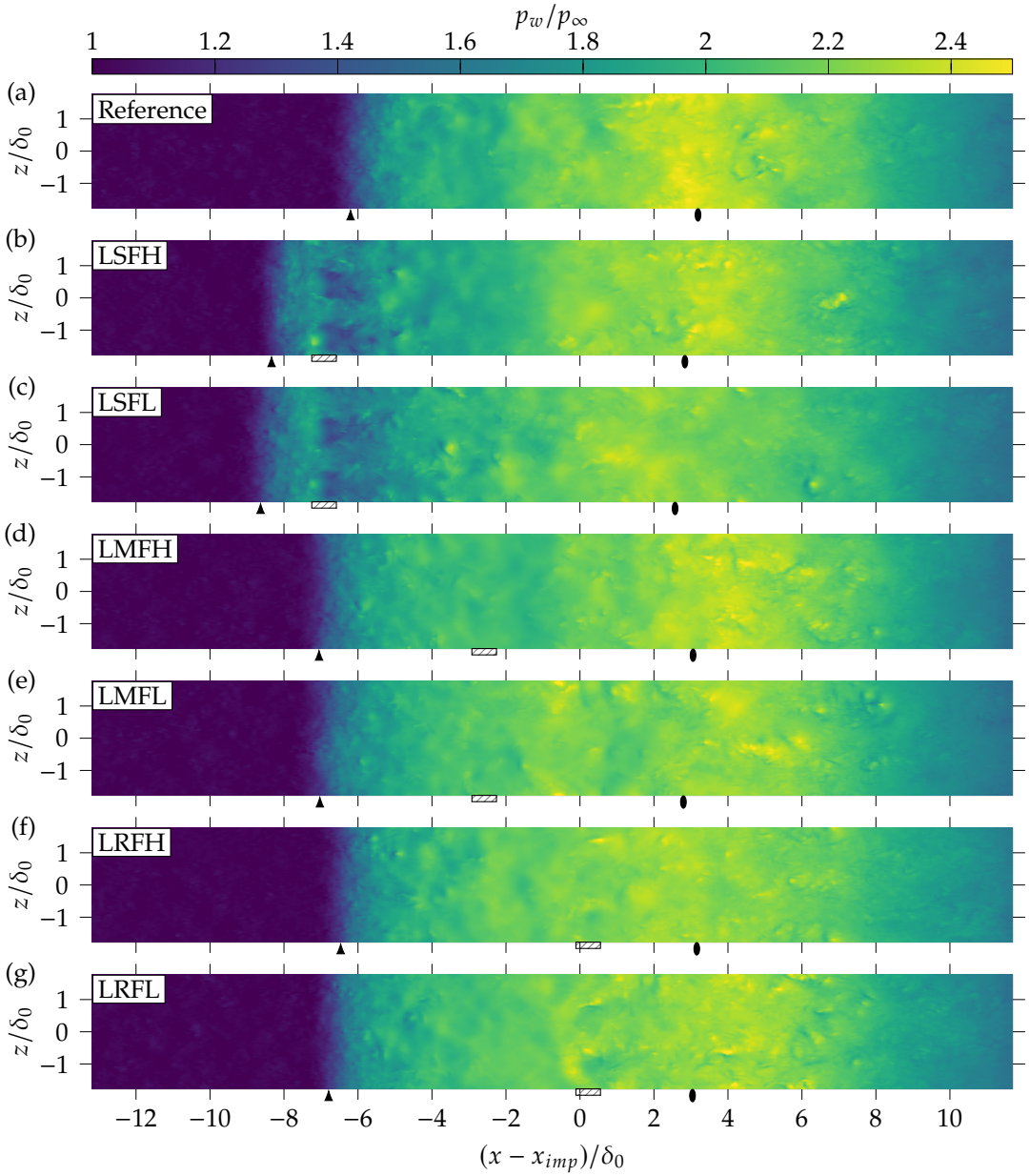


Figure C.10: Instantaneous p field at the wall comparison for: (a) Reference case, (b) case LSFH, (c) case LSFL, (d) case LMFH, (e) case LMFL, (f) case LRFH, and (g) case LRFL. The instantaneous separation and reattachment points are indicated by ▲ and ⬮ respectively. The AL is indicated by ▨.

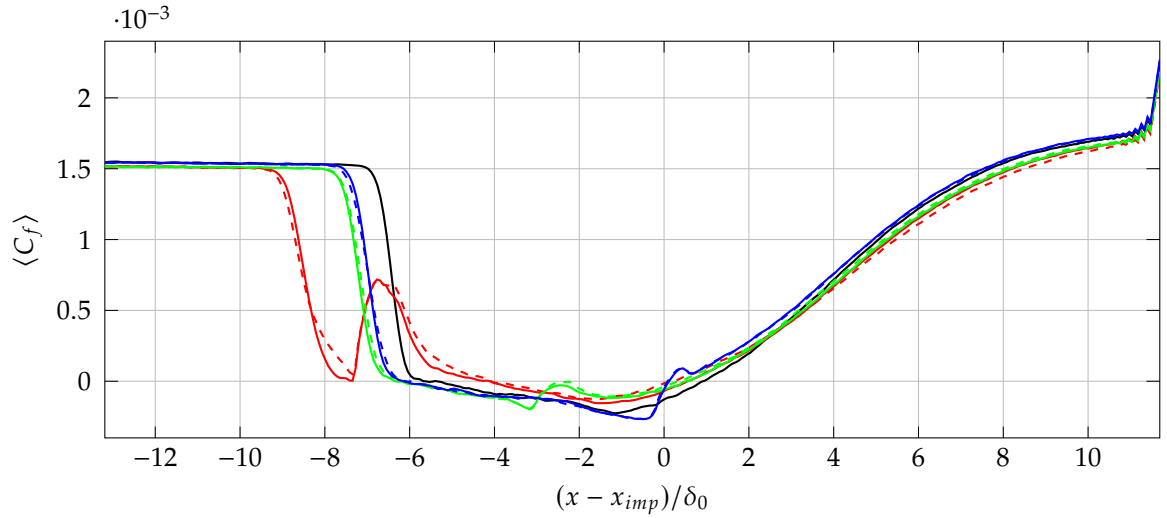


Figure C.11: Instantaneous span-wise mean skin friction from snapshots. For line legend see Table 4.1.

C.2. Instantaneous flow organization in 3D

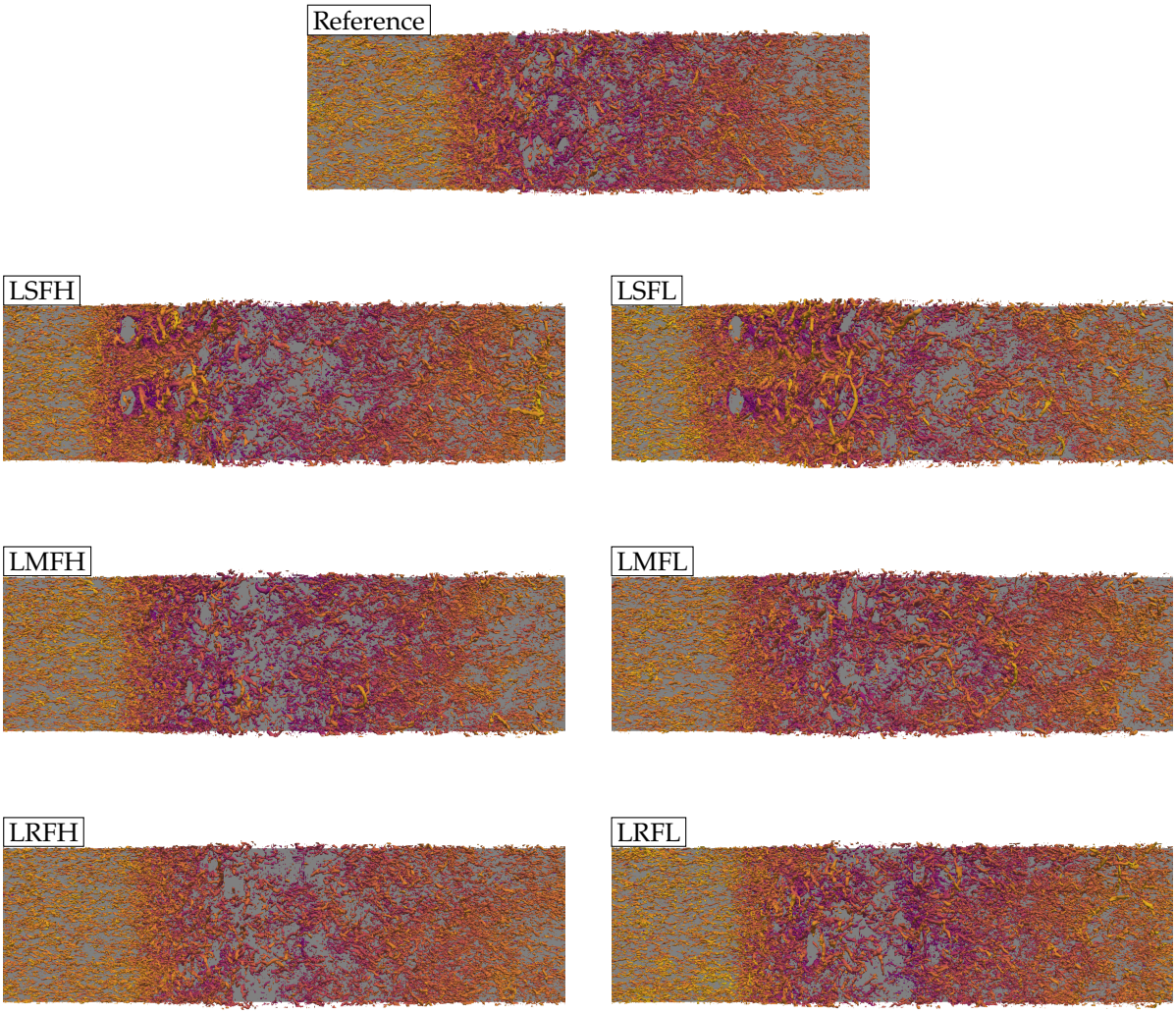


Figure C.12: Instantaneous vortical structures visualized with the λ_{ci} criterion and colored by the local streamwise velocity, viewed from above.

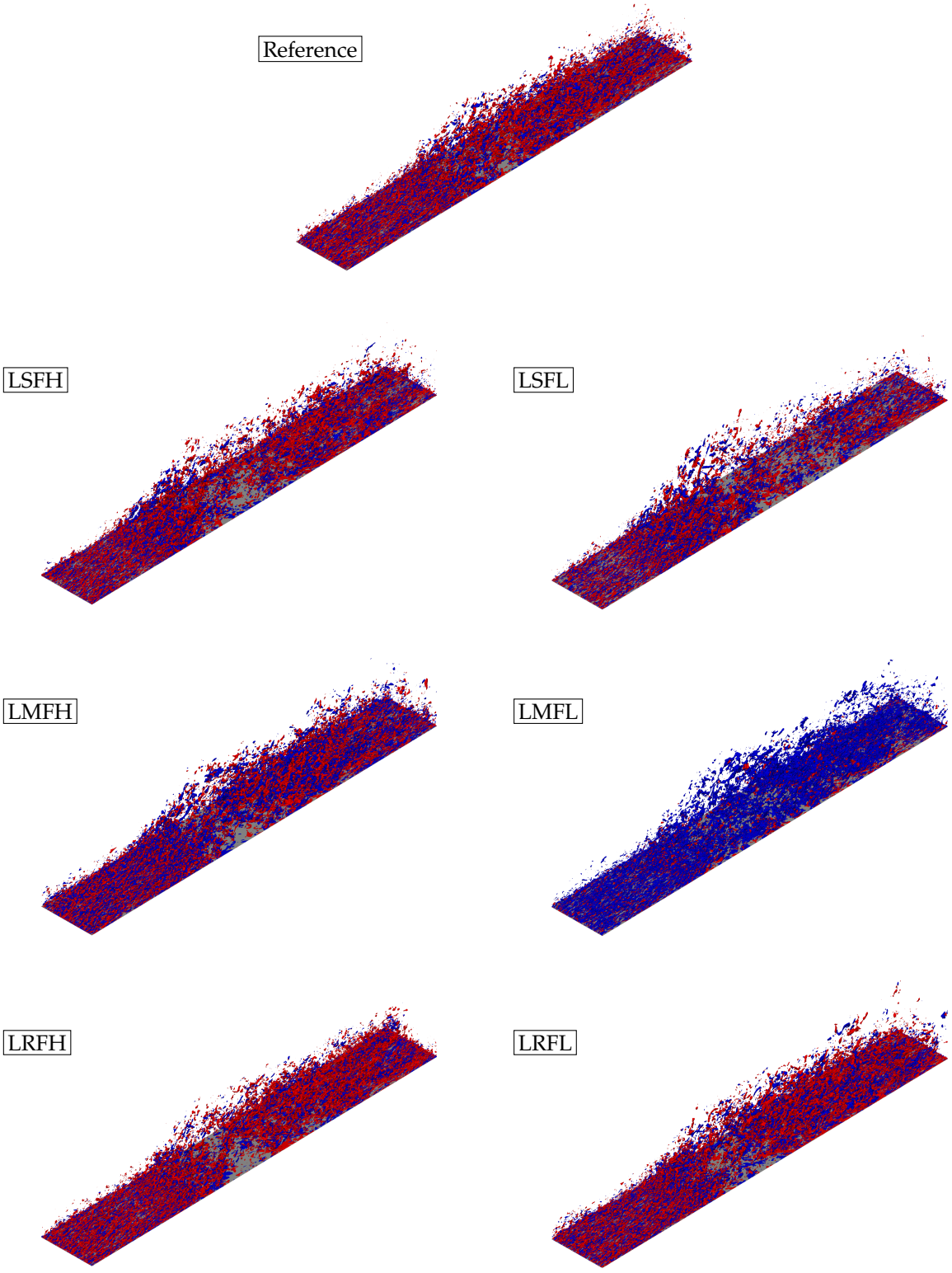


Figure C.13: Instantaneous vorticity visualized by an isocontour of ω_x, where red is counterclockwise and blue is clockwise.

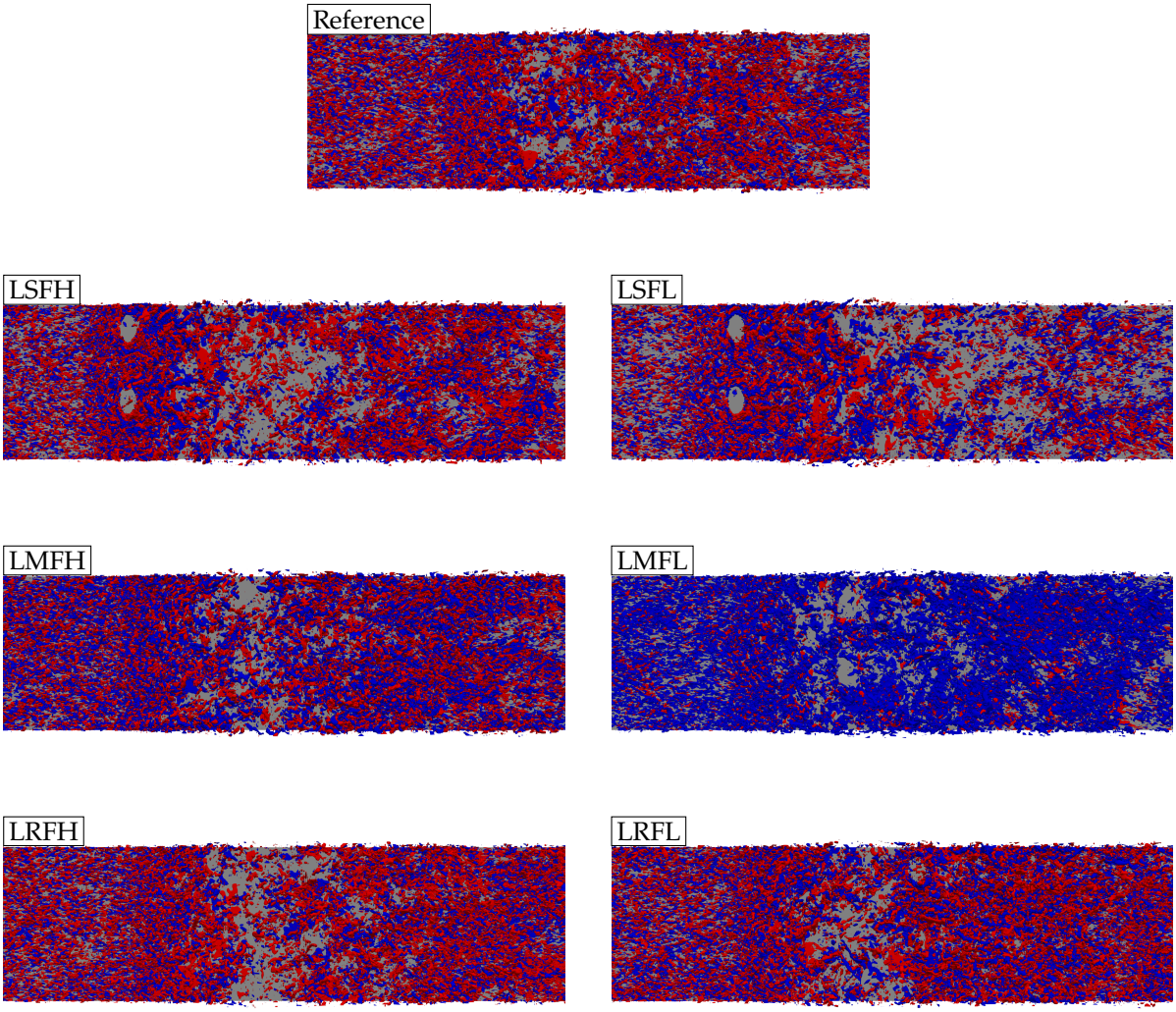


Figure C.14: Instantaneous vorticity visualized by an isocontour of ω_x, where red is counterclockwise and blue is clockwise, viewed from above.

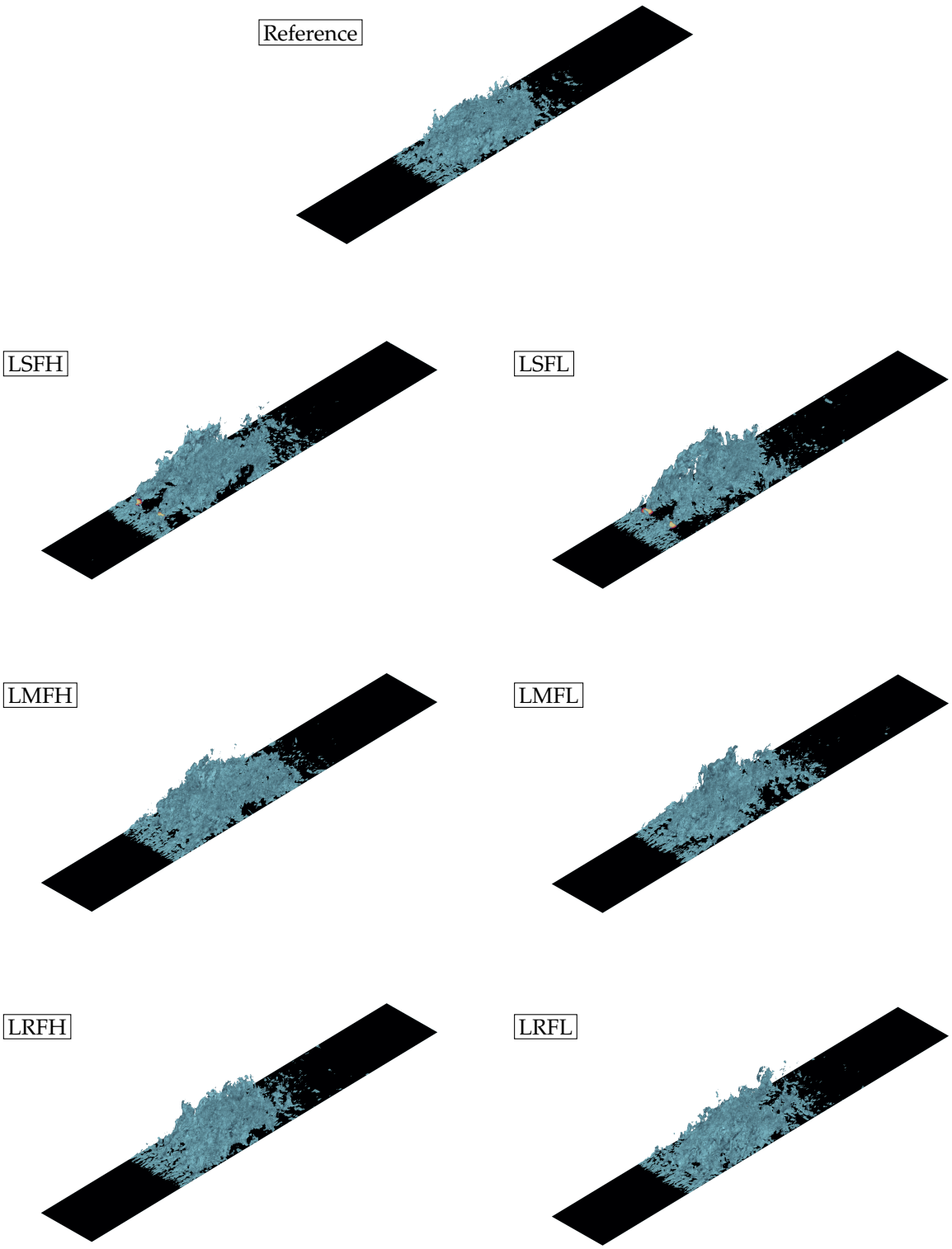


Figure C.15: Instantaneous bubble shape visualized with the iso-contour of $u = 0$.

C.3. Phase-averaged flow organization in 3D

C.3.1. Peak-phase-averaged

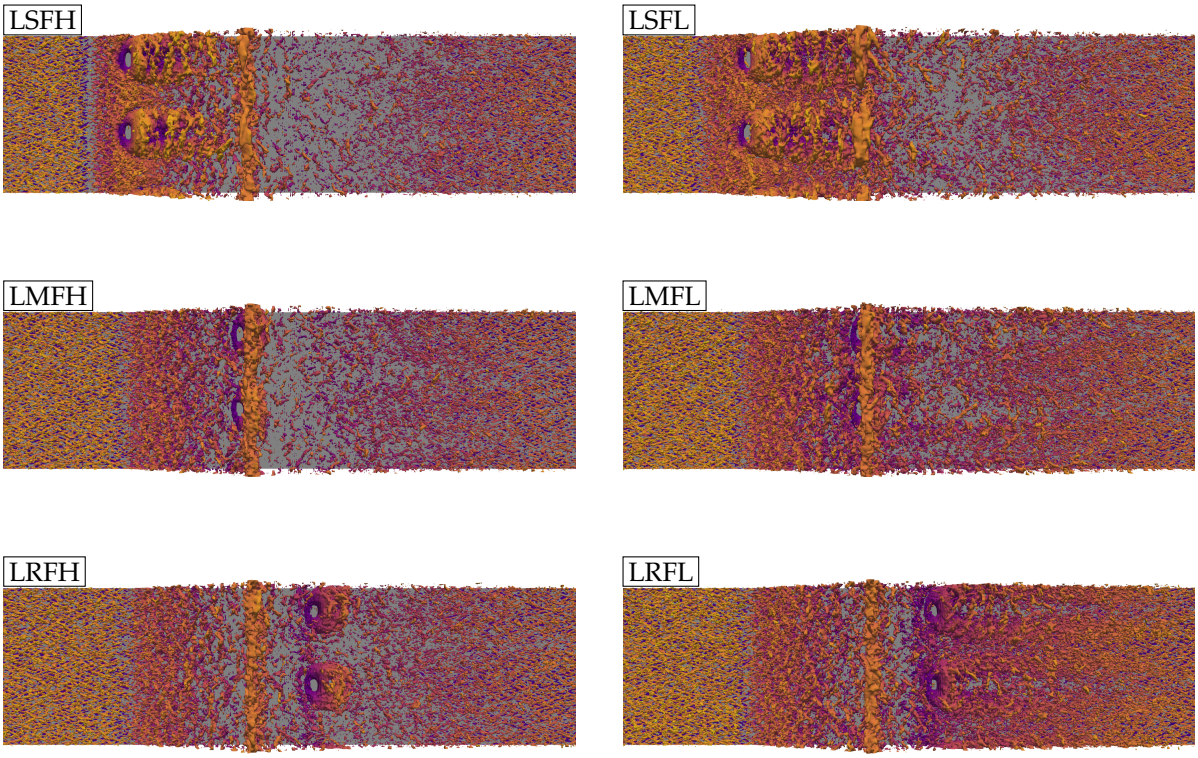


Figure C.16: Peak-phase-averaged vortical structures visualized with the λ_{ci} criterion and colored by the local streamwise velocity, viewed from above.

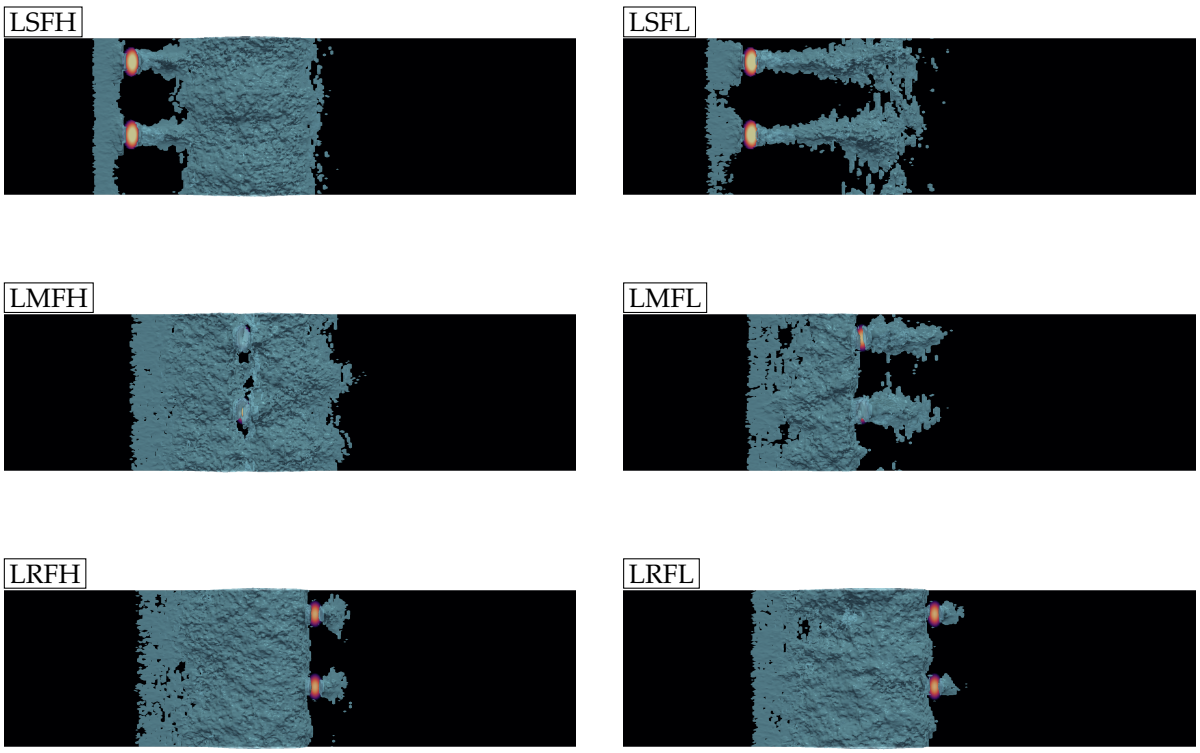


Figure C.17: Peak-phase-averaged bubble shape visualized with the iso-contour of $u = 0$, viewed from above.

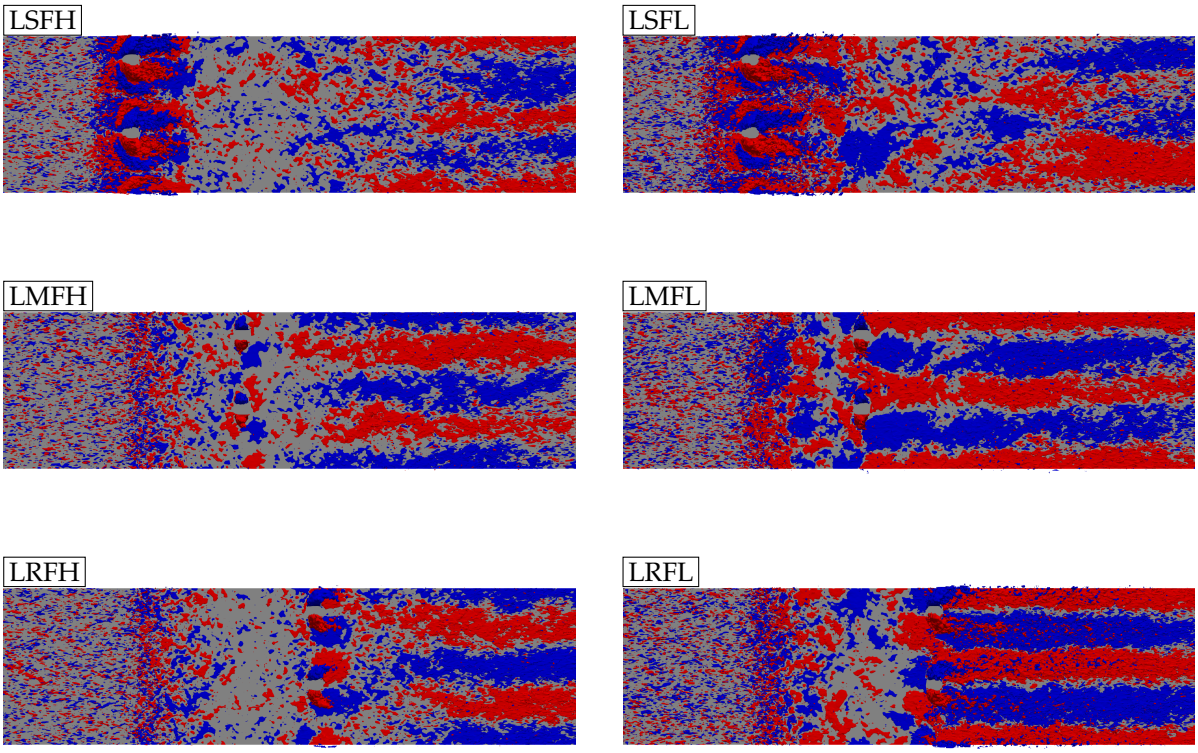


Figure C.18: Peak-phase-averaged vorticity visualized by iso-contours of ω_x for the control cases where red is ω_x = 0.2 and blue is ω_x = -0.2, viewed from above.

C.3.2. Injection-phase-averaged

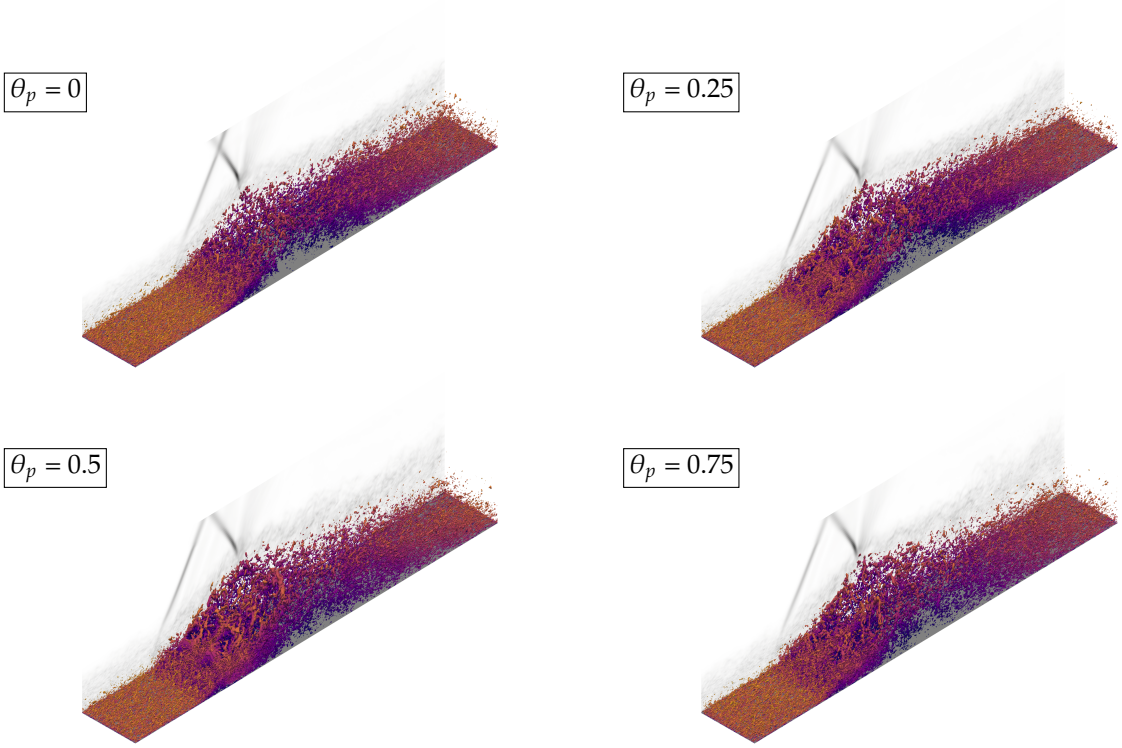


Figure C.19: Injection-phase-averaged vortical structures, visualized with the λ_{ci} criterion and colored by the local streamwise velocity for case LSFL. An isovalue of $\lambda_{ci}/u_\infty = 0.1021$ is used. A phase-averaged numerical Schlieren is shown in the background.

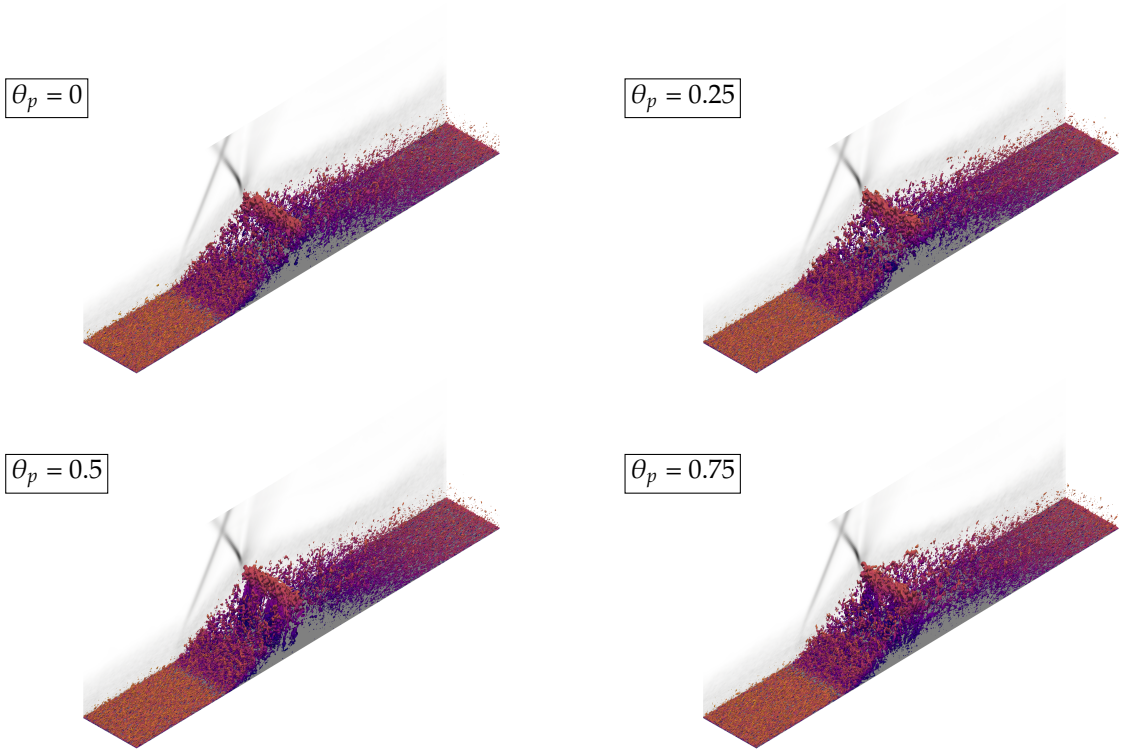


Figure C.20: Injection-phase-averaged vortical structures, visualized with the λ_{ci} criterion and colored by the local streamwise velocity for case LMFH. An isovalue of $\lambda_{ci}/u_\infty = 0.1021$ is used. A phase-averaged numerical Schlieren is shown in the background.

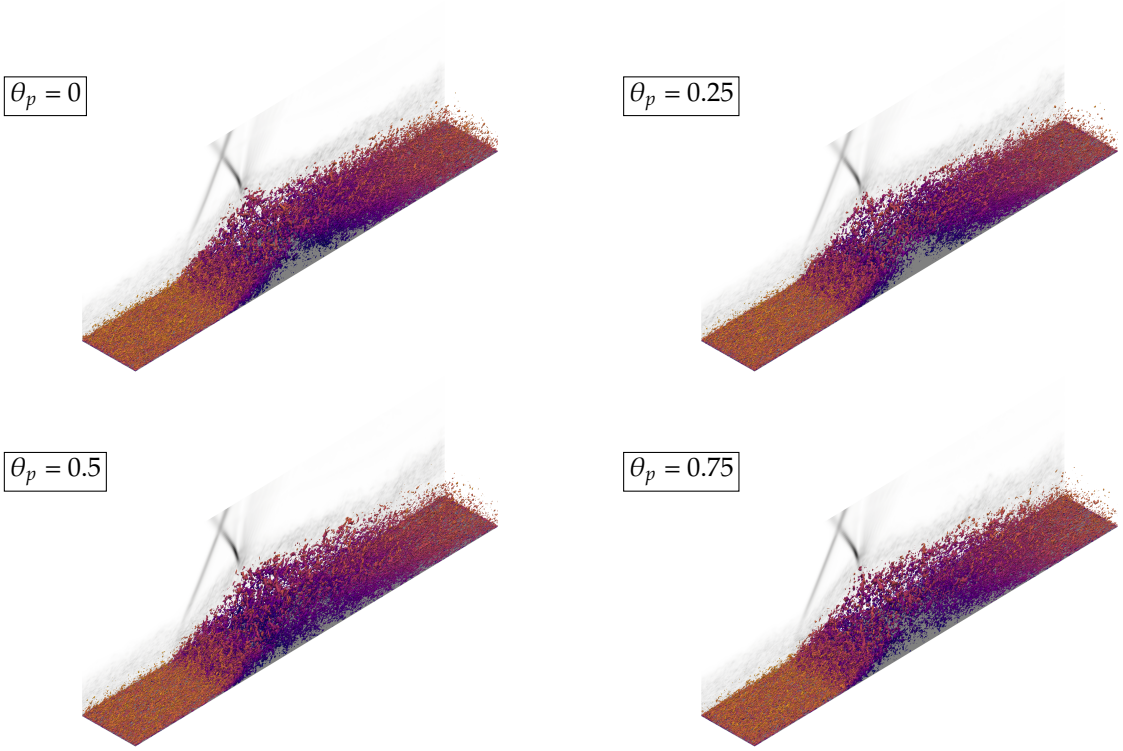


Figure C.21: Injection-phase-averaged vortical structures, visualized with the λ_{ci} criterion and colored by the local streamwise velocity for case LMFL. An isovalue of $\lambda_{ci}/u_\infty = 0.1021$ is used. A phase-averaged numerical Schlieren is shown in the background.

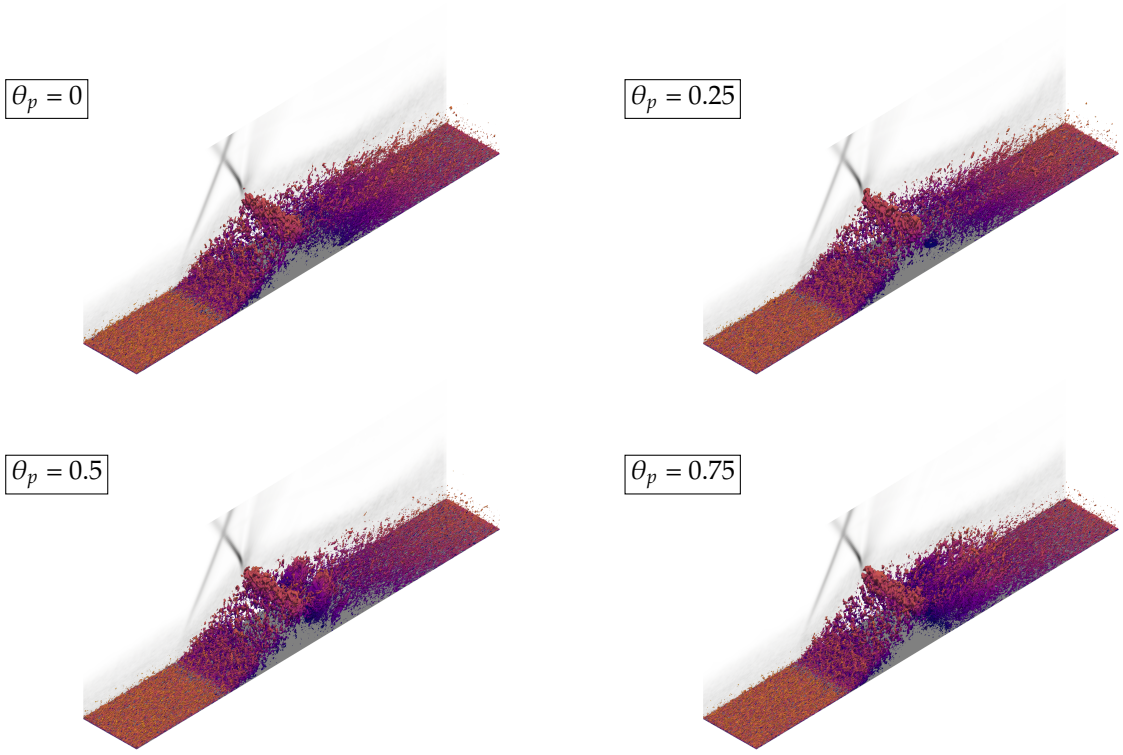


Figure C.22: Injection-phase-averaged vortical structures, visualized with the λ_{ci} criterion and colored by the local streamwise velocity for case LRFH. An isovalue of $\lambda_{ci}/u_\infty = 0.1021$ is used. A phase-averaged numerical Schlieren is shown in the background.

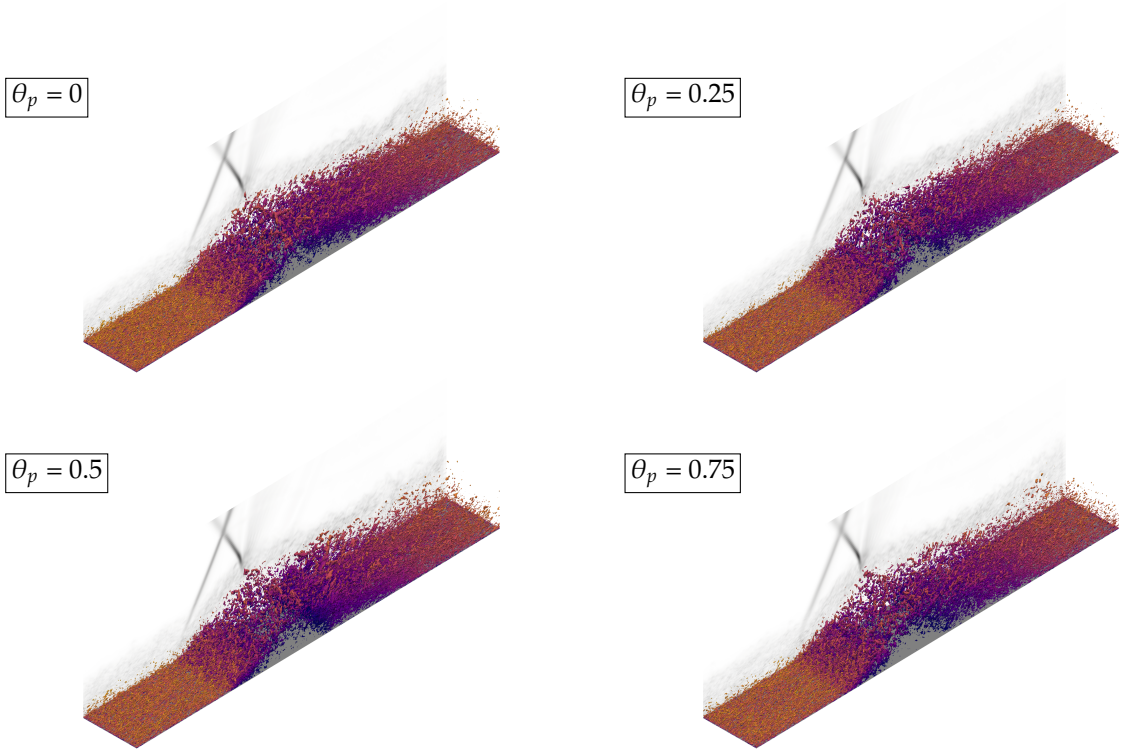


Figure C.23: Injection-phase-averaged vortical structures, visualized with the λ_{ci} criterion and colored by the local streamwise velocity for case LRFL. An isovalue of $\lambda_{ci}/u_\infty = 0.1021$ is used. A phase-averaged numerical Schlieren is shown in the background.

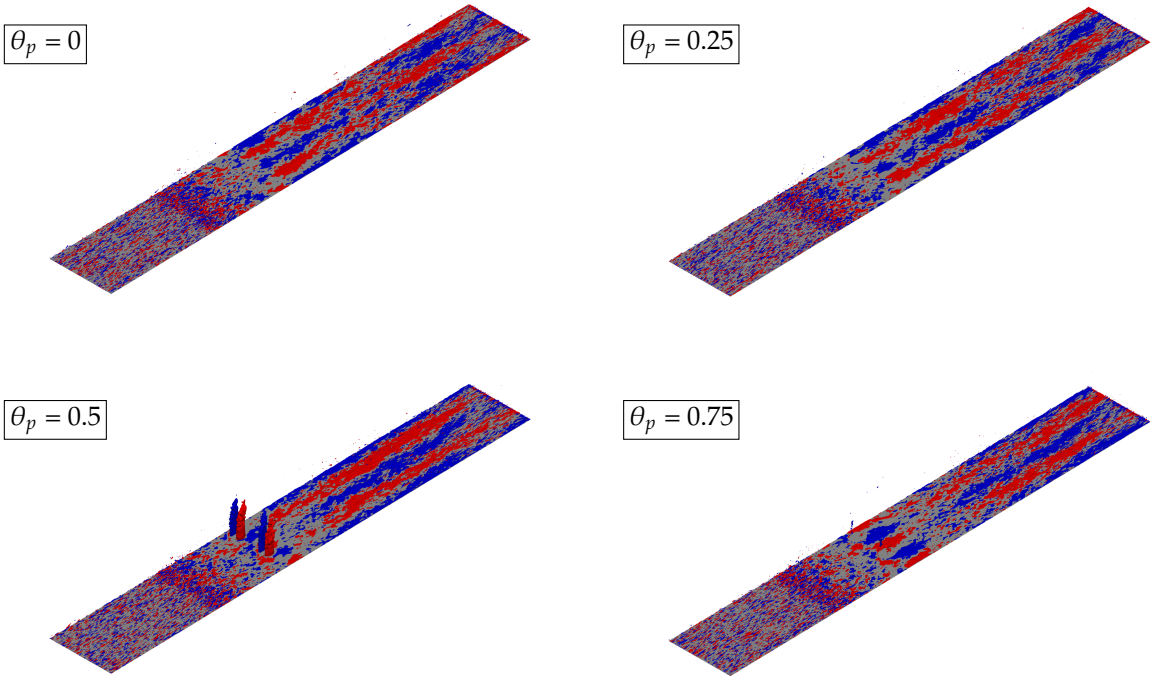


Figure C.24: Injection-phase-averaged vorticity visualized by iso-contours of ω_x for case LMFH, where red is ω_x = 0.2 and blue is ω_x = -0.2.

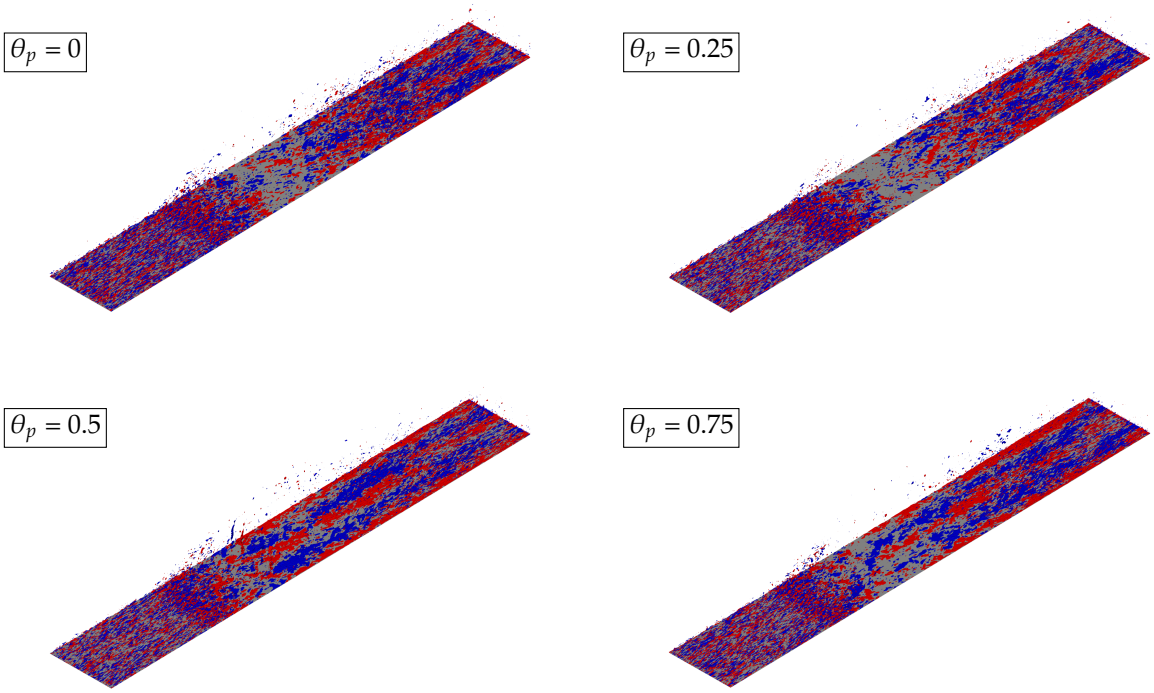


Figure C.25: Injection-phase-averaged vorticity visualized by iso-contours of ω_x for case LMFL, where red is ω_x = 0.4 and blue is ω_x = -0.4.

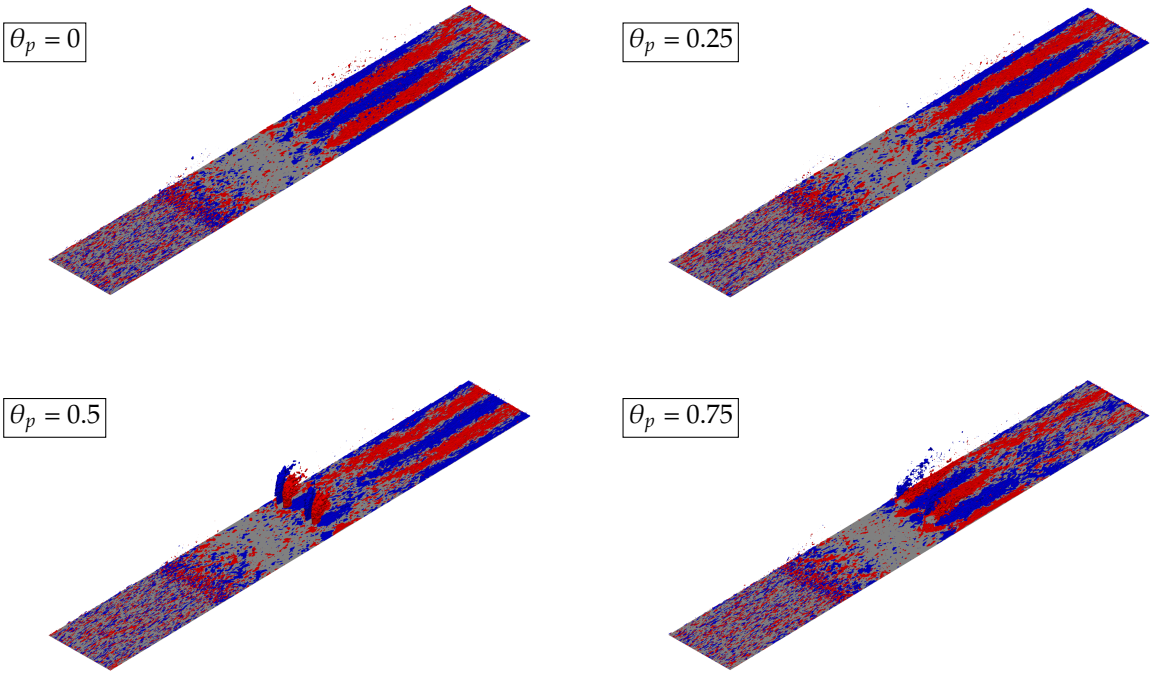


Figure C.26: Injection-phase-averaged vorticity visualized by iso-contours of ω_x for case LRFH, where red is ω_x = 0.2 and blue is ω_x = -0.2.

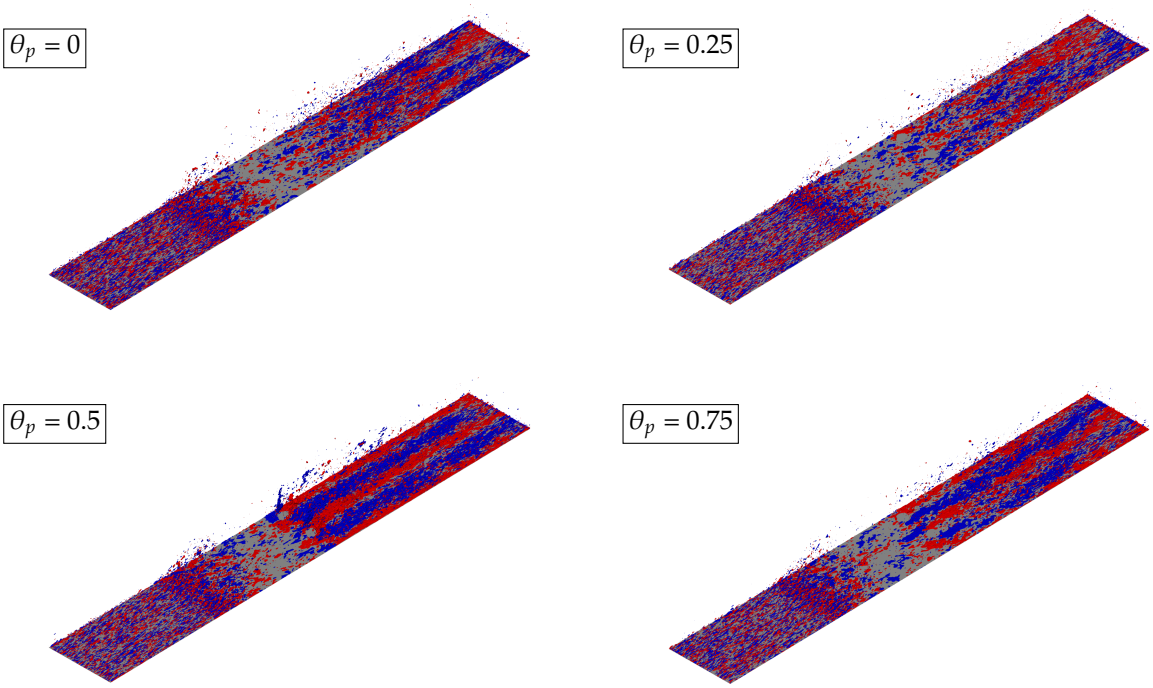


Figure C.27: Injection-phase-averaged vorticity visualized by iso-contours of ω_x for case LRFL, where red is ω_x = 0.4 and blue is ω_x = -0.4.

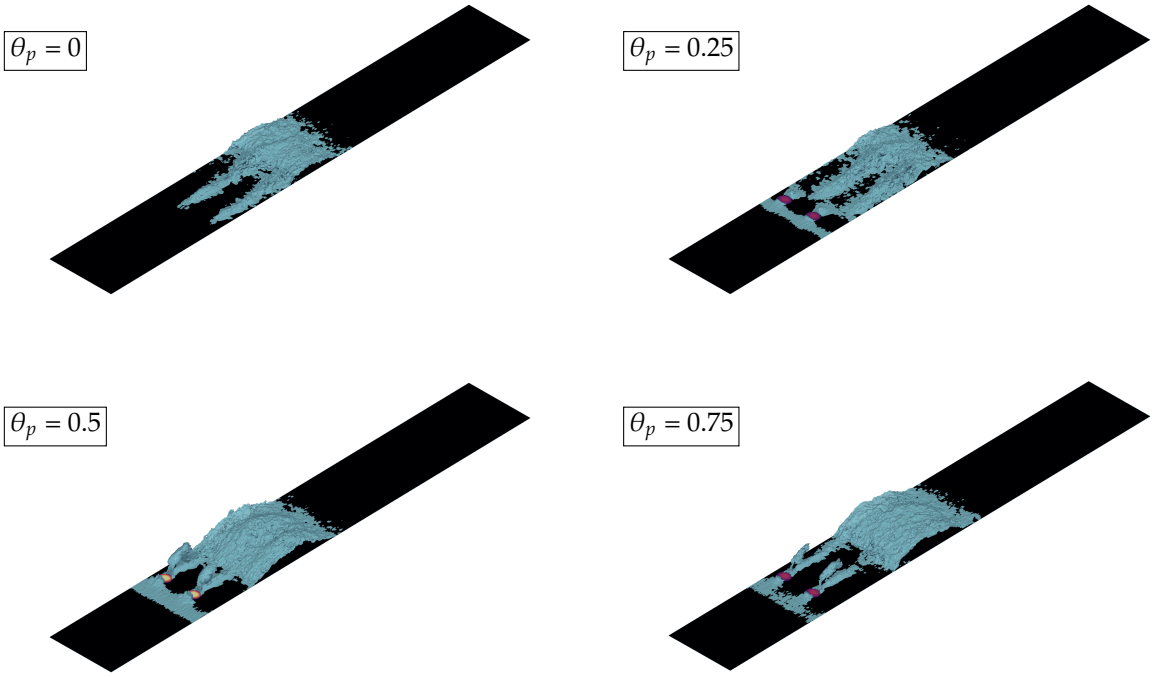


Figure C.28: Injection-phase-averaged bubble shape, visualized with the iso-surface of $u = 0$ for case LSFH.

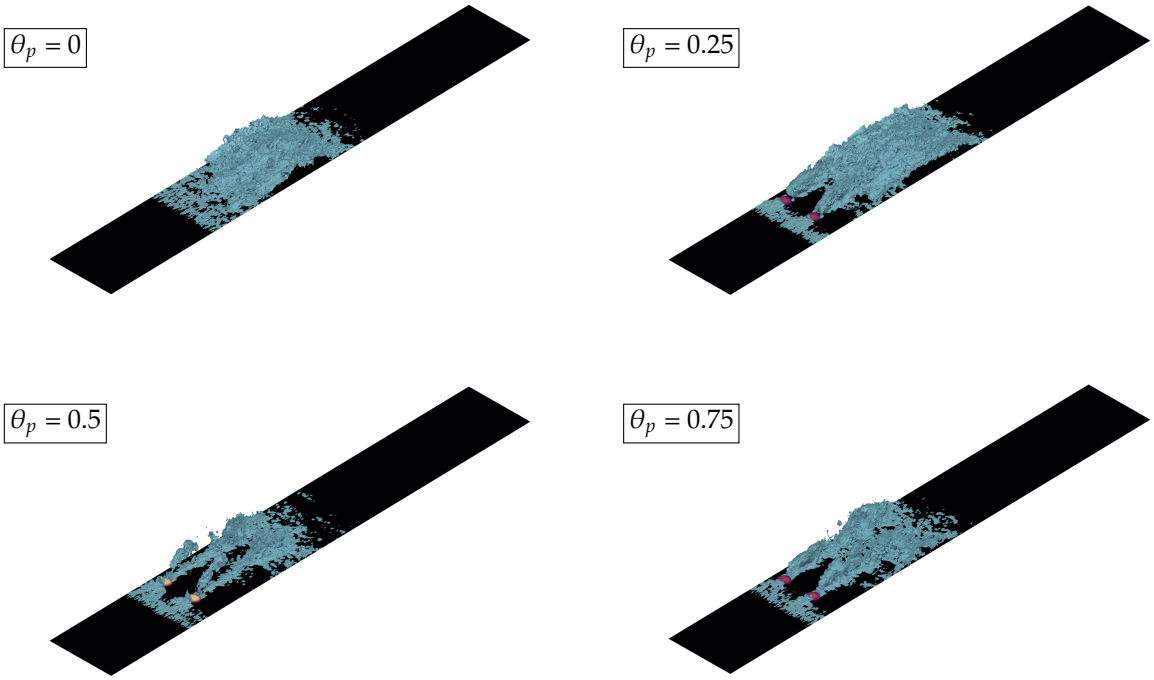


Figure C.29: Injection-phase-averaged bubble shape, visualized with the iso-surface of $u = 0$ for case LSFL.

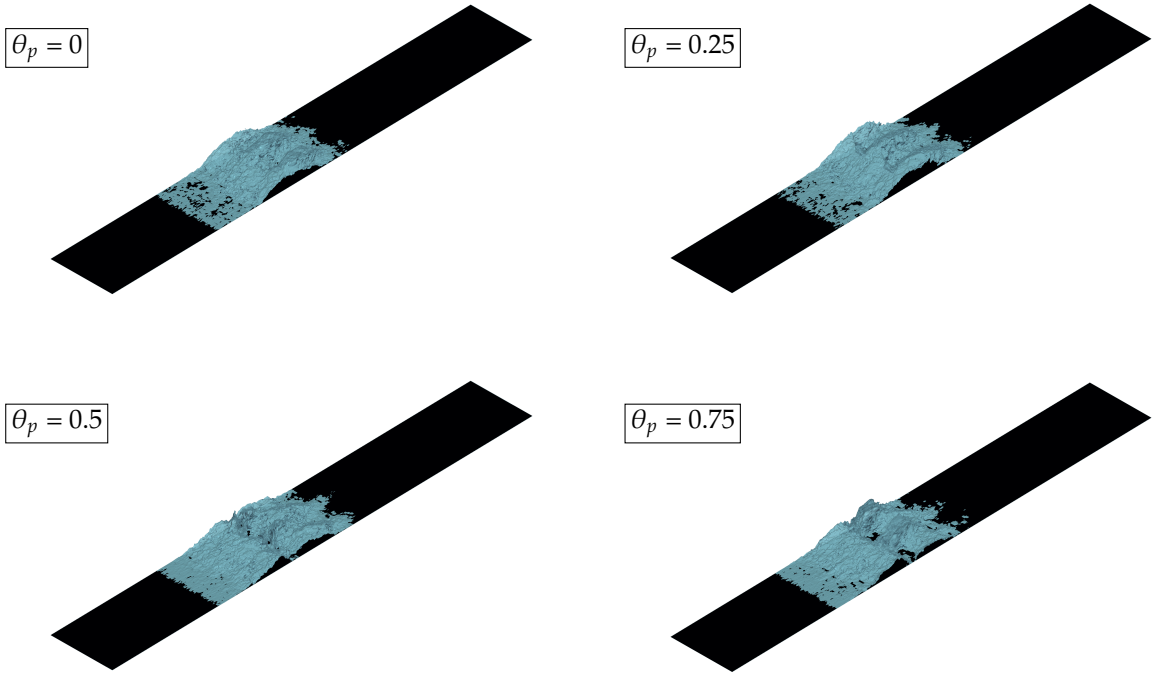


Figure C.30: Injection-phase-averaged bubble shape, visualized with the iso-surface of $u = 0$ for case LMFH.

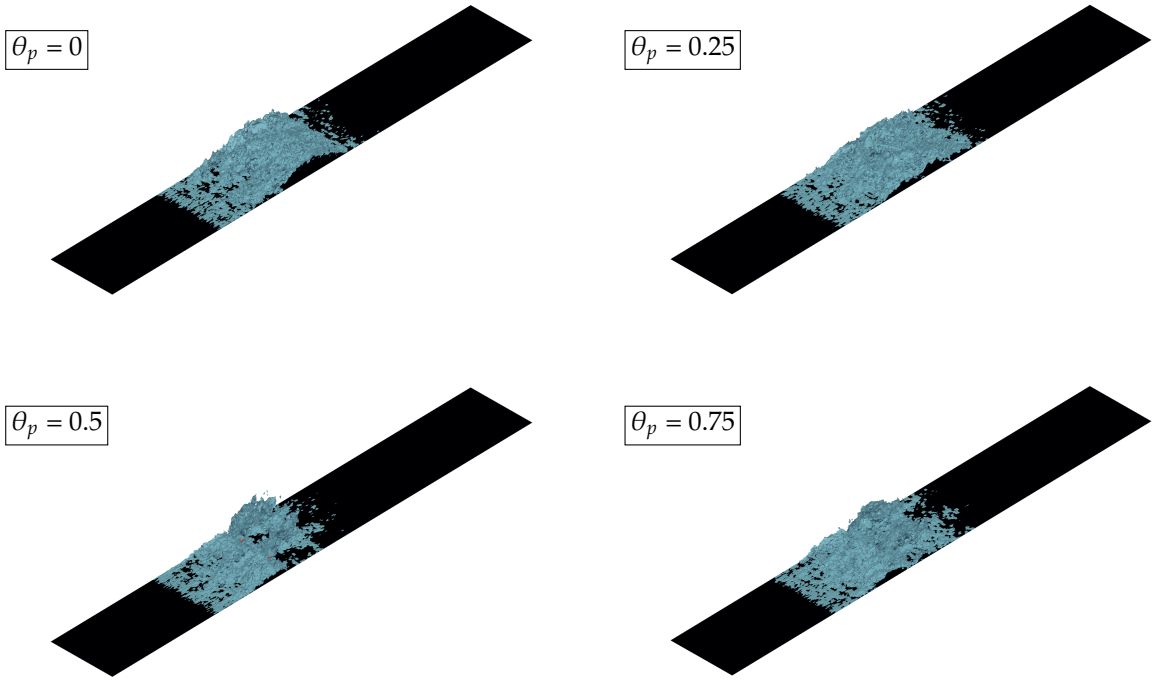


Figure C.31: Injection-phase-averaged bubble shape, visualized with the iso-surface of $u = 0$ for case LMFL.

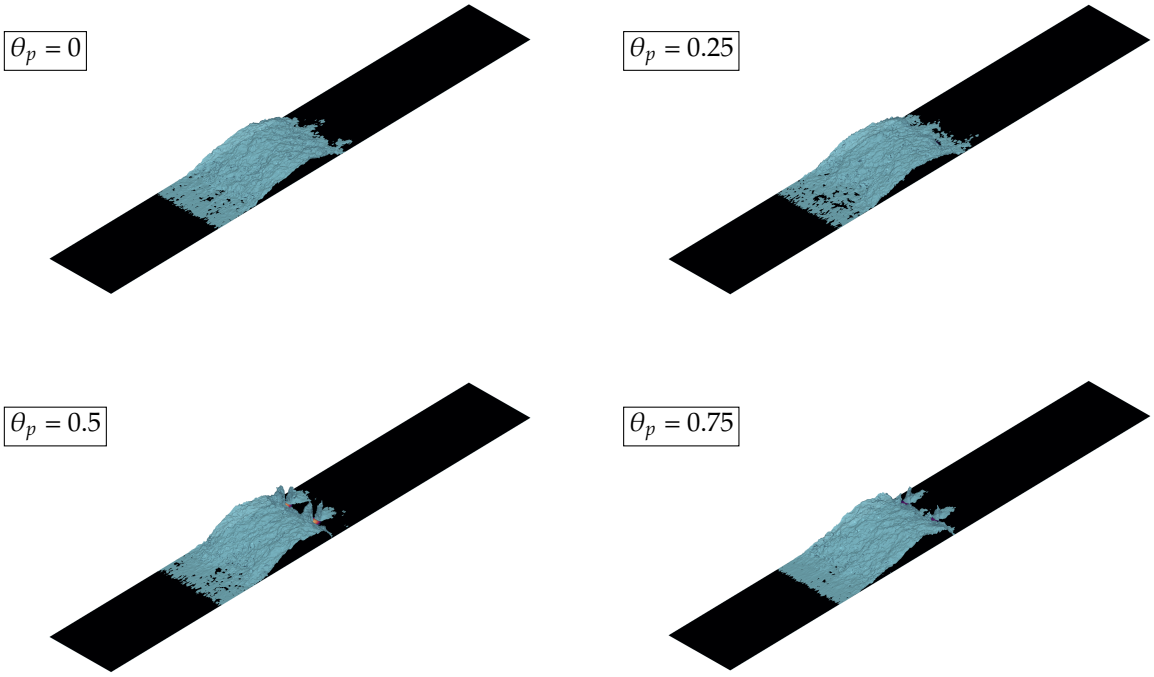


Figure C.32: Injection-phase-averaged bubble shape, visualized with the iso-surface of $u = 0$ for case LRFH.

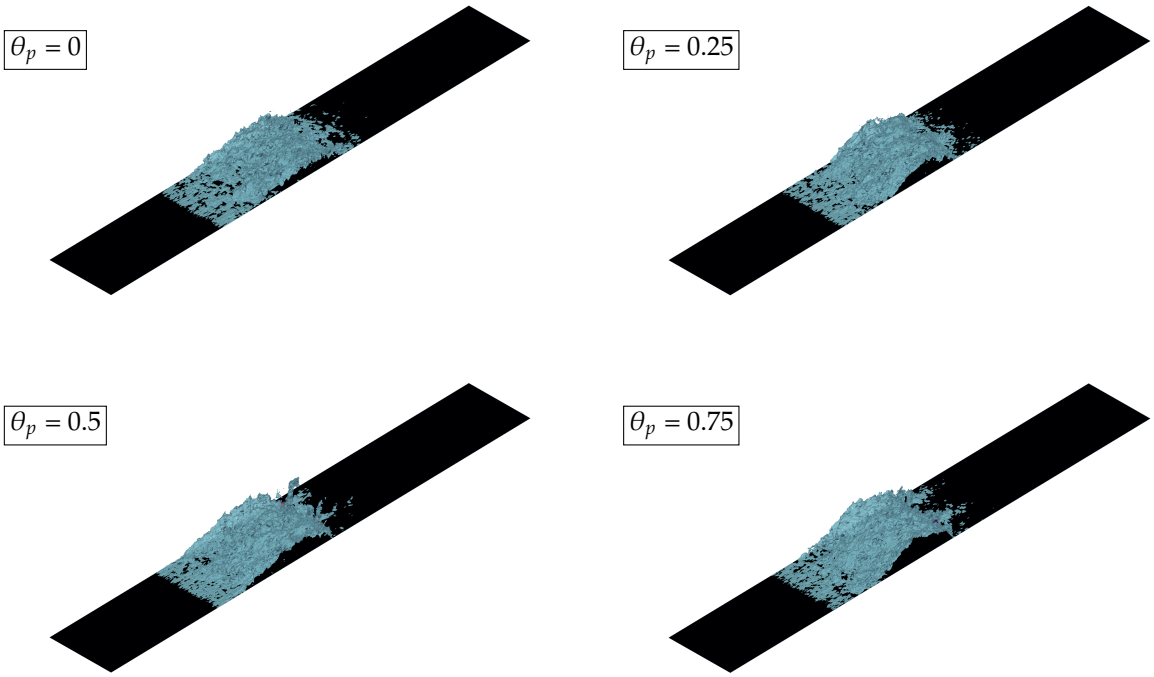


Figure C.33: Injection-phase-averaged bubble shape, visualized with the iso-surface of $u = 0$ for case LRFL.

C.4. Statistics

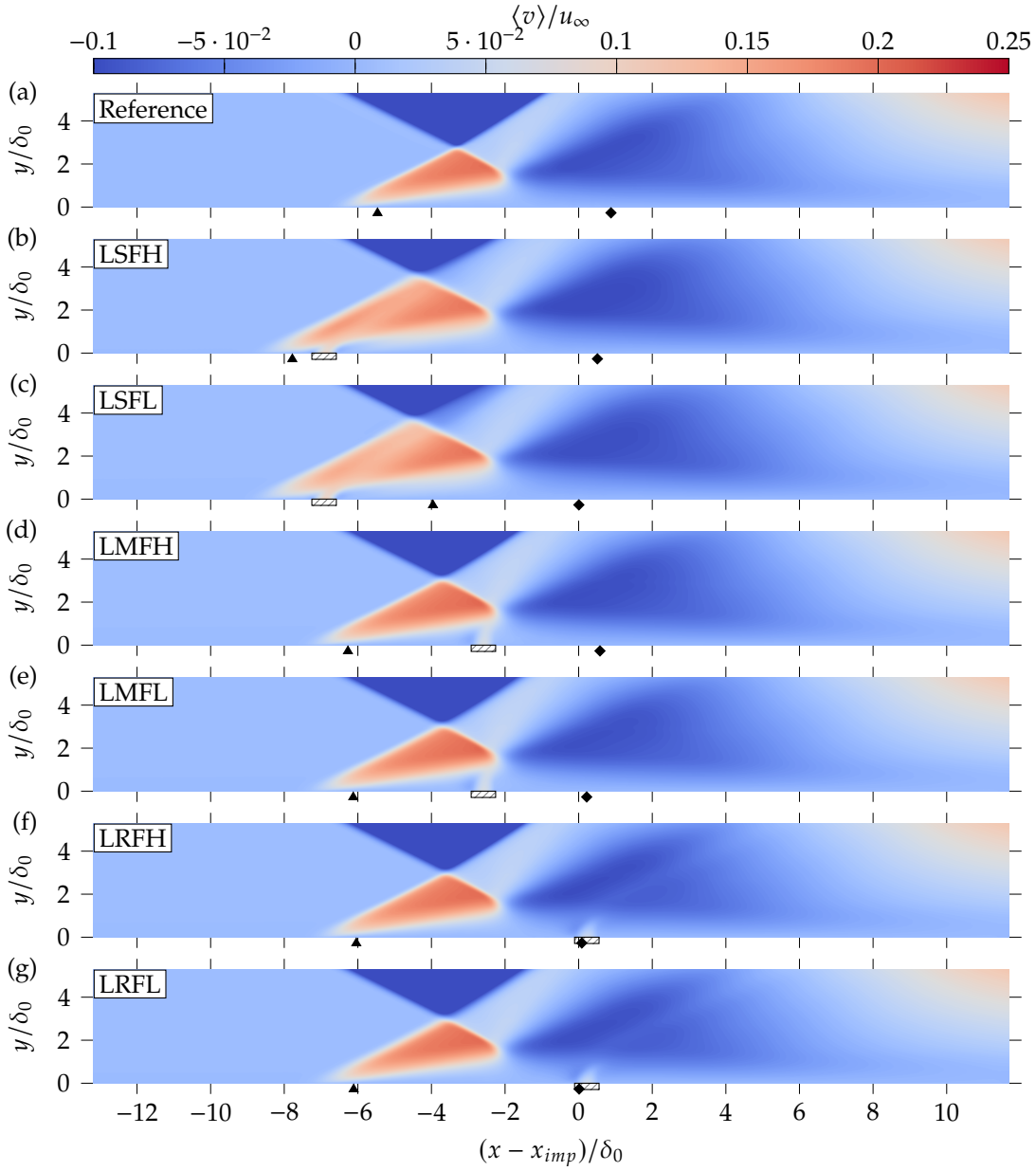


Figure C.34: Time- and spanwise-averaged wall-normal velocity v field comparison for: (a) Reference case, (b) case LSFH, (c) case LSFL, (d) case LMFH, (e) case LMFL, (f) case LRFH, and (g) case LRFL. The statistical separation and reattachment points are indicated by ▲ and ◆ respectively. The AL is indicated by ▨.

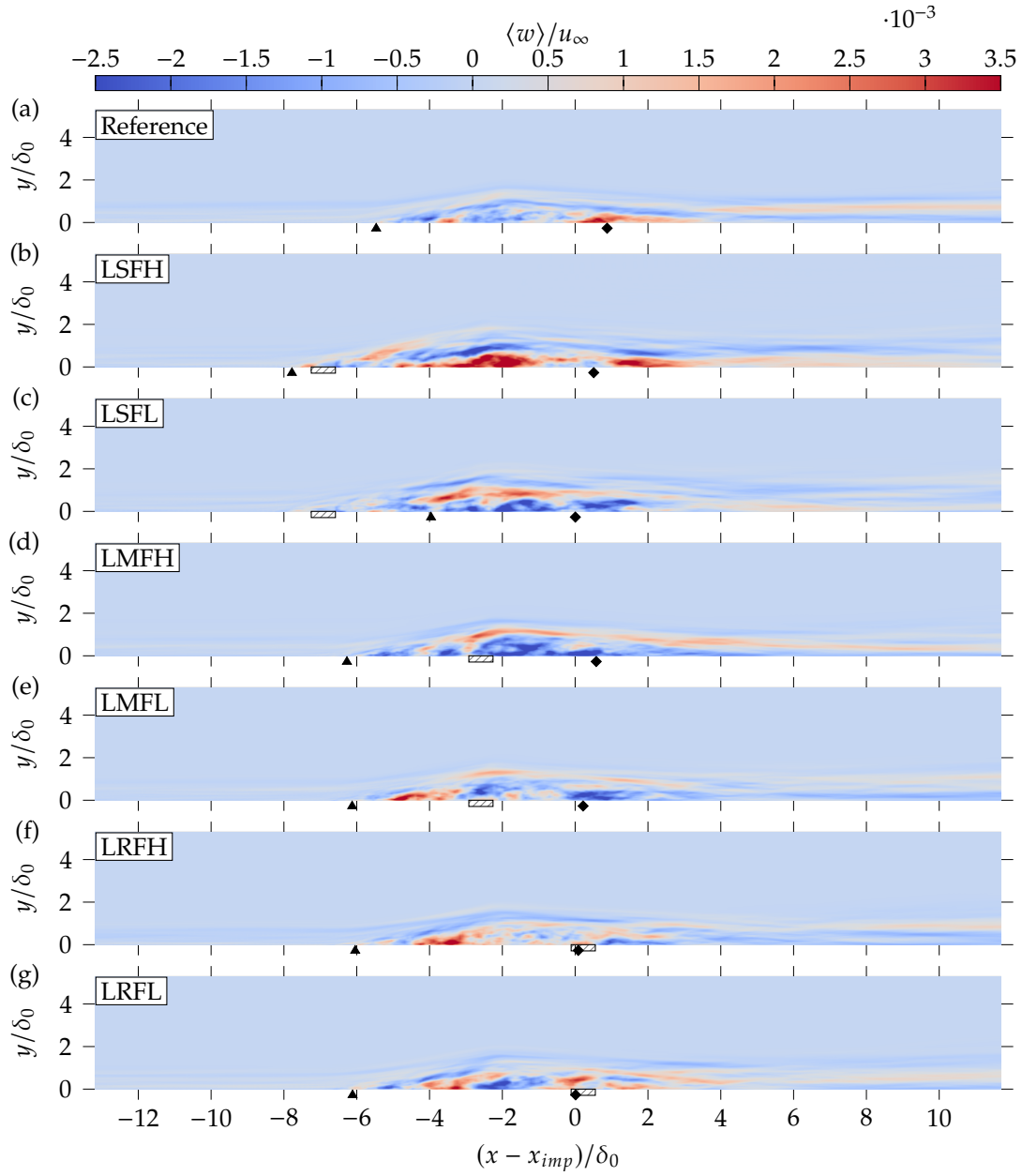


Figure C.35: Time- and spanwise-averaged spanwise velocity w field comparison for: (a) Reference case, (b) case LSFH, (c) case LSFL, (d) case LMFH, (e) case LMFL, (f) case LRFH, and (g) case LRFL. The statistical separation and reattachment points are indicated by ▲ and ◆ respectively. The AL is indicated by ▨.

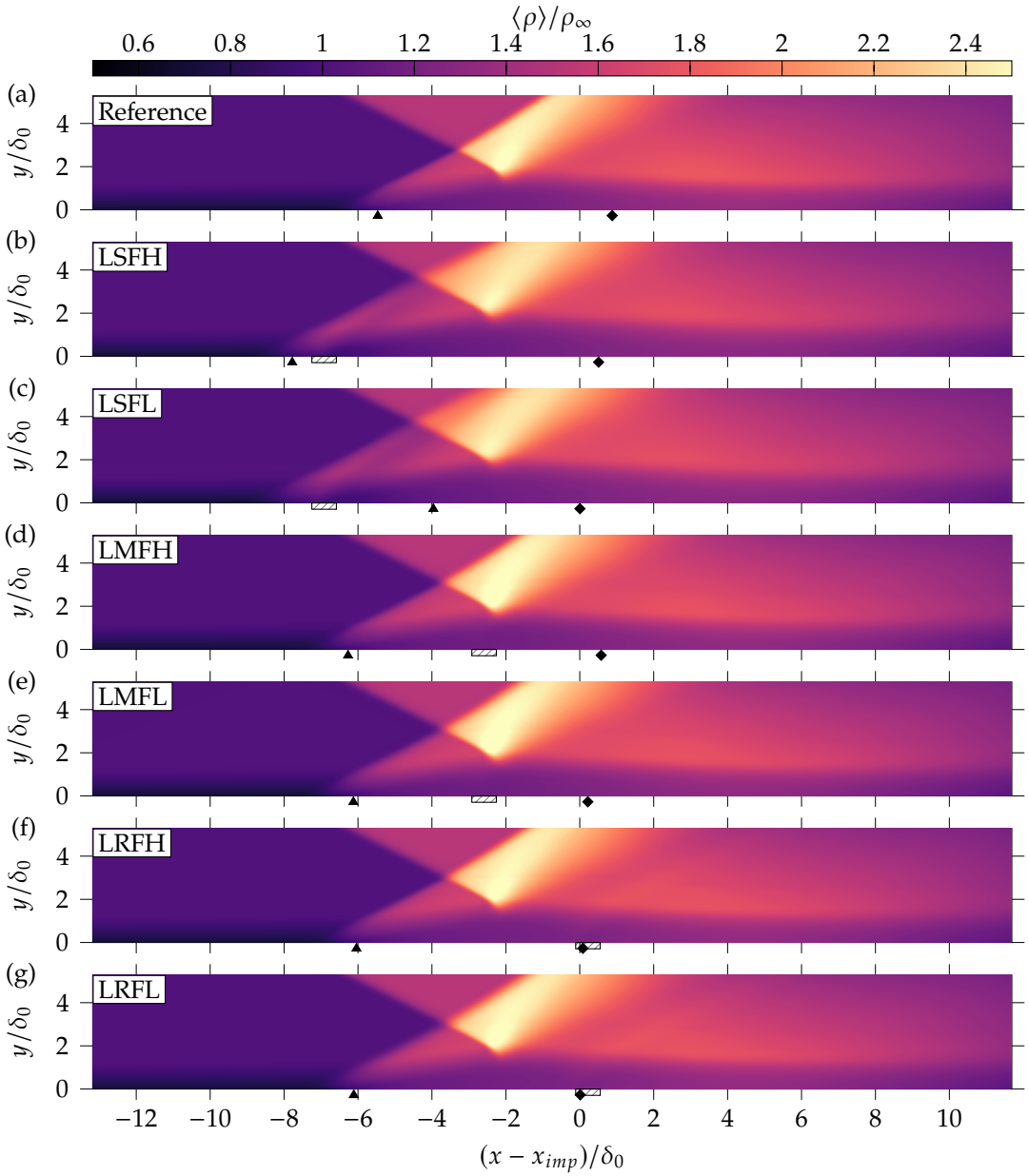


Figure C.36: Time- and spanwise-averaged density ρ comparison for: (a) Reference case, (b) case LSFH, (c) case LSFL, (d) case LMFH, (e) case LMFL, (f) case LRFH, and (g) case LRFL. The statistical separation and reattachment points are indicated by ▲ and ◆ respectively. The AL is indicated by ▨.

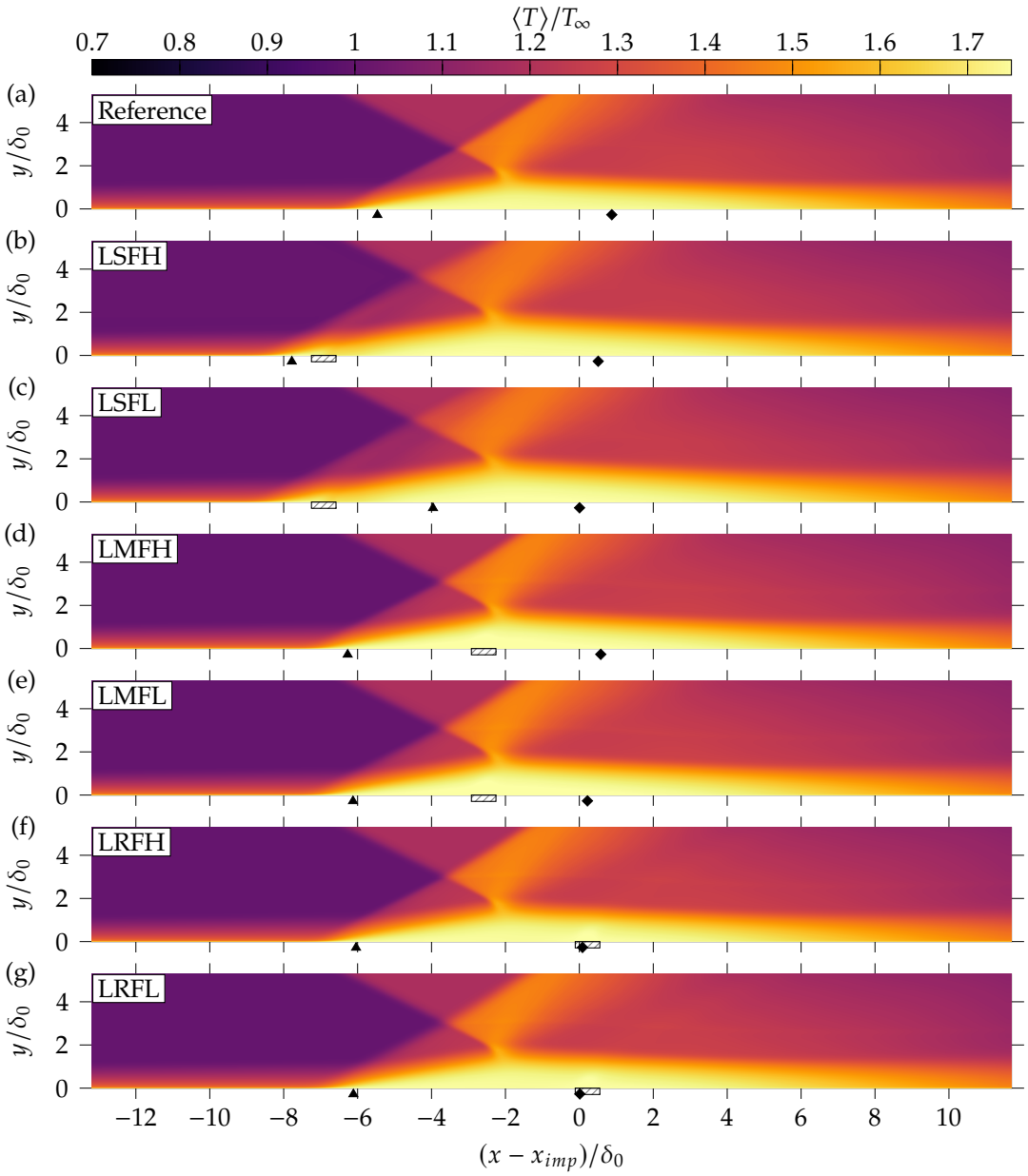


Figure C.37: Time- and spanwise-averaged temperature T comparison for: (a) Reference case, (b) case LSFH, (c) case LSFL, (d) case LMFH, (e) case LMFL, (f) case LRFH, and (g) case LRFL. The statistical separation and reattachment points are indicated by ▲ and ◆ respectively. The AL is indicated by ▨.

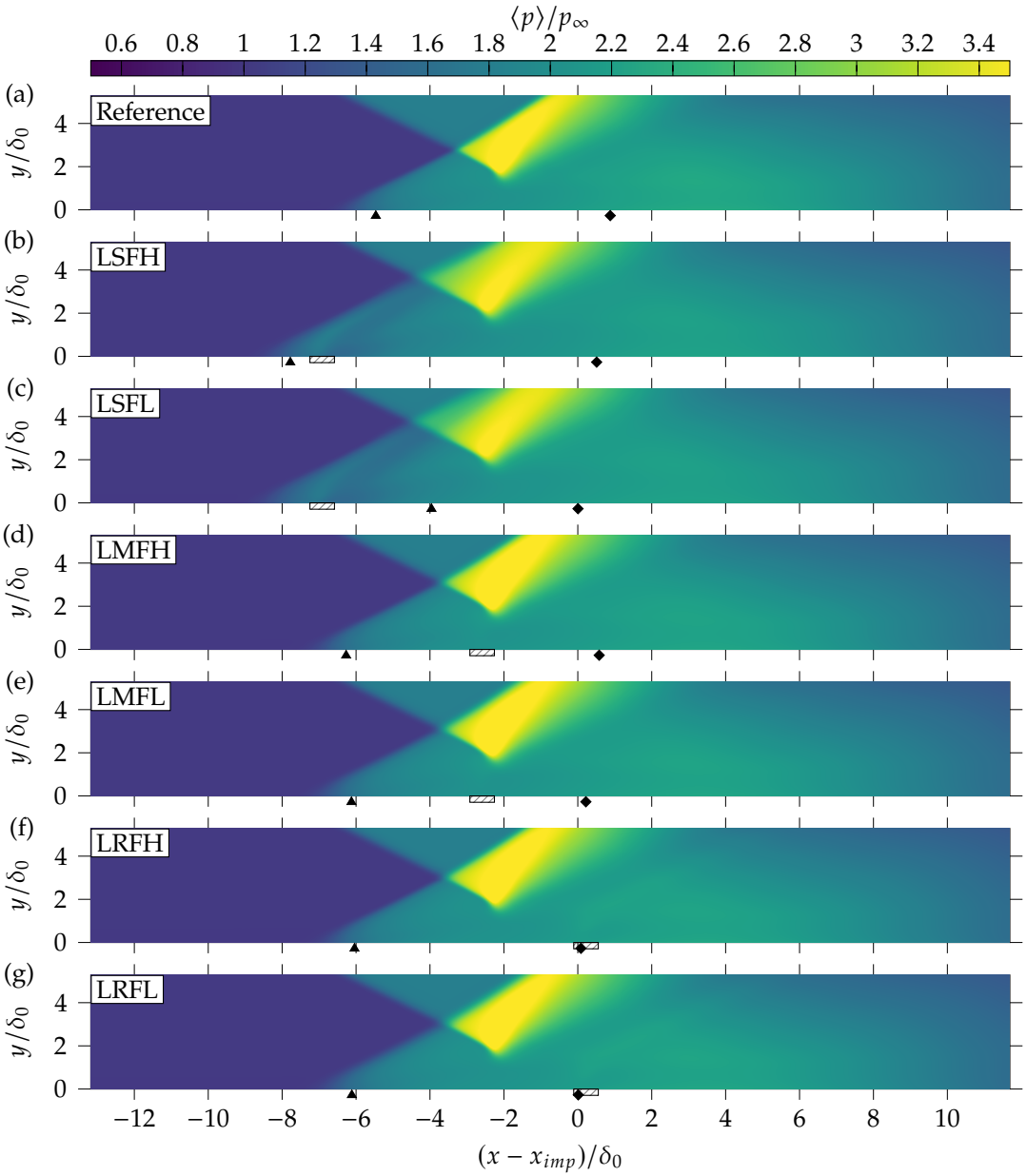


Figure C.38: Time- and spanwise-averaged pressure p comparison for: (a) Reference case, (b) case LSFH, (c) case LSFL, (d) case LMFH, (e) case LMFL, (f) case LRFH, and (g) case LRFL. The statistical separation and reattachment points are indicated by ▲ and ◆ respectively. The AL is indicated by ▨.

C.4.1. Reynolds Stresses

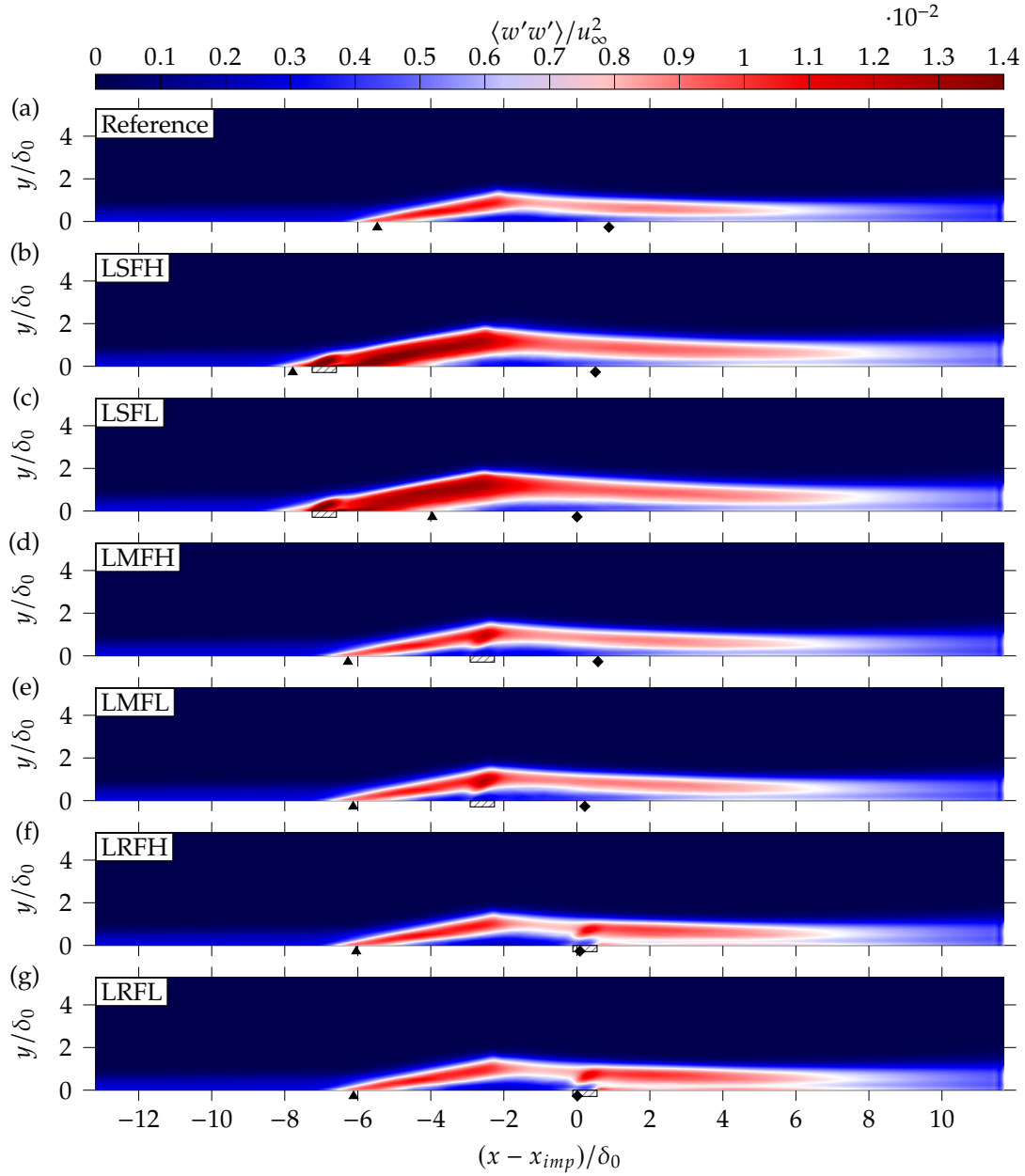


Figure C.39: Time- and spanwise-averaged Reynolds wall-normal stress $w'w'$ comparison for: (a) Reference case, (b) case LSFH, (c) case LSFL, (d) case LMFH, (e) case LMFL, (f) case LRFH, and (g) case LRFL. The statistical separation and reattachment points are indicated by ▲ and ◆ respectively. The AL is indicated by ▨.

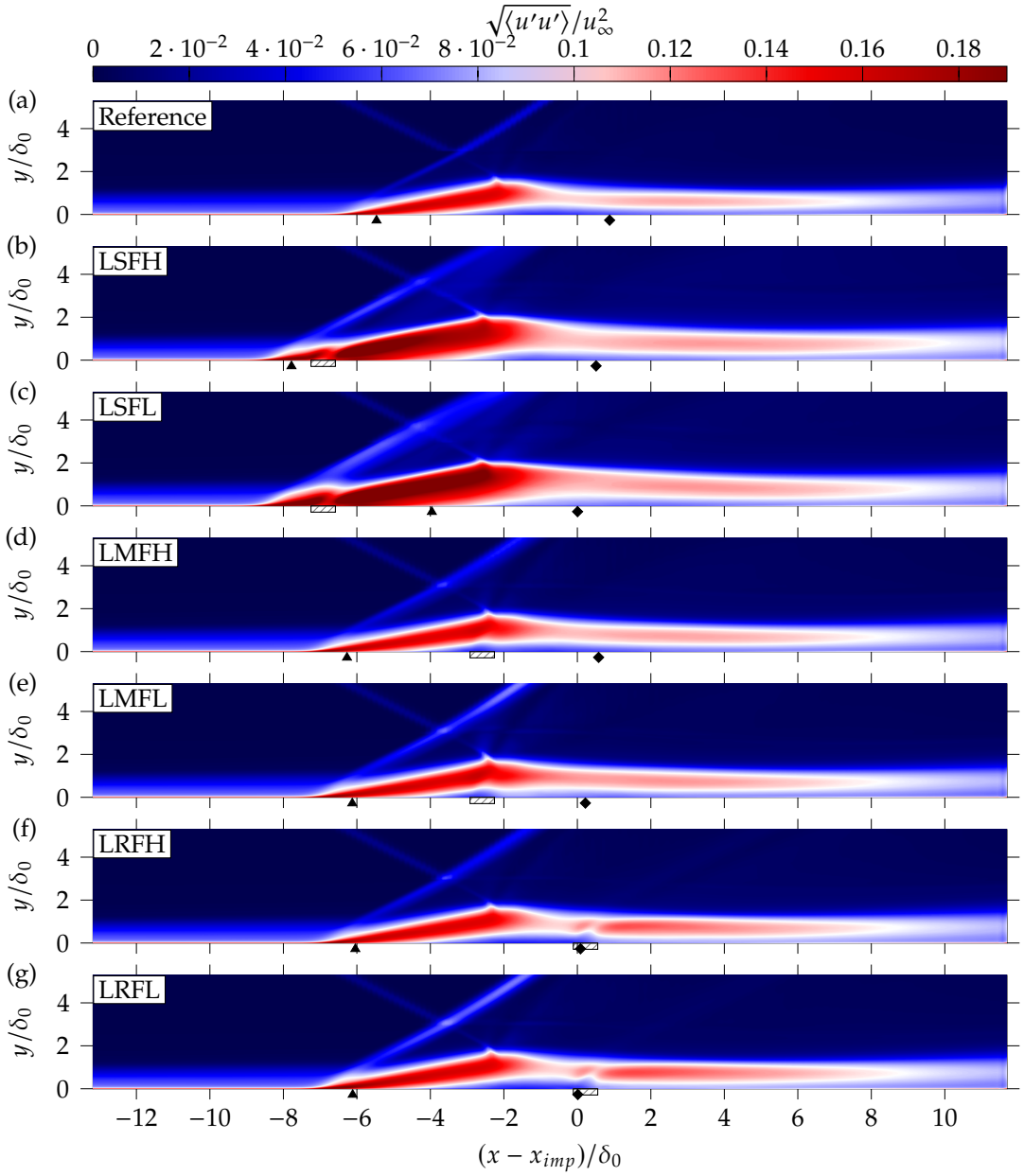


Figure C.40: Time- and spanwise-averaged RMS of $u'u'$ comparison for: (a) Reference case, (b) case LSFH, (c) case LSFL, (d) case LMFH, (e) case LMFL, (f) case LRFH, and (g) case LRFL. The statistical separation and reattachment points are indicated by ▲ and ◆ respectively. The AL is indicated by ▨.

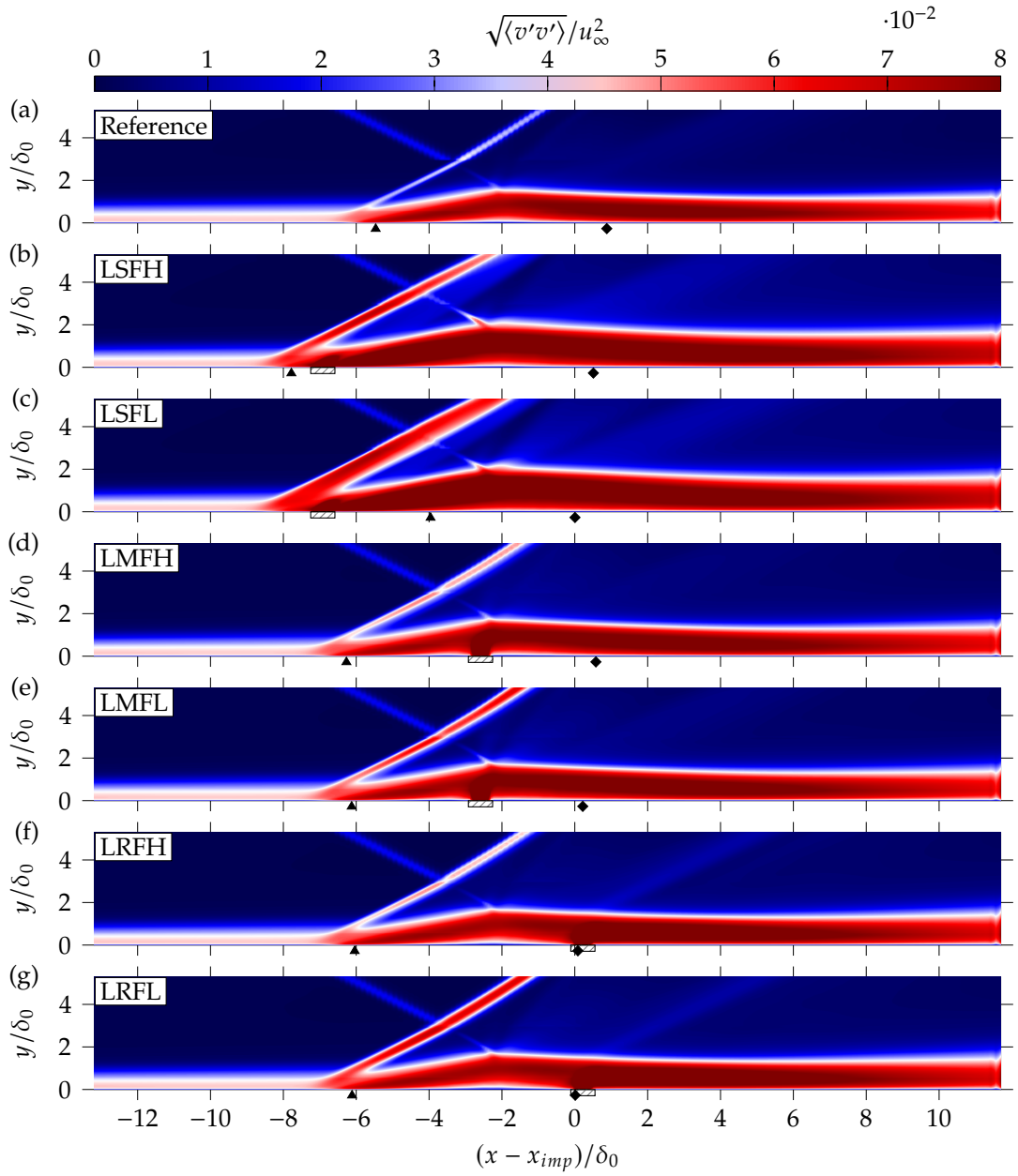


Figure C.41: Time- and spanwise-averaged RMS of $v'v'$ for: (a) Reference case, (b) case LSFH, (c) case LSFL, (d) case LMFH, (e) case LMFL, (f) case LRFH, and (g) case LRFL. The statistical separation and reattachment points are indicated by ▲ and ◆ respectively. The AL is indicated by ▨.

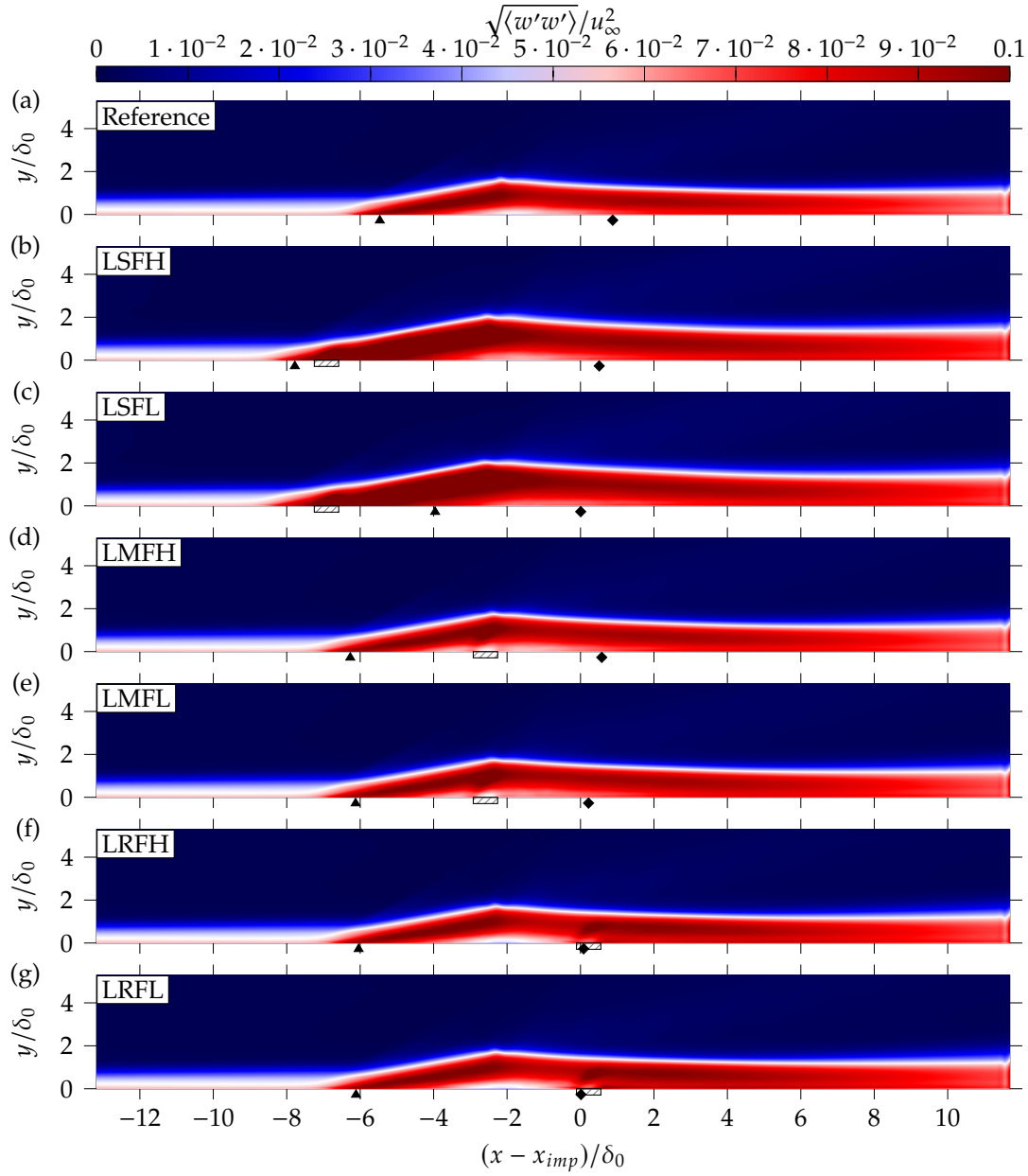


Figure C.42: Time- and spanwise-averaged RMS of $w'w'$ comparison for: (a) Reference case, (b) case LSFH, (c) case LSFL, (d) case LMFH, (e) case LMFL, (f) case LRFH, and (g) case LRFL. The statistical separation and reattachment points are indicated by ▲ and ◆ respectively. The AL is indicated by ▨.

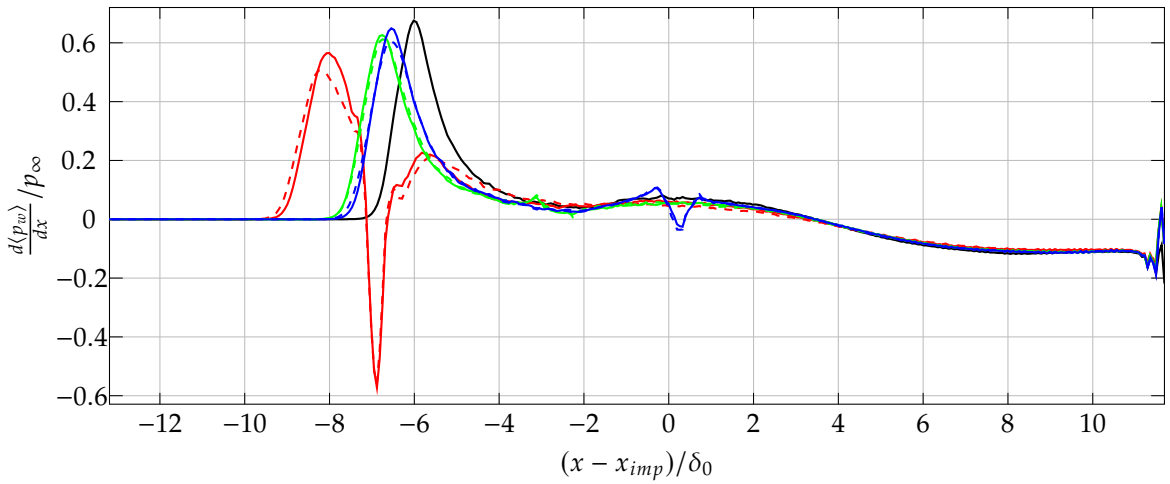


Figure C.43: Wall-pressure gradient for production cases. For line legend see Table 4.1.

C.5. Cross-Correlation

C.5.1. Bubble metrics

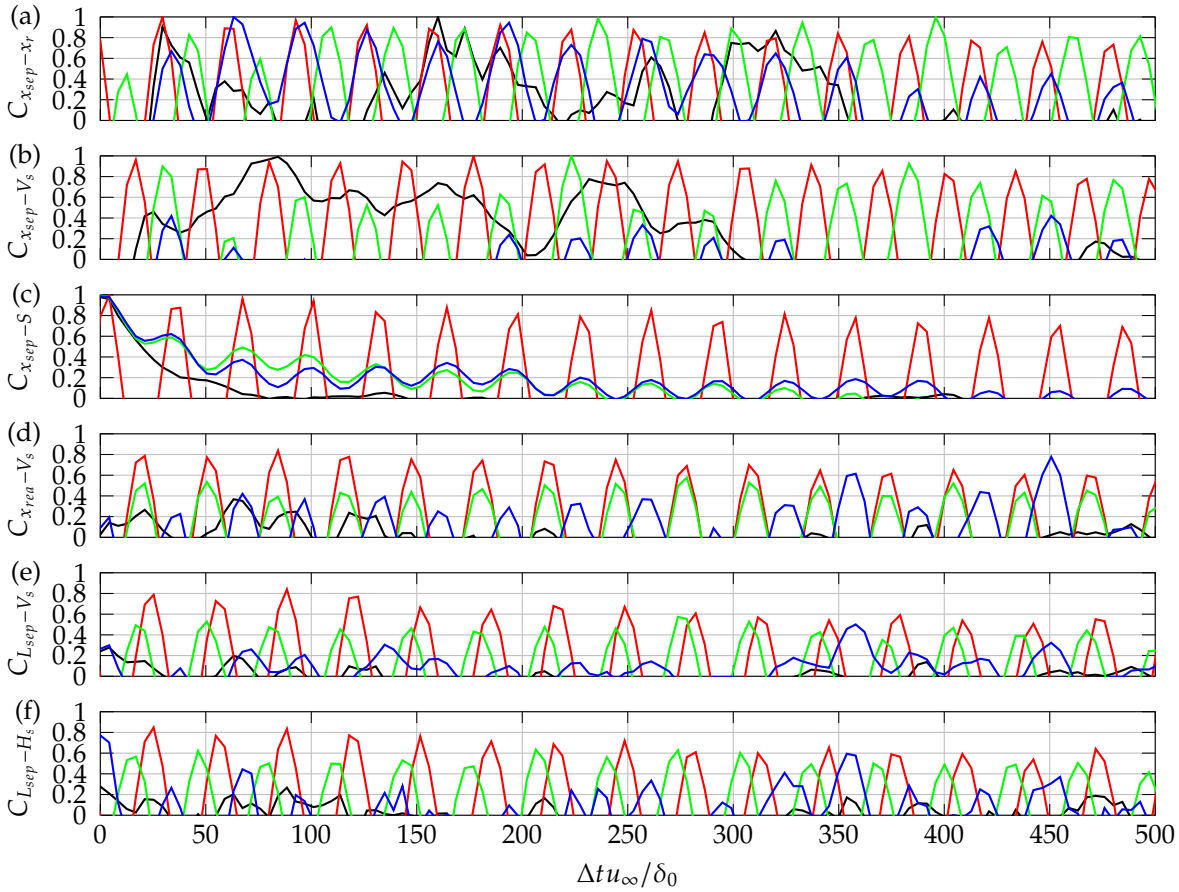


Figure C.44: Cross-correlation between different bubble metrics for the Reference and high-frequency production cases.

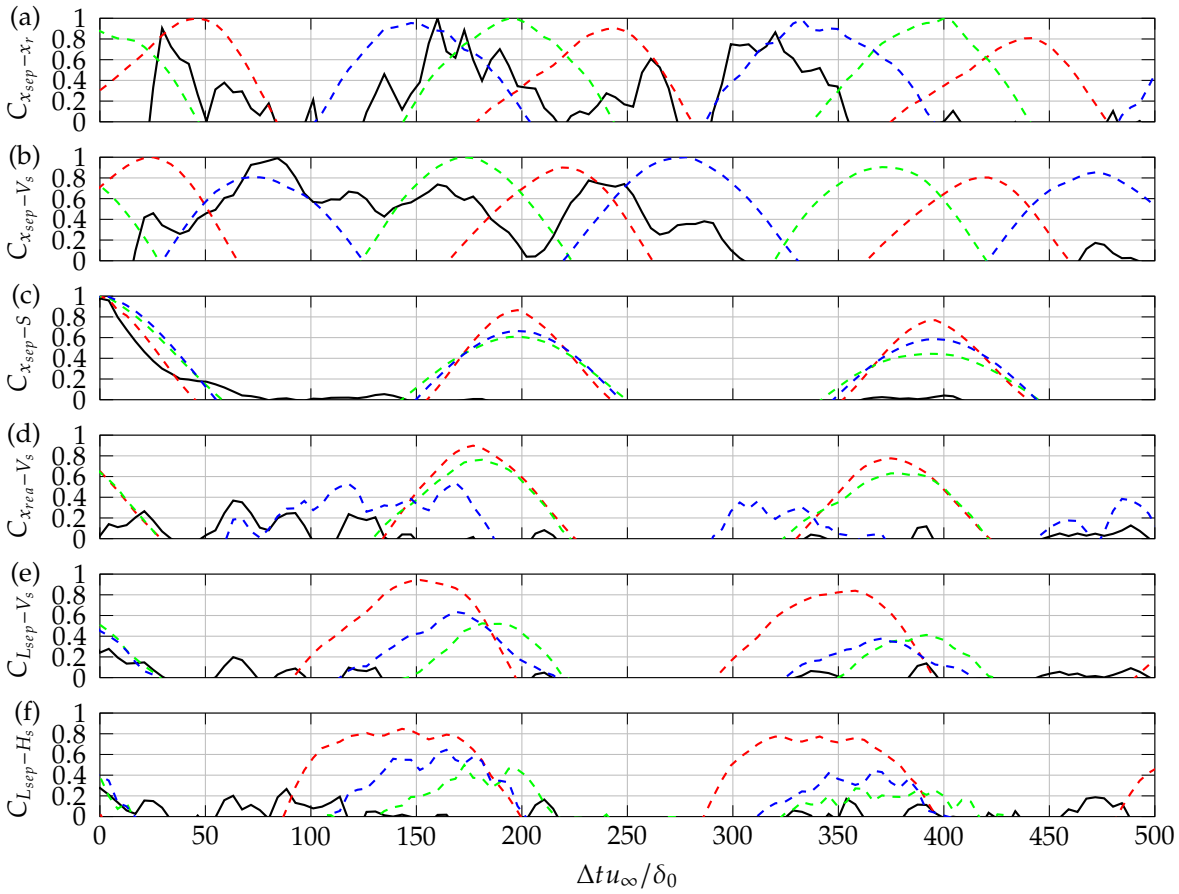


Figure C.45: Cross-correlation between different bubble metrics for the Reference and low-frequency production cases.

C.5.2. Injection velocity cross-correlation

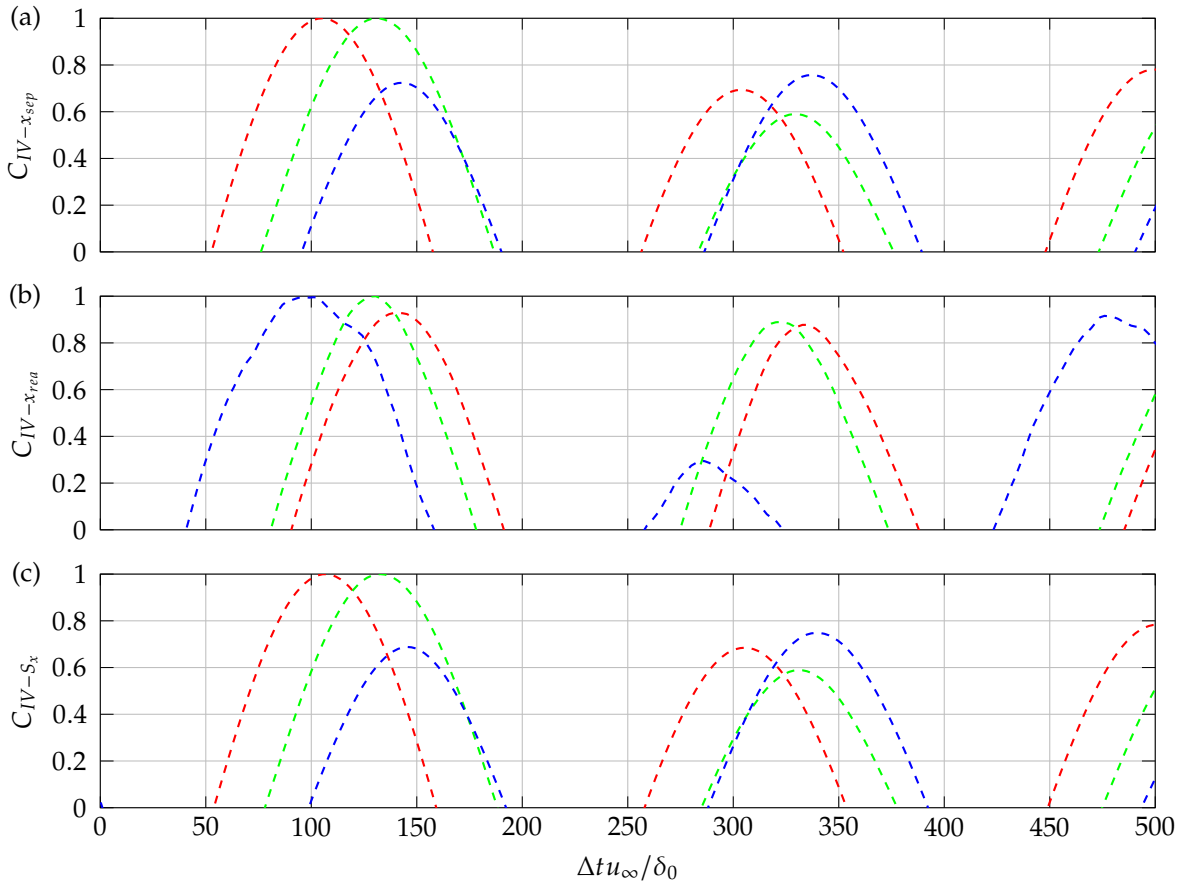


Figure C.46: Cross-correlation with injection velocity for the low-frequency production cases.

C.5.3. Pressure cross-correlation

C.5.3.1 Pressure at separation

C.5.3.2 Pressure at actuator

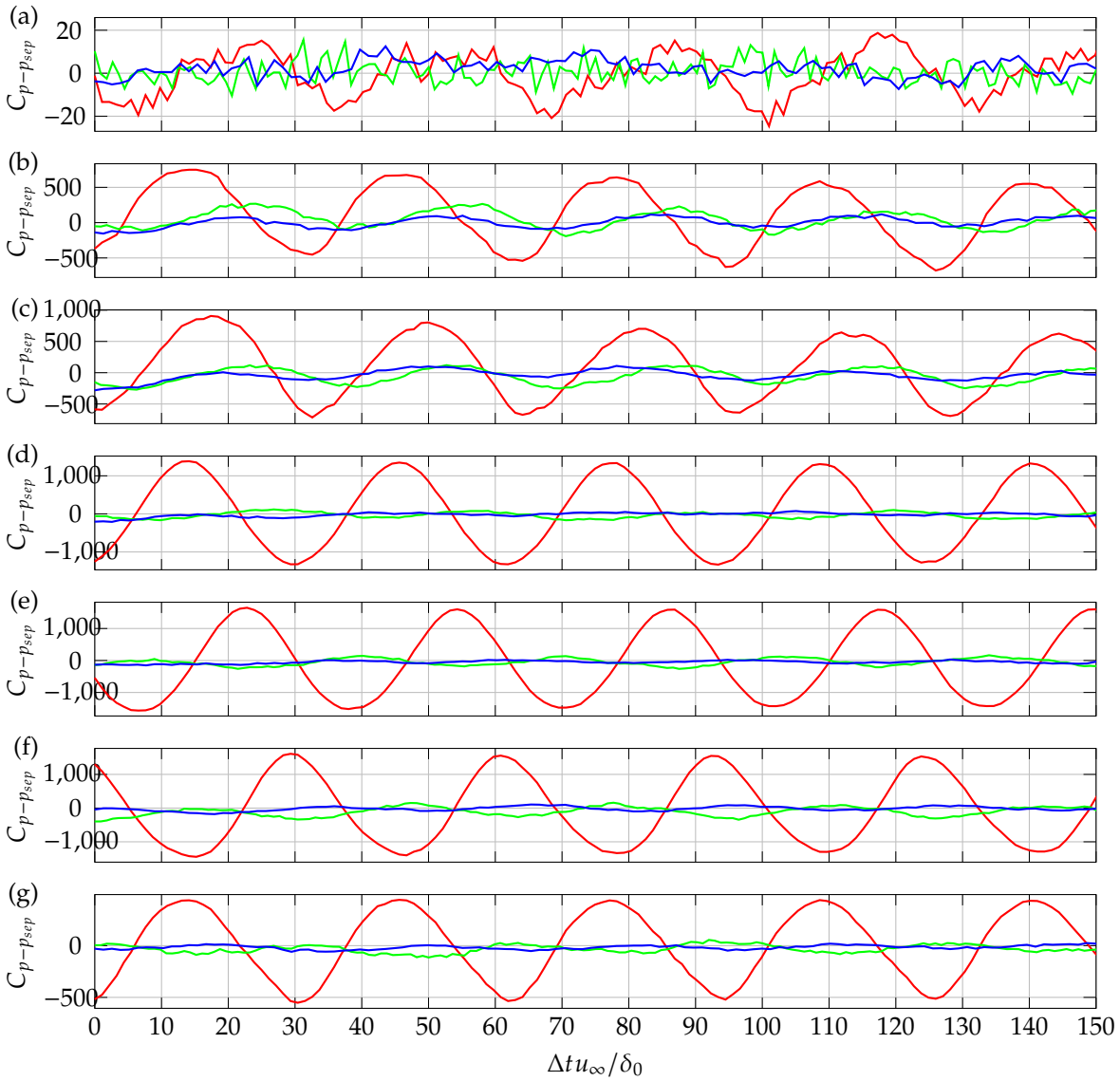


Figure C.47: Cross-correlation with pressure at S_x and the other probes for the high-frequency cases.

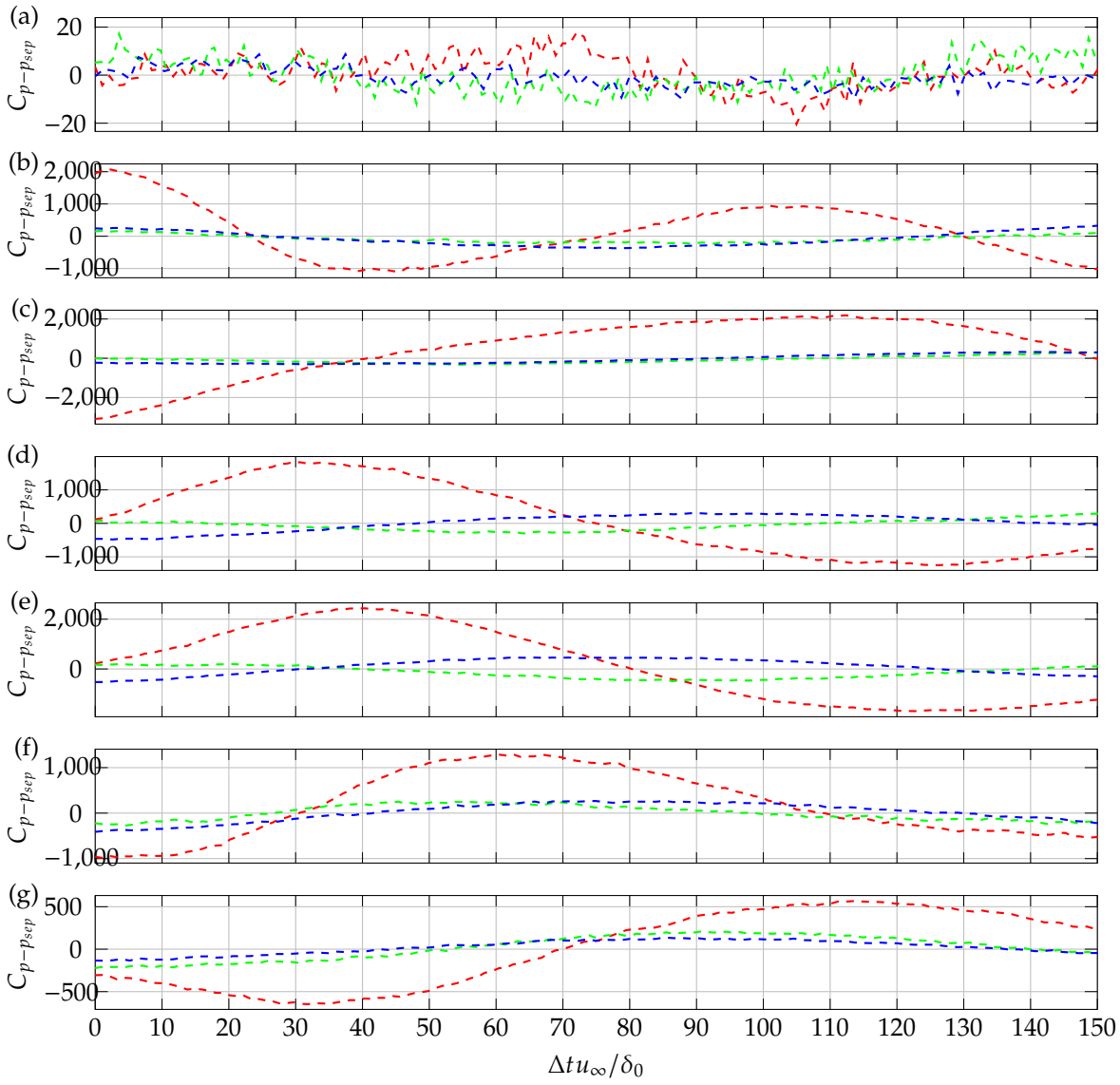


Figure C.48: Cross-correlation with pressure at S_x and the other probes for the low-frequency cases.

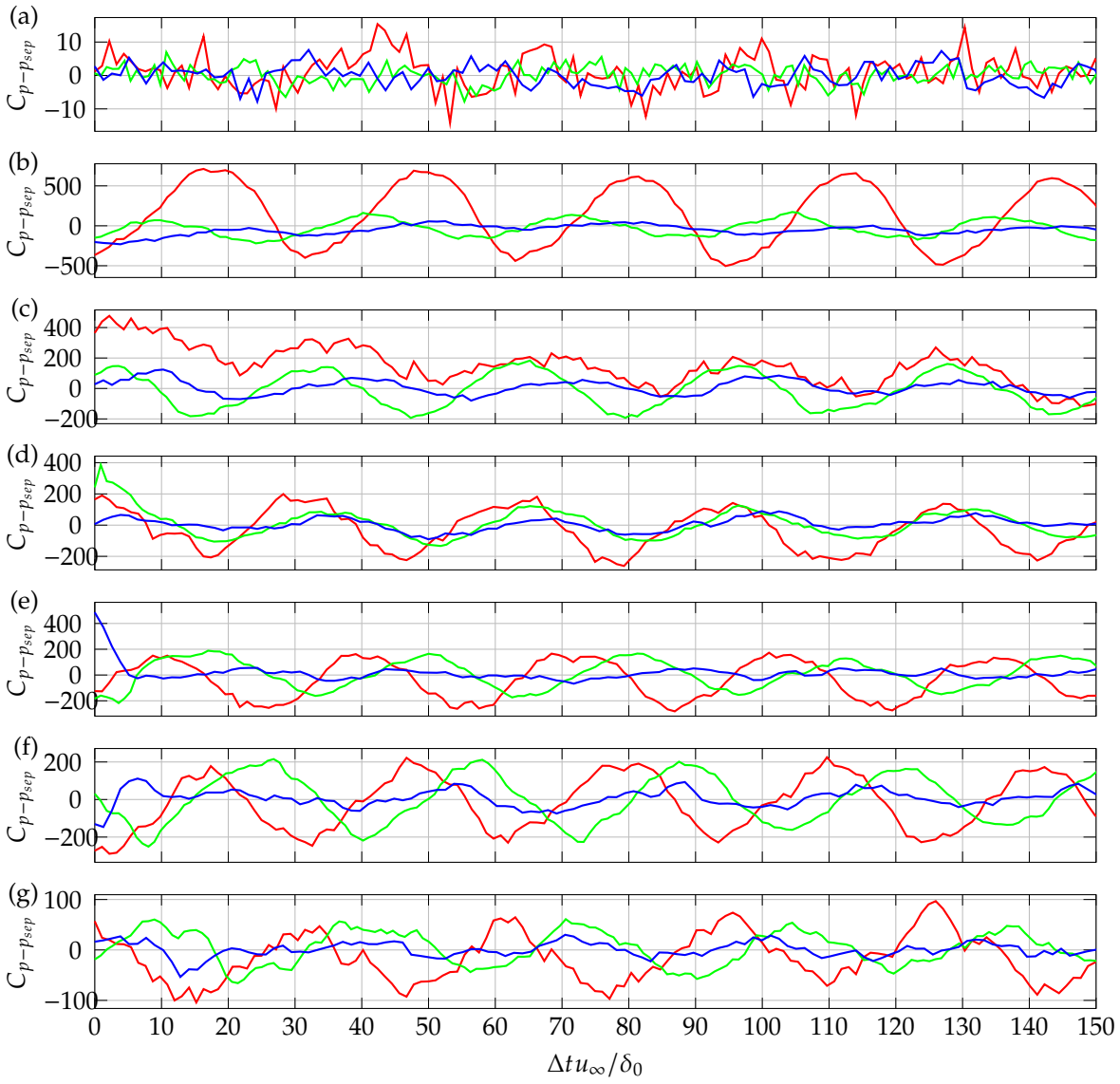


Figure C.49: Cross-correlation with pressure at AL and the other probes for the high-frequency cases.

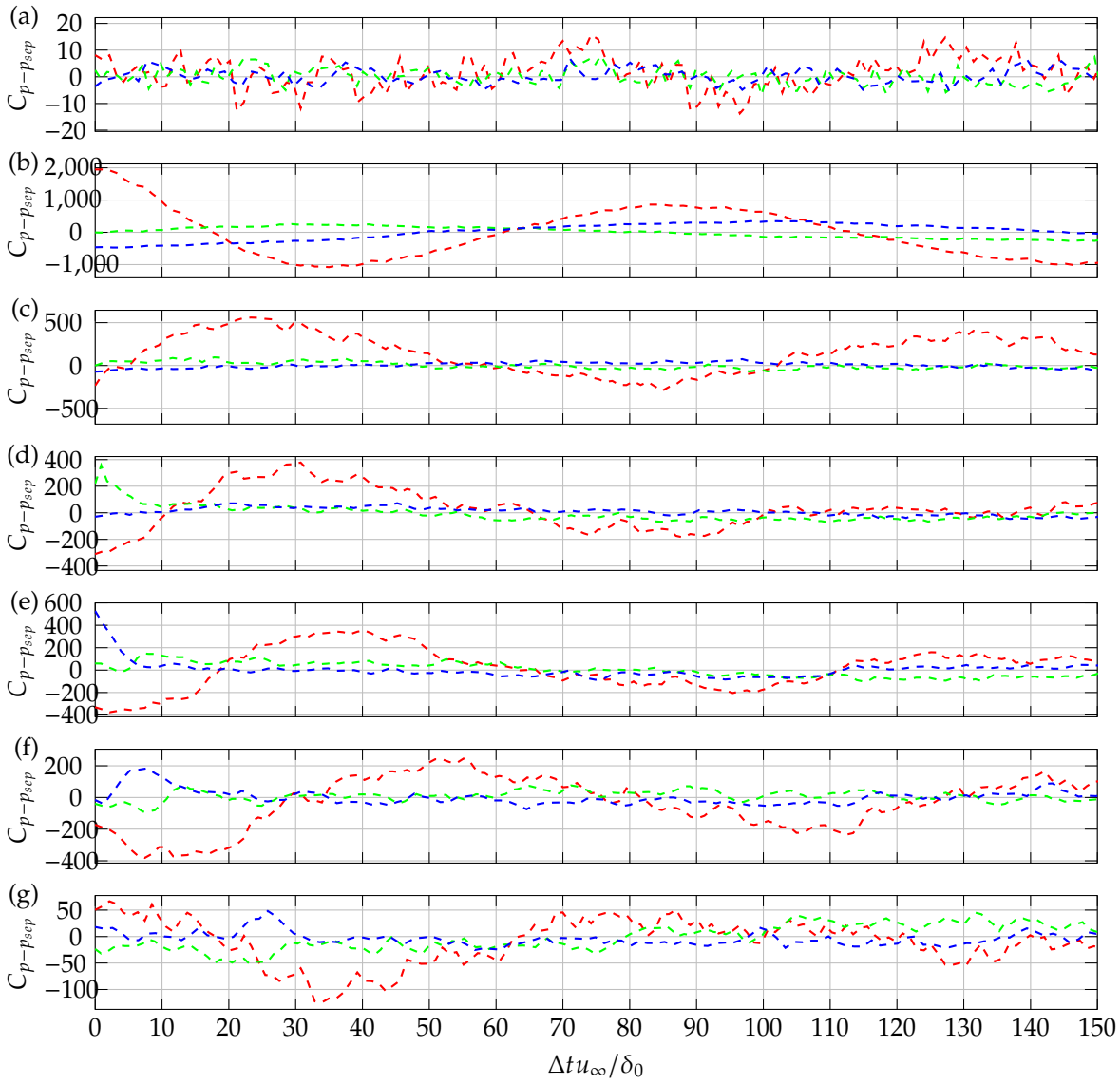


Figure C.50: Cross-correlation with pressure at AL and the other probes for the low-frequency cases.

C.5.4. Pressure cross-correlation separated per cases

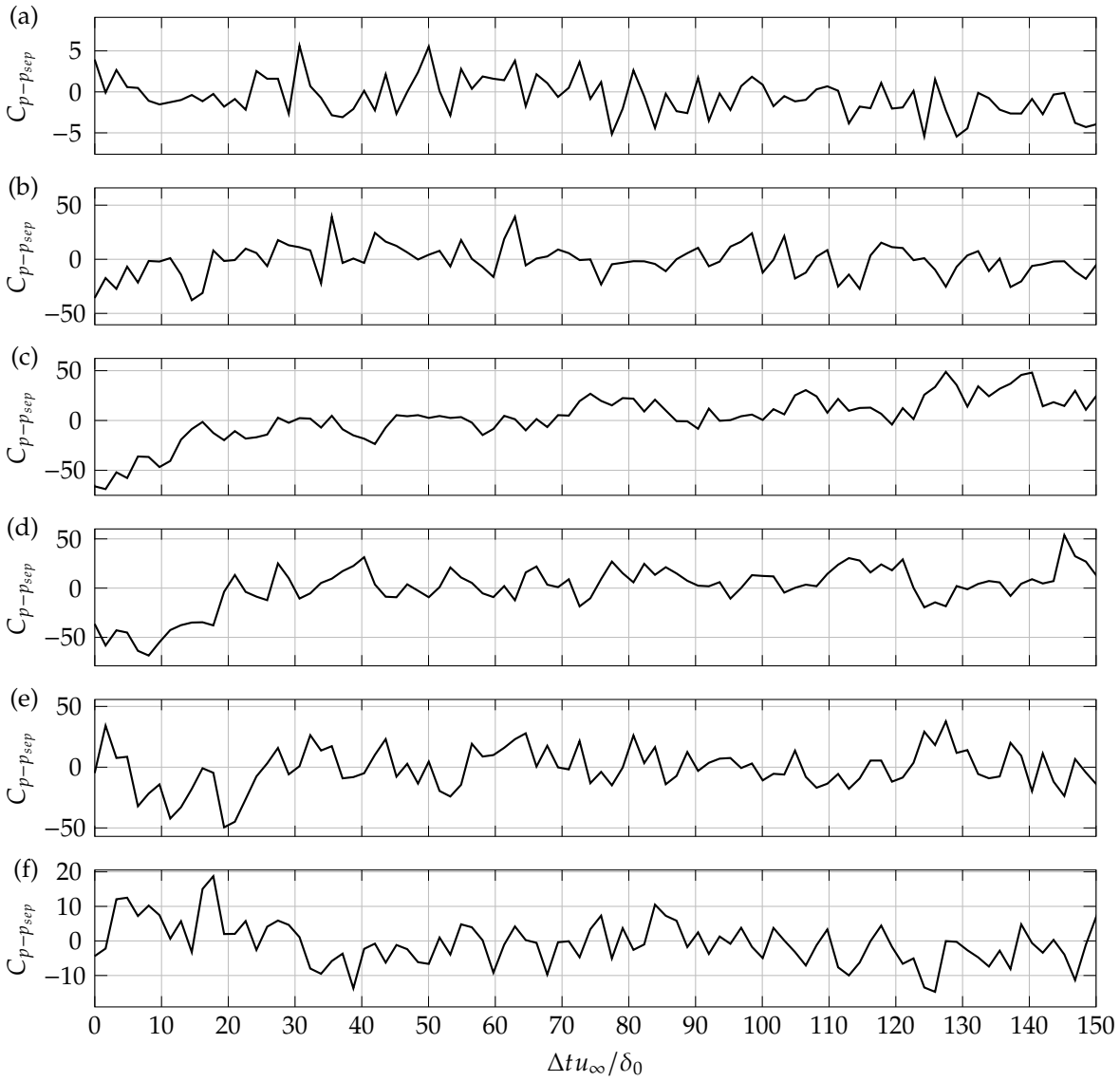


Figure C.51: Cross-correlation with pressure at S_x and the other probes for case Reference.

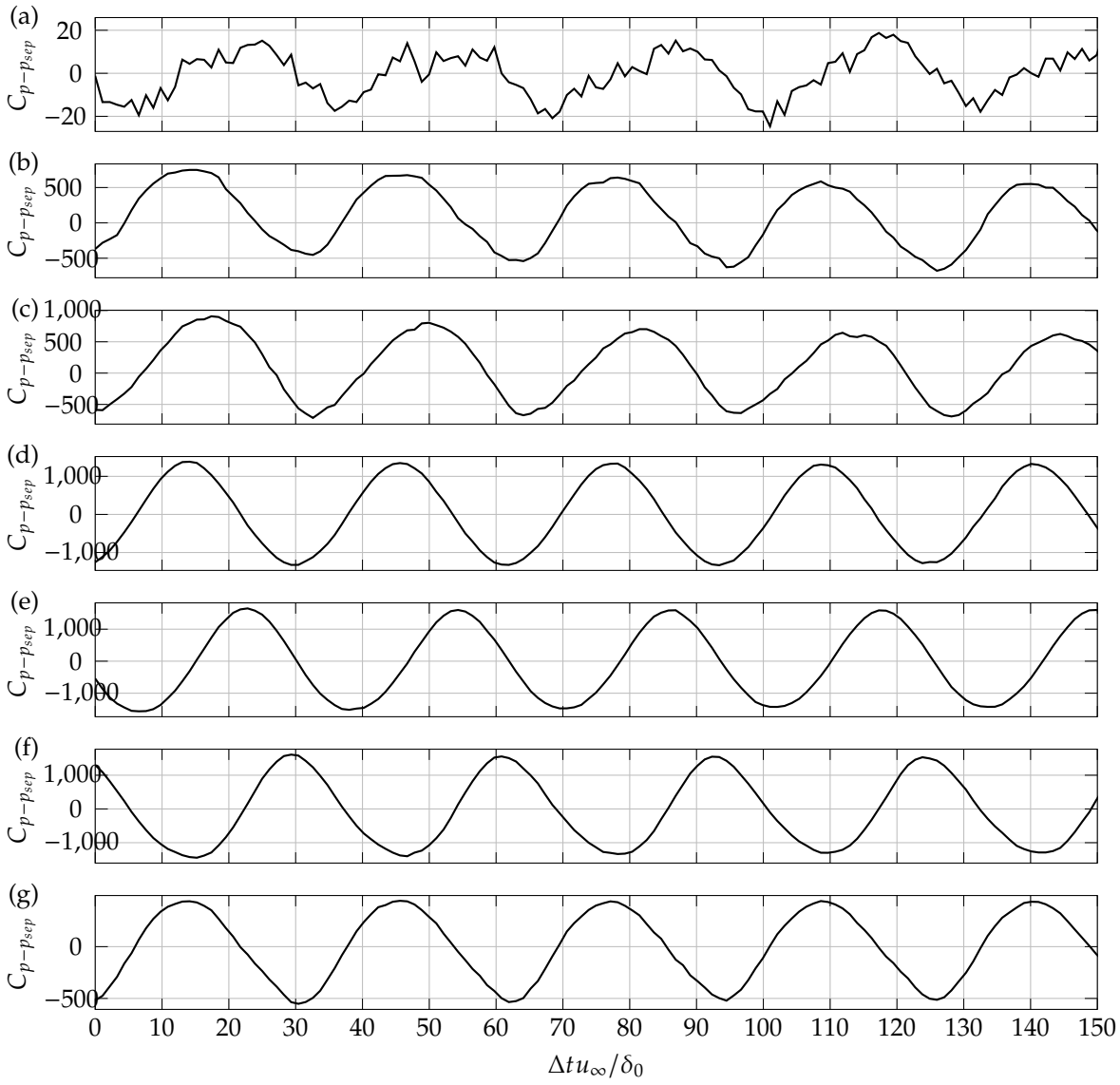


Figure C.52: Cross-correlation with pressure at S_x and the other probes for case LSFH.

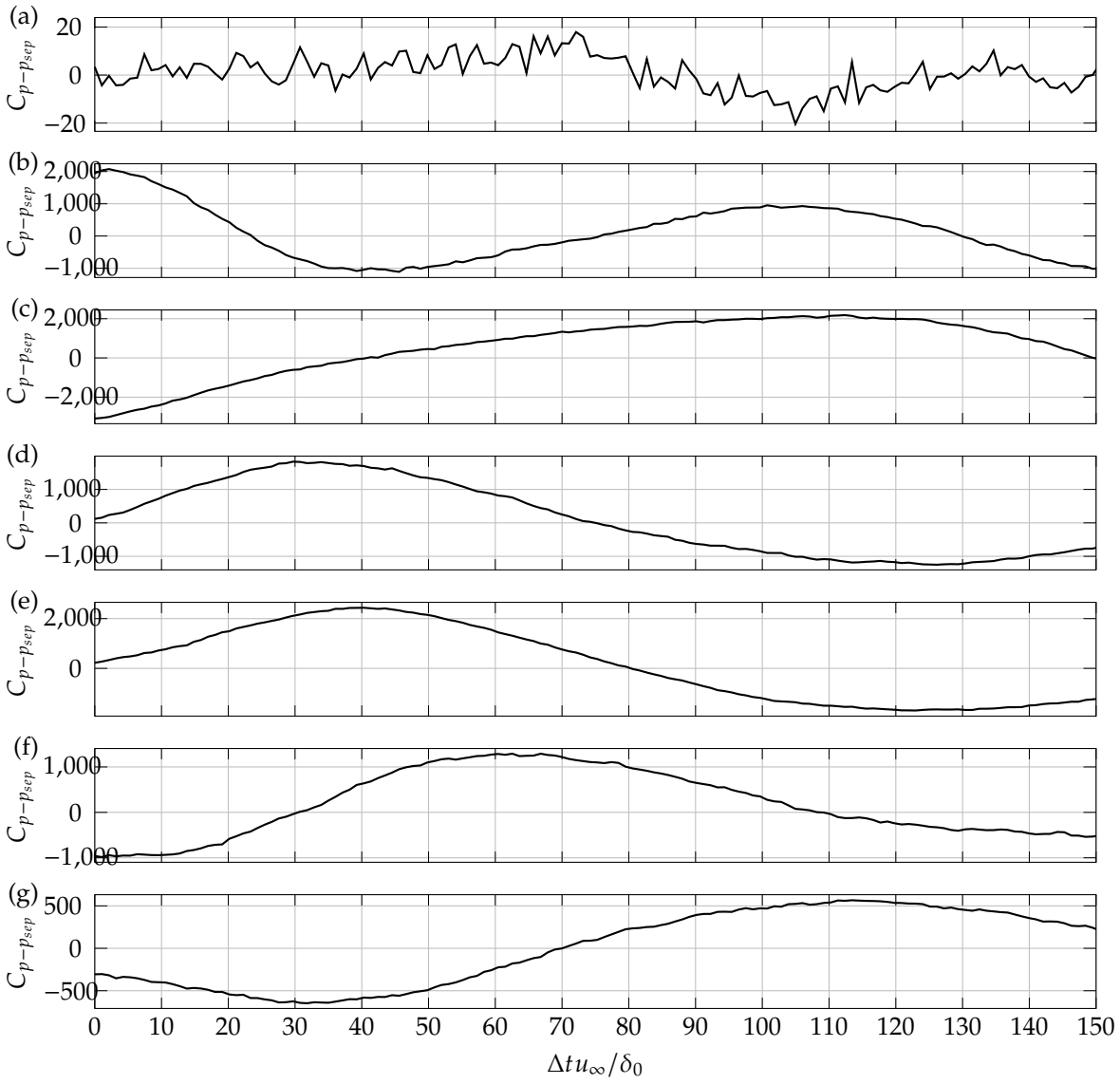


Figure C.53: Cross-correlation with pressure at S_x and the other probes for case LSFL.

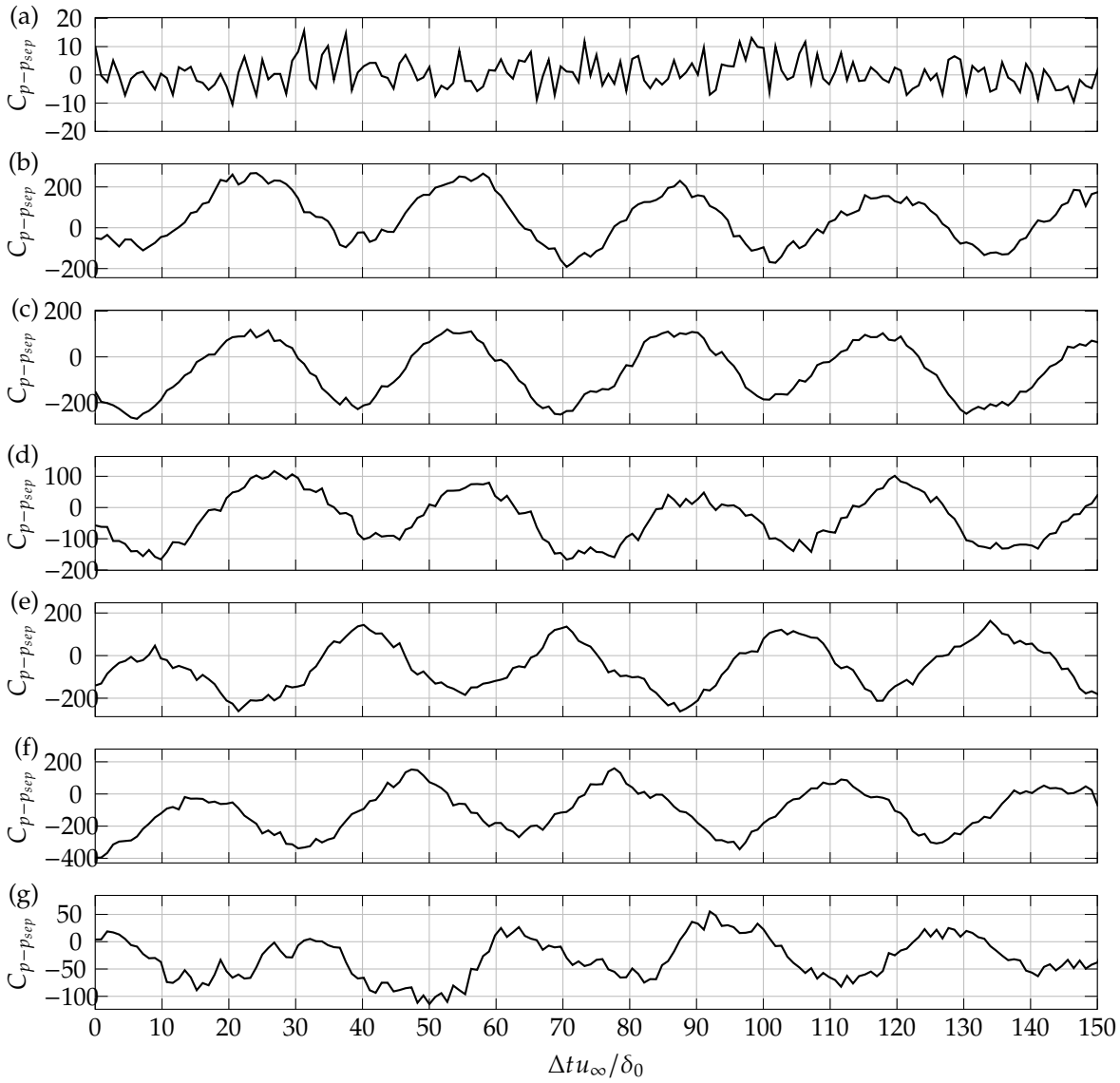


Figure C.54: Cross-correlation with pressure at S_x and the other probes for case LMFH.

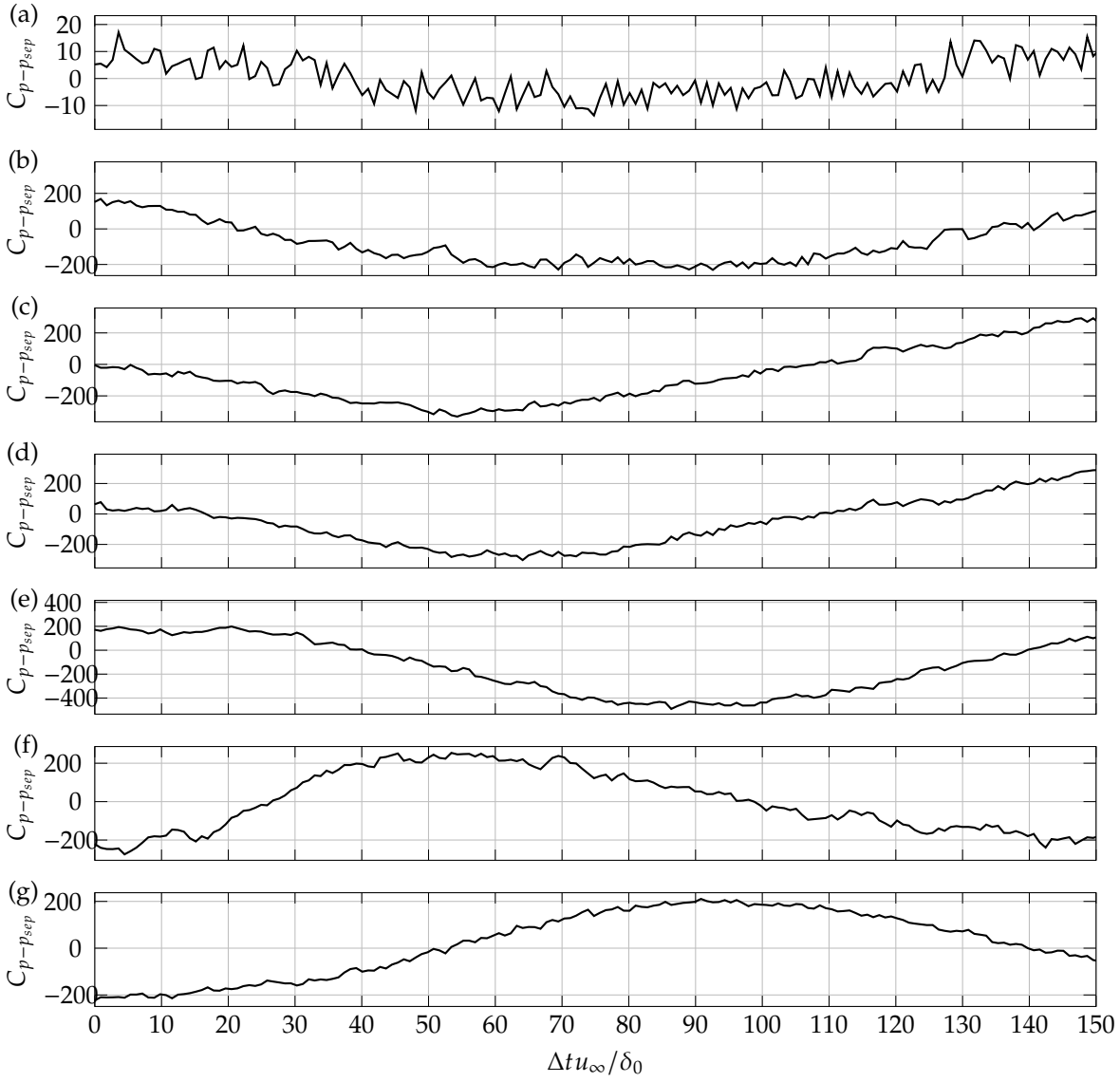


Figure C.55: Cross-correlation with pressure at S_x and the other probes for case LMFL.

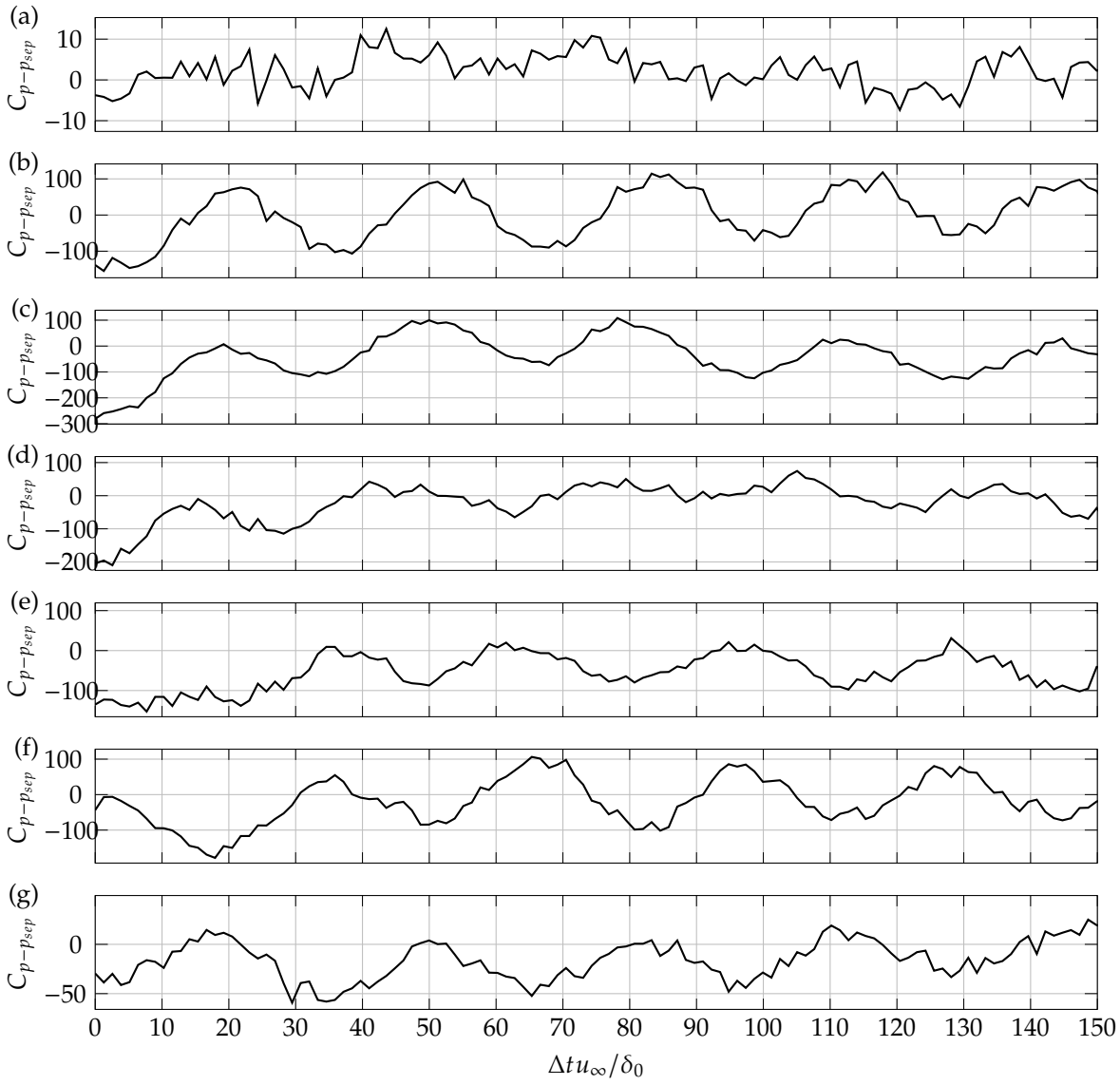


Figure C.56: Cross-correlation with pressure at S_x and the other probes for case LRFH.

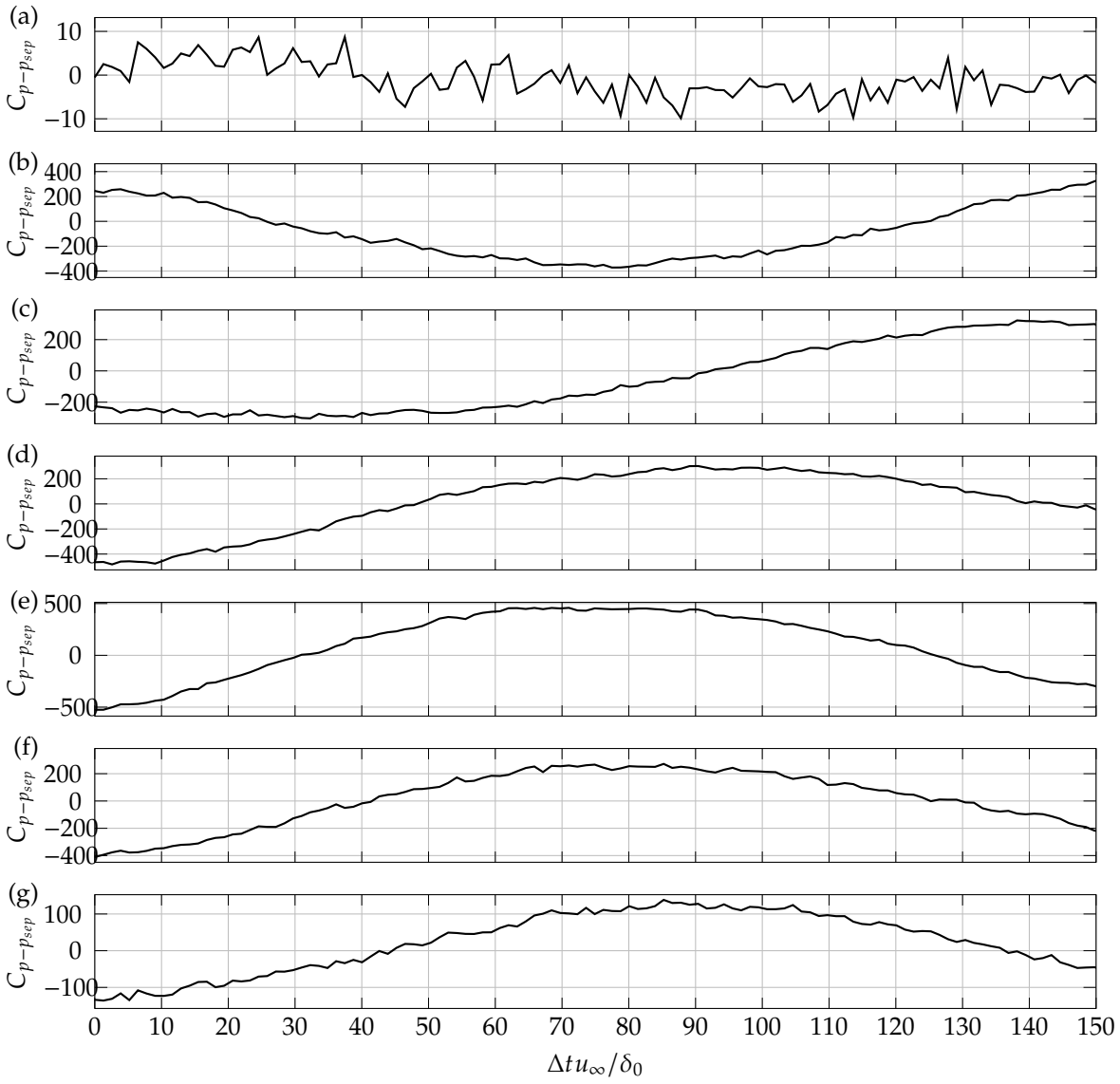


Figure C.57: Cross-correlation with pressure at S_x and the other probes for case LRFL.

C.6. Results separated per production case

C.6.1. Reference case

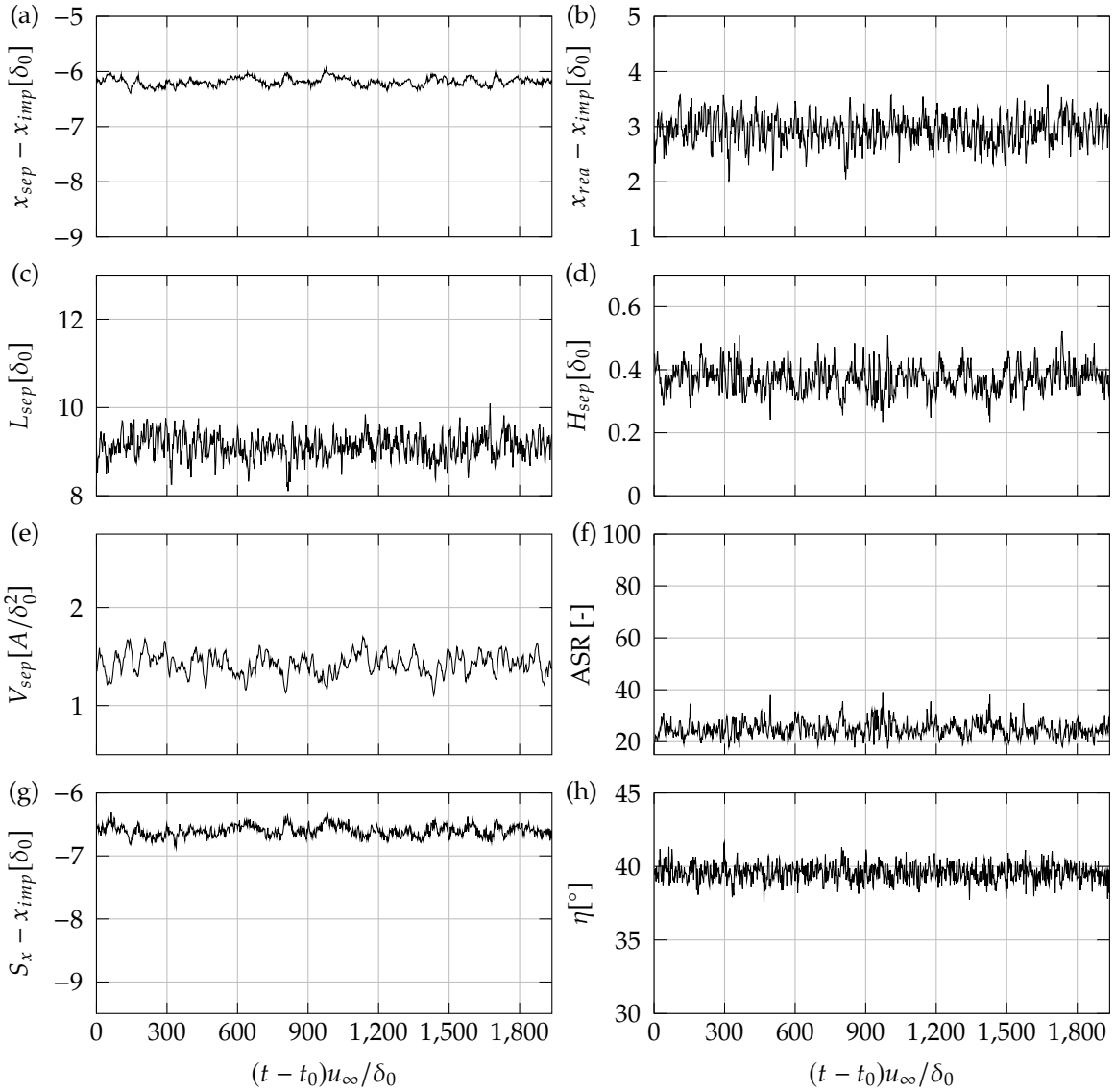


Figure C.58: Bubble motions case Reference: (a) x_{sep}, (b) x_{rea}, (c) L_{sep}, (d) H_{sep}, (e) V_{sep}, (f) ASR, (g) S_x and (h) η.

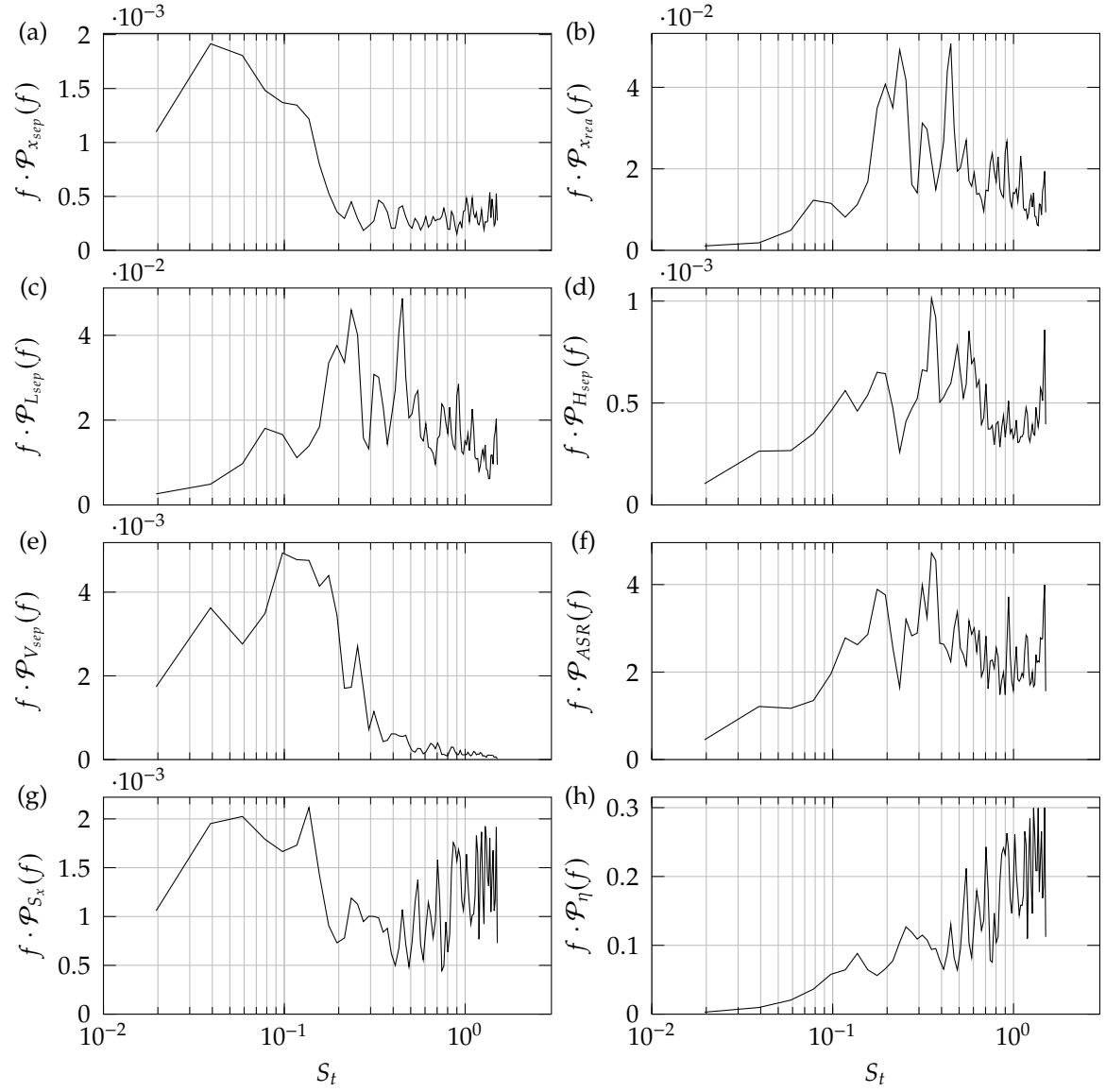


Figure C.59: PSDs of bubble motion case Reference: (a) x_{sep}, (b) x_{rea}, (c) L_{sep}, (d) H_{sep}, (e) V_{sep}, (f) ASR, (g) S_x and (h) η.

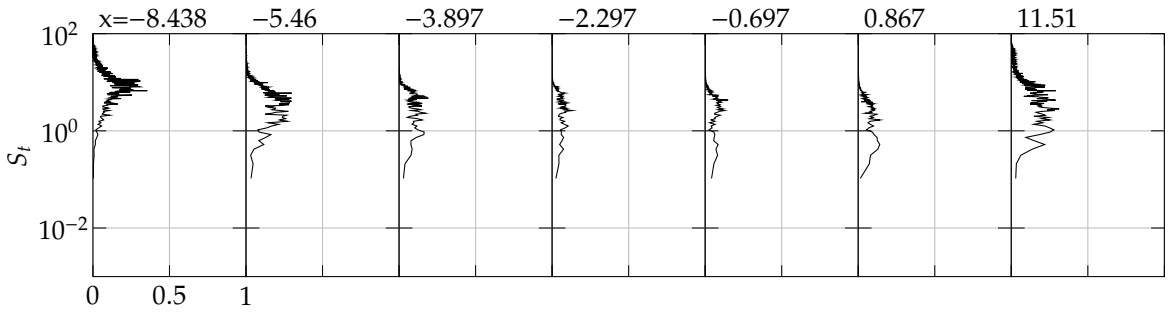


Figure C.60: PSDs of p'_w for case Reference at common locations.

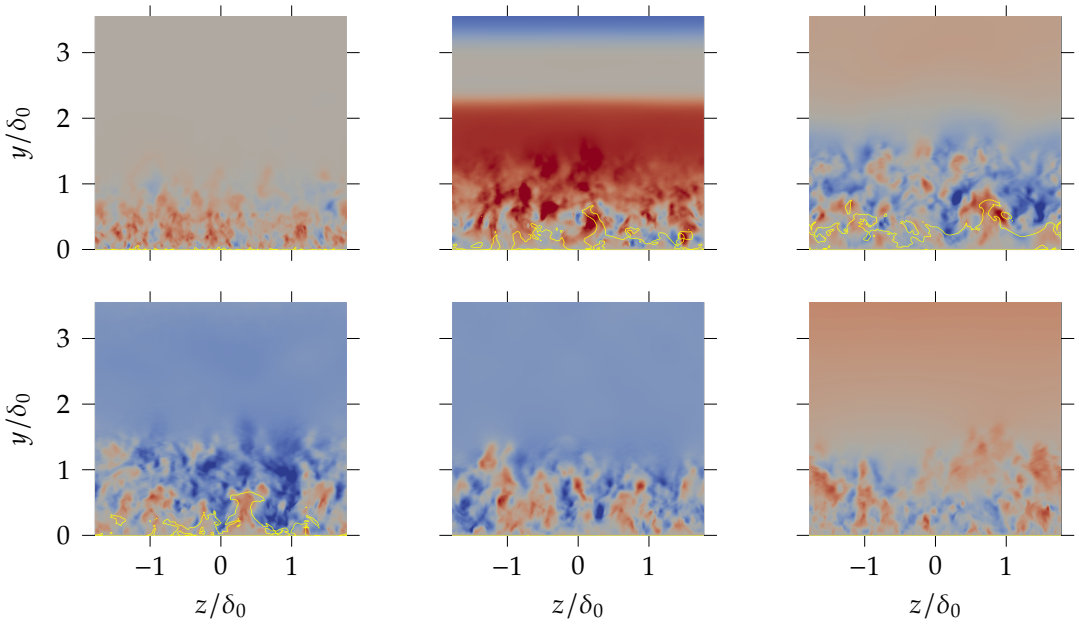


Figure C.61: Span-wise slices of v velocity at peak injection for case Reference. The yellow line indicates the contour of the separation bubble.

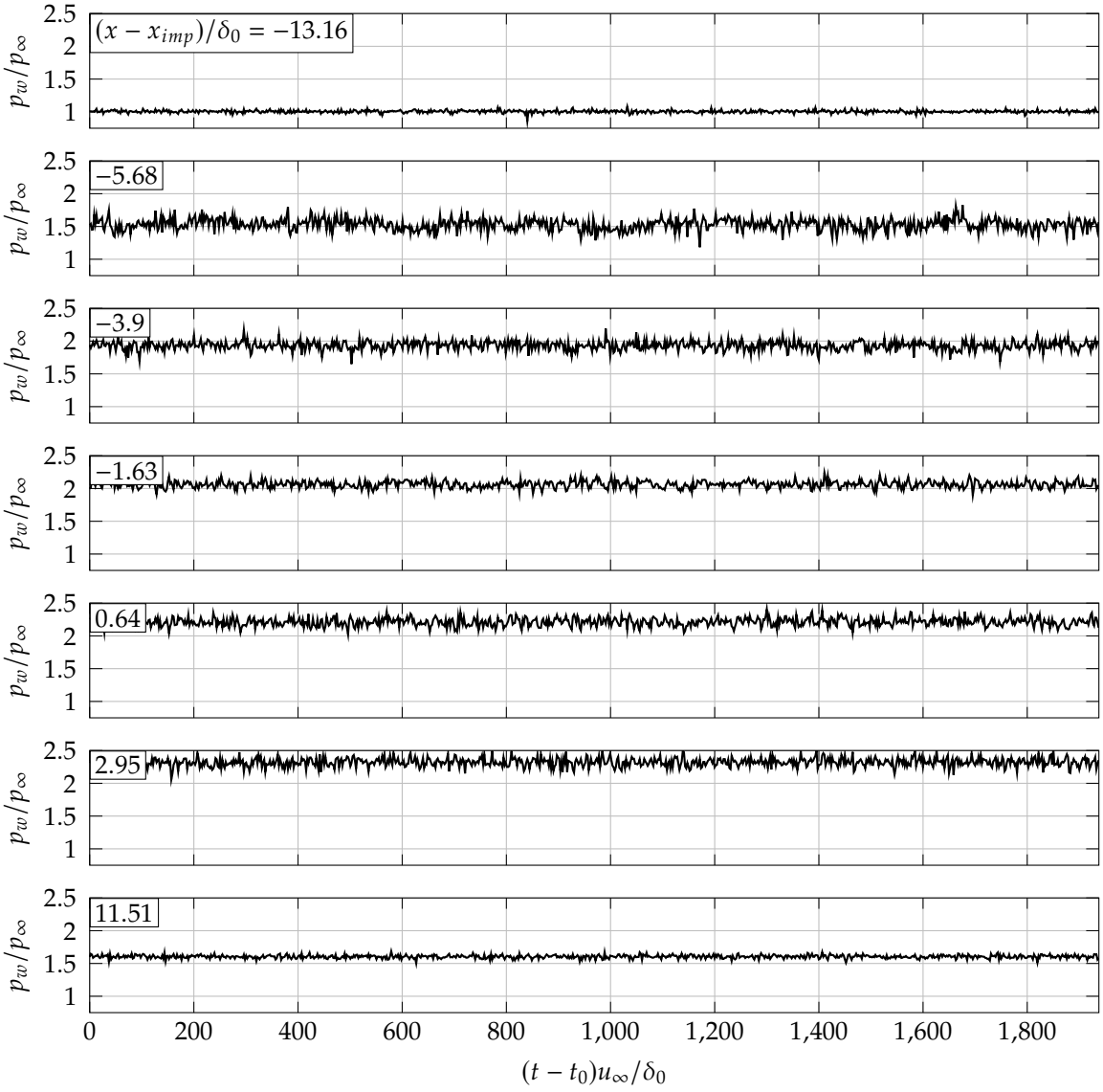


Figure C.62: Wall-pressure for case Reference obtained by probes placed at locations indicated in the top left corner of each plot.

C.6.2. Case LSFH

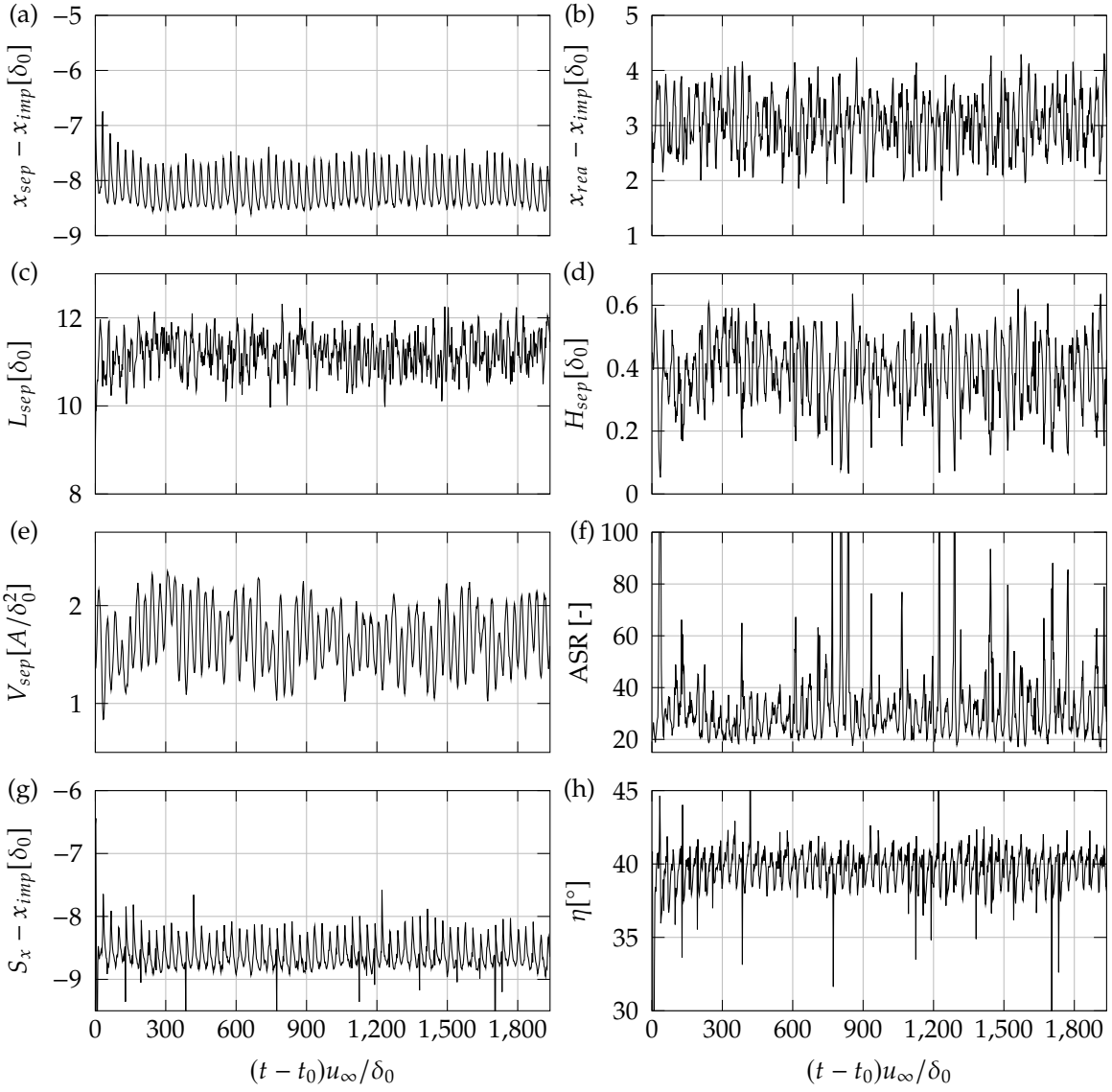


Figure C.63: Bubble motions case LSFH: (a) x_{sep}, (b) x_{rea}, (c) L_{sep}, (d) H_{sep}, (e) V_{sep}, (f) ASR, (g) S_x and (h) η.

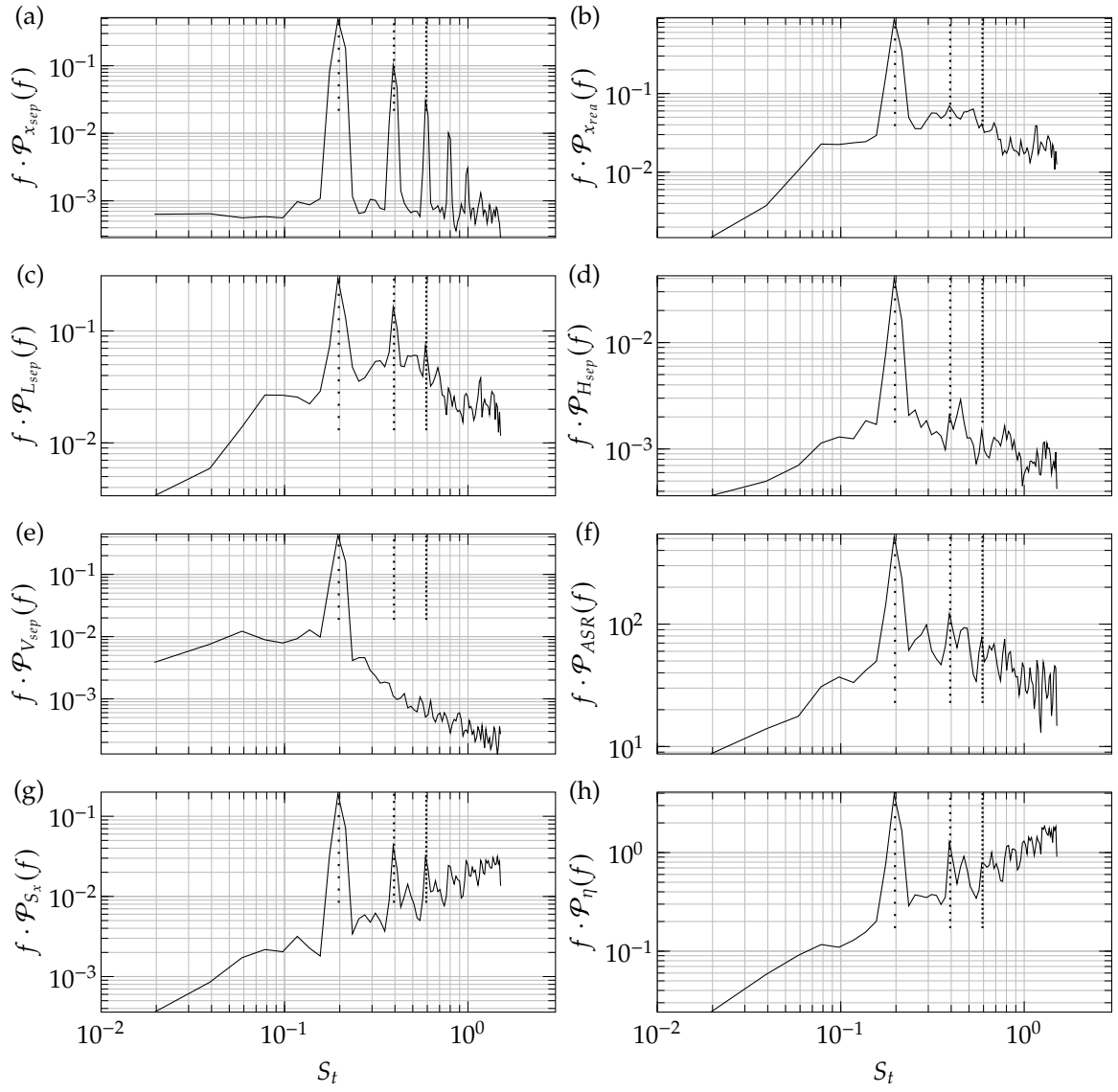


Figure C.64: PSDs of bubble motion case LSFH: (a) x_{sep}, (b) x_{rea}, (c) L_{sep}, (d) H_{sep}, (e) V_{sep}, (f) ASR, (g) S_x and (h) η.

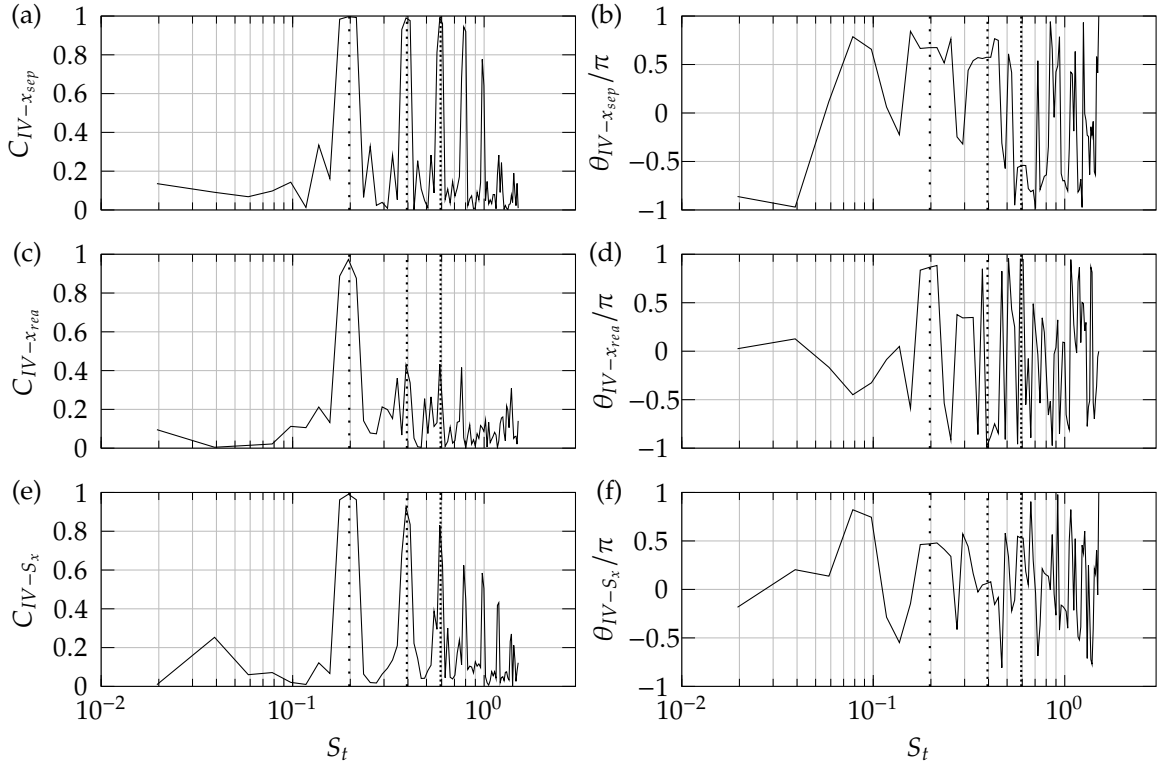


Figure C.65: Coherence and phase between bubble motion and injection velocity for LSFH. (a) Coherence and (b) Phase, between x_{sep} and IV, (c) Coherence and (d) Phase, between x_{rea} and IV.

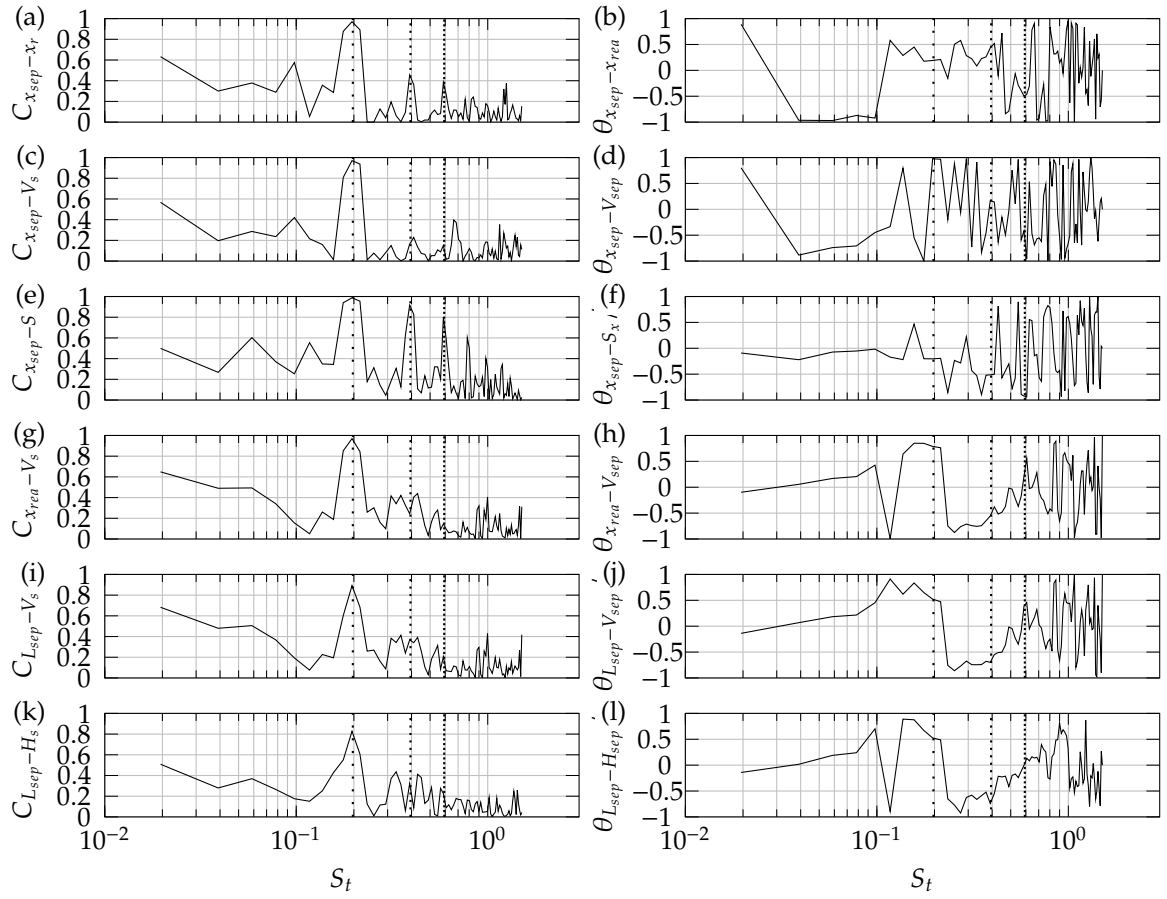


Figure C.66: Coherence and phase of bubble motion for production case LSFH.

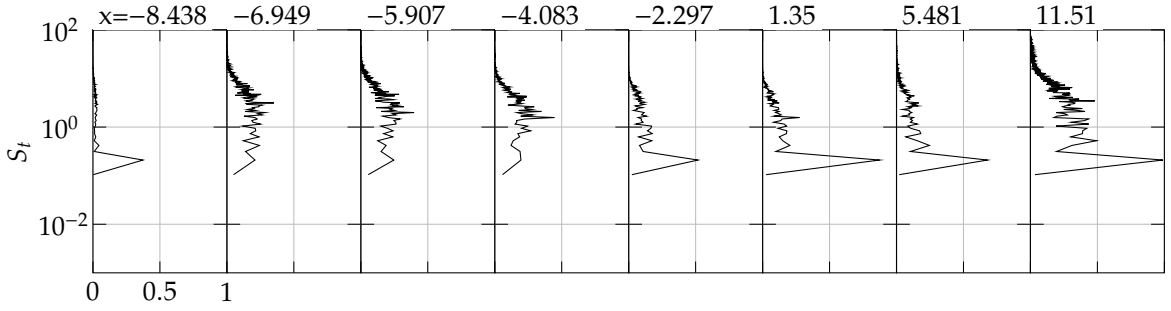


Figure C.67: PSDs of p'_w for case LSFHat selected locations.

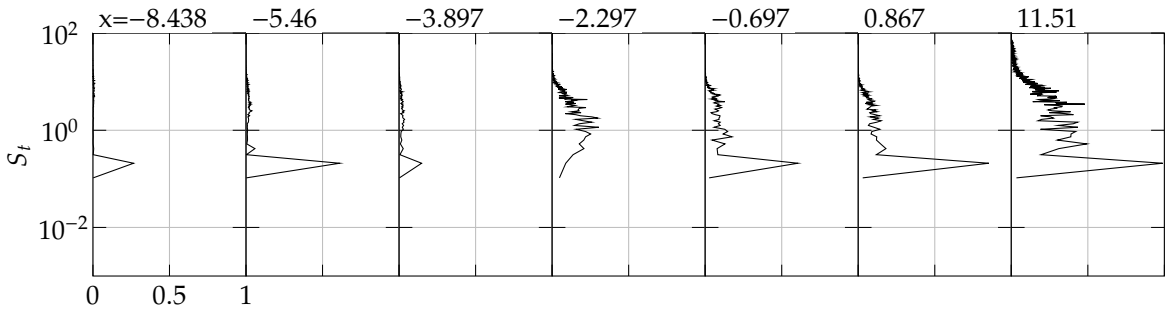


Figure C.68: PSDs of p'_w for case LSFH at common locations.

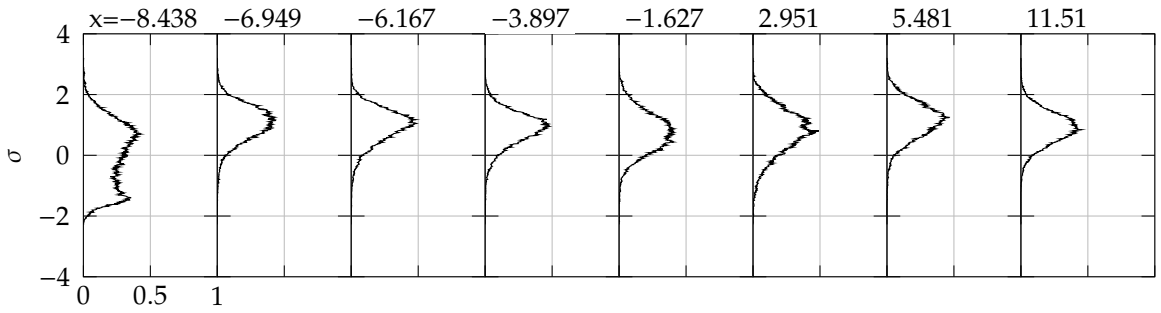


Figure C.69: PDFs of p'_w for case LSFH at selected locations, indicated with ▼ in Figure A.22.

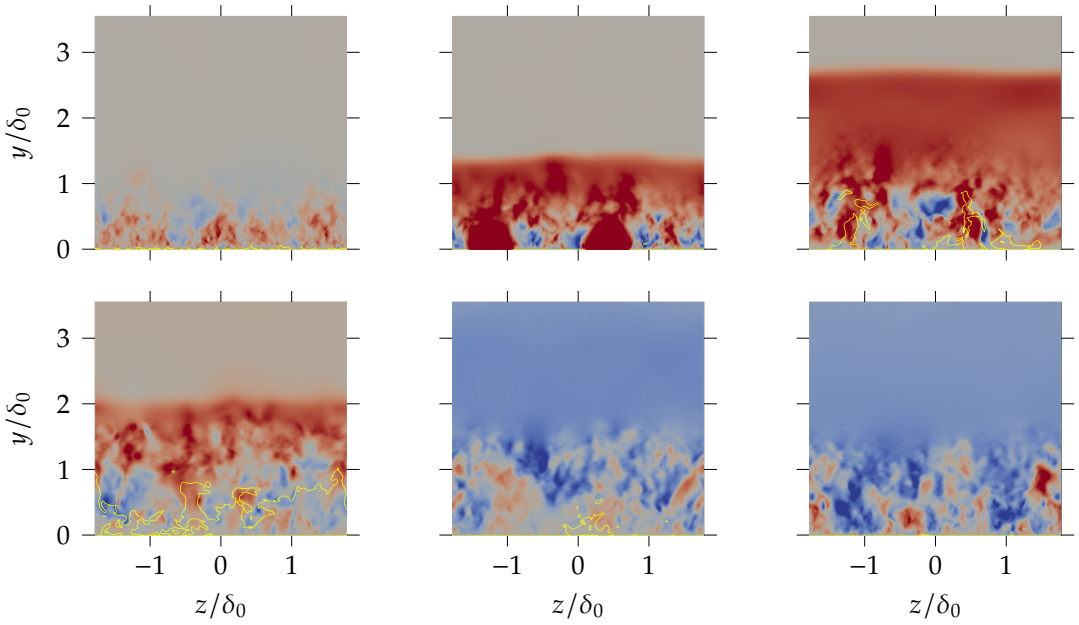


Figure C.70: Span-wise slices of v velocity at peak injection for case LSFH. The yellow line indicates the contour of the separation bubble.

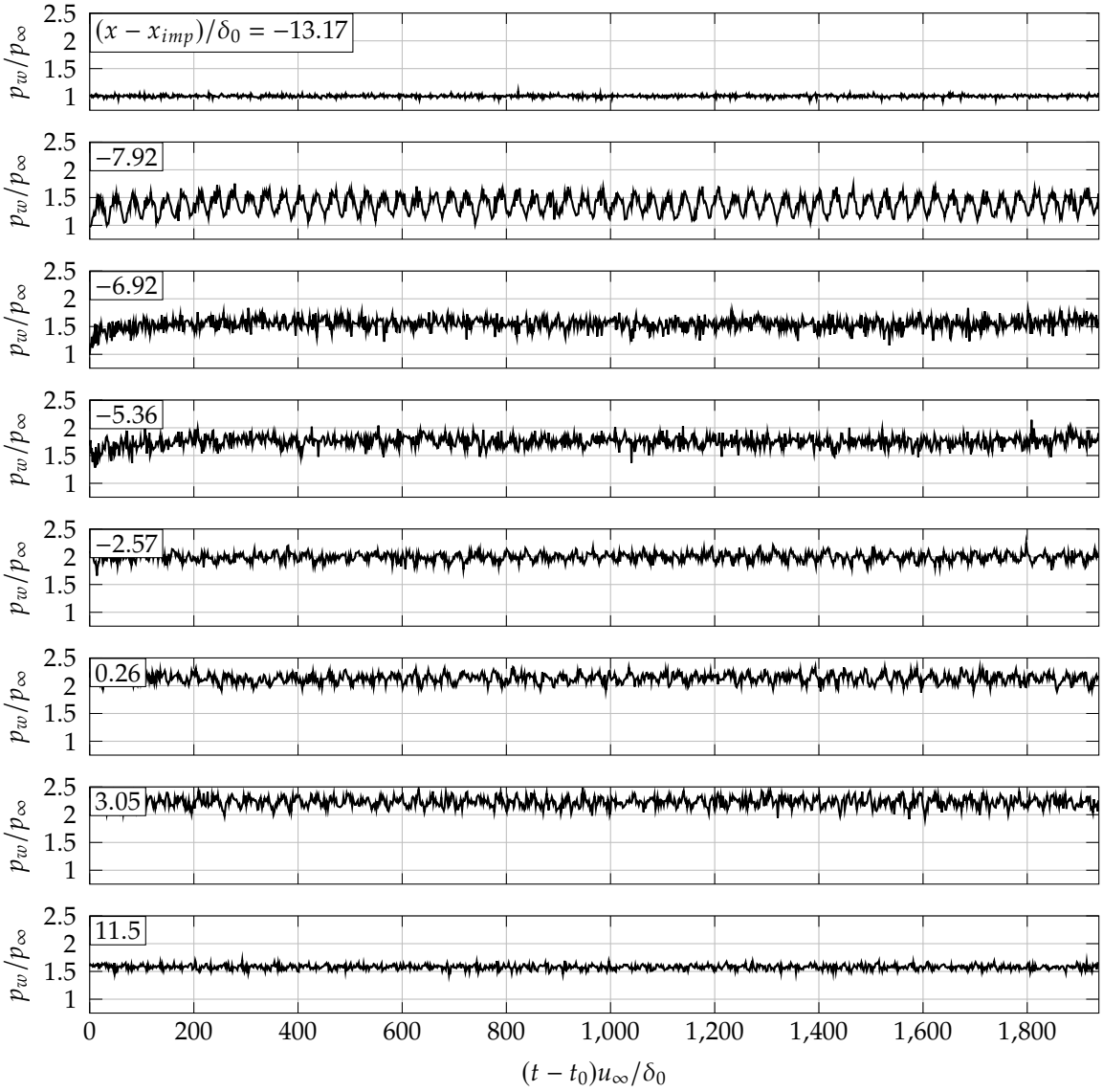


Figure C.71: Wall-pressure for case LSFH obtained by probes placed at locations indicated in the top left corner of each plot.

C.6.3. Case LSFL

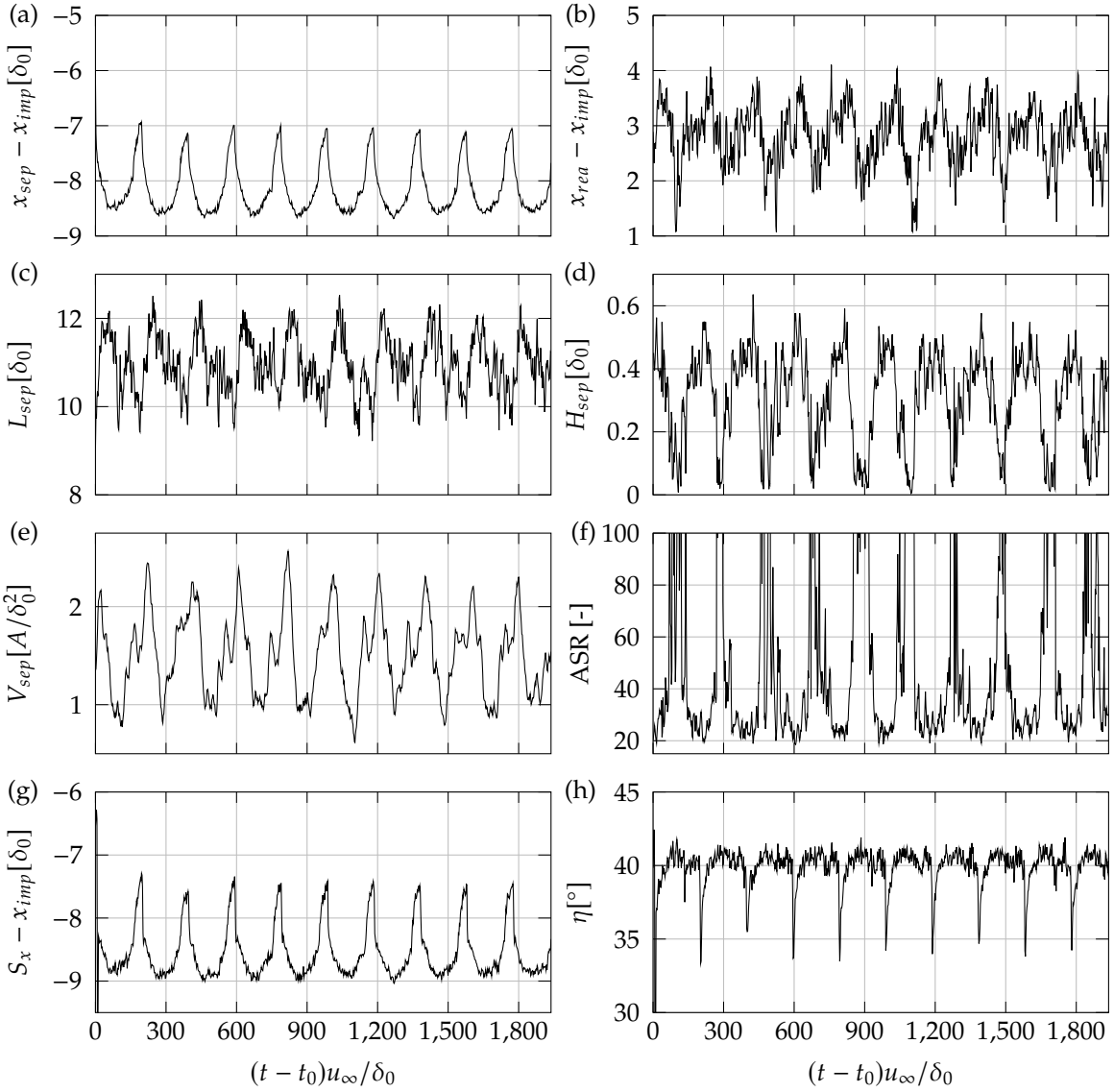


Figure C.72: Bubble motions case LSFL: (a) x_{sep}, (b) x_{rea}, (c) L_{sep}, (d) H_{sep}, (e) V_{sep}, (f) ASR, (g) S_x and (h) η.

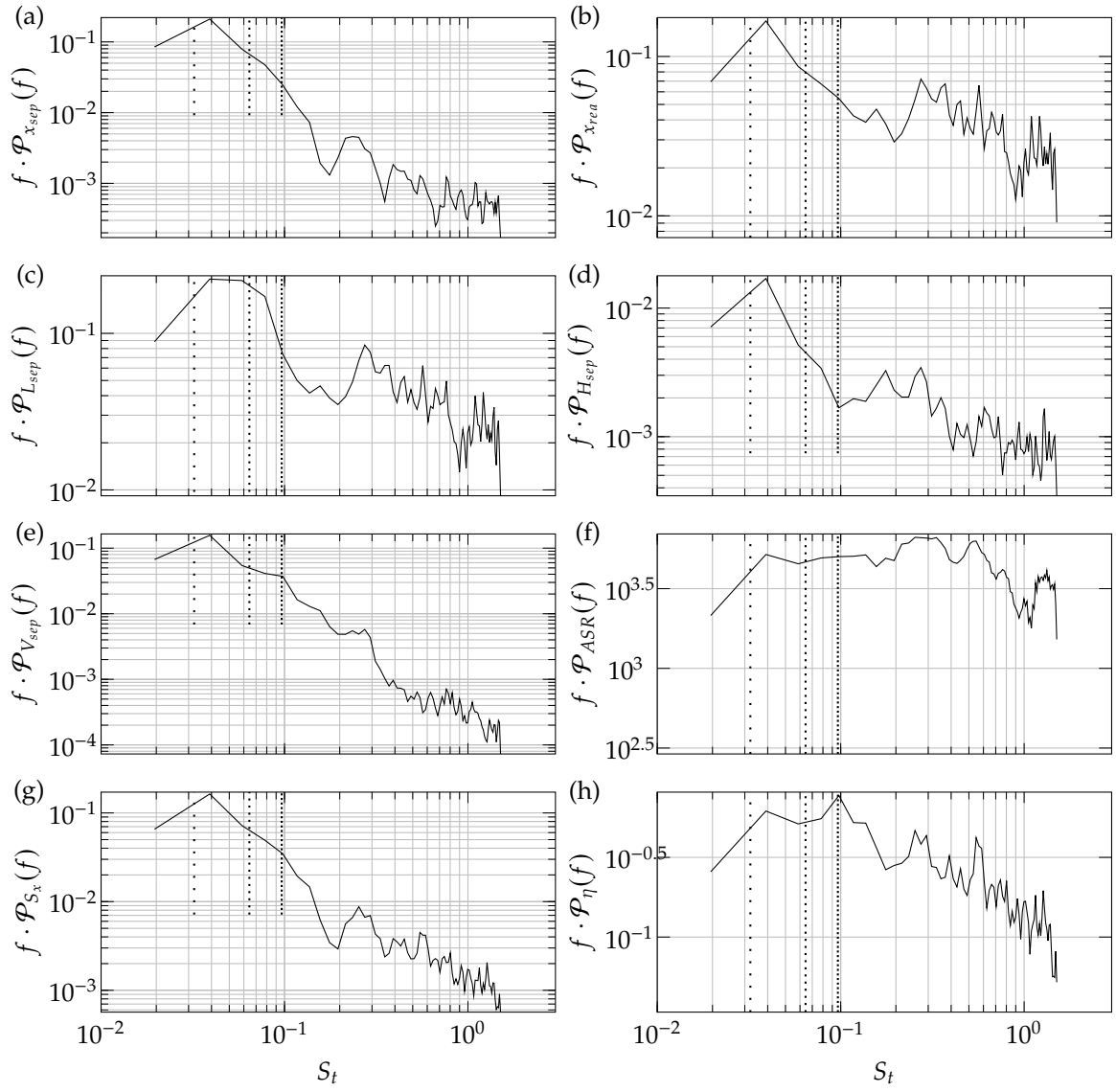


Figure C.73: PSDs of bubble motion case LSFL: (a) x_{sep}, (b) x_{rea}, (c) L_{sep}, (d) H_{sep}, (e) V_{sep}, (f) ASR, (g) S_x and (h) η.

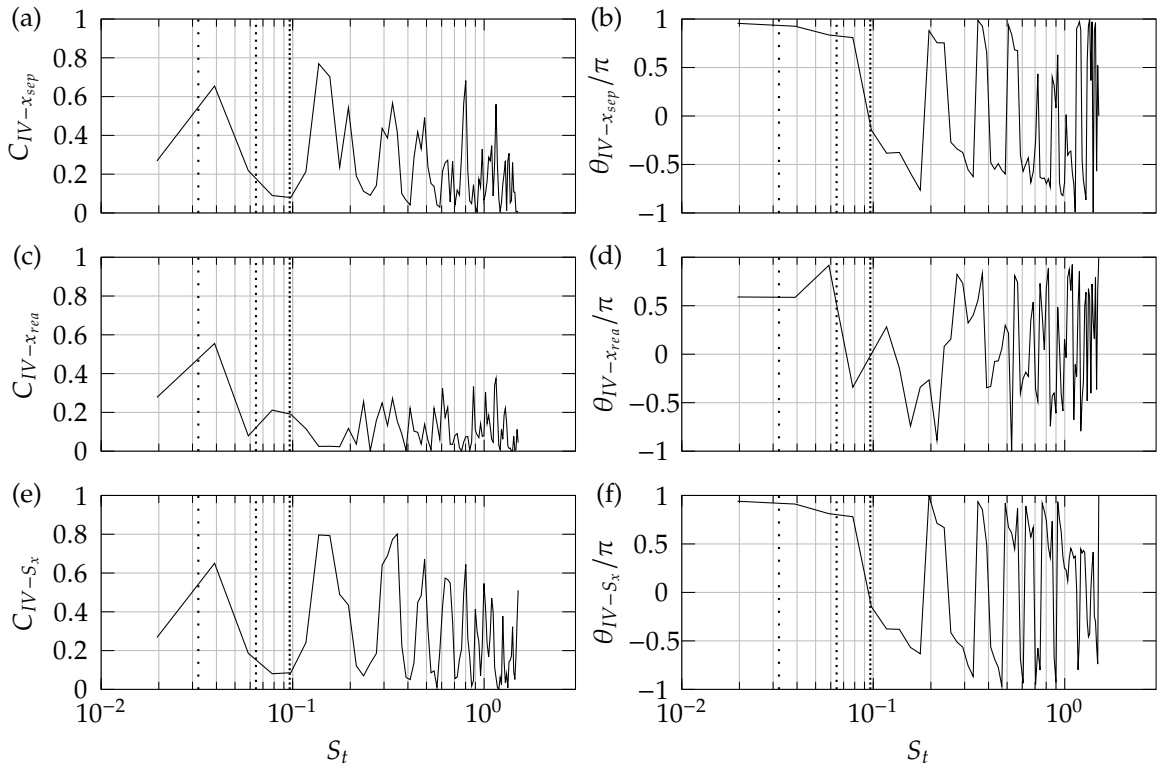


Figure C.74: Coherence and phase between bubble motion and injection velocity for LSFL. (a) Coherence and (b) Phase, between x_{sep} and IV, (c) Coherence and (d) Phase, between x_{rea} and IV.

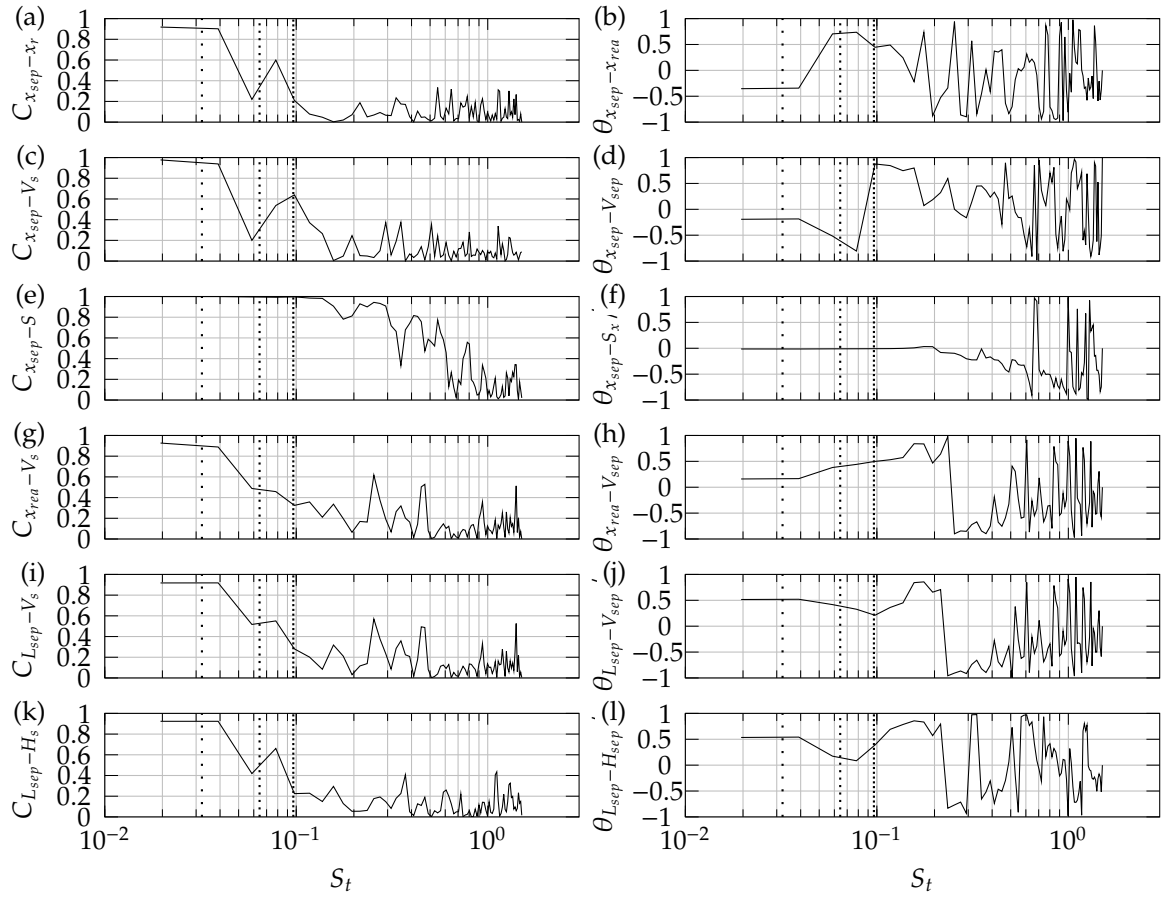


Figure C.75: Coherence and phase of bubble motion for production case LSFL.

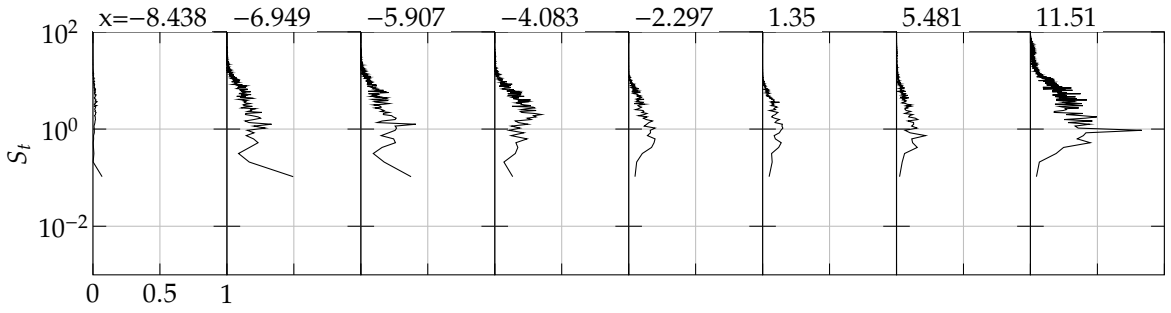


Figure C.76: PSDs of p'_w for case LSFLat selected locations.

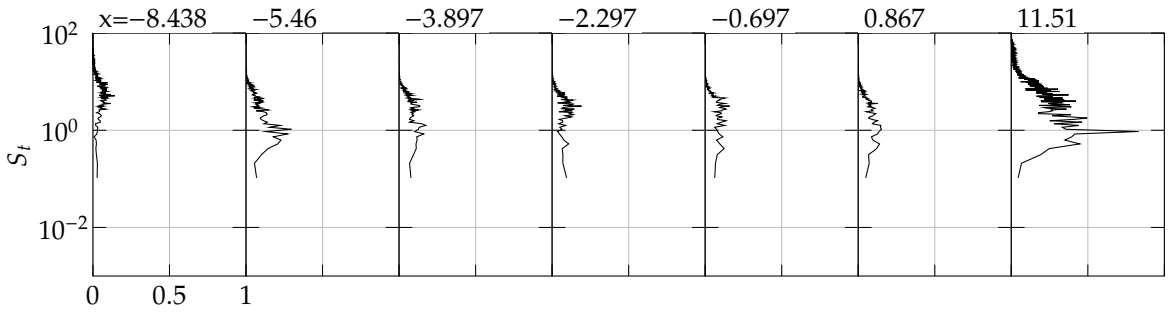


Figure C.77: PSDs of p'_w for case LSFL at common locations.

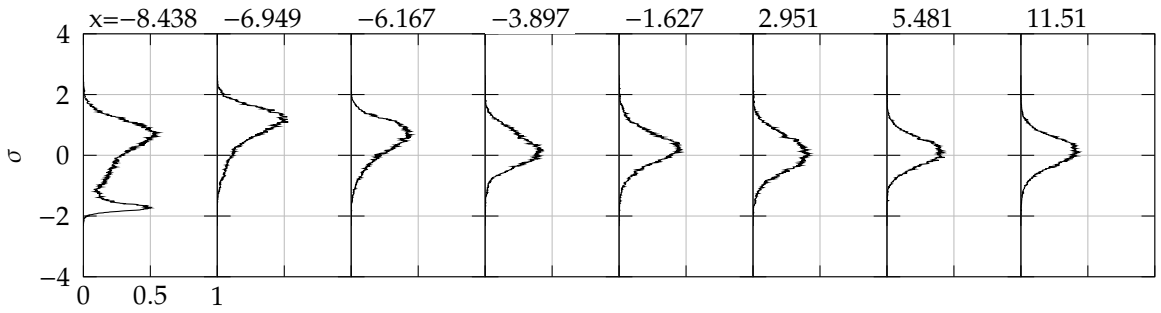


Figure C.78: PDFs of p'_w for case LSFL at selected locations, indicated with ▼ in Figure A.22.

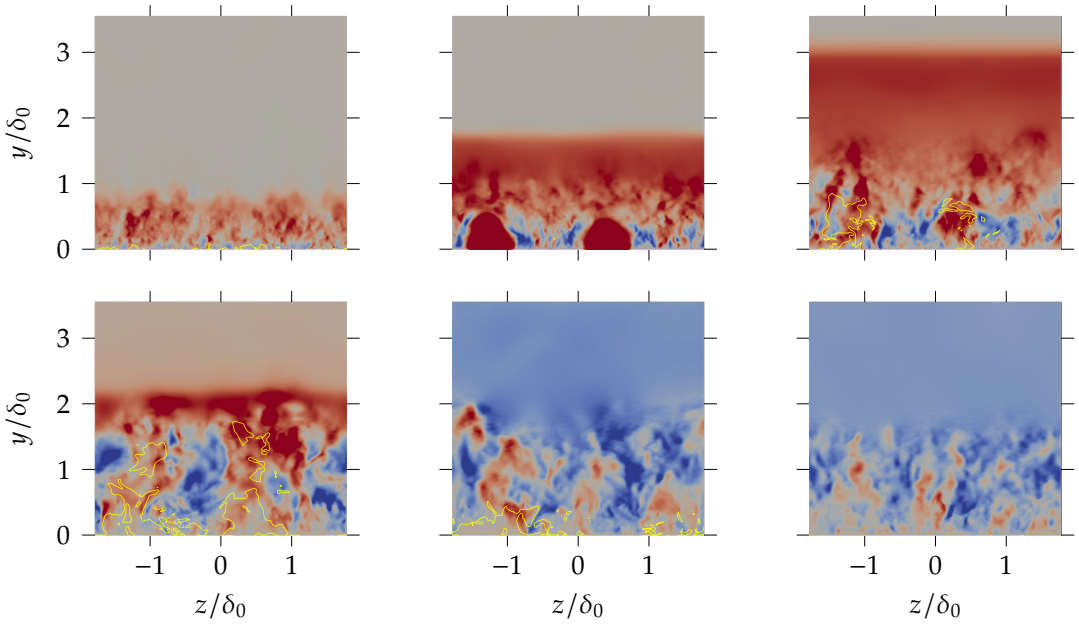


Figure C.79: Span-wise slices of v velocity at peak injection for case LSFL. The yellow line indicates the contour of the separation bubble.

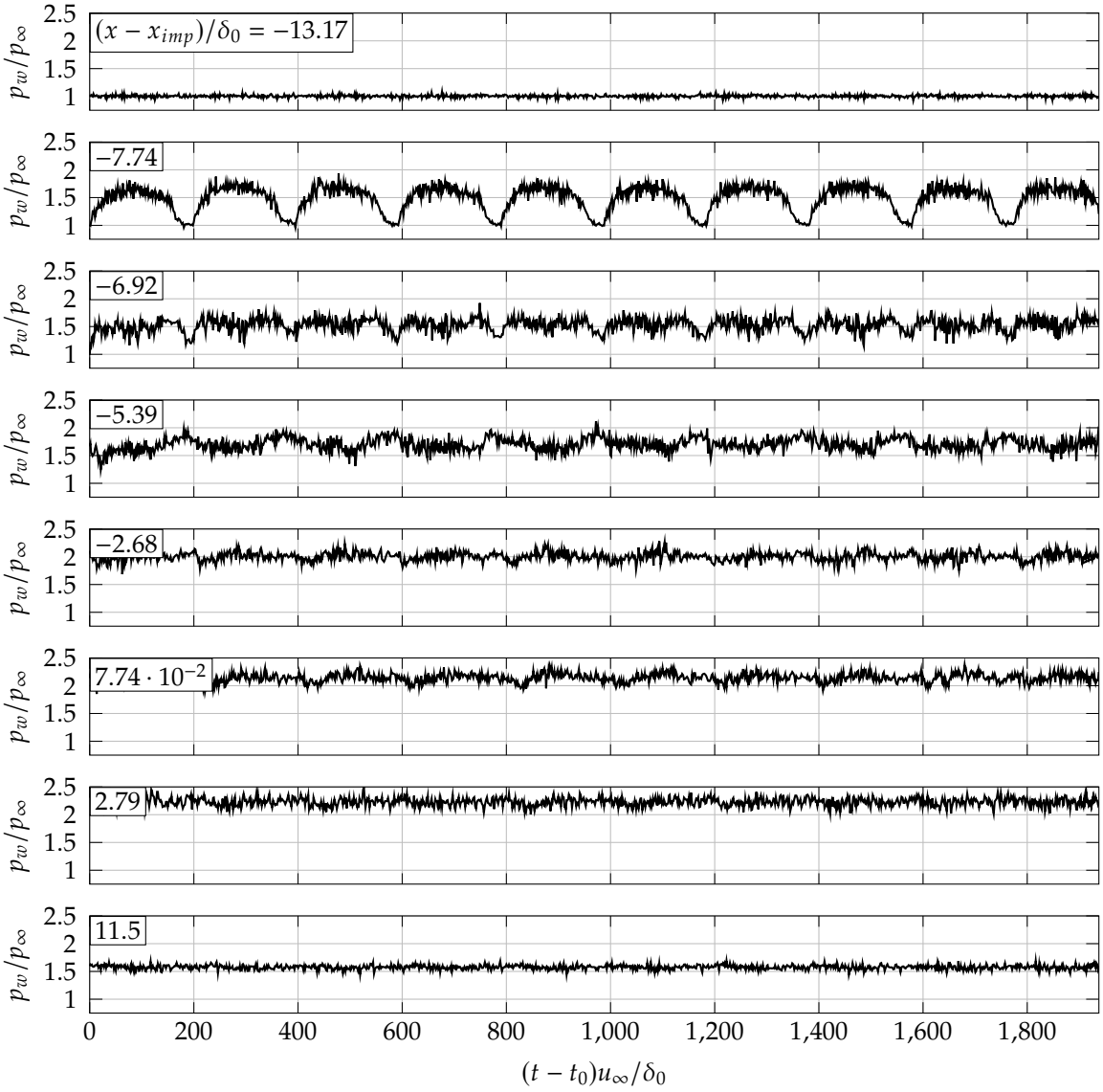


Figure C.80: Wall-pressure for case LSFL obtained by probes placed at locations indicated in the top left corner of each plot.

C.6.4. Case LMFH

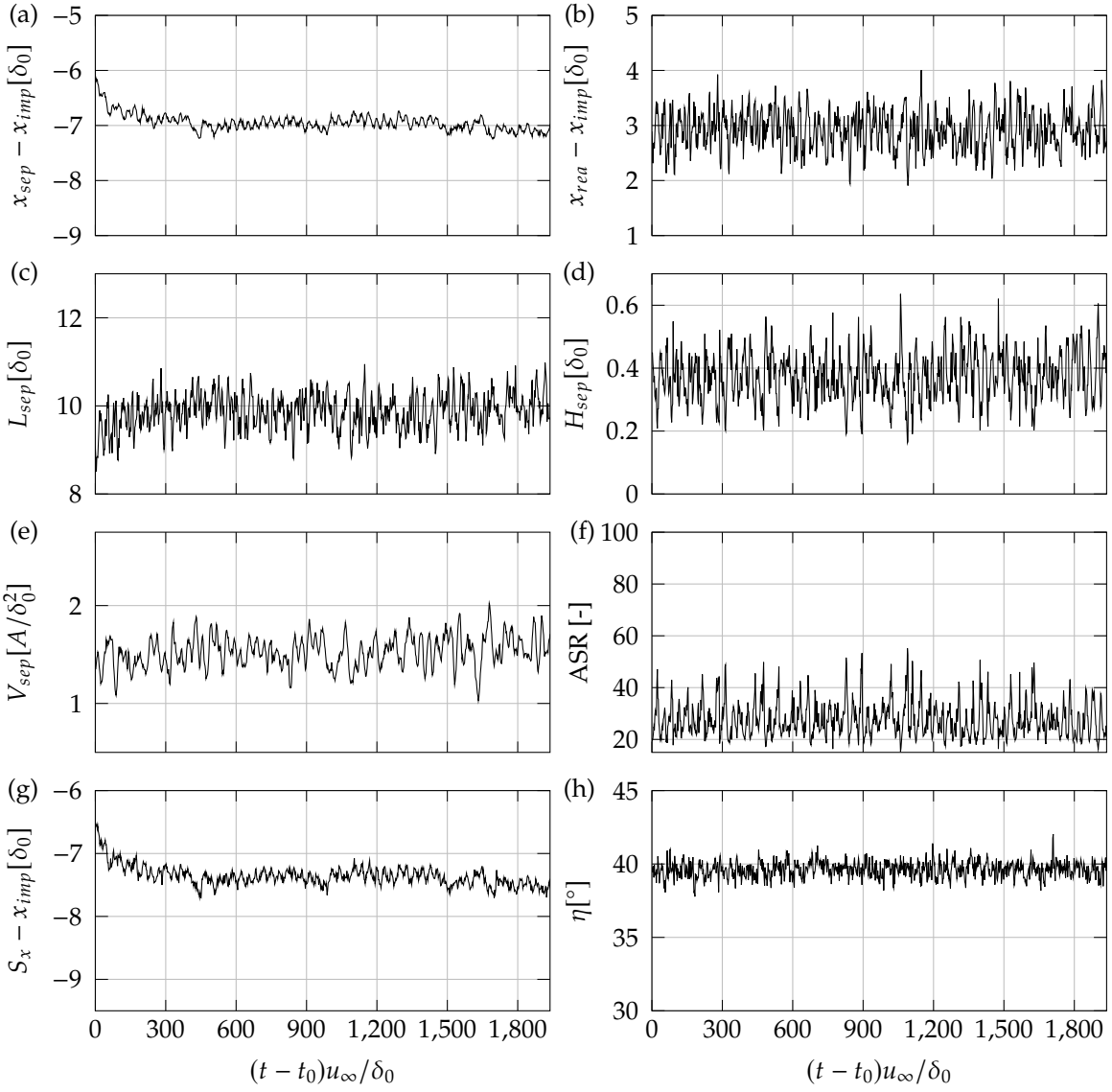


Figure C.81: Bubble motions case LMFH: (a) x_{sep}, (b) x_{rea}, (c) L_{sep}, (d) H_{sep}, (e) V_{sep}, (f) ASR, (g) S_x and (h) η.

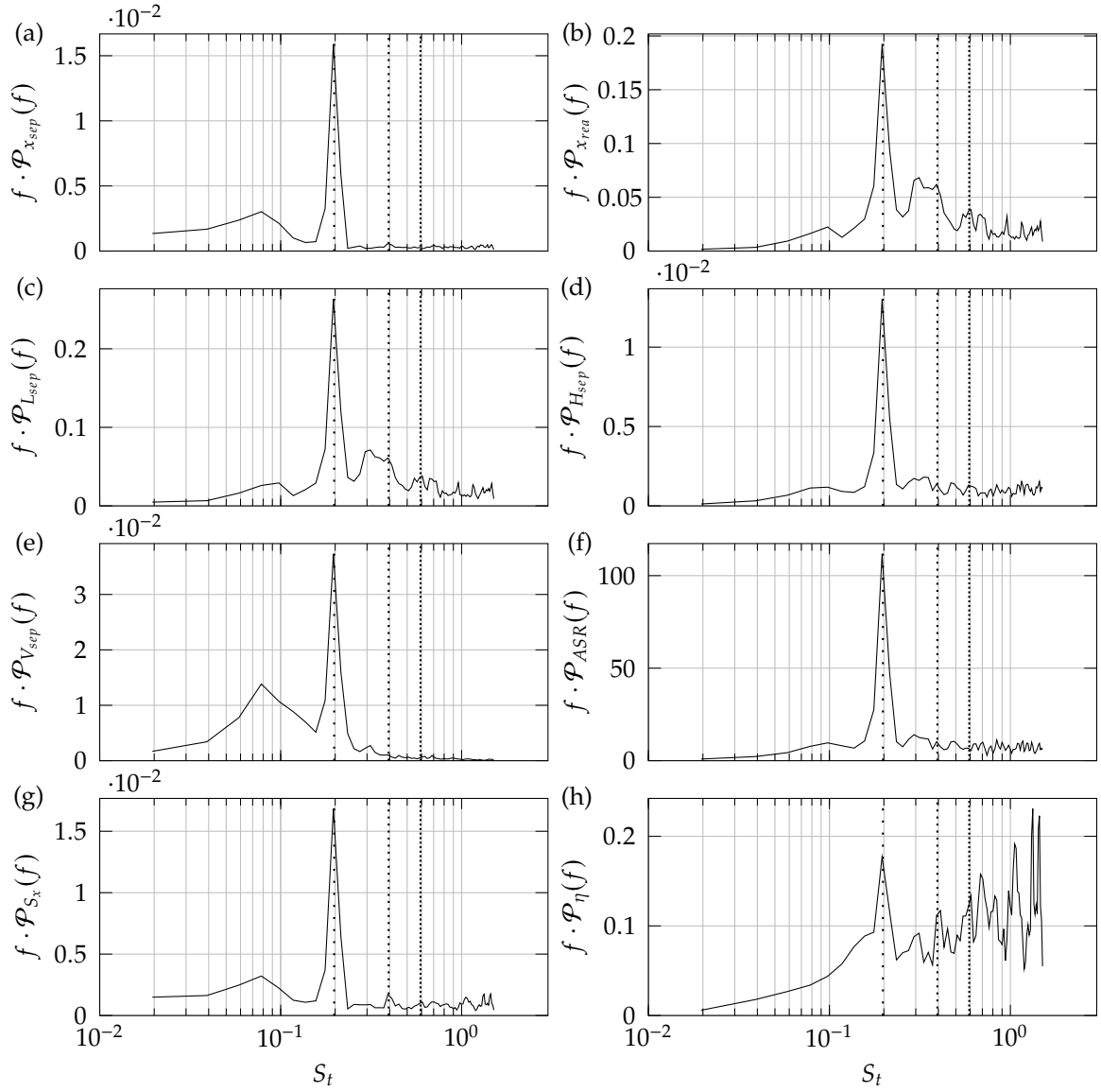


Figure C.82: PSDs of bubble motion case LMFH: (a) x_{sep}, (b) x_{rea}, (c) L_{sep}, (d) H_{sep}, (e) V_{sep}, (f) ASR, (g) S_x and (h) η.

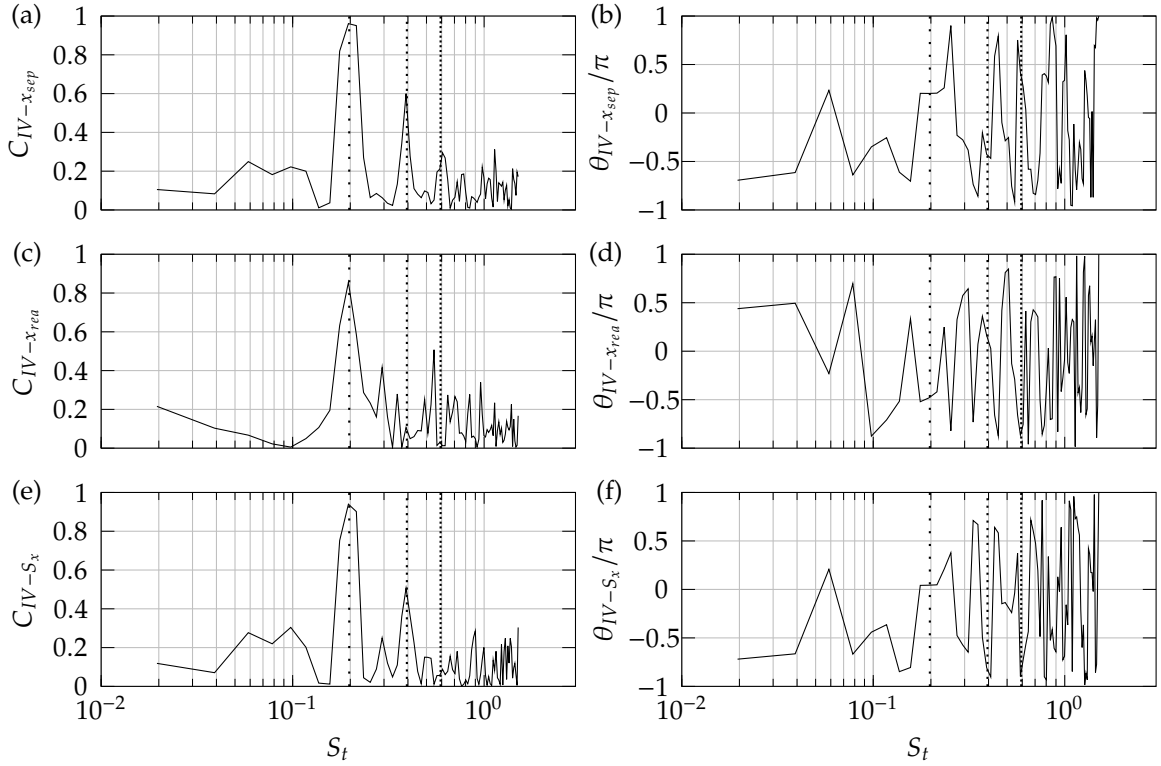


Figure C.83: Coherence and phase between bubble motion and injection velocity for LMFH. (a) Coherence and (b) Phase, between x_{sep} and IV, (c) Coherence and (d) Phase, between x_{rea} and IV.

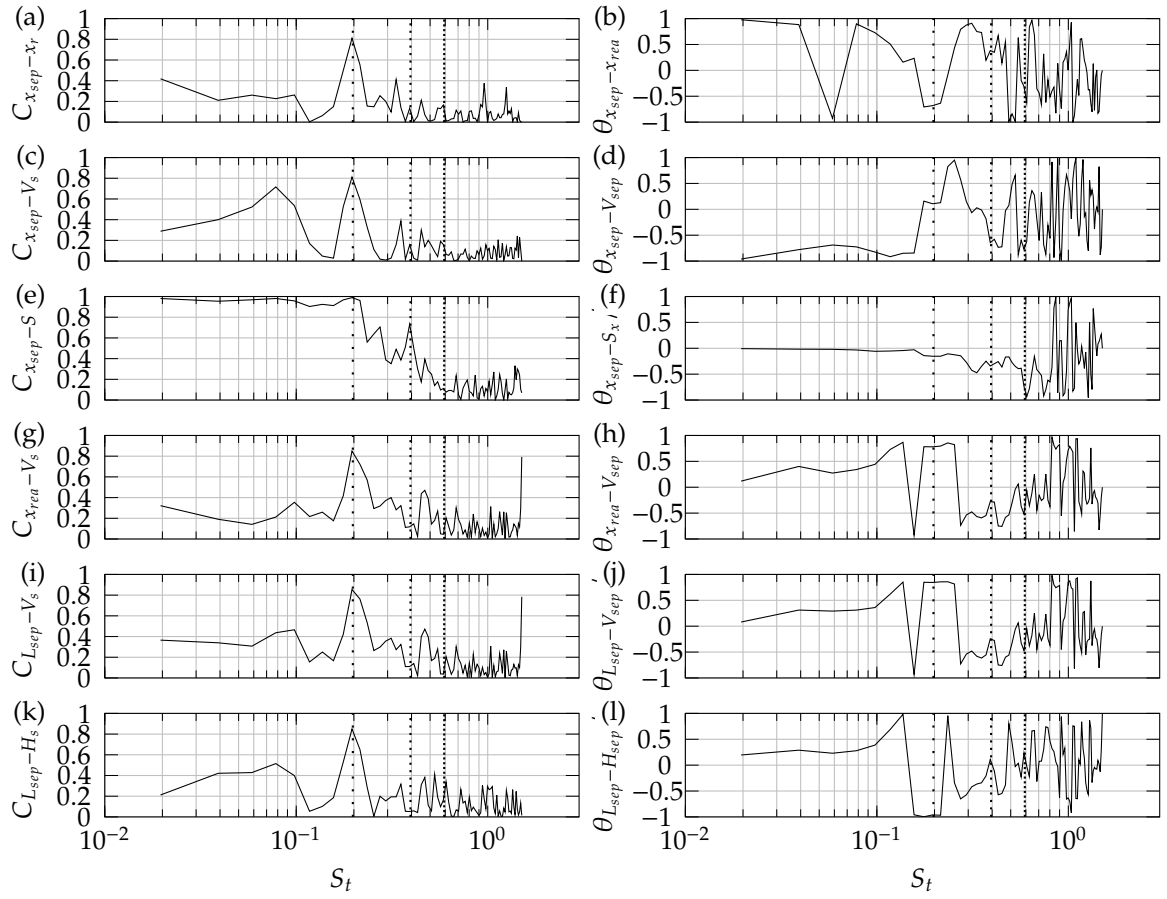


Figure C.84: Coherence and phase of bubble motion for production case LMFH.

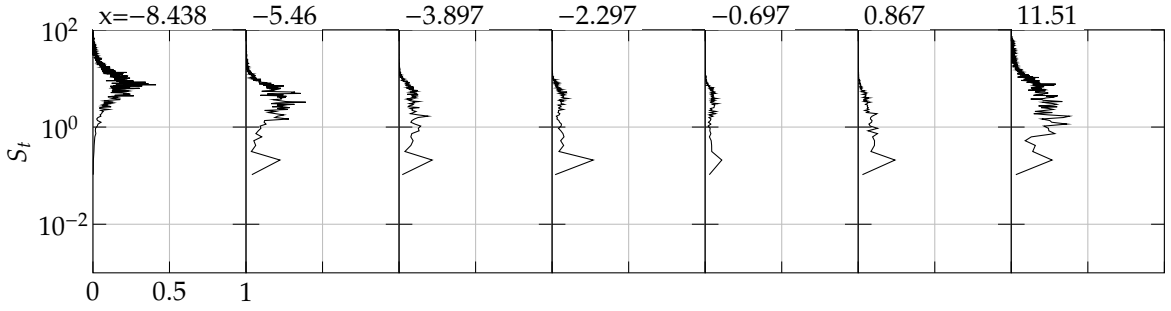


Figure C.85: PSDs of p'_w for case LMFH at common locations.

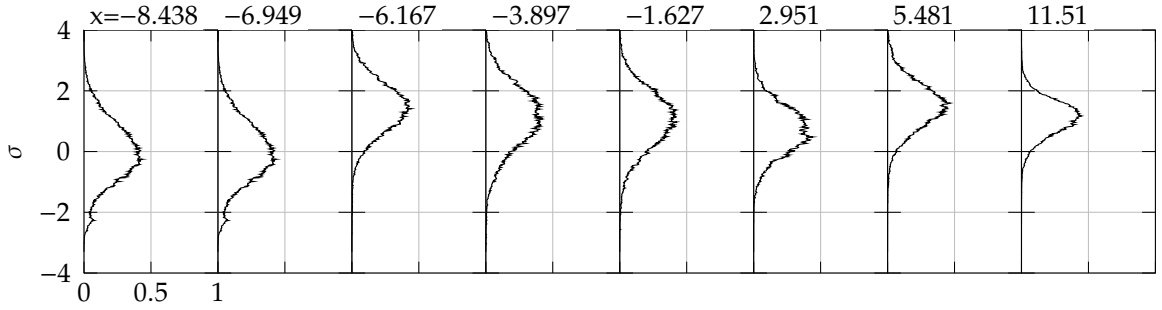


Figure C.86: PDFs of p'_w for case LMFH at selected locations, indicated with ▼ in Figure A.22.

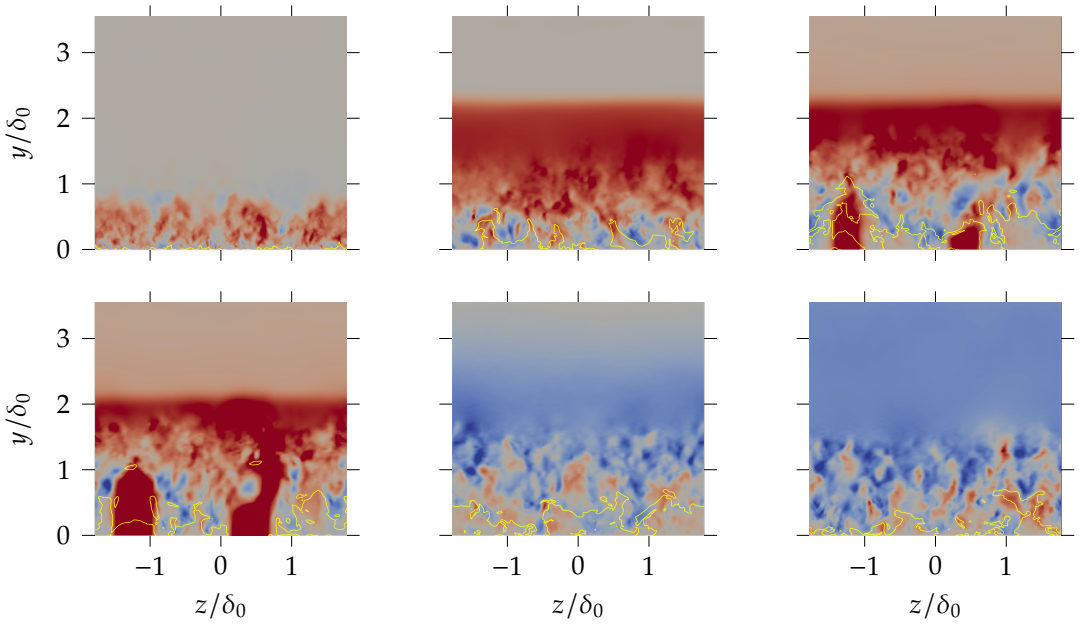


Figure C.87: Span-wise slices of v velocity at peak injection for case LMFH. The yellow line indicates the contour of the separation bubble.

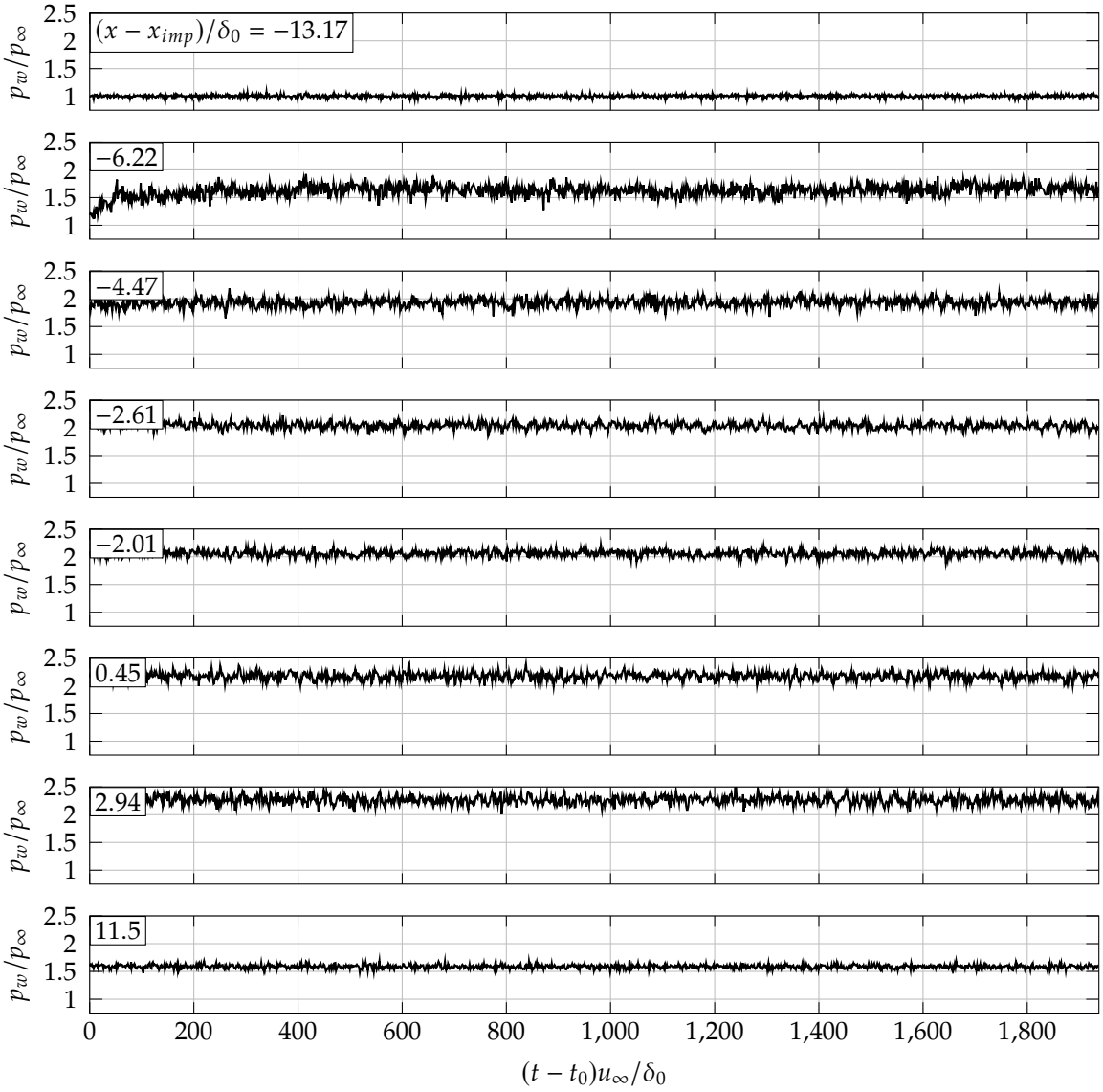


Figure C.88: Wall-pressure for case LMFH obtained by probes placed at locations indicated in the top left corner of each plot.

C.6.5. Case LMFL

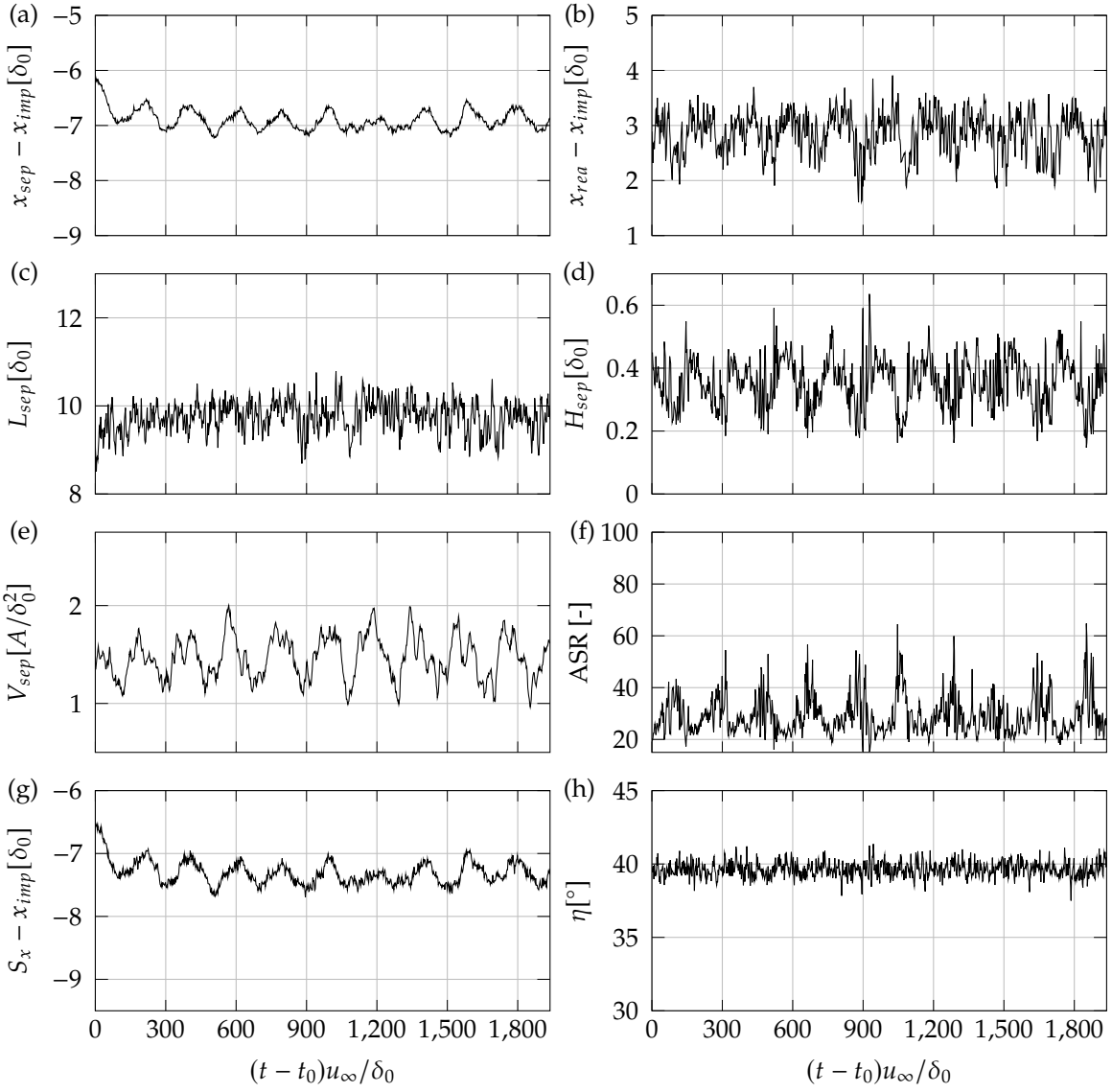


Figure C.89: Bubble motions case LMFL: (a) x_{sep}, (b) x_{rea}, (c) L_{sep}, (d) H_{sep}, (e) V_{sep}, (f) ASR, (g) S_x and (h) η.

Check commented figure below

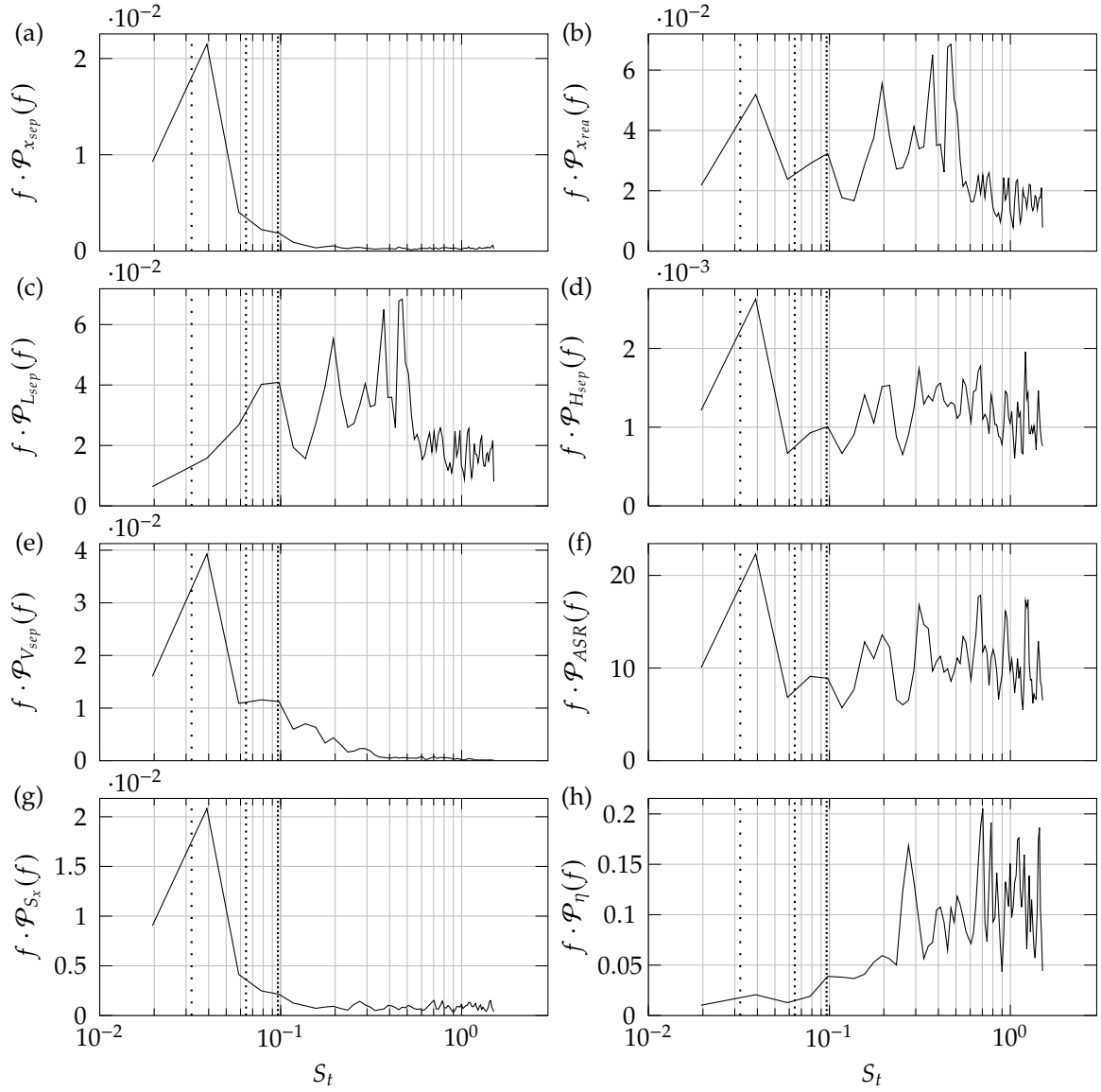


Figure C.90: PSDs of bubble motion case LMFL: (a) x_{sep}, (b) x_{rea}, (c) L_{sep}, (d) H_{sep}, (e) V_{sep}, (f) ASR, (g) S_x and (h) η.

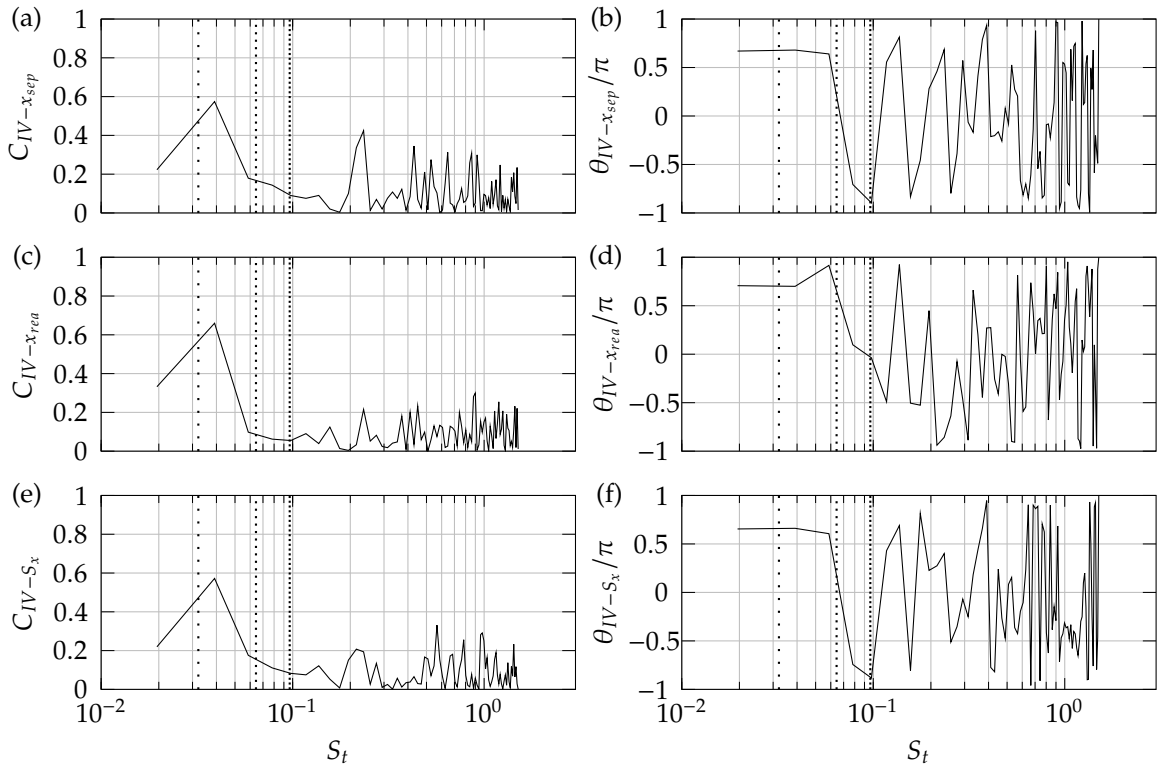


Figure C.91: Coherence and phase between bubble motion and injection velocity for LMFL. (a) Coherence and (b) Phase, between x_{sep} and IV, (c) Coherence and (d) Phase, between x_{rea} and IV.

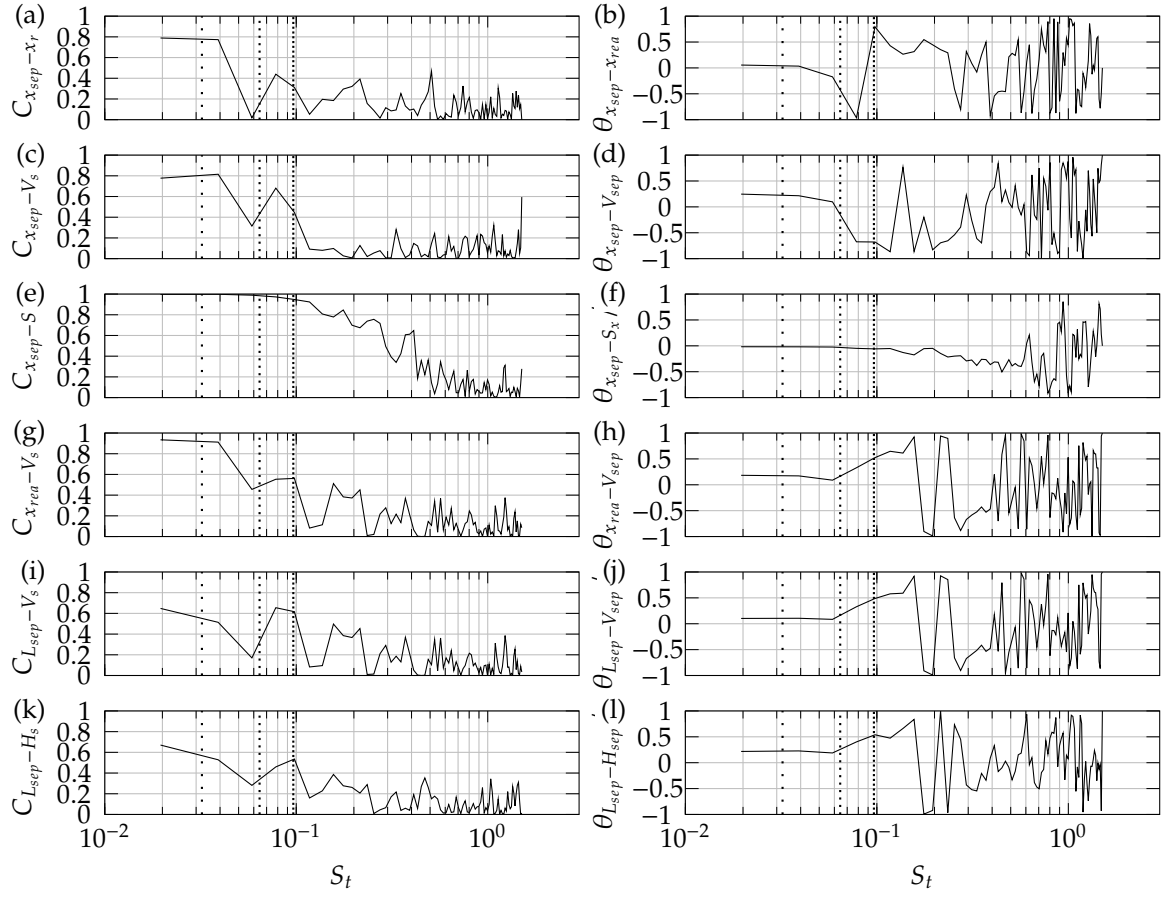


Figure C.92: Coherence and phase of bubble motion for production case LMFL.

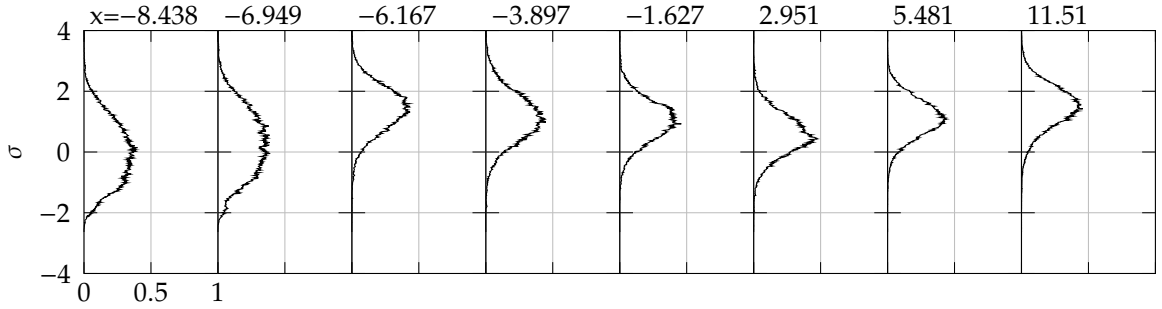


Figure C.93: PDFs of p'_w for case LMFL at selected locations, indicated with ▼ in Figure A.22.

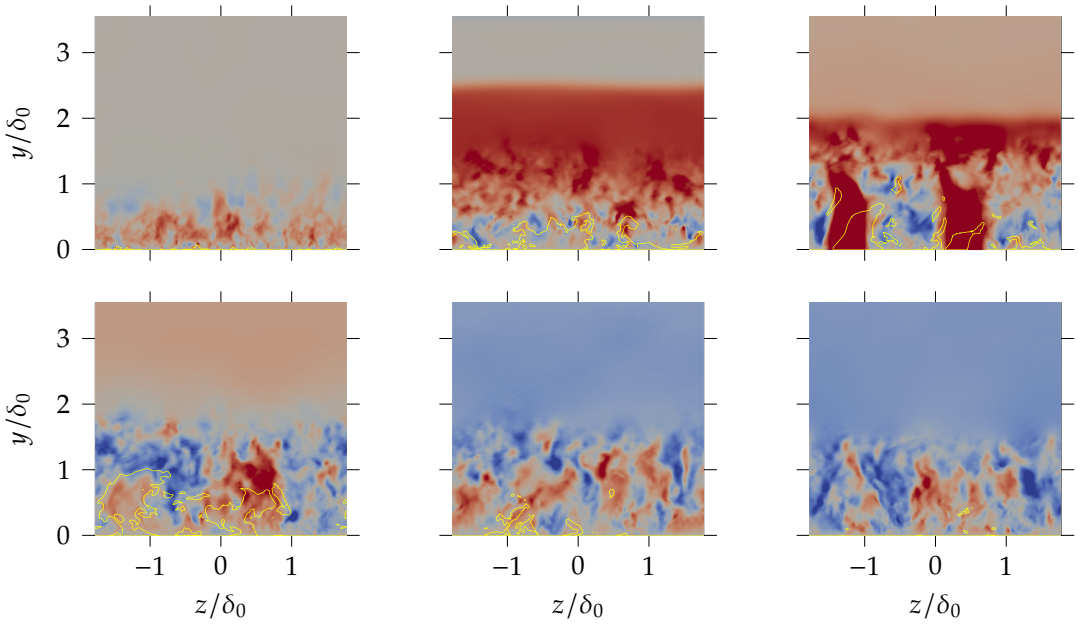


Figure C.94: Span-wise slices of v velocity at peak injection for case LMFL. The yellow line indicates the contour of the separation bubble.

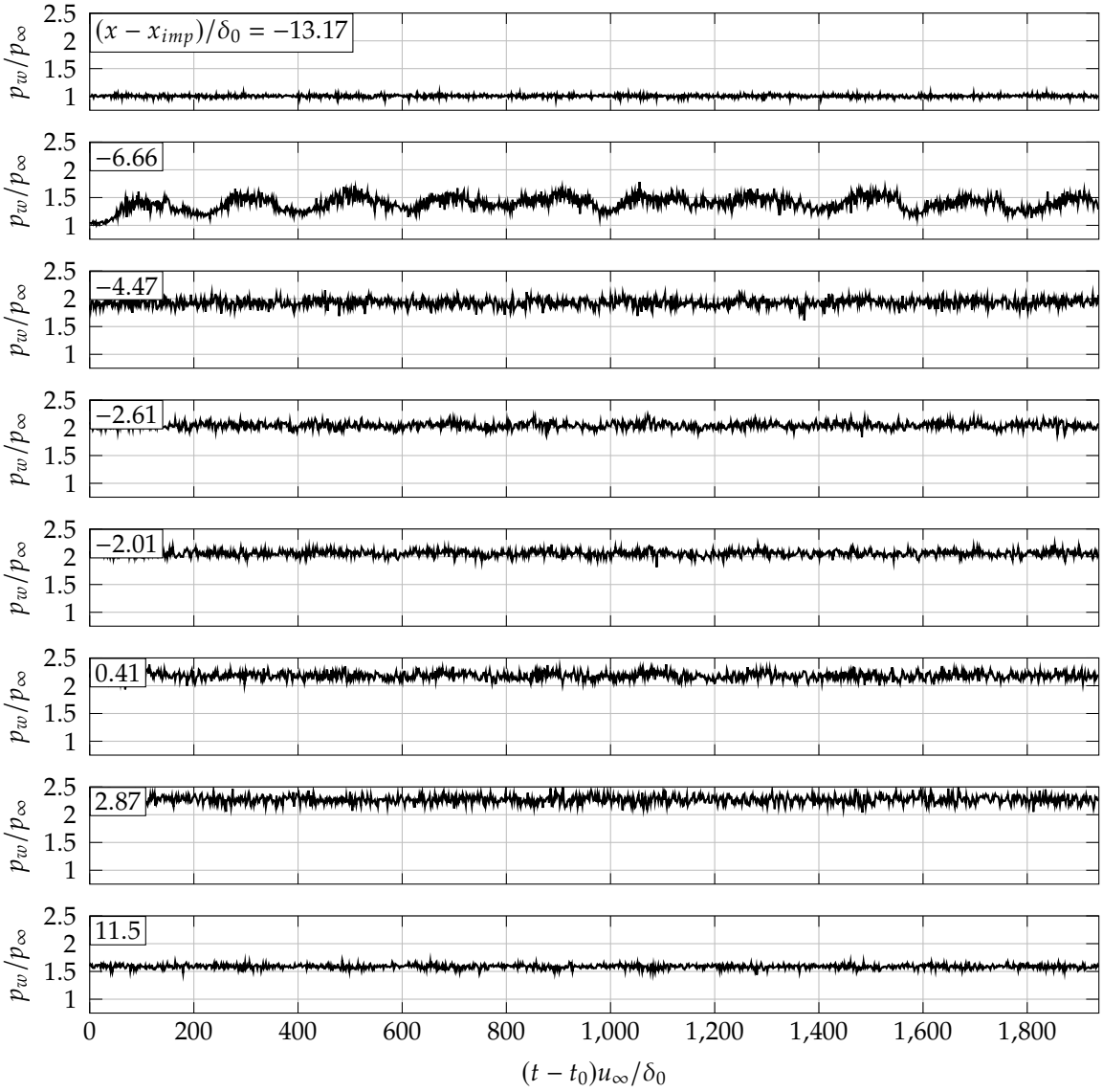


Figure C.95: Wall-pressure for case LMFL obtained by probes placed at locations indicated in the top left corner of each plot.

C.6.6. Case LRFH

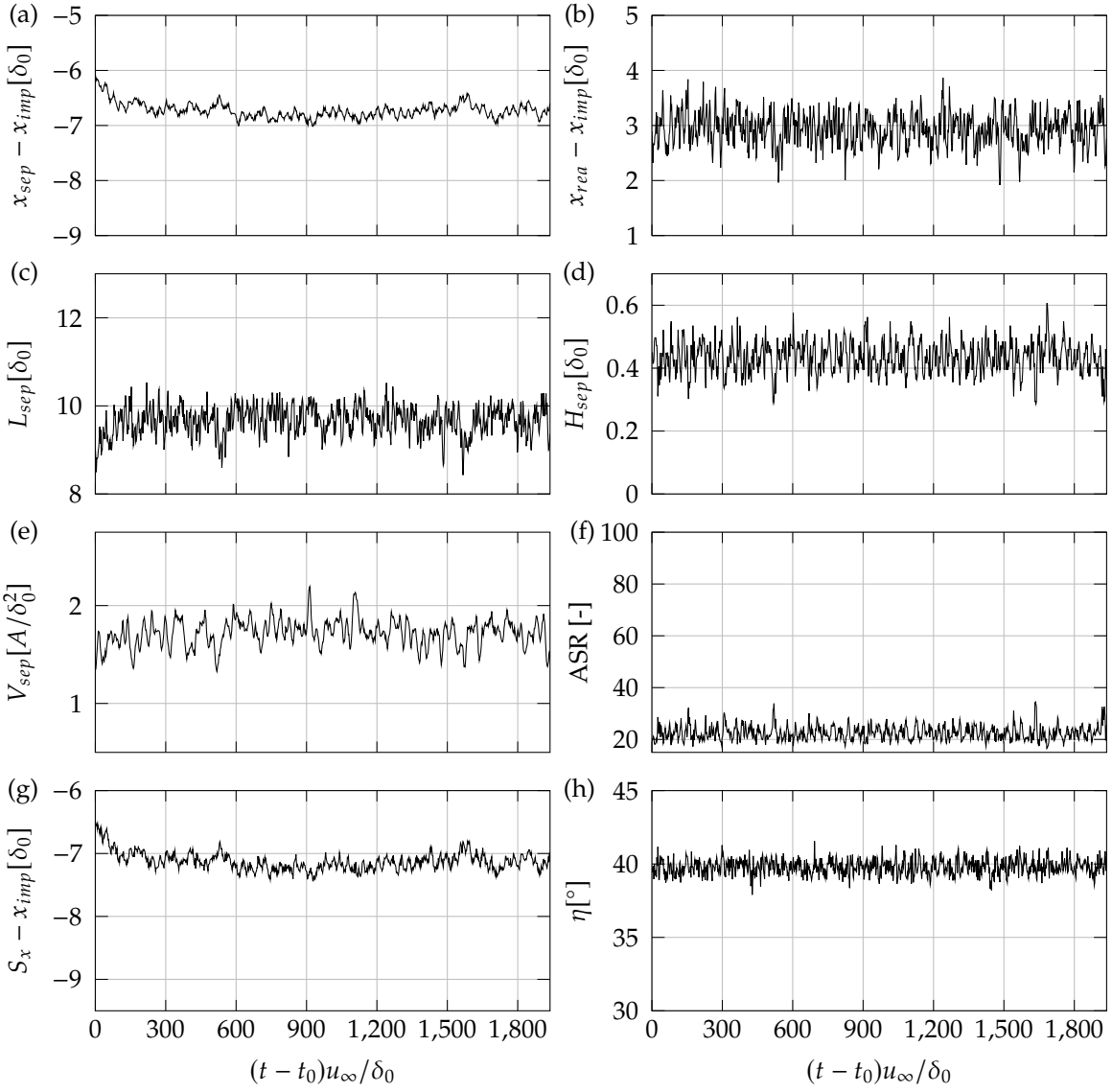


Figure C.96: Bubble motions case LRFH: (a) x_{sep}, (b) x_{rea}, (c) L_{sep}, (d) H_{sep}, (e) V_{sep}, (f) ASR, (g) S_x and (h) η.

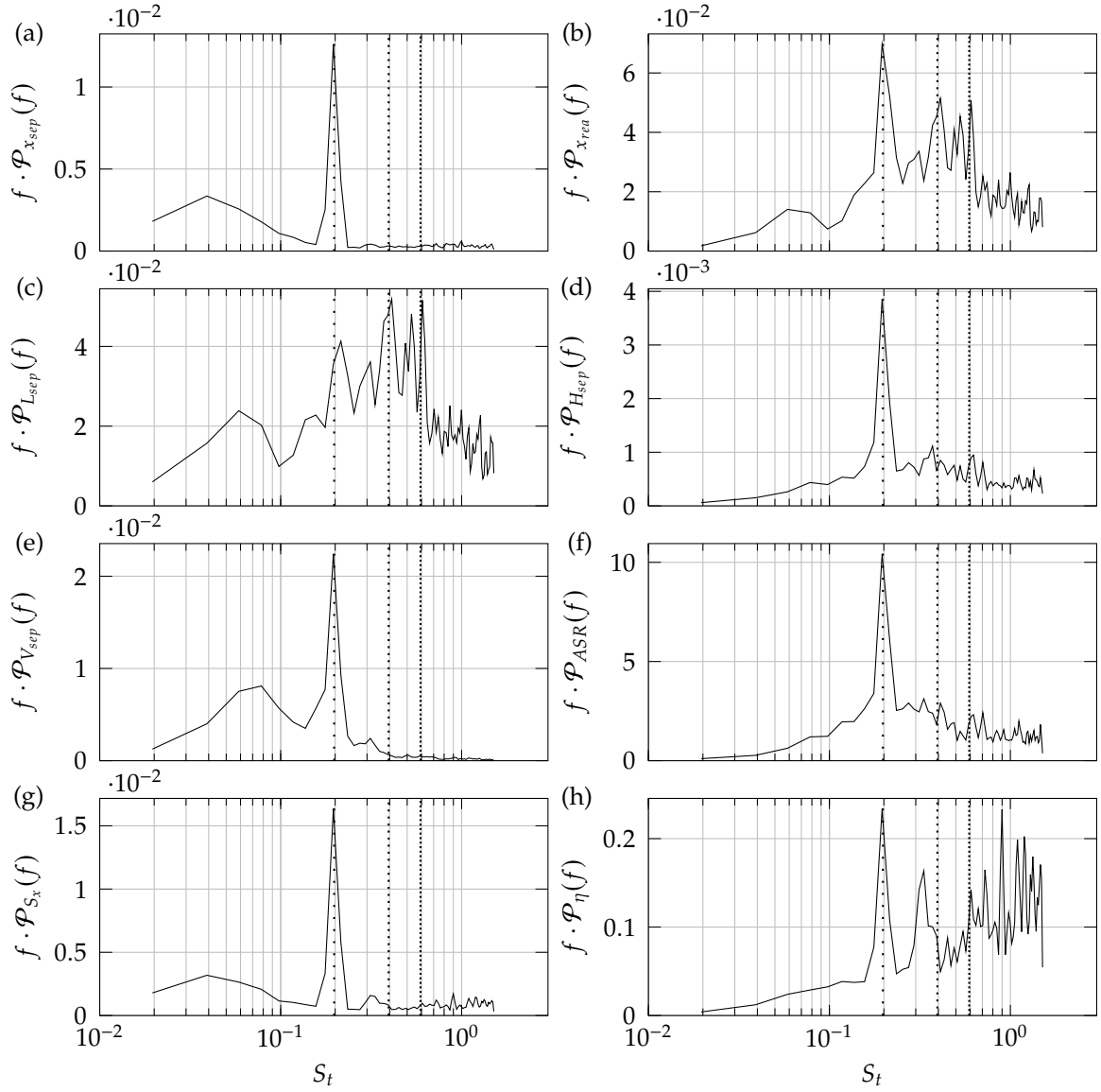


Figure C.97: PSDs of bubble motion case LRFH: (a) x_{sep}, (b) x_{rea}, (c) L_{sep}, (d) H_{sep}, (e) V_{sep}, (f) ASR, (g) S_x and (h) η.

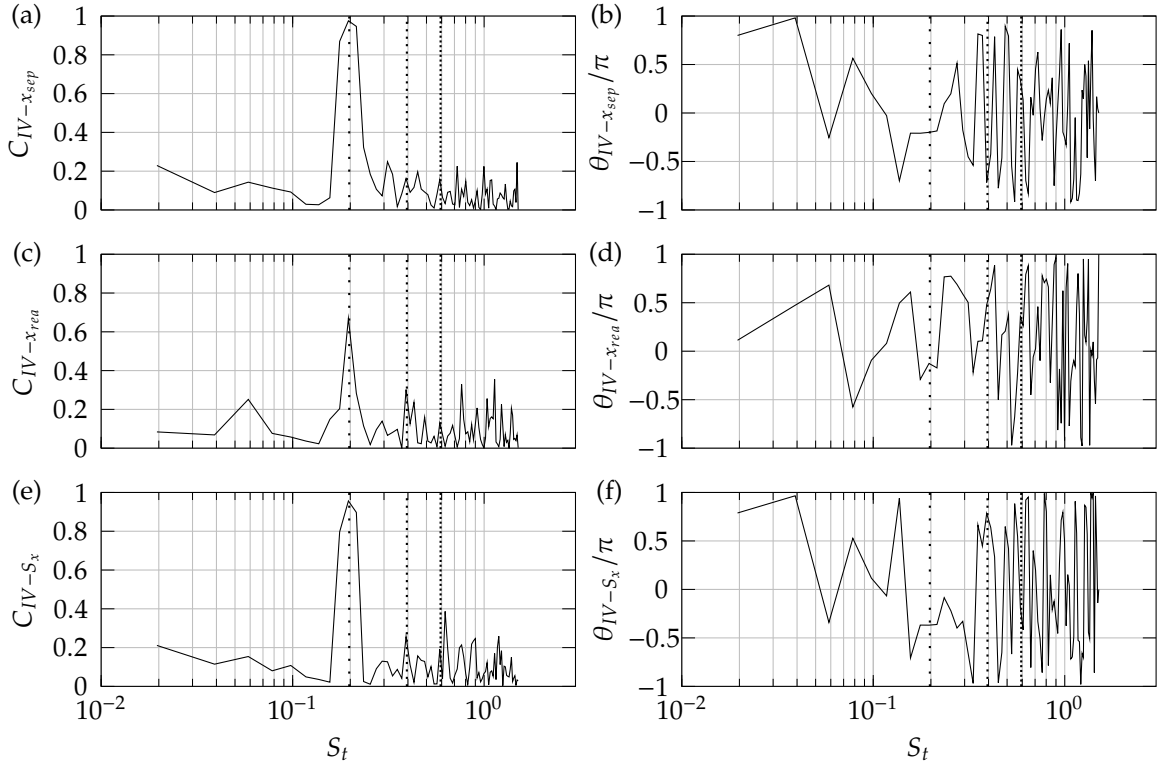


Figure C.98: Coherence and phase between bubble motion and injection velocity for LRFH. (a) Coherence and (b) Phase, between x_{sep} and IV, (c) Coherence and (d) Phase, between x_{rea} and IV.

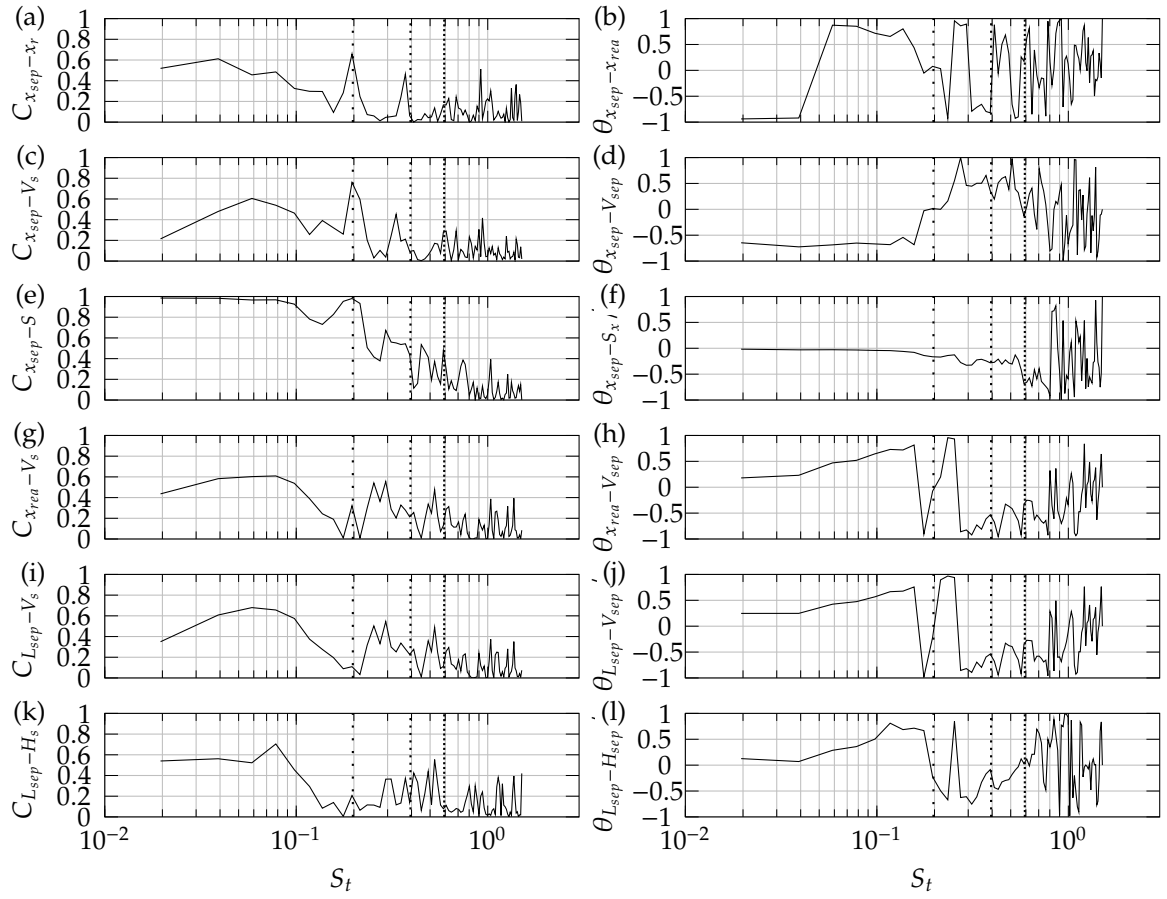


Figure C.99: Coherence and phase of bubble motion for production case LRFH.

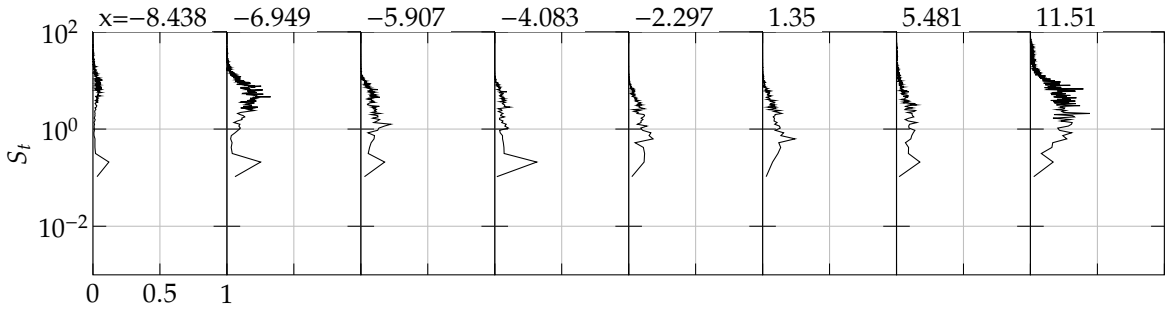


Figure C.100: PSDs of p'_w for case LRFHat selected locations.

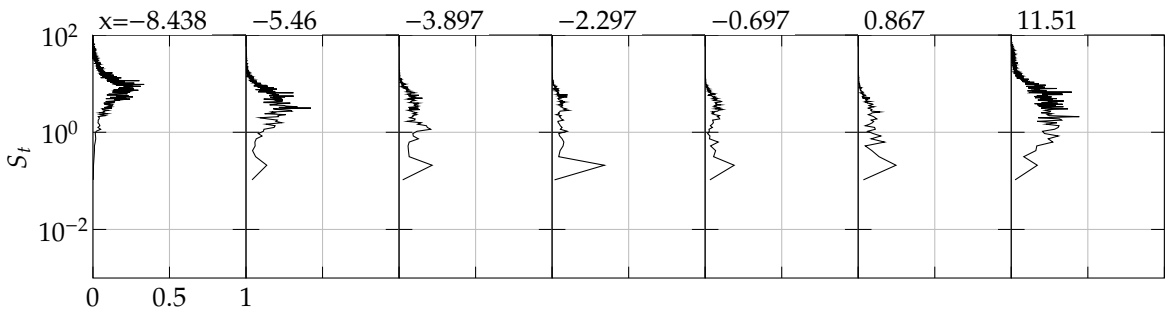


Figure C.101: PSDs of p'_w for case LRFHat common locations.

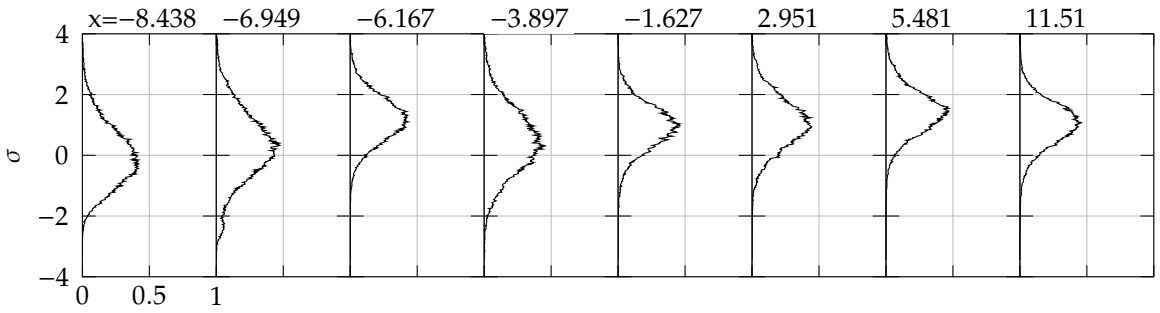


Figure C.102: PDFs of p'_w for case LRFH at selected locations, indicated with ▼ in Figure A.22.

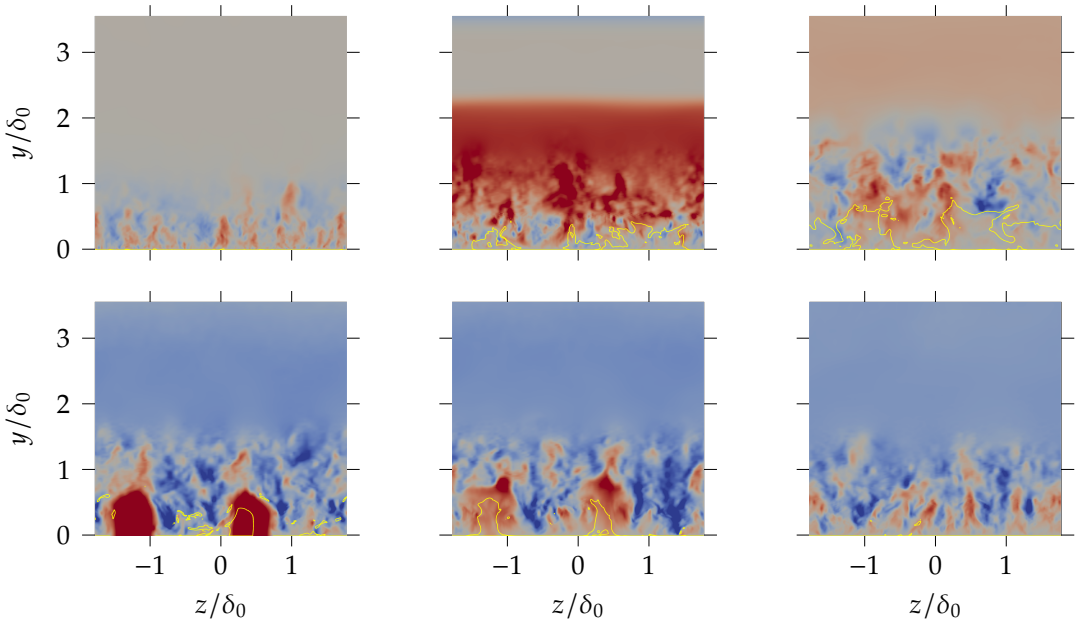


Figure C.103: Span-wise slices of v velocity at peak injection for case LRFH. The yellow line indicates the contour of the separation bubble.

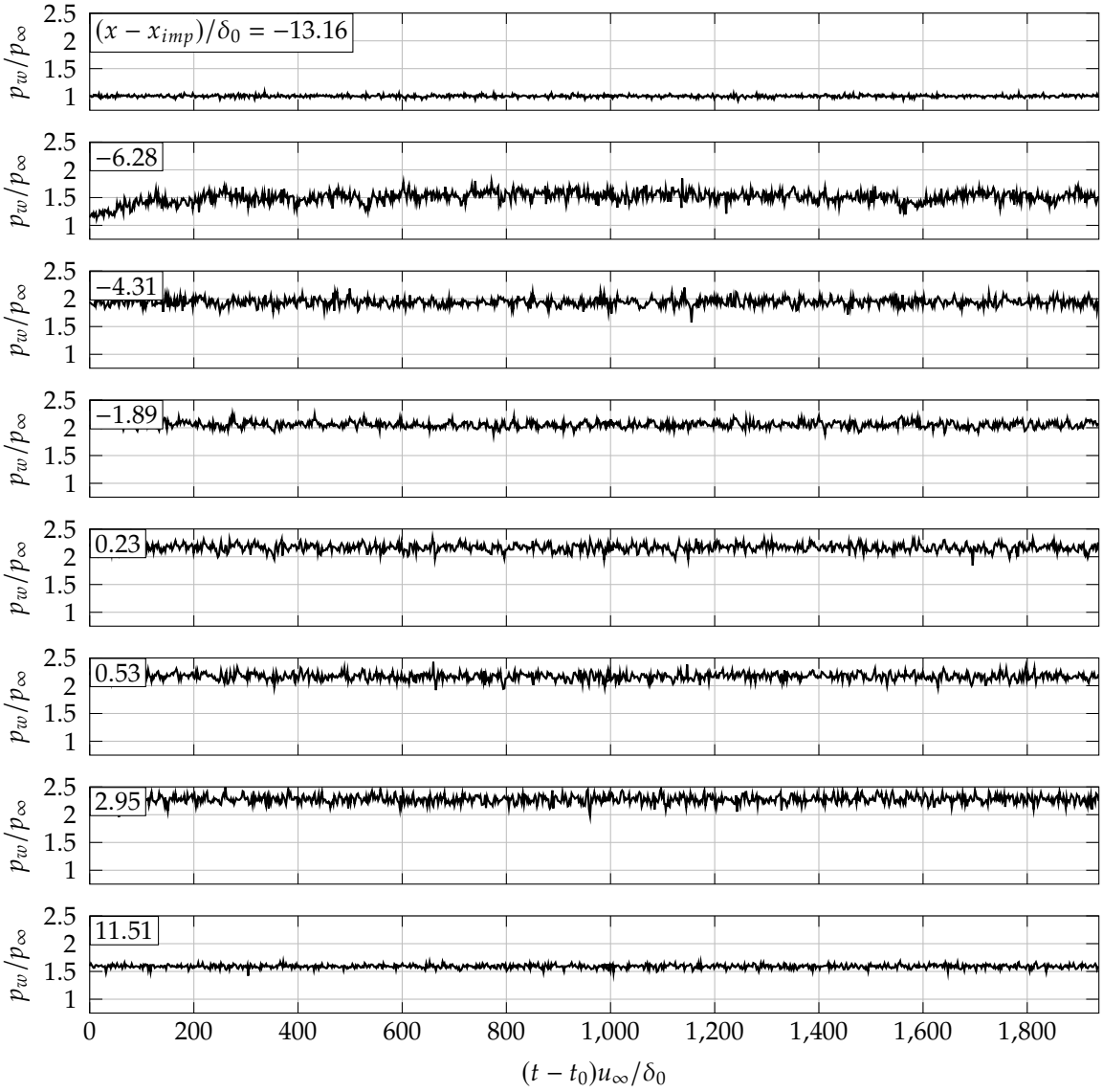


Figure C.104: Wall-pressure for case LRFH obtained by probes placed at locations indicated in the top left corner of each plot.

C.6.7. Case LRFL

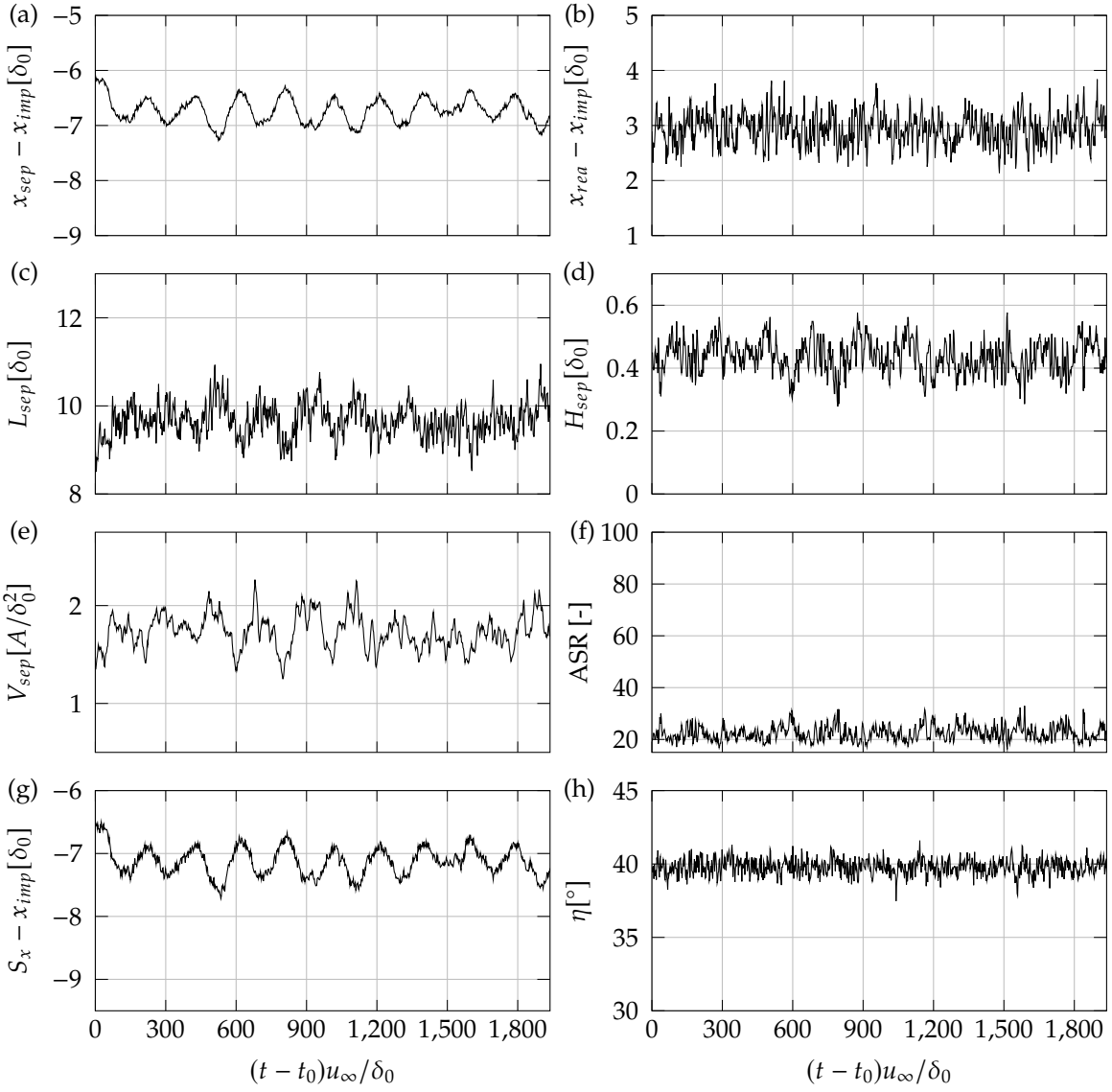


Figure C.105: Bubble motions case LRFL: (a) x_{sep}, (b) x_{rea}, (c) L_{sep}, (d) H_{sep}, (e) V_{sep}, (f) ASR, (g) S_x and (h) η.

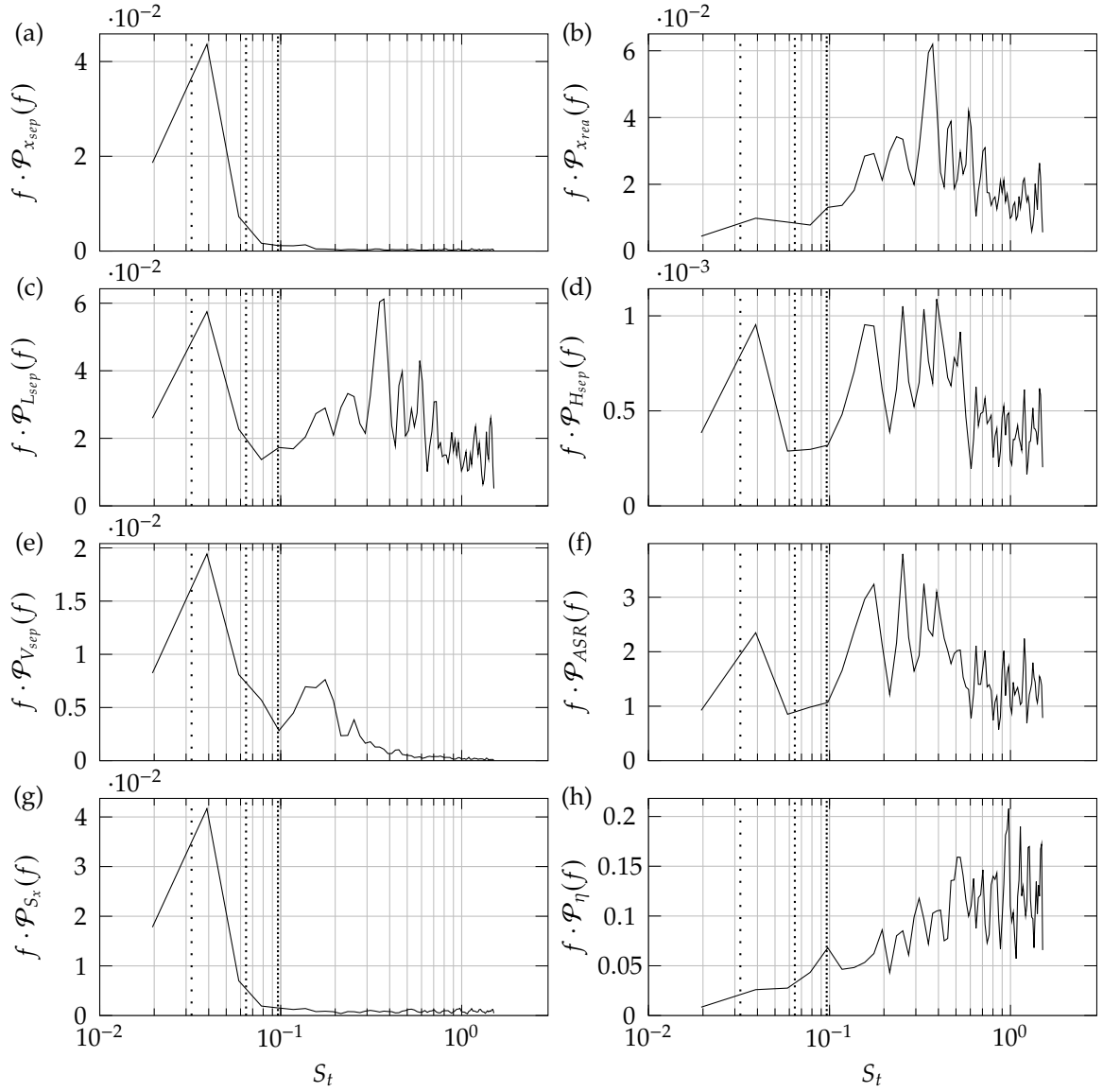


Figure C.106: PSDs of bubble motion case LRFL: (a) x_{sep}, (b) x_{rea}, (c) L_{sep}, (d) H_{sep}, (e) V_{sep}, (f) ASR, (g) S_x and (h) η.

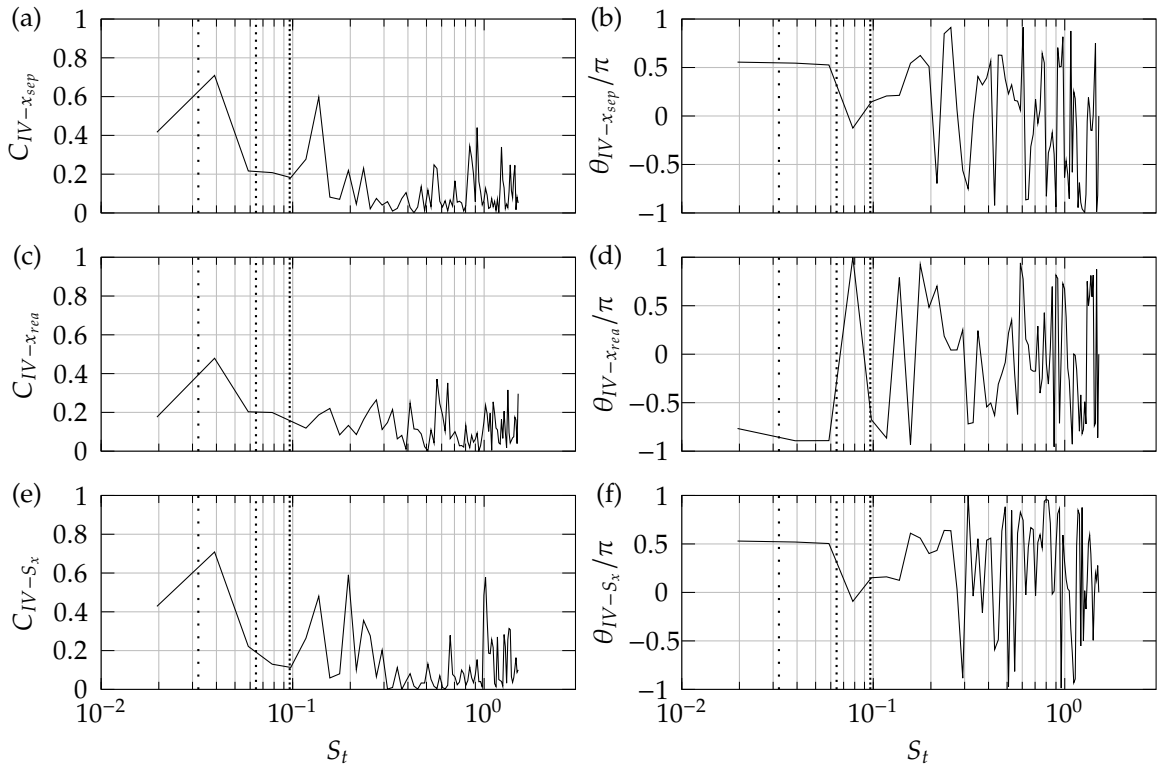


Figure C.107: Coherence and phase between bubble motion and injection velocity for LRFL. (a) Coherence and (b) Phase, between x_{sep} and IV, (c) Coherence and (d) Phase, between x_{rea} and IV.

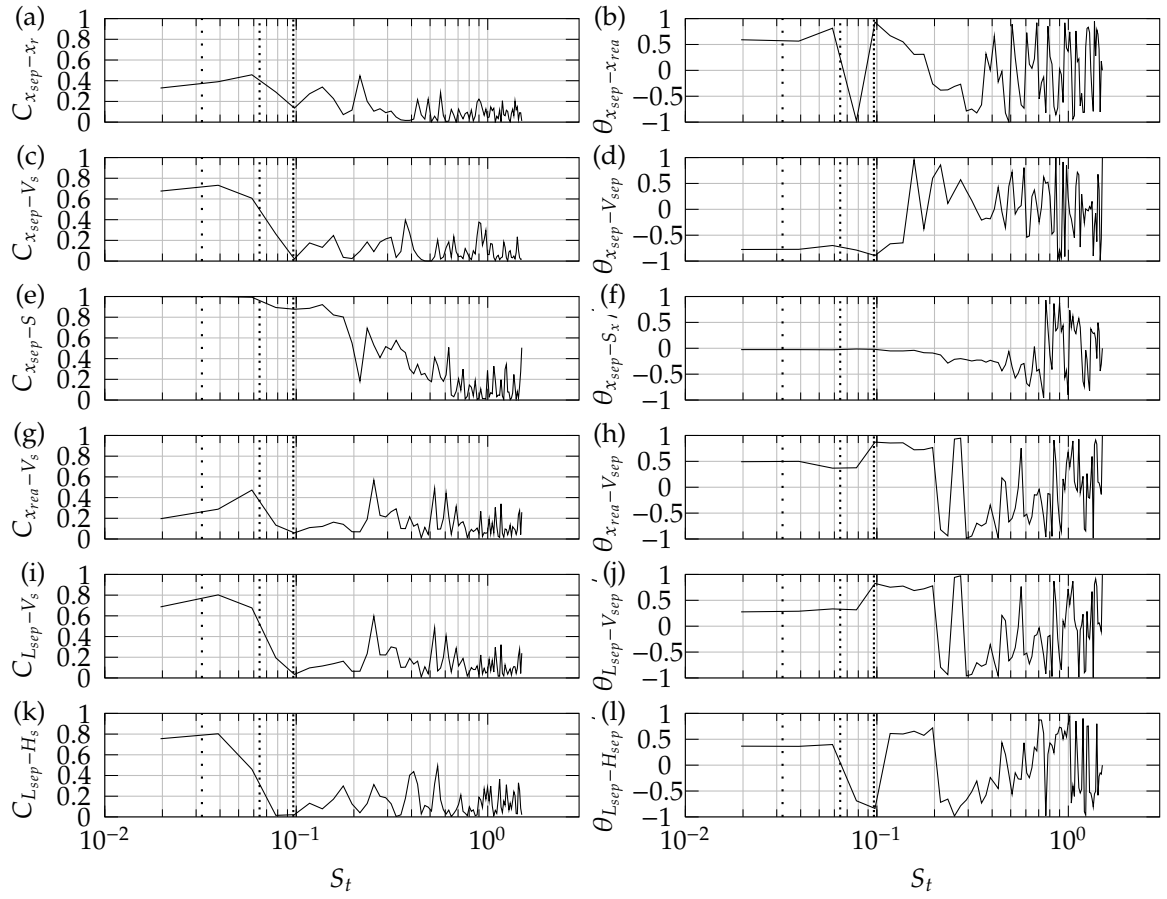


Figure C.108: Coherence and phase of bubble motion for production case LRFL.

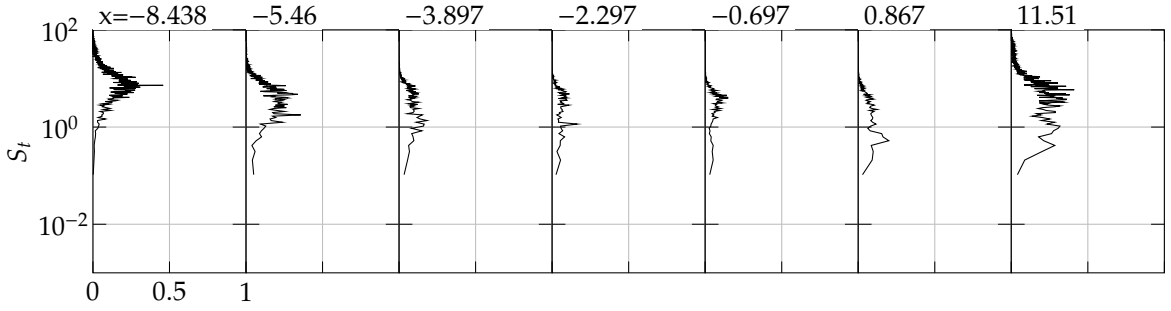


Figure C.109: PSDs of p'_w for case LRFL at common locations.

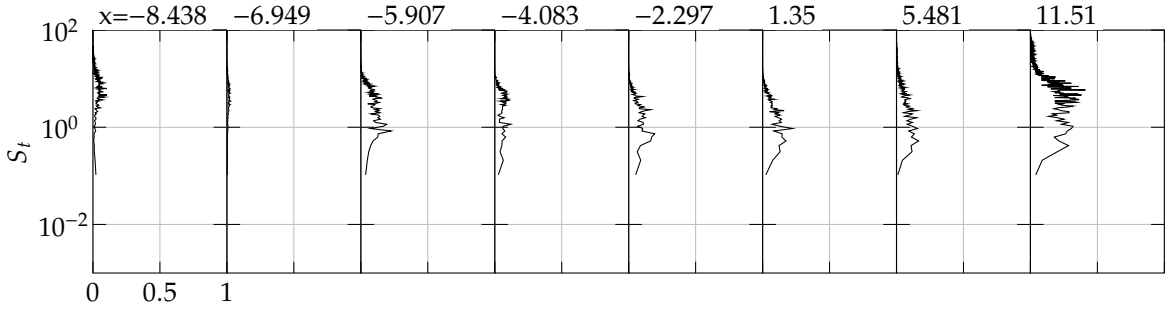


Figure C.110: PSDs of p'_w for the LRFLcase at selected locations.

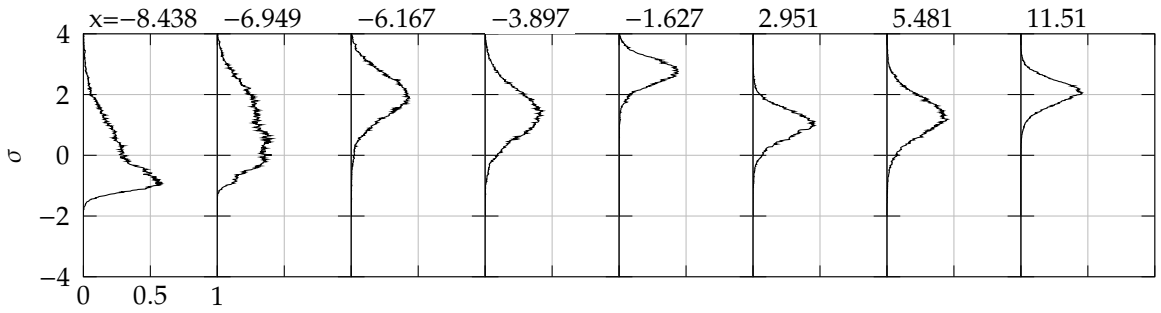


Figure C.111: PDFs of p'_w for case LRFL at selected locations, indicated with ▼ in Figure A.22.

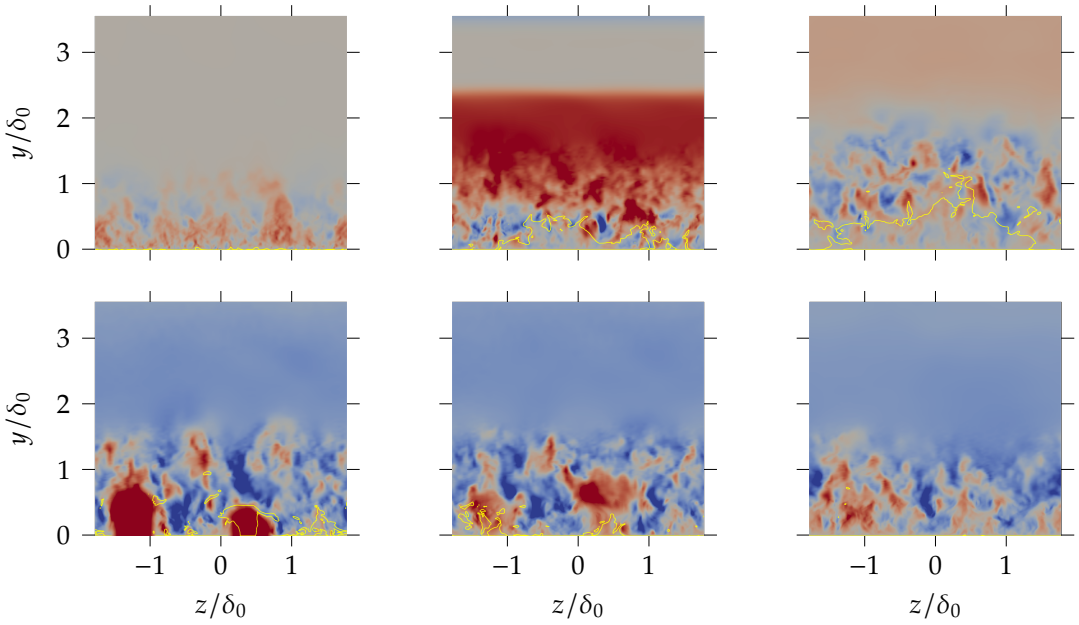


Figure C.112: Span-wise slices of v velocity at peak injection for case LRFL. The yellow line indicates the contour of the separation bubble.

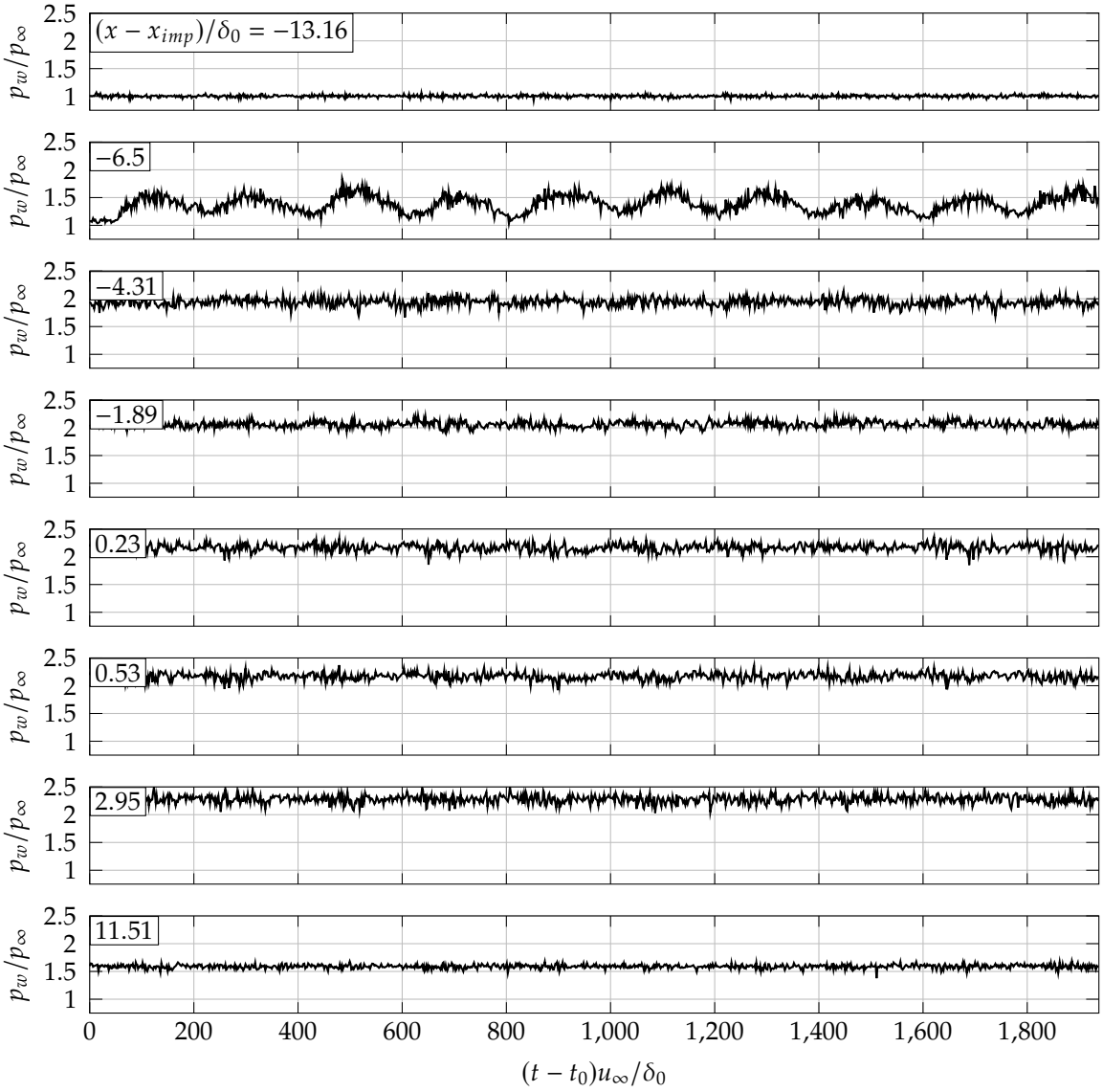


Figure C.113: Wall-pressure for case LRFL obtained by probes placed at locations indicated in the top left corner of each plot.